

The effect of H₂O on O₂ reduction in Li-O₂ batteries



Conrad Holc

Trinity College

Department of Materials

University of Oxford

A thesis submitted for the degree of Doctor of Philosophy

Trinity 2019

Declaration of Originality

I, Conrad Holc, hereby declare that this doctoral thesis, which is approximately 37300 words in length, has been written by me and is a record of work that I have carried out. The work presented here has not been submitted in any previous application for a higher degree.

Conrad Holc

Trinity 2019

Acknowledgments

Firstly, I would like to thank my supervisor, Professor Peter G. Bruce for the opportunity to work in his world-class battery group and for his advice and support throughout my DPhil research.

I am very grateful to Dr Lee R. Johnson for his electrochemical knowledge and continual guidance on my project. I also appreciate his advice on the revision of my thesis. I would like to thank Dr Zarko Jovanov for his help in the laboratory and gaining experience in the techniques and experiments that made this thesis possible. His expertise and patience were invaluable.

I would like to offer my thanks and gratitude to all group members, past and present, for making my time in the group so enjoyable and making sure that research was never dull. In particular, I would like to thank Dr Shanmu Dong, Dr Yuhui Chen, Dr Euan McTurk, Dr Lukas Lutz and Dr Xiangwen Gao for their discussions about Li-air batteries. I am grateful to Dr Ola Hekselman and Dr Nick Rees for their help and discussions concerning NMR measurements. I would like to thank Mr Rob House and Mr Dominic Förstermann for their assistance with the use of XRD instruments. I am grateful to Dr Stefanie Zekoll for help with SEM measurements. I would also like to thank Dr Andy Naylor, Dr Benjamin Bergner, Mr Alexander Pateman and Mr Gareth Hartley for their encouragement and friendship during my degree.

I would like to thank my colleagues at the University of Nottingham, Dr Sean Goodwin and Mr Rory McNulty, for their insightful comments on chapters in this thesis.

Finally, special thanks to my parents Michał and Elżbieta, my brother Sebastian, relatives in Poland, and grandmother Mirosława Holc and aunt Danuta Gadecka, who both sadly passed away recently and will be sorely missed. I would not have been able to achieve everything that I have without their continual support and love.

Abstract

There is significant interest in aprotic lithium-air batteries due to their high theoretical specific energy. During discharge, O_2 is reduced at the positive electrode and forms Li_2O_2 . Cells are typically discharged in O_2 , not air, because CO_2 and H_2O can interfere with the discharge reaction. However, lithium-air batteries will need to use atmospheric O_2 if they are to supplant state-of-the-art lithium-ion cells. Therefore, it is important to establish how detrimental CO_2 and H_2O are to the battery. The former is well-known to induce the formation of Li_2CO_3 in $Li-O_2$ batteries, but the recent work has suggested that H_2O appears to be beneficial at low concentrations in some solvents (e.g. glyme ethers), increasing discharge capacities and still forming Li_2O_2 , while in other solvents, such as acetonitrile (CH_3CN), $LiOH$ is the discharge product. Several mechanisms have been proposed to rationalise these findings, but as yet, there is no consensus on the role of H_2O on O_2 reduction.

The purpose of this work was to understand how H_2O affects O_2 reduction in electrolytes using acetonitrile (CH_3CN), dimethyl sulfoxide (DMSO) and tetraethylene glycol dimethyl ether (TEGDME) solvents, and, why the $4e^-$ reduction appears to be unfavourable at low H_2O concentrations. Electrochemical and spectroscopic analysis found that, in CH_3CN , $4e^-$ reduction occurred at lower H_2O concentrations than in DMSO and TEGDME. A mechanism based on the ability of the H_2O /solvent mixture to stabilise OH^- was proposed, with mixtures that stabilise OH^- promoting $4e^-$ O_2 reduction. The mechanism was confirmed by using pressure cells to identify the electrochemical reaction occurring during discharge. Cells using DMSO and TEGDME solvents underwent $2e^-$ O_2 reduction, even with 1 M H_2O concentrations. Finally, TEGDME cells were discharged in a 13% RH at 25 °C O_2 atmosphere, corresponding to 1 M H_2O in solution, and Li_2O_2 was confirmed as the discharge product, demonstrating that it is possible for electrolytes to withstand a near-atmospheric humidity.

Contents

Abbreviations	1
1. Introduction	5
1.1. Rechargeable batteries as an alternative to petroleum.....	5
1.2. Current state-of-the-art batteries	6
1.3. Lithium-air as an alternative	7
1.4. Early developments.....	9
1.5. Fundamental chemistry	10
1.5.1. Oxygen reduction reaction (ORR) mechanism	10
1.5.2. Oxygen evolution reaction (OER) mechanism.....	13
1.6. Solution and surface mechanisms of Li_2O_2 growth	18
1.7. The stability of key components of Li- O_2 batteries	21
1.7.1. Solvents	22
1.7.2. Salts.....	28
1.7.3. Carbon.....	30
1.7.4. Binders.....	31
1.7.5. Non-carbon positive electrodes	33
1.8. Negative electrodes	35
1.9. Strategies to reduce overpotentials and increase discharge capacity.....	37
1.9.1. Catalysts	37
1.9.2. Redox mediators	38
1.10. The effect of impurities present in air	40
1.10.1. CO_2 chemistry at the positive electrode	43

1.10.2.	H ₂ O chemistry at the positive electrode	44
1.11.	A universal mechanism describing the effect of H ₂ O on O ₂ reduction	49
1.12.	References	52
2.	Experimental methods and techniques.....	66
2.1.	Electrochemical measurements	66
2.2.	Rotating ring-disk electrode (RRDE) measurements	68
2.3.	On-line mass spectrometry.....	72
2.4.	Ultraviolet-visible (UV-vis) spectroscopy.....	73
2.5.	Fourier-transform infrared (FTIR) spectroscopy.....	76
2.6.	Raman spectroscopy and surface-enhanced Raman spectroscopy	76
2.7.	Nuclear magnetic resonance (NMR) spectroscopy.....	78
2.8.	X-ray diffraction (XRD)	79
2.9.	Scanning electron microscopy and energy-dispersive X-ray spectroscopy...	80
2.10.	References	81
3.	Effect of H ₂ O on O ₂ reduction in TBA ⁺ -based electrolytes	82
3.1.	Introduction	82
3.2.	Experimental	83
3.2.1.	Materials	83
3.2.2.	Voltammetry	84
3.2.3.	Simulations of voltammograms	84
3.3.	Electrochemical response of O ₂ /O ₂ ⁻ couple to H ₂ O	85
3.3.1.	Cyclic voltammograms	85
3.3.2.	Simulations of voltammetric responses	90

3.4.	Identification of reaction pathways in solvent/H ₂ O mixtures.....	94
3.5.	Chemical routes to protic O ₂ reduction products from O ₂ ⁻ and H ₂ O.....	102
3.6.	Spectroscopic identification of ORR intermediates/products	106
3.7.	Conclusions	110
3.8.	References.....	112
4.	Effect of H ₂ O on aprotic O ₂ reduction in Li ⁺ -based electrolytes	115
4.1.	Background on O ₂ reduction	115
4.2.	Experimental.....	116
4.2.1.	Materials	116
4.2.2.	Rotating ring-disk electrode (RRDE) preparation	117
4.2.3.	Nuclear magnetic resonance (NMR) spectroscopy.....	118
4.2.4.	Determination of ANs of solvent/H ₂ O mixtures	118
4.2.5.	Raman spectroscopy	119
4.3.	Electrochemical response of O ₂ /O ₂ ⁻ couple to H ₂ O.....	120
4.4.	Identification of reaction pathways in solvent/H ₂ O mixtures.....	126
4.5.	Chemical routes to protic O ₂ reduction products from O ₂ ⁻ and H ₂ O.....	137
4.6.	Spectroscopic identification of ORR intermediates/products	138
4.7.	OH ⁻ formation mechanism in mixed organic solvent/H ₂ O electrolytes.....	141
4.7.1.	Solvent effects on the 4e ⁻ O ₂ reduction reaction	142
4.7.2.	Stabilisation of OH ⁻	143
4.7.3.	H ₂ O/solvent interactions.....	147
4.7.4.	Implications of mechanism on solvent choice.....	149
4.8.	Conclusions	150

4.9. References.....	151
5. Discharge studies of Li-O ₂ cells under wet conditions.....	154
5.1. Experimental	155
5.1.1. Two-electrode cell components.....	155
5.1.2. Pressure cells	156
5.1.3. Relative humidities	157
5.1.4. Open cell discharges.....	158
5.1.5. Post-discharge characterisation	159
5.2. Identification of reactions occurring in full cells	160
5.2.1. Discharge studies using pressure cells	160
5.2.2. <i>Ex situ</i> characterisations	166
5.3. Discharging cells in a humid O ₂ atmosphere	168
5.3.1. Equilibria between H ₂ O in the vapour and solution phases.....	168
5.3.2. Characterisation of discharged cells.....	173
5.4. Conclusions	179
5.5. References.....	179
6. Perspectives and future work	181
Appendix 1: N ₂ electrochemistry.....	183
Appendix 2	198

Abbreviations

AFM	Atomic force microscopy
AN	Acceptor number
CH ₃ CN	Acetonitrile
CV	Cyclic voltammogram
DEC	Diethyl carbonate
DEMS	Differential electrochemical mass spectrometry
DME	1,2-dimethoxyethane
DMSO	Dimethyl sulfoxide
DN	Donor number
EC	Ethyl carbonate
E _{P,ox}	Oxidation peak potential
E _{P,red}	Reduction peak potential
Et ₃ PO	Triethylphosphine oxide
FEV	Fully electric vehicle
FTIR	Fourier-transform infrared
GHU	Gas-handling unit
GC	Glassy carbon
H-bonding	Hydrogen bonding
i _L	Limiting current

$i_{P,ox}$	Oxidation peak current
$i_{P,red}$	Reduction peak current
j	Current density
Li-O ₂	Lithium-oxygen
LiClO ₄	Lithium perchlorate
LiPF ₆	Lithium hexafluorophosphate
LiTf	Lithium triflate
LiTFSI	Lithium bis(trifluoromethanesulfonyl)imide
Li _x FePO ₄	Partially delithiated lithium iron phosphate
MS	Mass spectrometer
NMR	Nuclear magnetic resonance
NPG	Nanoporous gold
OER	Oxygen evolution reaction
ORR	Oxygen reduction reaction
PC	Propylene carbonate
PE	Polyethylene
PEO	Poly(ethylene)oxide
Ph ₂ POCl	Diphenylphosphinic chloride
PP	Polypropylene
PTFE	Polytetrafluoroethylene
PVDF	Polyvinylidene difluoride

$Q_{\text{ox}}/ Q_{\text{red}}$	Coulombic efficiency
RH	Relative humidity
RRDE	Rotating ring-disk electrode
RTIL	Room temperature ionic liquid
SE	Solid electrolyte
SEI	Solid-electrolyte interphase
SEM	Scanning electron microscopy
SERS	Surface-enhanced Raman spectroscopy
TBA	Tetrabutylammonium
TBAClO ₄	Tetrabutylammonium perchlorate
TBAOH	Tetrabutylammonium hydroxide
TEGDME	Tetraethylene glycol dimethyl ether
TTF	Tetrathiafulvalene
XPS	X-ray photoelectron spectroscopy
XRD	X-ray diffraction
$Y_{\text{Li}_2\text{O}_2}$	Lithium peroxide yield
δ	Chemical shift
ΔG	Change in Gibbs free energy
ΔH_{mix}	Enthalpy of mixing

1. Introduction

1.1. Rechargeable batteries as an alternative to petroleum

There is a need to reduce the world's dependency on fossil fuels as the greenhouse gas emissions associated with burning these fuels contributes to the warming global climate. Approximately two-thirds of oil is used for transportation, so reducing the dependence of vehicles on petroleum products is an important goal towards energy sustainability¹. Furthermore, petrol and diesel-powered motor vehicles generate harmful compounds, such as nitrogen oxides, which contribute to urban pollution and smog². The electrification of the transportation sector would be a significant step towards the goal of reducing greenhouse gas emissions. It would also reduce pollution in cities by moving the generation of pollutants to power stations or prevent them entirely, if renewable sources are used to generate electricity.

Electric vehicles are one of the most promising solutions and car manufacturers have been producing both hybrid and fully electric vehicles (FEVs) for several years. Initially, FEVs suffered from short driving ranges, which was due to the poor specific energies of lithium-ion batteries (LIBs) used in the vehicles³. However, developments in LIB technology have overcome this limitation. FEVs, such as those made by Tesla, have driving ranges in excess of 300 miles, but are too expensive for the mass market, which prevents their widespread use. Transition metals are used in LIBs and are often expensive, one reason the cost of such FEVs is high. However, development of a battery system with high specific energy and using cheaper materials than LIBs would revolutionise the transportation sector by allowing the manufacture of FEVs with mass-market appeal (comparable cost and driving range to petrol vehicles). Provided the electricity used to charge FEVs were derived from renewable or low carbon sources such as solar or nuclear power, greenhouse gas emissions from the transportation sector would be reduced.

1.2. Current state-of-the-art batteries

Secondary batteries have progressed from heavy metal systems (lead-acid, nickel-cadmium and nickel-metal hydride) to Li-based chemistry^{4,5}. All of these batteries rely on reactions involving light elements; the former utilise protons, while the latter use Li^+ ions. Theoretically, this would make the battery lightweight. However, all these battery chemistries require heavy metals, which undergo changes to their oxidation state as part of the reaction involving H^+ or Li^+ at an electrode. One of the key targets in battery development is to increase the energy density of rechargeable batteries. This can be achieved by increasing the voltage and/or capacity per unit mass/volume of the battery, as the energy density is the product of these two values. Using a metallic Li anode would increase LIB energy density as Li has a high theoretical capacity of 3860 mAh g^{-1} . However, Li readily forms dendrites on cycling, which presents a safety hazard as internal short-circuits could occur, so an intercalation anode, with lower specific capacity, is used. Li-based batteries have nevertheless superseded the heavy metal systems because the former operate at higher voltages, typically around 3.7 V compared to 1.2 V for nickel-cadmium and nickel-metal hydride batteries. This is because Li is one of the most electropositive elements (-3.04 V versus the standard hydrogen electrode). As a result, the energy density of LIBs is up to five times that of nickel-metal hydride batteries.

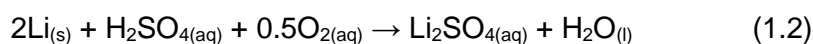
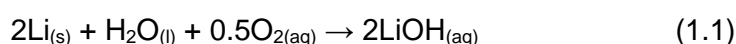
An example of a LIB consists of Li^+ ions intercalated in a graphite (Li_xC_6) negative electrode and layered-oxide ($\text{Li}_{1-x}\text{T}^{\text{M}}\text{O}_2$) positive electrode, where T^{M} is a transition metal. The Li^+ ions are shuttled between the electrodes during operation of the battery. During discharge, Li^+ ions are removed from the negative electrode and intercalate into the positive electrode; the process is reversed on charge. The energy density of this LIB is much lower than if a Li negative electrode were used. The intercalation electrodes add mass to the battery, but only Li^+ ions contribute to the charge storage. This additional mass reduces the energy density of the cell significantly. It is, therefore, no surprise that the energy density of LIBs is only 5 times greater than lead-acid batteries^{5,6}. Other

layered-oxides are also used, and example of which is the Ni-rich $\text{LiNi}_{0.8}\text{Mn}_{0.1}\text{Co}_{0.1}\text{O}_2$. This has a theoretical capacity of 275 mAh g^{-1} (ref. 7).

1.3. Lithium-air as an alternative

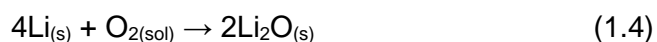
Lithium-air (Li-air) batteries have the potential to provide a much more energy dense battery that would be practical in FEVs. The theoretical gravimetric energy density is 3505 Wh kg^{-1} , based on the mass of lithium peroxide (Li_2O_2). This is approximately 9 times higher than the value for a lithium cobalt oxide-based LIB⁸. Hence, significant research and development of Li-air technology should provide sufficiently energy-dense batteries for FEVs to supersede fossil fuel-powered vehicles.

There are several types of Li-air battery designs^{5,6,9,10}, which will be discussed below. Schematic representations of each design are shown in Figure 1.1. The aqueous Li-air battery produces LiOH in an alkaline electrolyte (Equation 1.1). Acidic electrolytes produce lithium salts, an example of which is given in Equation 1.2. The lithium salt that forms on discharge is soluble in aqueous electrolytes, so can remain in solution. However, it is possible for the LiOH concentration to reach the saturation concentration, in which case, further discharge of the cell results in precipitation of the monohydrate, $\text{LiOH}\cdot\text{H}_2\text{O}$ ¹¹.

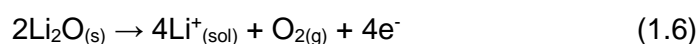
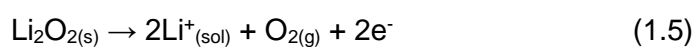


The lithium negative electrode must be protected by a Li^+ -conducting membrane or solid electrolyte interphase (SEI), typically a glass or ceramic, as exposed Li metal would react with H_2O in the electrolyte.

The non-aqueous Li-air battery utilises an aprotic, organic solvent and forms Li_2O_2 (Equation 1.3) and/or lithium oxide (Li_2O) (Equation 1.4) on discharge.



Lithium oxides are insoluble in organic solvents, so the discharge products form on the positive electrode, which leads to clogging of pores and passivation of the surface as the lithium oxides are electrically insulating. On charging, Li_2O_2 (Equation 1.5) and Li_2O (Equation 1.6) are decomposed to reform Li at the negative electrode and O_2 at the positive electrode.



The Li negative electrode spontaneously forms an SEI on contact with the electrolyte via a self-limiting reaction, which preserves the bulk of the negative electrode.

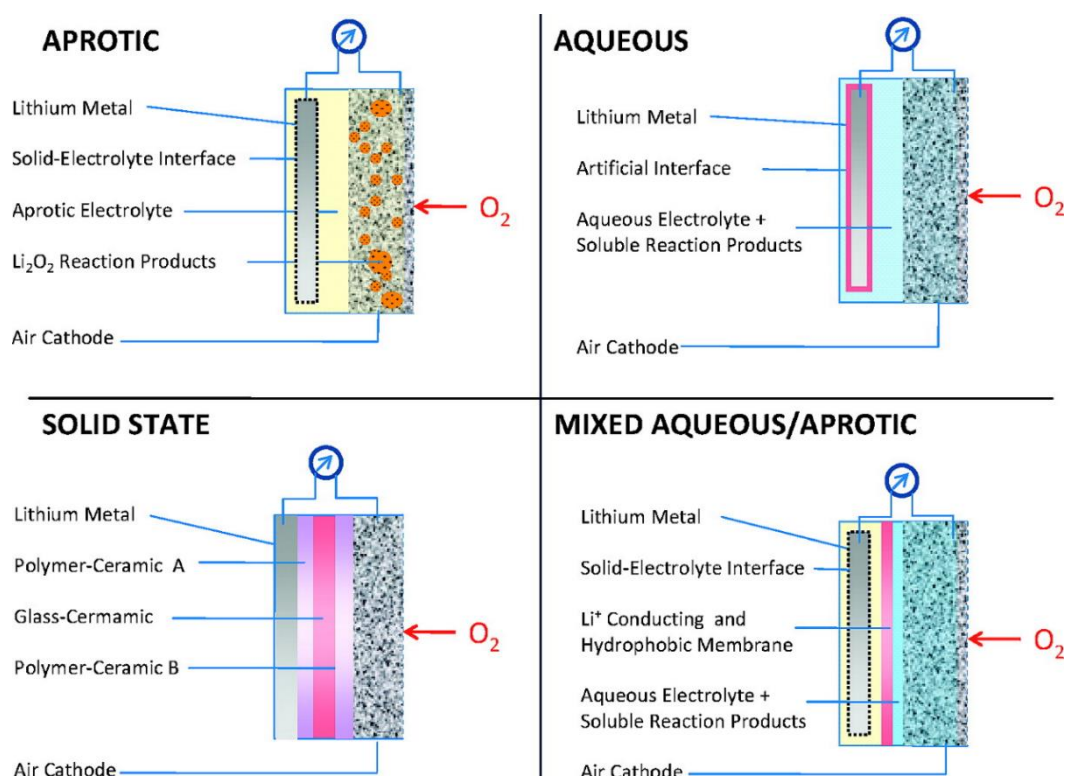


Figure 1.1: Schematics of the various possible types of Li- O_2 batteries. Reproduced from ref. 5.

A hybrid aqueous non-aqueous Li-air battery combines aspects of both of the previously mentioned designs^{12,13}. The negative electrode is exposed to the non-aqueous electrolyte so that an artificial SEI is not required. Li^+ passes through the organic electrolyte and a Li^+ -conducting ceramic, which is also hydrophobic to prevent water ingress into the non-aqueous electrolyte. It then reacts with reduced O_2 species in the aqueous electrolyte to form LiOH , which remains in solution.

A solid-state Li-air battery is also possible¹⁴, where the Li^+ moves through a solid electrolyte to the positive electrode and forms Li_2O_2 , analogous to the non-aqueous battery. However, the solid electrolyte must have sufficient Li^+ conductivity to allow reasonable discharge rates.

The goal of Li-air research is a battery that uses ambient air. However, almost all studies use pure O_2 to remove the effects of H_2O and CO_2 , meaning the system usually studied is the lithium-oxygen (Li-O_2) battery. Henceforth, Li-O_2 will be used to refer to studies using O_2 .

1.4. Early developments

Li-air batteries were proposed in the 1970s after work on other metal-air batteries had been investigated, but was not considered to be electrically rechargeable¹⁵. The first demonstration of a rechargeable non-aqueous Li-air battery was reported in 1996 by Abraham and Jiang¹⁶, where a gel polymer electrolyte was used. A qualitative analysis of the carbon positive electrode and Raman spectroscopy were used to confirm that the discharge product was Li_2O_2 . Despite the large overpotential, the study demonstrated the possibility of harnessing the Li/O_2 couple in a secondary battery. Subsequent studies explored the effect of electrolyte composition and positive electrode formulation on the discharge capacity, rate capability and rechargeability^{17,18}. Several liquid electrolytes commonly used in LIBs were tested to determine the physical properties relevant to the performance of the battery. Ogasawara *et al.* demonstrated that a Li_2O_2 -packed positive

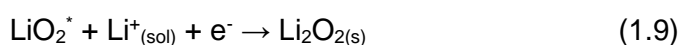
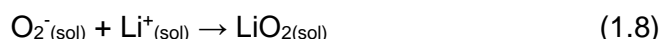
electrode can be oxidised and evolves O_2 , undergoing the $2e^-$ oxidation proposed in Equation 1.5, by using *in situ* differential electrochemical mass spectrometry (DEMS)¹⁹. This was the first proof that the proposed Li/O_2 couple could indeed be exploited in a rechargeable battery.

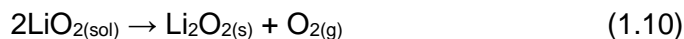
1.5. Fundamental chemistry

An understanding of the reactions that occur during (dis)charge is imperative for the successful development of the $Li-O_2$ battery. The discharge proceeds via the lithium superoxide (LiO_2) intermediate to form Li_2O_2 . However, solvent effects can influence how Li_2O_2 forms. On charge, there is less consensus about the mechanism. There is evidence that Li_2O_2 directly decomposes to Li and O_2 , but also that LiO_2 -like species are produced as an intermediate on charge. Both the reduction and oxidation mechanisms are explored in detail presently.

1.5.1. Oxygen reduction reaction (ORR) mechanism

There have been many studies that have attempted to elucidate the discharge and charge mechanisms. Oxygen reduction first begins with a $1e^-$ reduction of O_2 to superoxide (O_2^-) (Equation 1.7), identical to the reaction in Li^+ -free organic electrolytes^{20,21}. O_2^- then associates with Li^+ forming LiO_2 (Equation 1.8). There are two possible routes by which Li_2O_2 subsequently forms^{21,22}. If the LiO_2 is on the surface of the electrode (LiO_2^*), it can undergo a further $1e^-$ reduction and directly form Li_2O_2 (Equation 1.9). Alternatively, LiO_2 can chemically disproportionate, forming Li_2O_2 and O_2 (Equation 1.10). This chemical step is possible both at the surface, and in solution.





O_2 reduction has been studied in organic solvents for many years. Bulky ammonium salts, e.g. tetrabutylammonium (TBA^+), are often used in the electrolyte as they only bind weakly to the electrochemically generated O_2^- . TBA^+ forms an ion pair with O_2^- , TBA-O_2 (ref. 21). O_2^- has been proven to be soluble and stable in the solvents used in Li-O_2 studies^{22,23}.

LiO_2 is thermodynamically unstable, disproportionating to Li_2O_2 and O_2 . However, it can be kinetically stabilised by some solvents. Laoire *et al.* explained the stabilisation by considering the effect of the solvent on Li^+ (ref. 21). They used Pearson's hard soft acid-base theory to rationalise which mechanism occurs²⁴. Considering first only the ionic interactions, O_2^- is a soft base, whereas Li^+ is a hard acid. This results in a poor interaction between the ions as Equations 1.7 and 1.8 occur during the ORR. Disproportionation produces O_2^{2-} , a harder base, which interacts more strongly with Li^+ . This results in a stable discharge product, Li_2O_2 . Solvent molecules complex Li^+ , with the assumption that four solvent molecules form a co-ordination sphere around each Li^+ (ref. 25). Solvent basicity can be characterised by using the Gutmann donor number (DN), where a higher number indicates stronger basicity²⁶. Laoire *et al.* reported that when Li^+ is solvated by high DN solvents such as dimethyl sulfoxide (DMSO), the acidity of Li^+ is reduced, making it softer²¹. This improves the interaction with O_2^- and results in two separate reductions peaks (Figure 1.2) corresponding to Equations 1.7 and 1.9. This is contrasted with acetonitrile (CH_3CN) and dimethoxyethane (DME), which have lower DNs, so does not modulate the acidity of Li^+ significantly enough to stabilise LiO_2 . This is demonstrated by a single cathodic peak, which contains both O_2/O_2^- and $\text{O}_2^-/\text{O}_2^{2-}$ reductions.

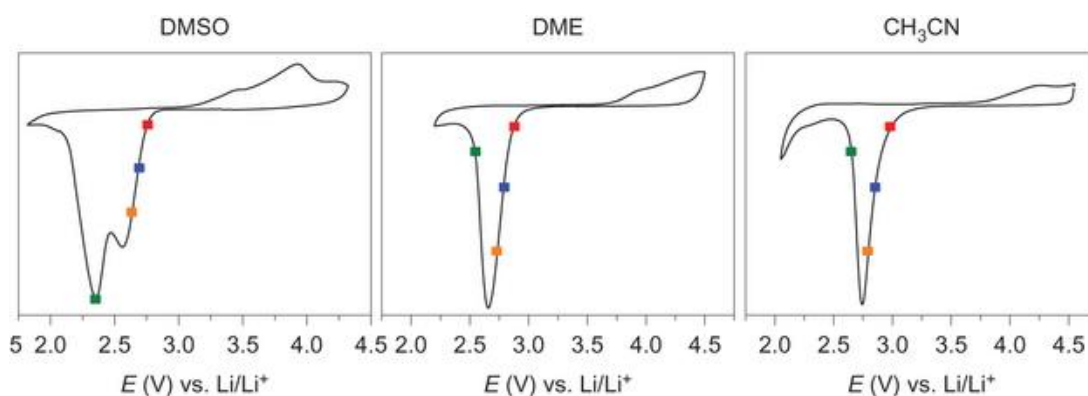


Figure 1.2: Cyclic voltammograms (CVs) of O₂ reduction in Li⁺-containing electrolytes. Each solvent is indicated above the CV. DMSO has two distinct reduction peaks (~2.6 and ~2.3 V), while DME and acetonitrile (CH₃CN) only have one reduction peak (~2.7 and 2.75 V, respectively). The coloured squares correspond to data not shown here and should be ignored. Adapted from ref. 22.

Johnson *et al.* developed the concept of surface and solution mechanisms and proposed that LiO₂ solubility dictates to what extent the surface and solution mechanisms occur²². An equilibrium is established between surface-adsorbed and dissolved LiO₂. The equilibrium can be summarised by Equation 1.11.



The position of the equilibrium depends predominantly on the solvent-ion interactions, and the estimated ΔG° values for Equation 1.11 for each of the solvents in the study followed the trend seen experimentally. The solubility of the cations, in particular, is highly solvent dependent. They go on to show that, in high DN solvents, Li₂O₂ forms by disproportionation and results in toroidal particles, while in low DN solvents, direct electrochemical reduction of LiO₂* produces a thin conformal film on electrodes (Figure 1.3). Aetukuri *et al.* also reported the same unifying mechanism based on Equation 1.11, but by using H₂O as an additive to stabilise O₂⁻ due to the high acceptor number (AN) of H₂O (ref. 27).

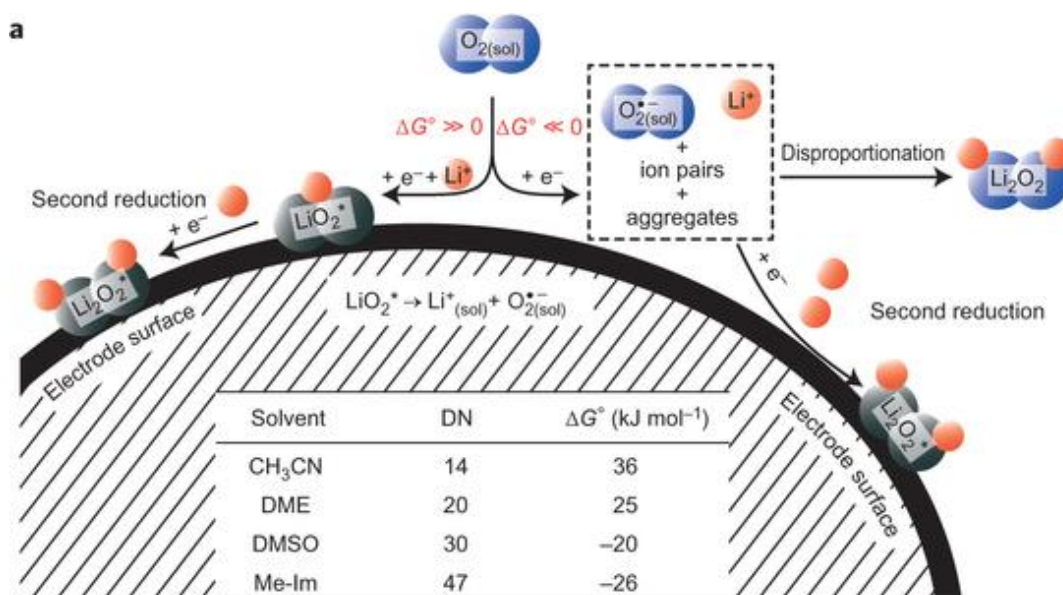


Figure 1.3: A schematic of the surface and solution-based mechanisms. The ΔG° values for the dissolution of LiO_2^* are shown in the table. Adapted from ref. 22.

Black *et al.* provided further evidence of disproportionation by adding O_2^- (formed by reacting potassium superoxide (KO_2) with a crown ether) to a Li-based electrolyte²⁸. Li_2O_2 was formed and O_2 gas evolved, which is only possible if LiO_2 formed and disproportionates.

1.5.2. Oxygen evolution reaction (OER) mechanism

Laoire *et al.* proposed an OER mechanism based on electrochemical experiments²¹. They suggested that Li_2O_2 oxidises directly to Li^+ and O_2 (Equation 1.12), as the reversible O_2/O_2^- couple is not seen in cyclic voltammograms (CVs) if Li_2O_2 is formed on discharge^{20,21}.



Peng *et al.* used *in situ* surface-enhanced Raman spectroscopy (SERS) to monitor the formation and oxidation of Li_2O_2 on a Au electrode²⁹. While LiO_2 was seen on reduction, it was absent on oxidation. The instability of an electrolyte, propylene carbonate (PC), towards LiO_2 and O_2^- , was also used to test whether oxidation proceeds via LiO_2 . If these intermediates were to form on charge, they would attack PC and produce carbonate

species that could undergo oxidation themselves, producing CO_2 . In their DEMS experiment, O_2 was the predominant gas evolved, with no detection of CO_2 (ref. 29).

Lu and Shao-Horn used a potentiostatic intermittent titration technique and galvanostatic intermittent titration technique to probe the kinetics of oxidation³⁰. They hypothesised a three-stage mechanism, where the first involves Li^+ deintercalation and forms LiO_2 on the surface of the particle. This must then disproportionate to produce O_2 in order to be consistent with DEMS experiments, which show O_2 evolution during this initial stage of charging³¹. The second stage involves oxidation of bulk Li_2O_2 and the final stage, at high potentials, involves decomposition of side-products and electrolyte³⁰.

Gallant *et al.* extended this mechanism to consider the differing charge profile behaviour exhibited by discs and small particles (Figure 1.4)³². The delithiation (first stage) progressed for a longer time in the particles before the bulk oxidation occurred. Both the surface area to volume fraction and surface composition were reported to affect the charge profile. The former determines the extent to which delithiation occurs, with particles delithiating for longer times than discs due to a larger surface area to volume ratio. The latter was suggested to affect the overpotential required for delithiation. Previous work has shown that discs and toroids are predominantly composed of O-rich (0001) surfaces³³. X-ray absorption near edge structure (XANES) data suggested that the Li_2O_2 particles had surfaces that were not as O-rich. Gallant *et al.* suggested that the surface could be (1-100), as computational studies have suggested that this surface may have a lower overpotential than the (0001) surface, which would fit with the observed results³⁴. The authors go on to speculate that the bulk oxidation is a two-phase process where Li_2O_2 and O-rich species are both present. However, as highlighted by Luntz and McCloskey, it is hard to see why the delithiation would terminate once the bulk of the Li_2O_2 was exposed, and a new process requiring a larger overpotential would dominate³¹. Furthermore, to be consistent with DEMS results^{35,36}, the first stage requires that LiO_2 disproportionation be fast to produce the O_2 that is detected experimentally.

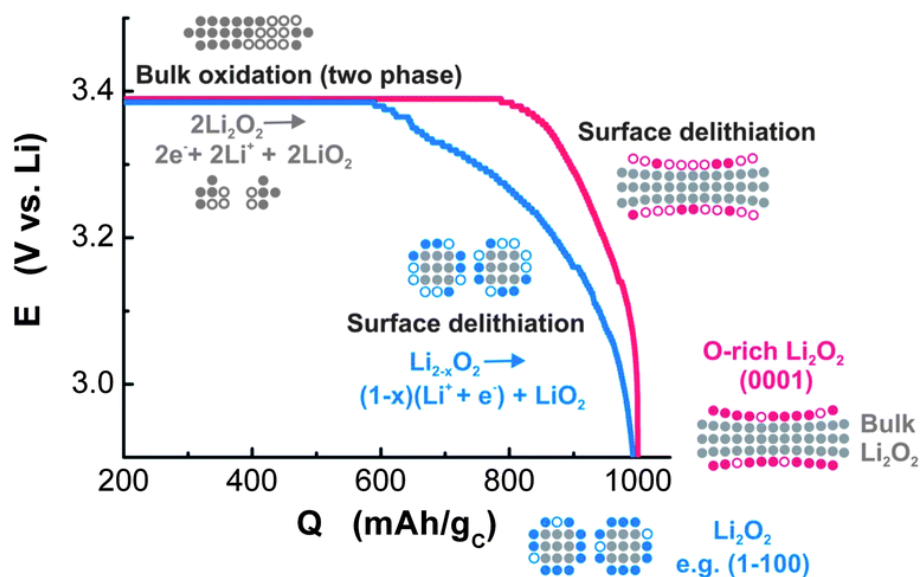


Figure 1.4:The two different charge processes. Surface delithiation occurs first before the bulk is exposed and oxidised. Reproduced from ref. 32.

Computational studies have been carried out to model how the OER. Kang *et al.* provided theoretical evidence for off-stoichiometric delithiation, whereby $\text{Li}_{2-x}\text{O}_2$ is formed³⁷. This creates Li vacancies that are fairly mobile, allowing clusters of LiO_2 to form on the Li_2O_2 particle. They go on to suggest that LiO_2 either dissolves into the electrolyte or decomposes to release Li^+ and O_2 . Based on *in situ* SERS results²⁹, they conclude that LiO_2 would immediately decompose, in agreement with Lu and Shao-Horn³⁰. Radin and Siegel reported a two-stage charging process, dependent on the overpotential applied³⁸. Thin Li_2O_2 deposits can be oxidised at low overpotentials *via* electron-tunnelling, while thicker deposits require higher overpotentials and charge transport occurs *via* polaron hopping³⁸. Further experimental evidence for the mechanisms in references 30, 37 and 38 was provided by Ganapathy *et al.*³⁹ Using *operando* X-ray diffraction (XRD), they found little change in Li_2O_2 intensity and lattice parameters on initial charging. This occurred at low potentials, and was attributed to the decomposition of thin and amorphous Li_2O_2 deposits, as suggested by reference 38. The second stage of charging consisted of a higher voltage plateau, where the Li_2O_2 intensity

and occupancy decreased continuously. This is consistent with the second stage process in reference 38 proceeding via the solid solution mechanism in reference 37.

Based on thermodynamics alone, the equilibrium potential for Li_2O_2 formation is 2.96 V. It has been suggested that other factors are responsible for the overpotentials seen. A study by Viswanathan *et al.* showed that the fundamental overpotentials are quite small (<0.4 V) for reasonably high current densities⁴⁰. These fundamental kinetic overpotentials are dictated by the chemistry occurring at the positive electrode surface and cannot be overcome. Thus, the authors attributed the large overpotentials seen in cells to iR losses from cell impedance.

Højberg *et al.* carried out an impedance study to assign impedances to specific processes occurring within the cell during cycling⁴¹. On charging, the total resistance of the cell remained relatively constant, despite the steady increase in charge voltage. The authors use this to suggest that the charge voltage is a mixed potential of the cell resistance and the voltage required to oxidise decomposition products e.g. lithium carbonate (Li_2CO_3).

The OER mechanism requires charge transport between the Li_2O_2 deposits and the electrode and electrolyte. The insulating nature of Li_2O_2 can make e^- -transport and Li^+ transport slow. Which one is slower will determine the kinetics of oxidation. Zhong *et al.* first reported the *in situ* observation of Li_2O_2 oxidation using transmission electron microscopy (TEM)⁴². Their setup consisted of multi-walled carbon nanotubes (MWCNTs) supporting Li_2O_2 particles, with a Li^+ -conducting solid electrolyte (SE) coated on a Si nanowire. They found that electro-oxidation preferentially occurred at the MWCNT/ Li_2O_2 interface, and not at the Li_2O_2 /SE interface (Figure 1.5).

This suggests that e^- -transport may be the limiting factor for oxidation. If Li^+ -transport had been slower, oxidation would first have been seen at the Li_2O_2 /SE interface. Due to the high potentials required for the experiments, the authors noted that e^- -transport

limitations may not be the limiting factor in batteries utilising liquid electrolytes and low charge rates⁴².

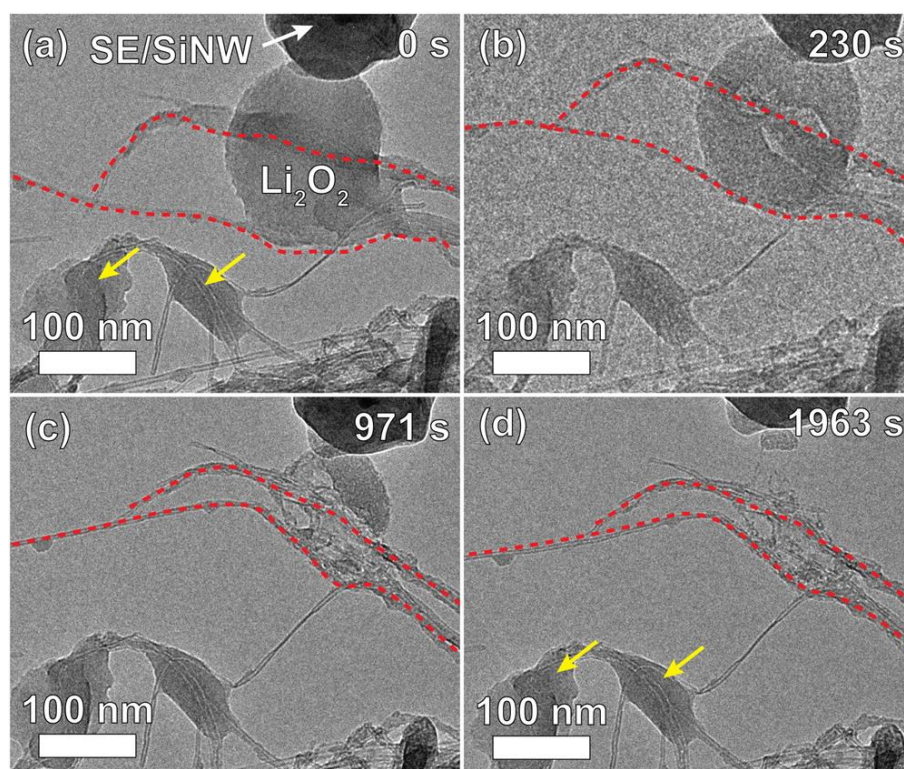


Figure 1.5: *In situ* TEM images of the electro-oxidation of a Li_2O_2 particle on carbon nanotubes (CNT), indicated with the red dashed lines. A silicon nanowire (SiNW) coated with a Li^+ conducting solid electrolyte (SE) provide contact with the Li_2O_2 particle. As oxidation proceeds, the particle shrinks more by the MWCNTs than by the SE/SiNW, indicating e^- -transport limits oxidation under the experimental conditions. Two other Li_2O_2 particles, indicated by arrows, are used by the authors as a reference against morphological changes due to beam exposure. Reproduced from ref. 42.

However, a later study⁴³ using *in situ* atomic force microscopy (AFM) and a liquid electrolyte supported the findings of Zhong *et al.* With a thick Li_2O_2 layer, the oxidation was difficult to detect at low overpotentials. Only small changes in the surface morphology were seen below 4.38 V. When held at this potential, the decomposition of Li_2O_2 was too fast to produce clear micrographs. This suggested that the decomposition

occurred at the electrode/ Li_2O_2 interface, as the AFM tip would be unable to detect changes below the surface⁴³.

1.6. Solution and surface mechanisms of Li_2O_2 growth

The morphology of Li_2O_2 particles produced on discharge is dependent on multiple factors, including discharge rate^{44,45}, solvent²² and temperature⁴⁶. There are two types of morphology typically reported, which are thin conformal films covering the electrode surface (Figure 1.6) and large particles, often described as toroids (Figure 1.7). The mechanism by which each forms is different.

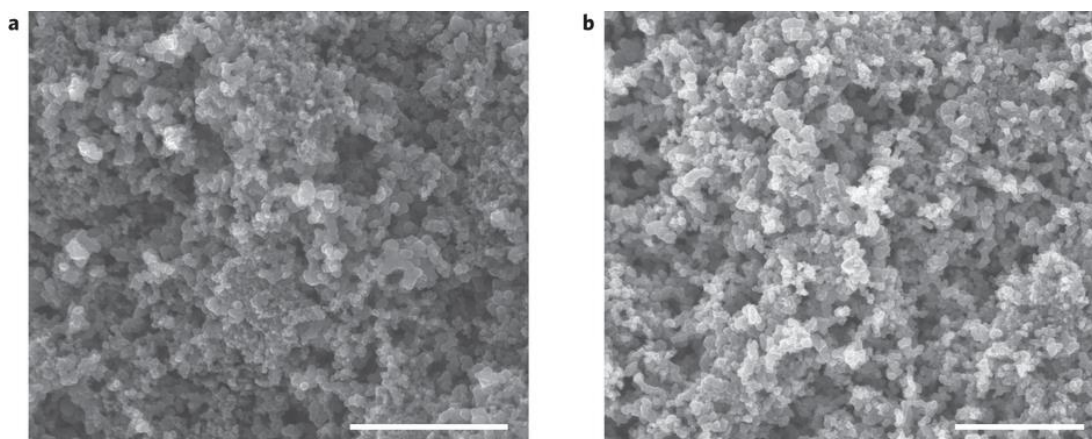


Figure 1.6: SEM images of (a) pristine and (b) discharged carbon positive electrodes in an electrolyte that undergoes the surface mechanism. As the Li_2O_2 film is thin, the images are almost indistinguishable. Reproduced from ref. 27.

Films grow on the surface of the electrode when the surface mechanism dominates. Once discharge begins, LiO_2 forms on the surface and remains there due to poor solubility. It then forms Li_2O_2 on the surface, by further reduction or disproportionation. This means that layers of Li_2O_2 build up on surface. Due to the insulating nature of Li_2O_2 , this passivates the surface of the electrode. Therefore, subsequent Li_2O_2 deposits where the electrode surface is still exposed or where the film is thin enough to allow e^- -transport through the Li_2O_2 layer. There is limited ability for the deposits to grow out from the

electrode (thicken) before passivation occurs. This results in the thin conformal films seen by some groups^{22,32,35,45}.

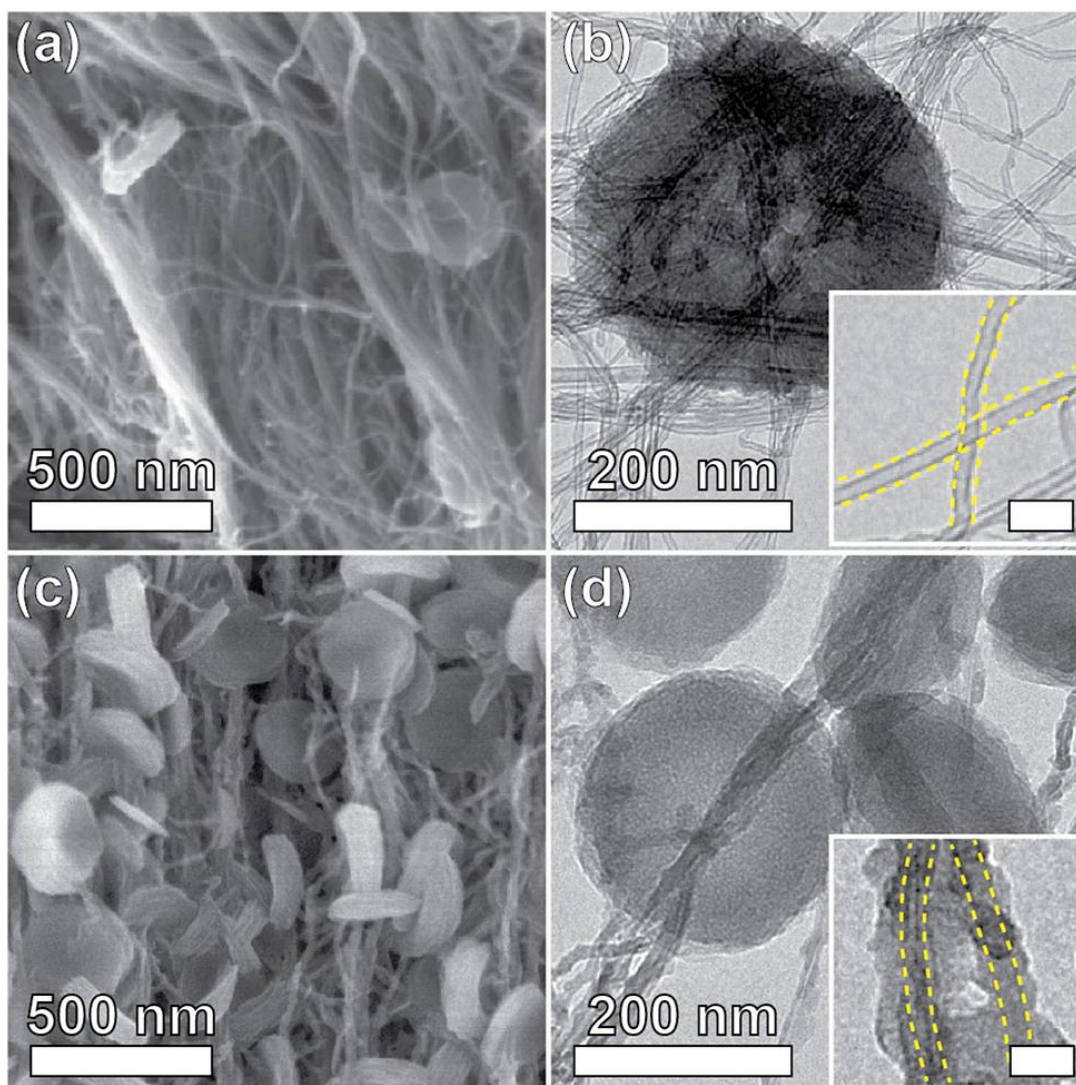


Figure 1.7: (a) and (c) SEM and (b) and (d) TEM images of toroids formed on freestanding carbon nanotube positive electrodes. The dashed lines indicate the carbon nanotubes. Reproduced from ref. 33.

Toroids, on the other hand, require a solution mechanism to form. The LiO_2 intermediate dissolves at the electrode surface and then diffuses away. It can then precipitate out elsewhere, e.g. on a particle of Li_2O_2 , and disproportionate on the surface of that particle. Solvation allows Li_2O_2 to form far from the electrode surface and produces crystalline toroids. Inherent solubility of the LiO_2 intermediate in high DN solvents is one route by

which the toroids could form²². It has been suggested by Aetukuri *et al.* that H₂O is also responsible for the solubilisation of LiO₂ (ref. 27). The effect of H₂O will be considered in detail in Section 1.10.2.

Luntz and McCloskey³¹ suggested that the variation in particle size in ethereal electrolytes reported by others^{28,33,39,42,45,47-53} may be in part due to H₂O contamination, possibly from improper drying of components or poor gas handling. Others have also reported only observing toroids in tetraethylene glycol dimethyl ether (TEGDME) with added H₂O (ref. 54). However, since this potential effect of H₂O was highlighted, a study reported toroids from SEM data when using TEGDME with <10 ppm H₂O as the solvent⁵⁵. The situation is no less clear with anhydrous DMSO. Studies have shown the formation of toroids²², bundles of nanosheets with some forming toroids⁵⁶, and only large agglomerates of thin sheets⁵⁷.

As the precise role H₂O plays is not fully understood currently, its effect on morphology remains unresolved and further studies looking closely at Li₂O₂ morphology must endeavour to achieve anhydrous conditions for all components (electrodes, separators, salt, solvents, purging O₂ gas, *etc.*) if they are to truly discriminate between dry and wet systems.

The current density (j) during discharge is important in controlling whether the solution or surface mechanism is dominant. Mitchell *et al.* reported toroids at low j , and smaller, irregular particles at higher j on carbon nanotubes³³. They ascribed the varying morphology to the overpotential for nucleation, based on the Volmer-Weber island growth model. At low j , the overpotential is small (i.e. close to the thermodynamic potential for Li₂O₂ formation). Therefore, the driving force for nucleation is small, resulting in few sites where deposition occurs. This allows growth of few, but large, particles. Higher j require larger overpotentials, which creates more nucleation sites so more particles can grow. In addition, they reported that the particles are formed of aligned plate-like Li₂O₂ crystallites, which splay as the particle grows, to produce toroids.

Adams *et al.* showed that, at low j , toroids are formed, but as j is increased these particles become smaller and more numerous, and at even higher j , only the film morphology is seen⁴⁵. The authors ascribed the changing morphology to the competing kinetics of LiO₂ solvation and Li₂O₂ formation (chemically and electrochemically). At low j , solvation is faster than the disproportionation or direct reduction of LiO₂, which allows growth *via* solution mechanism. At higher j , LiO₂ cannot dissolve from the electrode surface before it is reduced or disproportionates directly on the surface *via* surface migration.

Computational studies have also produced reasonably accurate models for toroid/film nucleation. Horstmann *et al.* suggested that the transition from toroids to films occurred at the exchange current of the ORR⁴⁴. The model presented by Lau and Archer quantitatively described the discharge profile and showed that sudden death of batteries discharging at low current densities is due to nucleation of many small particles⁵⁵. As the surface is consumed by toroids, the overpotential increases at the exposed positive electrode surface, increasing the nucleation rate. This produces many particles late into discharge, which leads to passivation.

1.7. The stability of key components of Li-O₂ batteries

Of key importance is the stability of all components to the various chemical species present in a battery when discharging, charging and at rest. Chemical and/or electrochemical instability will lead to parasitic reactions that will lead to premature failure of a battery. The Li-O₂ battery differs from LIBs in that new chemical species are produced during operation of the battery, which requires all battery components to additionally withstand O₂⁻, LiO₂ and Li₂O₂.

There are several ways to quantify the stability of a cell. These methods use the assumption of ideal Li₂O₂ formation and decomposition chemistry as described in Section 1.5. DEMS can be used to determine the e⁻/O₂ ratio, which is expected to be 2.00 if Li₂O₂ is the only product. The only gas that should be detected on charge is O₂;

any other gases (e.g. H₂ or CO₂) imply unwanted discharge products. The yield of Li₂O₂, (Y_{Li₂O₂}), is expected to be 100%, based on the charge, and assuming no side-products form. The ratio of O₂ gas consumed and evolved (OER/ORR) should be 1.00.

One very important component of the Li-O₂ battery is the electrolyte. It is in contact with both electrodes and must be stable to the potentials applied during cycling as well as the chemical species that form during operation. However, research has shown that many solvents and salts, which have been used in studies, are in fact unstable.

The other major source of side reactions is the positive electrode. Carbon was the initial choice for the positive electrode material due to a range of suitable properties, e.g. conductivity, porosity. Problems have been found with the use of carbon and the polymer binders sometimes included in the positive electrode. Hence, there has been development of non-carbon positive electrodes with improved stability since carbon instability was identified.

1.7.1. Solvents

Early studies into Li-O₂ batteries utilised organic carbonates as the solvent in the electrolyte, because these solvents had been extensively used in Li-ion batteries. The most notable of these is PC. It is used in LIBs as it has a range of desirable properties, including a high dielectric constant, a large electrochemical stability window and low volatility⁵⁸. Reports using carbonate-based electrolytes claimed Li₂O₂ was the dominant product using *ex-situ* spectroscopic techniques and XRD⁵⁹⁻⁶¹. However, capacity fading was often observed. One posited explanation for this effect included pore blocking in the carbon positive electrodes which would reduce the active surface area on subsequent cycles⁵⁹. However, other groups began to report carbonate species, principally Li₂CO₃ and lithium alkylcarbonates (LiRCO₃) as the main products, using a variety of spectroscopic techniques⁶²⁻⁶⁴. Freunberger *et al.* also reported these discharge products⁶⁵. They also suggested that capacity fading was due to the build-up of these products on repeated cycling. McCloskey *et al.* employed DEMS experiments to show

the instability of carbonate electrolytes compared with DME, an ether-based electrolyte⁶³. The carbonate electrolytes produced CO₂ throughout charge, even when a 1:2 PC:DME mixed solvent was used (Figure 1.8). Computational studies support the experimental data^{66,67}. These reports demonstrated the importance of spectroscopy in linking the observed cycling behaviour to the true electrochemistry occurring in a battery.

Ethers have replaced organic carbonates as the solvent of choice due to several advantages. They are often stable to high voltages (~4 V vs Li⁺/Li), are low cost and compatible with Li negative electrodes. They are also relatively stable towards O₂⁻, which improves cyclability. Read showed that ethers were a suitable alternative to organic carbonates before carbonate instability was even known⁶⁸. Ethers and organic carbonates have similar O₂ solubilities, but the lower viscosity of ethers improves the discharge capacity of cells¹⁸. Freunberger *et al.* reported that ethers undergo decomposition and suggested a mechanism by which O₂⁻ abstracts a proton from the ether⁶⁹. This initiates a set of reactions, producing Li₂CO₃ and LiRCO₃.

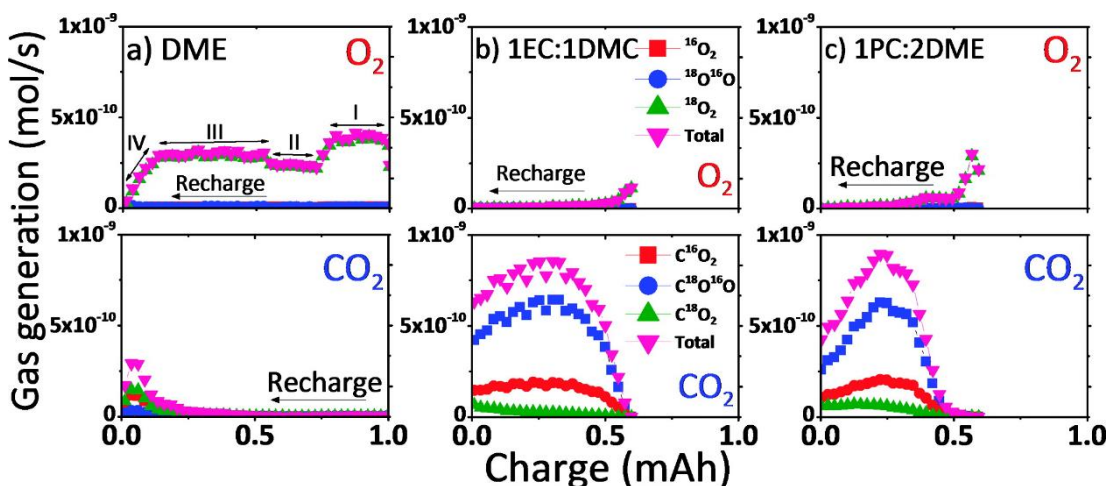


Figure 1.8: O₂ and CO₂ gas evolution profiles on charging positive electrodes in electrolytes containing (a) DME, (b) 1:1 mixture of ethyl carbonate/dimethyl carbonate (EC:DMC) and (c) 1:2 mixture of PC/DME. Only DME produces significant amounts of O₂, while carbonyl-based electrolytes predominantly evolve CO₂ on charge, indicating their instability on discharge. Reproduced from ref. 63.

McCloskey *et al.* screened a range of solvent and salt combinations to assess the rechargeability of commonly used electrolytes³⁶. They found that the most stable solvents were CH₃CN and ethers, particularly DME. They possessed OER/ORR values of ~0.9 and ~0.8, respectively. CH₃CN is not commonly used for two-electrode cells due to instability towards the Li negative electrode. Hence, ethers, particularly DME and TEGDME have been used extensively in research. The OER/ORR values of ~0.8 do however indicate parasitic chemistry. The e⁻/O₂ on discharge for DME on discharge was close to 2.00 but on charge it was ~2.6-2.7, suggesting that parasitic reactions were occurring on charge.

However, it is also possible that after discharge, the Li₂O₂ reacts chemically with the electrolyte and/or positive electrode. In this way, the e⁻/O₂ ratio on discharge would still be ~2.00, but it would deviate significantly more on charge³¹. This suggests that decomposition may be more complex than the mechanism suggested by Freunberger *et al.*⁶⁹ Determining Y_{Li₂O₂} resolves this uncertainty as it would detect a loss of Li₂O₂ after discharge. McCloskey *et al.* developed an iodometric titration to quantitatively measure Li₂O₂ deposited on a positive electrode⁷⁰. When used in conjunction with DEMS, it showed that less Li₂O₂ was formed than expected based on the O₂ gas consumed, demonstrating that electrolyte and/or positive electrode decomposition occurs. Interestingly, they presented data showing a correlation between discharge rate and Y_{Li₂O₂} (Figure 1.9). At high rates, Y_{Li₂O₂} was close to the expected value, but as the rate decreased, Y_{Li₂O₂} reduced (Figure 1.9a). However, the DEMS data shows that the electrochemical behaviour is unchanged with rate (Figure 1.9b). This is indirect evidence for the chemical reaction of Li₂O₂ with cell components. At lower rates, the discharge proceeds for a longer time, which exposes the electrolyte and positive electrode to Li₂O₂ for more time and would allow slow chemical reactions to occur, whereas at high rates there is insufficient time for slow reactions to occur so Li₂O₂ loss is reduced.

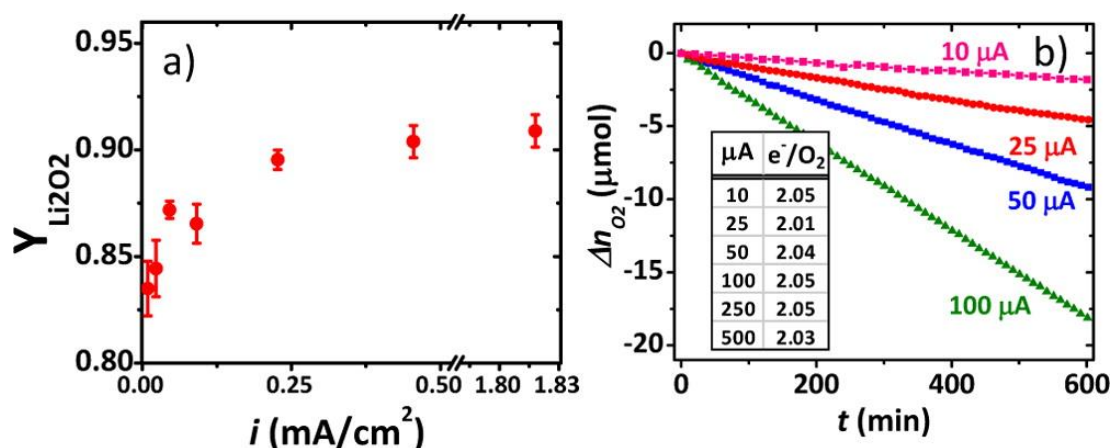
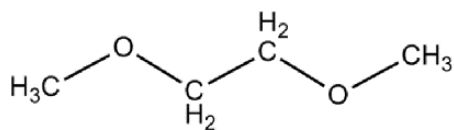


Figure 1.9: (a) The relationship between discharge current and Li_2O_2 yield. Ideal Li_2O_2 formation results in a $Y_{\text{Li}_2\text{O}_2}$ value of 1.00 (*i.e.* 100%) (b) O_2 consumption at various discharge rates. Inset: e^-/O_2 values for various discharge rates. Reproduced from ref. 70.

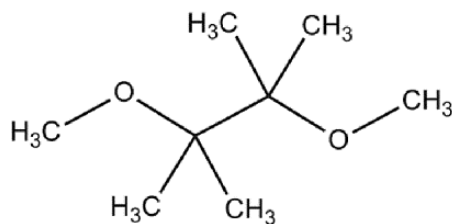
Black *et al.* chemically produced LiO_2 using KO_2 and a crown ether to produce free O_2^- (ref. 28). A Li salt was then added to produce LiO_2 . This procedure was carried out in TEGDME to test its stability to attack from LiO_2 . It was found to be stable to LiO_2 . Adams *et al.* synthesised a novel solvent (Figure 1.10), which is more resistant to attack from O_2^- by replacing reactive protons with methyl groups⁷¹. The synthesis of new solvents may lead to the discovery of one stable enough for Li- O_2 batteries.

Other solvents have also been considered, but were not found to be better than ethers. DMSO has been used as the solvent in batteries and was shown to be rechargeable and exhibit only a small amount of side reactions^{72,73}. DMSO is also commonly used as a solvent in CVs. However, it is known that Li_2O_2 can react with DMSO^{74,75}, and has been shown to react over the course of days to produce LiOH and Li_2CO_3 , though it was stable over shorter timescales (10 minutes)^{75,76}. This means that DMSO is unsuitable for practical batteries. However, for short timescale experiments (*e.g.* CVs) it is a useful solvent, as its high DN allows the solution-based ORR mechanism to be studied (Section 1.5.1). It is also known that DMSO can react with O_2^- (ref. 77) or LiO_2 in the presence of a carbon positive electrode⁷⁴.

Nitriles are less commonly used in batteries, and as such there has been less investigation of their stabilities. CH_3CN is known to be stable in the short-term, based on O_2 redox experiments^{20,21}. However, it is unlikely to be used in the electrolyte due to its high volatility. Hence, other nitriles have been investigated to replace CH_3CN . On the basis of computational experiments, pivalonitrile ($t\text{-BuCN}$) was found to be more stable than CH_3CN to attack by O_2^- and Li_2O_2 ^{78,79}. Laino *et al.* reasoned that $t\text{-BuCN}$ would be more stable than CH_3CN as nucleophilic attack by O_2^{2-} requires close contact, something which the bulky tertiary butyl group restricts to an extent⁷⁹. The nitrile group can also be attacked at the C of the CN group⁷⁸. Benzonitrile derivatives were found to be stable when the aromatic ring contained electron-donating groups *ortho* or *para* to the CN, reducing the nitrile nucleophilicity⁷⁸. Despite the stability demonstrated above, ethers remain the solvent of choice.



1,2-dimethoxyethane



2,3-dimethyl-2,3-dimethoxybutane

Figure 1.10: The novel solvent (bottom) synthesised by Adams *et al.*, based on DME (top). The protons have been replaced methyl groups. Adapted from ref. 71.

Amides have also been considered due to their stability to attack by O_2^- . Computational studies found amides had higher activation energies to O_2^- attack than other classes of solvents⁷⁸. N,N -Dimethylformamide was found to be unstable, with minor amounts of

decomposition products detected, even after the first discharge. Subsequent cycling resulted in a build-up of these products in the positive electrode, leading to capacity fading⁸⁰. Dimethylacetamide (DMA) was also considered and ¹H NMR showed CH₃CO₂Li and HCO₂Li both formed on discharge⁸⁰. Amides are also known to react with Li metal, resulting in soluble species that can oxidise on charge⁸¹. This complicates any potential use of amides in practical Li-O₂ cells.

Room temperature ionic liquids (RTILs) are an alternative to conventional electrolytes, with potential application in the Li-O₂ system because of certain favourable characteristics, including hydrophobicity, stability, and low volatility and flammability. The properties of RTILs can be adjusted by the specific choice of cation and anion, but care must be taken to ensure stable ions are used. It was suggested that imidazolium cations would be unstable to nucleophilic attack by O₂⁻, based on CVs and calculated Mulliken charges⁸². Pyrrolidinium and piperidinium-based cations, however, were suggested as stable to O₂⁻, as their Mulliken charges are negative, implying lower reactivity towards nucleophiles^{82,83}. A thorough study by Das *et al.* determined the stability of several cations used as RTILs using DEMS⁸⁴. 1-butyl-2,3-dimethyl-imidazolium was found to decompose, based on the deviation of the e⁻/O₂ values from 2.00, which were 2.14 and 8.26 for discharge and charge, respectively. Despite little CO₂ being detected on charge, the value implies a substantial amount of parasitic reactions occurring on charge⁸⁴. The value of 2.14 for discharge appears far more acceptable, but also indicates a significant degree of decomposition. Hayyan *et al.* used a very similar cation, 1-butyl-3-methylimidazolium, and determined its instability towards chemically and electrochemically generated O₂⁻ using gas chromatography-mass spectrometry⁸⁵. They proposed that imidazolium ions react with O₂⁻ and form 2-imidazolone-based molecules, based on the identification of 1-butyl-3-methylimidazolone.

Das *et al.* found that *N*-methyl-*N*-propyl-pyrrolidinium and *N*-methyl-*N*-butyl-pyrrolidinium were the most stable RTILs of those tested⁸⁴. However, they still underwent

decomposition on charge, making them unsuitable for long-term cycling. Further research into stable RTILs is still needed.

1.7.2. Salts

The choice of salt is critical for the electrolyte. It must be sufficiently soluble in the chosen solvent to facilitate ion transport, the anion must be inert to all components within the battery and be stable to Li_2O_2 and its reactive intermediates¹⁰. If it suffers from even a small amount of instability, cyclability will be compromised.

One of the first salts identified to decompose in Li-O_2 batteries was lithium hexafluorophosphate (LiPF_6). It is a commonly used salt in LIBs, but Oswald *et al.* used X-ray photoelectron spectroscopy (XPS) to show that exposure of Li_2O_2 to LiPF_6 resulted in LiF formation on the surface of Li_2O_2 particles⁸⁶. The PF_6^- anion hydrolyses to produce HF , which leads to LiF formation, but the authors suggested an additional reaction between Li_2O_2 and the salt as the H_2O content was too low to account for the amount of LiF observed. Others confirmed the instability of LiPF_6 with a range of techniques⁸⁷⁻⁹⁰. Oswald *et al.* also considered the stability of lithium bis(oxalato)borate (LiBOB) and lithium perchlorate (LiClO_4)⁸⁶. The former was also unstable to Li_2O_2 , but the latter was found to suffer little or no decomposition.

XPS was used to detect salt decomposition products on discharged positive electrodes by Veith *et al.*⁸⁹ All salts in the study (LiPF_6 , lithium bis(trifluoromethanesulfonyl)imide (LiTFSI), lithium tetrafluoroborate (LiBF_4), and LiClO_4) were found to degrade to some degree, but LiClO_4 was the most stable, in agreement with reference 86. LiClO_4 was found to be stable in a 1:1 mixture of ethylene carbonate/diethyl carbonate (EC/DEC)⁹¹, indicating that a holistic approach to the electrolyte must be pursued to find a combination of salt and solvent which are suitable. Lithium tetracyanoborate has also been found to be unstable in long chain ethers⁹².

A comprehensive study of the most common salts used in Li-O₂ batteries was carried out by Nasybulin *et al.* using TEGDME⁹³. A summary of their findings is shown in Figure 1.11. XRD data only showed very limited decomposition, but this only indicates a lack of crystalline decomposition products. XPS was used to detect amorphous products. LiBF₄ and LiBOB were unstable, confirming other reports^{86,89}. LiBOB decomposes to oxalate compounds, similar to that reported by Oh *et al.*, who found lithium oxalate as the main decomposition product of the salt in PC⁹⁴.

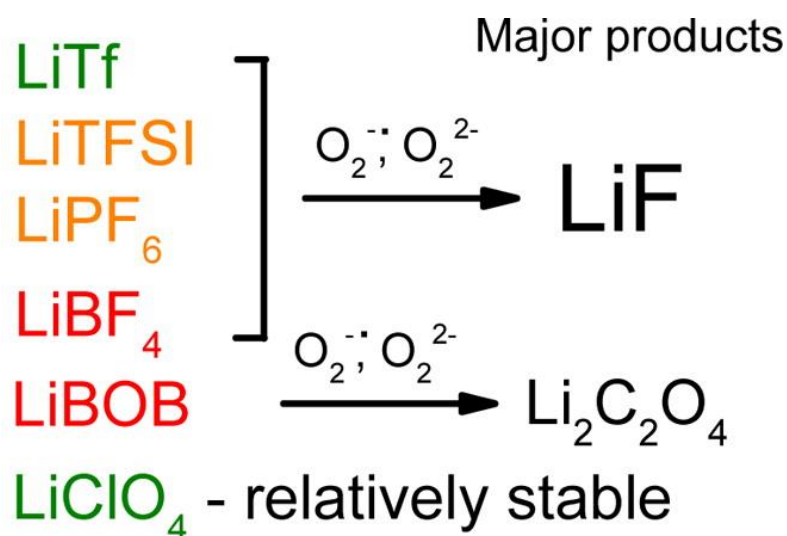


Figure 1.11: Summary of the decomposition products of various salts. LiClO₄ and LiBr (not shown) are stable, while other salts decompose to the products shown. Reproduced from ref. 93.

Based on these reports, the decomposition of LiBOB appears to be independent of solvent, so it is probably caused by O₂⁻ or Li₂O₂. LiPF₆ was highly unstable and LiTFSI was also found to be unstable. Lithium trifluoromethanesulfonate (LiTf) was more stable than the related LiTFSI salt. However, using ¹⁹F NMR, the LiF peak was seen for all the F-containing salts. LiClO₄ and LiBr were both stable, with the finding for LiClO₄ contradicting earlier work^{89,95}. The discrepancy was explained by the chemical instability of LiClO₄ to the X-ray beam, which led to LiCl formation on continued exposure. Hence, of the salts tested by the authors, only LiClO₄ and LiBr are stable salts.

There is now interest in molten salts as they could be used in place of salt solutions. Eutectic mixtures of alkali metal nitrate salts are used to lower the melting point^{96,97}.

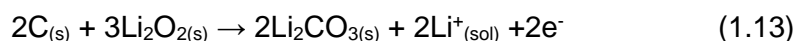
1.7.3. Carbon

Carbonaceous positive electrodes have been the most common choice for galvanostatic studies because carbons can produce high surface area positive electrodes and are sufficiently e⁻-conducting to support cycling. There are, however, issues with the stability of carbon positive electrodes, which have been documented.⁹⁸⁻¹⁰²

McCloskey *et al.* used a ¹³C-enriched positive electrode combined with DEMS to determine whether the positive electrode interacts with Li₂O₂ or intermediate species⁹⁸. They suggested that Li₂O₂ reacts with the carbon positive electrode to form a thin film directly on the surface. Towards the end of charging, this can be oxidised, and is seen in the DEMS results, where around 50% of evolved CO₂ is ¹³C-labelled. The Li₂CO₃ film is self-limiting as the initial formation protects the positive electrode from contact with the bulk of the Li₂O₂ deposits.

Thotiyil *et al.* devised an approach to determine the source of CO₂ from the solid deposits on the positive electrode⁹⁹. ¹³C positive electrodes were used in conjunction with electrolytes without ¹³C-enrichment. The positive electrodes were extracted at different stages of (dis)charge and washed with acid and Fenton's reagent. The former evolves CO₂ from Li₂CO₃ and the latter oxidises lithium carboxylates, again producing CO₂. The evolved gases were analysed by mass spectrometry. The authors found very little ¹³CO₂ on discharge, indicating that the positive electrode is stable on discharge. On charging, ¹³CO₂ was detected above 3.5 V, becoming an increasing proportion of the total CO₂ given off as charging progressed. Continued cycling resulted in accumulation of Li₂¹³CO₃. It was also reported that the positive electrode does not decompose in the absence of Li₂O₂, and chemical decomposition with Li₂O₂ is limited, since if this were to occur, ¹³CO₂ would be seen at potentials below 3.5 V. Therefore, the carbon positive electrode is primarily unstable during cycling at higher potentials.

A solid-state nuclear magnetic resonance (NMR) study by Leskes *et al.* supported these conclusions and proposed a possible route by which the positive electrode decomposes¹⁰¹. Based on the rapid decrease in intensity of the $\text{Li}_2^{17}\text{O}_2$ signal in ^{17}O spectra on charging, it was suggested that the Li_2CO_3 forms *via* Equation 1.13.

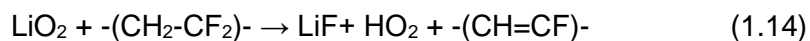


Gallant *et al.* and Itkis *et al.* used XANES to provide further evidence of Li_2CO_3 at the carbon/ Li_2O_2 interface, and also suggested that Li_2CO_3 forms on discharge^{100,102}. Itkis *et al.* suggest that O_2^- is responsible for carbon reactivity.

Xu *et al.* presented evidence against carbon instability, reporting that all Li_2CO_3 was formed from electrolyte decomposition in their study¹⁰³. Their suggestion is based on solid-state NMR data that disagrees with Leskes *et al.* However, given that some Li_2CO_3 formation was attributed to the positive electrode in their mass spectrometry data⁹⁹, it seems likely that the positive electrode is indeed unstable on charging.

1.7.4. Binders

Positive electrodes can contain binders but they also suffer from instability. One of the most commonly used binders, polyvinylidene difluoride (PVDF), was identified as being unstable by Black *et al.*²⁸ When PVDF was added to a solution containing chemically generated LiO_2 , it released gas for a short time and the solution immediately turned brown, which darkened over 1 hour. The XRD pattern showed some Li_2O_2 was produced but KF and LiF signals were stronger. The F^- source is the PVDF binder. New peaks were seen in ^{13}C NMR spectra, attributed to $=\text{C}-\text{H}$ and $=\text{C}-\text{F}$. PVDF is known to undergo dehydrofluorination, as the H atom is relatively acidic. Organic and alkaline bases are capable of abstracting the H atom, followed by the subsequent loss of F^- , to produce a $\text{C}=\text{C}$ bond (Equation 1.14). O_2^- is a stronger base than OH^- (ref. 77), so is more sensitive to the acidic proton in PVDF. This discolouration has also been observed by others with only Li_2O_2 present¹⁰⁴, suggesting that Li_2O_2 is a strong enough base to attack PVDF.



Younesi *et al.* also showed that PVDF decomposes in a battery using XPS⁹². After cycling PVDF-containing positive electrodes in fluorine-free electrolytes, a peak characteristic of LiF was seen, again suggesting PVDF is unstable. LiF forms in LIBs as part of the SEI layer and protects the negative electrode. However, in a Li-O₂ battery, the presence of LiF will be detrimental to the lifetime and performance of the battery. It is electrically insulating and cannot be oxidised on charge. This leads to accumulation on repeated cycling which passivates the positive electrode.

Nasybulin *et al.* screened a range of commonly used polymer binders using XRD and XPS¹⁰⁵. The binders were ball-milled with KO₂ and XRD data suggested that polytetrafluoroethylene (PTFE), polypropylene (PP) and polyethylene (PE) were stable to O₂⁻. XPS was then used on these binders, as well as PVDF, to further probe their stability, because XRD is insensitive to amorphous products and thin films of products on the surface of particles. PVDF was confirmed to be unstable to both KO₂ and Li₂O₂, as previously discussed. The results for PTFE were ambiguous. The C1s spectra had additional peaks when ball-milled with KO₂ and Li₂O₂, but the F1s spectra were unchanged. PP had small additional peaks indicating some instability, while PE was found to be stable to KO₂ and Li₂O₂. The authors noted that ball-milling produces a high-energy environment where the reactivity of the binders may be increased and not accurately represent the conditions in a cycled cell. Therefore, some polymers, particularly PP and PTFE, may still be suitable for practical positive electrodes. Amanchukwu *et al.* also performed a stability study on several polymers, but added solutions containing the polymers to Li₂O₂ powder¹⁰⁶. Of the polymers common to both studies, there was broad agreement in identifying the unstable polymers, but Amanchukwu *et al.* suggest that, PTFE, polyethylene oxide (PEO) and poly(methyl methacrylate) are stable¹⁰⁶. However, Beyer *et al.* reported that PEO reacts on charge¹⁰⁷.

1.7.5. Non-carbon positive electrodes

Considering the stability issues identified earlier, attempts have been made at synthesising non-carbon positive electrodes to produce a battery with improved cycling. Peng *et al.* used a nanoporous gold (NPG) positive electrode to reduce the degree of parasitic chemistry⁷². The battery maintained a capacity retention of 95% after 100 cycles and had low charge overpotentials throughout cycling. Gold would not be appropriate for a practical positive electrode due to high cost and mass, but the study demonstrated the potential of using non-carbon materials either solely as an electrode or coated on carbon to protect it from oxidation.

Further progress was made when Thotiyl *et al.* reported the stable cycling of a titanium carbide (TiC) positive electrode using a DMSO-based electrolyte¹⁰⁸. Capacity retention over 100 cycles was >98% (Figure 1.12) and showed reproducible (dis)charge profiles. Very small amounts of side products were found, even after 100 cycles and the e^-/O_2 values on the 100th cycle were 2.00 and 2.02 for discharge and charge, respectively. The stability of TiC was attributed to the surface chemistry. XPS data showed the surface was rich in TiOC and TiO₂. TiC was compared with SiC, which cycled poorly. SiC did not have an oxide layer.

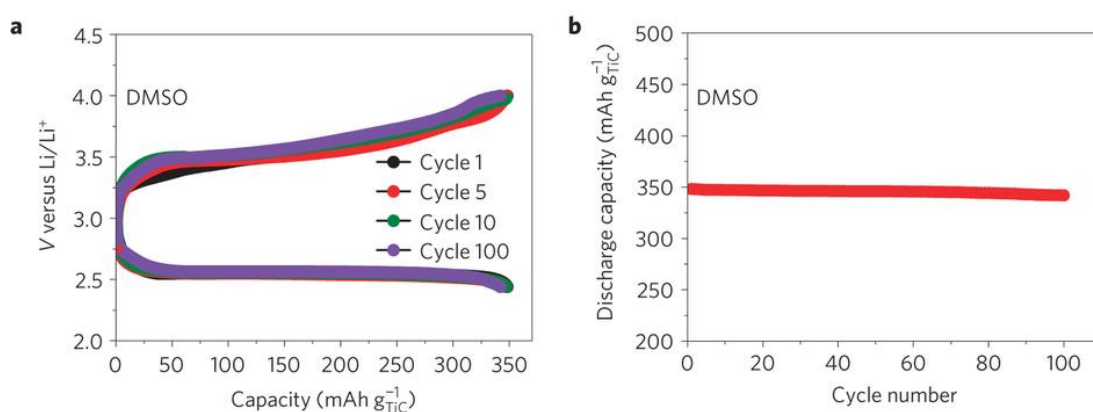


Figure 1.12: (a) Selected galvanostatic discharge/charge cycles of a TiC positive electrode in 0.5 M LiClO₄ in DMSO showing stable cycling. (b) Capacity retention for the cell in (a). Reproduced from ref. 108.

Adams *et al.* probed the nature of the TiC surface further¹⁰⁹. They found that a well-performing TiC sample had a smaller oxide layer than suggested by Thotiyl *et al.*¹⁰⁸, based on the relative intensities of TiO₂, TiOC and TiC in XPS spectra. TEM images showed crystallinity to the edge of the TiC particles, implying a very thin oxide layer which protects the positive electrode from oxidation while allowing facile e⁻-transport.

Mo₂C was considered by Kundu *et al.*¹¹⁰ It has an oxide layer consisting of MoO_{2+δ} which again acts as a protecting layer. However, it reacts with Li₂O₂ to form Li_xMoO₃, which delithiates within the OER potential range, thus competing with Li₂O₂ oxidation and severely impacting on the reversibility of the battery.

A Ti₄O₇ positive electrode was reported by Kundu *et al.*¹¹¹, which had a low charge overpotential. XPS data revealed that on discharge a surface layer of TiO₂ and TiO_{2-x} formed. The substoichiometric TiO_{2-x} is electronically conducting, permitting e⁻-transport from the bulk Ti₄O₇. A Pt-modified TiO₂ positive electrode has also been shown to possess excellent stability¹¹².

Other metal oxide positive electrodes have also been investigated, some of which may also catalyse the ORR and/or OER, providing an additional benefit to substituting the carbon for another active positive electrode material. There are several examples of Co₃O₄ positive electrodes with varying microstructures being employed as the positive electrode¹¹³⁻¹¹⁵. When nanoneedle Co₃O₄ was used, high discharge capacities were reported (4500 mAh g⁻¹) on the first discharge but cycling led to destruction of the nanoneedle structure¹¹⁴. Al₂O₃ has been used to coat defect sites on a carbon positive electrode, thus reducing the rate of parasitic chemistry¹¹⁶. FeO_x has also been used to successfully protect carbon from attack¹¹⁷.

These examples demonstrate the potential benefit that thin surface layers can afford to the bulk material in a positive electrode, provided the layer is carefully selected to be

inert to Li_2O_2 and its intermediates as well as providing the electrical conductivity required of the positive electrode.

1.8. Negative electrodes

The high theoretical capacity of Li- O_2 batteries is based on the use of Li metal as the negative electrode. However, it has been known from LIB development that Li is unsuitable as a negative electrode due to a number of issues, including dendrite formation. Furthermore, there are additional issues unique to using O_2 . At the very least, the negative electrode is exposed to O_2 and possibly O_2^- in a closed system, but if using ambient air as the O_2 supply, CO_2 , H_2O and N_2 must be filtered out by some form of membrane to prevent them passing through the cell and reacting with the negative electrode.

Assary *et al.* investigated the effect of O_2 crossover on the Li negative electrode in a TEGDME electrolyte¹¹⁸. The negative electrode reacted with O_2 and the solvent to form predominantly LiOH as well as some Li_2CO_3 after very few cycles, as observed by *in situ* XRD. Density functional theory calculations supported the experimental data.

One method of suppressing Li negative electrode reactivity is by the use of chemicals that undergo a self-limiting reaction with the negative electrode to form a stable SEI. Walker *et al.* reported a rechargeable battery utilising LiNO_3 and DMA, which achieved more than 80 cycles on shallow cycling⁸¹. They suggested that the stability of the cell was partly due to the formation of an SEI on the negative electrode by NO_3^- (Equation 1.15). The SEI is Li_2O , as LiNO_2 is a soluble species.



In subsequent work, Giordani *et al.* found that the SEI required O_2 to protect the negative electrode well on repeated cycling and suggested that LiNO_2 reacts with O_2 , regenerating LiNO_3 , so that the electrolyte is not depleted on cycling¹¹⁹. Uddin *et al.* confirmed the reaction mechanism, and noted that this system allows the SEI to respond to the

changing morphology of the negative electrode as Li is stripped and plated on cycling¹²⁰. However, they did not comment on the fact that the Li negative electrode reacts irreversibly, which would likely limit the rechargeability of a practical cell somewhat, and would certainly necessitate an excess of Li as the negative electrode to compensate for the continual Li₂O formation. However, they suggest their approach solves the problem of O₂ crossover and would negate the need for a protective membrane or ceramic on the negative electrode.

Another approach was taken by Liu *et al.*, who used fluoroethylene carbonate to produce an artificial SEI comprised mostly of LiF and Li₂CO₃, which greatly enhanced negative electrode stability¹²¹. SEM images showed that the protected negative electrode was much smoother on cycling compared to an unprotected negative electrode. An artificial SEI (e.g. LISICON¹²²) can also be placed between the negative electrode and the liquid electrolyte.

Cs⁺ was used to produce a self-healing effect on dendritic growth by Ding *et al.*¹²³ Any raised areas of Li on the negative electrode would attract the Cs⁺ and adsorb on these raised areas. The concentration of Cs⁺ was carefully controlled so that the applied potential was higher than the thermodynamic potential for Cs to electroplate on the negative electrode, but low enough to allow Li plating. The authors proposed that the adsorbed Cs⁺ acted as an electrostatic shield, repelling Li⁺ from the raised features, forcing it to plate onto smoother areas of the negative electrode (Figure 1.13). Cs⁺ was also shown to be able to smoothen pre-existing dendrites¹²³. These results were not carried out in a Li-O₂ battery, so, while promising, this approach may be unsuitable for Li-O₂ chemistry, with potential reactivity towards O₂⁻.

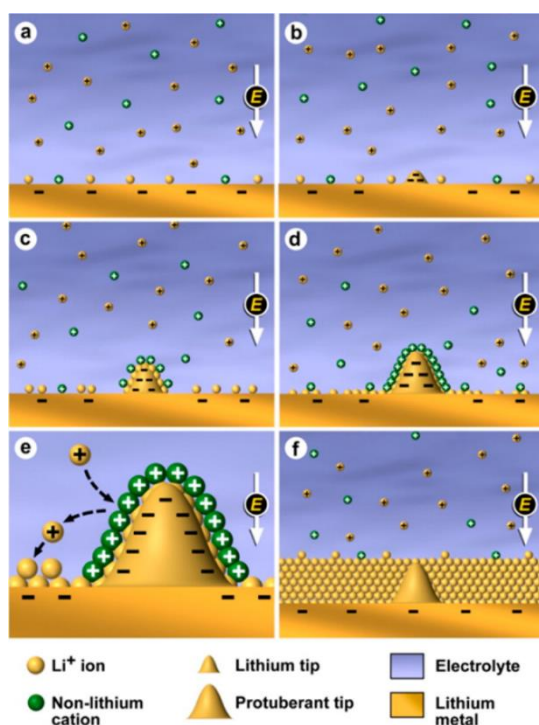


Figure 1.13: Schematic of the mechanism by which Cs^+ and other cations can suppress the growth of dendrites. As the tip grows (b), the cations are attracted to it (c) and completely cover it (d). They can then repel Li^+ (e) preventing further growth, so that deposition occurs around the tip, resulting in planar growth (f). Reproduced from ref. 123.

1.9. Strategies to reduce overpotentials and increase discharge capacity

If overpotentials could be reduced, the efficiency of the battery would be improved. There are two main routes by which this could be achieved; solid catalysts incorporated into the positive electrode and soluble redox mediators (RMs). It is also possible to increase discharge capacity by either designing specific catalyst architectures or using redox mediators to delay positive electrode passivation. The use of catalysts and RMs are discussed below.

1.9.1. Catalysts

Catalysts have been seen as a potential solution to reducing overpotentials. However, they will only be an effective solution if they are to alleviate the cause of the overpotential. Given that there is still debate as to whether the oxidation of Li_2O_2 has small

overpotentials⁴⁰ or is the cause of significant polarisation^{30,32}, the possible utility of catalysts remains uncertain.

The unique requirements of Li-O₂ chemistry are problematic if catalysts are used in the positive electrode. A catalyst, by definition, is a substance that promotes a given reaction by offering a low energy reaction pathway whilst not being consumed during the reaction. When “catalysts” are used in the Li-O₂ system, Li₂O₂ will form on their surfaces, causing passivation. This means it is unavailable to catalyse further O₂ reduction. It is, therefore, not a catalyst in the strictest sense. Once the cell is charged, the Li₂O₂ is removed and only then is the “catalyst” recovered. Hence, these added substances are not truly catalysts, though they can improve the performance of cells before being passivated. Some reports have attempted to synthesise catalysts with specific architectures to delay passivation, e.g. mesoporous pyrochlores¹²⁴ and nanoneedles¹¹⁵.

1.9.2.Redox mediators

An alternative method of increasing capacity and reducing overpotentials is by using one or more RMs, which has been an area of significant research in recent years. RMs work by decoupling O₂ electrochemistry from the storage of Li₂O₂. Taking the charge as an example, RM is oxidised to RM⁺, diffuses away from the electrode and oxidises Li₂O₂, which regenerates RM (Figure 1.14). In this way, Li₂O₂ that is electrically disconnected from the electrode can be oxidised. It also results in lower charging potentials, reducing decomposition reactions that would otherwise have occurred during charge. The soluble nature of RM⁻ and RM⁺ means that reduction and oxidation can occur far away from the electrode, preventing passivation and filling more of the cell volume with Li₂O₂ that can still be oxidised despite no contact with the positive electrode.

Tetrathiafulvalene (TTF) was used by Chen *et al.* as an oxidation mediator to charge cells at high rates for 100 cycles (Figure 1.15), which would not be possible in the absence of TTF¹²⁶. A subsequent study used electrochemical quartz crystal microbalance measurements to show TTF fully removed all Li₂O₂ deposited on the

electrode¹²⁷. Ethyl viologen has been used as reduction mediator, but decomposes when its concentration is too high, making it unsuitable for practical batteries¹²⁸.

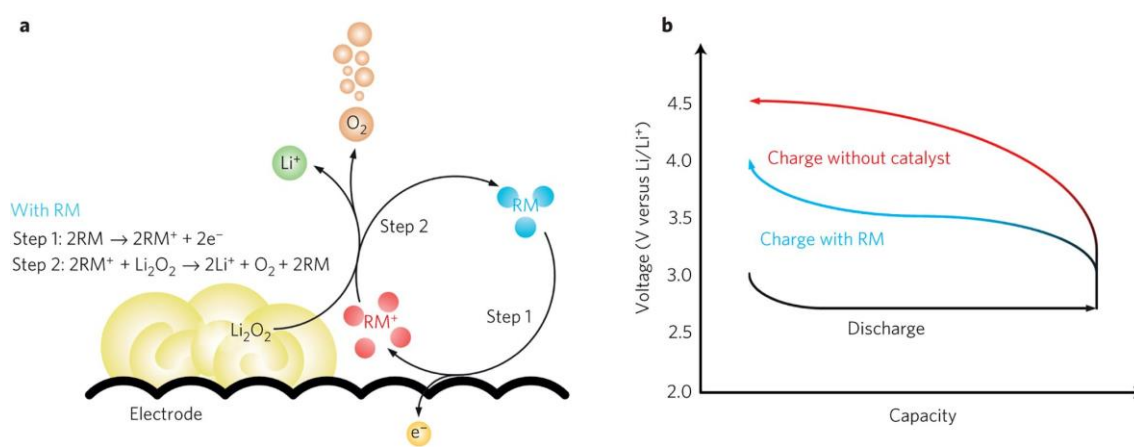


Figure 1.14: Schematics showing how a mediator oxidises Li_2O_2 on charge (a) and its effect on the load curve. Reproduced from ref. 125.

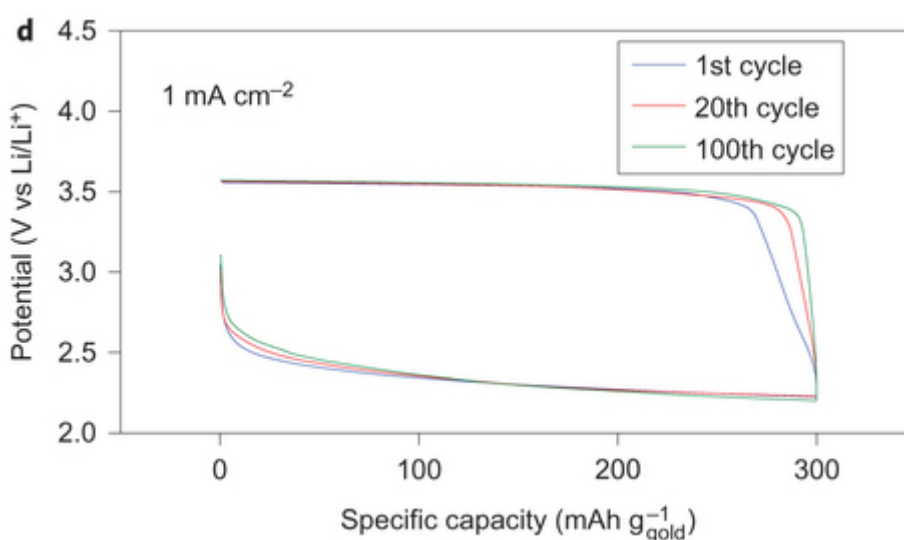


Figure 1.15: Selected cycles of a cell containing TTF galvanostatically cycling at 1 mA cm^{-2} with a nanoporous gold positive electrode. Reproduced from ref. 126.

Since this initial work, several oxidation mediators have been reported^{129,130}. 2,2,6,6-tetramethylpiperidinyloxy (TEMPO) was used by Bergner *et al.*, who found that it reduced the charge overpotential by 500 mV^{131,132}.

Discharge mediators have also been reported. Gao *et al.* used a benzoquinone molecule, 2,5-di-*tert*-butyl-1,4-benzoquinone (DBBQ) to promote solution-phase growth of Li_2O_2 in DME, which ordinarily forms Li_2O_2 via the surface mechanism (Figure 1.16)¹³³.

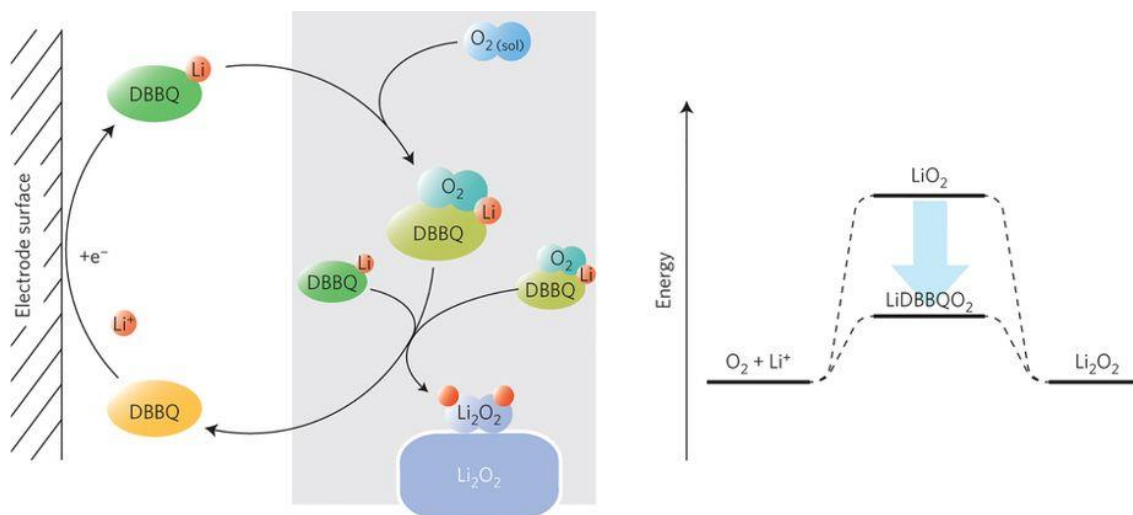


Figure 1.16: Schematic of the mechanism through which DBBQ promotes solution-phase growth of Li_2O_2 . Reproduced from ref. 133.

They proposed that the reduced DBBQ^- binds to Li^+ and O_2 to form a new intermediate species, LiDBBQO_2 , which reduces the discharge overpotential. LiDBBQO_2 subsequently disproportionates to give Li_2O_2 , O_2 and regenerating DBBQ . In a subsequent report, they combined DBBQ with TEMPO, creating a dual-mediator system, which was able to cycle repeatedly and avoided parasitic electrochemistry by virtue of the mediators¹³⁴. However, it should be noted that their cell required a solid electrolyte to protect the negative electrode from shuttling of the mediators, which is likely to be an issue for any homogenous catalyst.

1.10. The effect of impurities present in air

The use of ambient air as the source of O_2 is one of the main reasons Li-air batteries could surpass LIB technology. However, this open system introduces the possibility of contamination with other gaseous components of air. If ambient air were used to supply a Li-air battery, N_2 , Ar, H_2O and CO_2 would enter the battery, in addition to O_2 . If these

gases interfere with the electrochemical processes during cycling or chemically react with battery components or Li_2O_2 , they would need to be removed from the gas stream prior to entering the battery. The need to purify the gas stream has important implications for the device-level performance of the battery, in particular, the gravimetric and volumetric energy densities (Wh kg^{-1} and Wh L^{-1} , respectively) that could be achieved¹³⁵. This is because the addition of a gas-handling unit (GHU) could add significant mass and volume to a Li-air battery, reducing the gravimetric and volumetric energy densities that could be realistically achieved. The impact of the GHU on these device-level energy densities will be determined by how efficiently the GHU will be required to remove atmospheric gases.

Gallagher *et al.* performed a techno-economic analysis that considered the implications for the battery, assuming a worst-case scenario where the GHU was designed to achieve H_2O and CO_2 levels of <1 ppm in the gas stream¹³⁵. They found that, at a device-level, the GHU would account for 33% of the mass of the battery, resulting in a practical gravimetric energy density of 386 Wh kg^{-1} , but if a GHU were not necessary, this would increase to 573 Wh kg^{-1} (Figure 1.17). Therefore, this highlights the importance of not only optimising the cell chemistry, but also the auxiliary components (*e.g.* GHU, thermal management systems), which will form part of the device. Furthermore, if the cell chemistry could be designed to tolerate adverse conditions, such as the presence of some H_2O and/or CO_2 , the size, mass and complexity of the GHU could be reduced, concurrently increasing the device-level energy densities. This highlights the importance of establishing how tolerant Li-air batteries are to H_2O and CO_2 .

While the focus of gaseous contaminants in Li-air batteries is mainly concerned with reactions at the positive electrode, it should be noted that the main constituent gases of the atmosphere, excluding Ar, could react with a metallic Li negative electrode. N_2 , H_2O , CO_2 and O_2 react with Li to form Li_3N , LiOH , Li_2CO_3 and Li_2O , respectively. Due to these reactions, and other issues involving the use of metallic Li discussed in Section 1.8, some

form of Li^+ -conducting solid electrolyte layer will likely be required to protect a Li electrode from reactions with dissolved gases and the electrolyte.

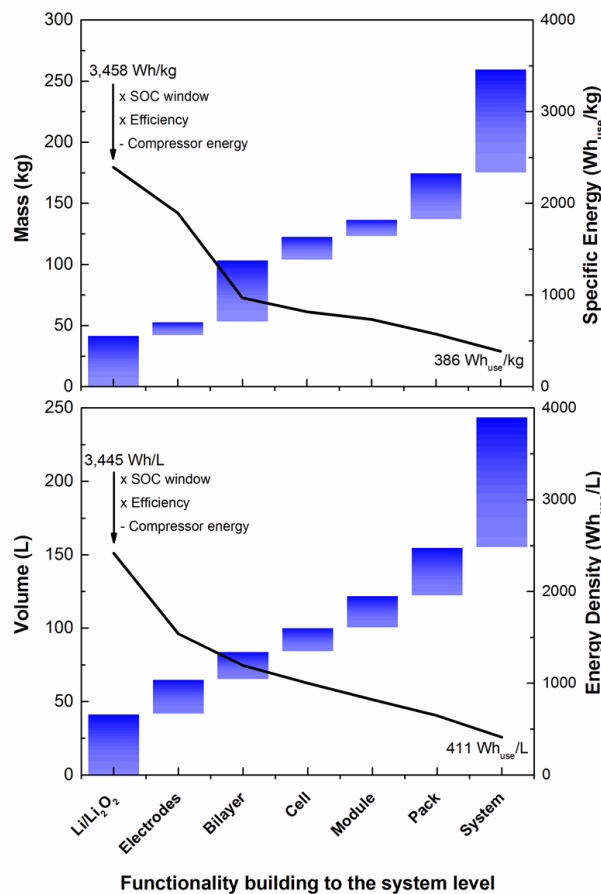
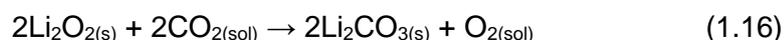


Figure 1.17: Mass and volume contributions of various components of a Li-air battery and their effects on the gravimetric and volumetric energy densities of the battery. The system bar consists of the GHU required to produce a dry and CO_2 -free gas stream (<1 ppm H_2O , <1 ppm CO_2). Reproduced from ref. 135.

The situation at the positive electrode is more complex than at the negative electrode, since atmospheric gases could react with O_2 reduction intermediates and the Li_2O_2 discharge product. Of the main atmospheric gases, neither Ar nor N_2 will react with Li_2O_2 or its intermediates, so only CO_2 and H_2O are of concern. Significant research has been conducted on their effects on O_2 reduction at the positive electrode, which is discussed below.

1.10.1. CO₂ chemistry at the positive electrode

The formation of Li₂CO₃ is considered detrimental to Li-O₂ cells, as it is difficult to oxidise completely during charge, resulting in its accumulation as the cell is cycled repeatedly. Li₂O₂ is known to react with CO₂ (Equation 1.16) and this reaction is spontaneous. Therefore, if CO₂ is dissolved in the electrolyte, it will react over time with Li₂O₂ formed during discharge. Because of this reaction alone, CO₂ will almost certainly have to be prevented from dissolving into the electrolyte, by, for example, using a GHU or a gas-selective membrane permeable to O₂ but not CO₂.



Takechi *et al.* provided one of the first reports concerning CO₂ in Li-O₂ batteries¹³⁶. They found that CO₂ increased the discharge capacity three-fold and that Li₂CO₃ was the discharge product. However, they used organic carbonate solvents, which have since been shown to decompose to Li₂CO₃ when attacked by the O₂⁻ intermediate. A subsequent report by Gowda *et al.* used DME as the solvent and found Li₂CO₃ formed on discharge in an O₂/CO₂ gas mixture¹³⁷. Furthermore, they found that Li₂CO₃ oxidation required potentials in excess of 4 V, which could also lead to electrolyte decomposition.

CO₂ has also been found to react with O₂ reduction intermediates, inducing a number of chemical and electrochemical reactions, ultimately producing Li₂CO₃. Theoretical calculations by Lim *et al.* suggested that a solvent with high dielectric constant (ϵ) will screen Li⁺ and O₂⁻ from each other more than a solvent with a low ϵ ¹³⁸. This makes the reaction between CO₂ and O₂⁻ more favourable, which begins a chain of reactions ultimately leading to Li₂CO₃. Cells discharged in DMSO and DME-based electrolytes, high and low ϵ solvents, respectively, showed only Li₂CO₃ for DMSO, while DME produced both Li₂O₂ and Li₂CO₃. The effect of solvents on the reaction pathway leading to Li₂CO₃ was further developed by Yin *et al.*, who showed that depending on the solvent, CO₂ reacts with either O₂⁻, LiO₂ or Li₂O₂, though all pathways ultimately lead to Li₂CO₃

(Figure 1.18)¹³⁹. They suggested that it is the DN of the solvent that determines whether CO₂ reacts with O₂⁻ (high DN solvents) or with LiO₂ and/or Li₂O₂ (low DN solvents).

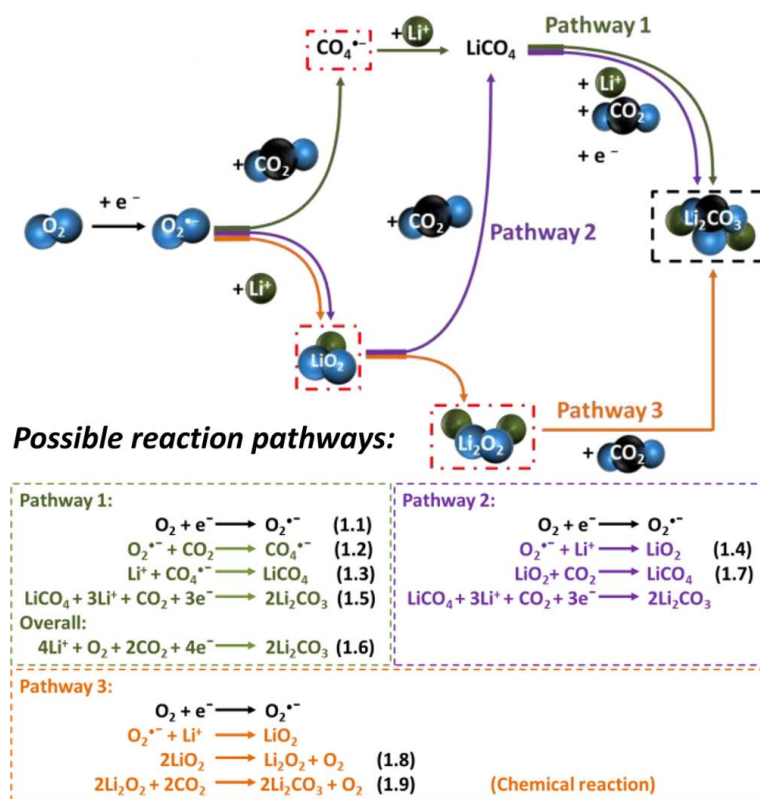
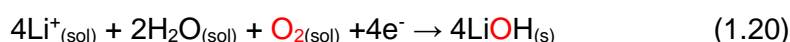
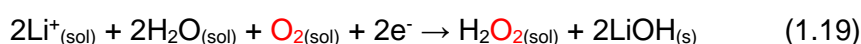
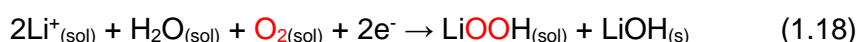


Figure 1.18: Schematic of the various reaction mechanisms that lead to the formation of Li₂CO₃ when in an O₂/CO₂ gas mixture. Pathway 1 occurs in high DN solvents, while Pathways 2 and 3 occur in low DN solvents. Reproduced from ref. 139.

1.10.2. H₂O chemistry at the positive electrode

Before discussing relevant work on the effect of H₂O, terminology regarding the O₂ reduction products requires clarification. The standard O₂ reduction reaction that occurs is the 2e⁻ reduction of O₂ to Li₂O₂ (Equation 1.17). If H₂O is present, other 2e⁻ reduction products are possible, namely LiOOH (Equation 1.18) and H₂O₂ (Equation 1.19). While these reactions also produce LiOH, this is a result of the **exchange of Li⁺ for a proton from H₂O**. If the 4e⁻ reduction occurs, LiOH is the sole product (Equation 1.20). As LiOH can form in both the 2e⁻ and 4e⁻ reduction reactions, discussions regarding LiOH could be referring to either the 2e⁻ reduction reactions (Equations 1.18 and 1.19) or the 4e⁻

reduction (Equation 1.20). Therefore, to avoid confusion, one must consider the oxidation state change of oxygen atoms originating from O_2 (highlighted in red in Equations 1.17-1.20) and not from H_2O (which is always O^{2-}). To avoid ambiguity, when O_2 reduction products are discussed in this thesis, $LiOH$ refers to the $4e^-$ reduction only (O^0 to O^{2-}) and peroxy- species (Li_2O_2 , $LiOOH$, H_2O_2 , HO_2^-) refer to $2e^-$ reduction (O^0 to O^-).



The positive electrode was initially assumed to be very sensitive to the presence of H_2O , as Li_2O_2 is known to spontaneously react with H_2O to form $LiOH$ ⁵⁴. Furthermore, H_2O can participate directly in O_2 reduction electrochemistry, where it acts as a proton donor, allowing various protic O_2 products such as H_2O_2 , HO_2^- and OH^- to form. Indeed, this is exploited in aqueous Li-air batteries, where $LiOH$ is the desired product. Therefore, it was expected that any H_2O present in the electrolyte would lead to formation of $LiOH$, which results in poor cycling. This is due to the large overpotential required to oxidise $LiOH$ ¹⁴⁰.

However, recently several groups have reported that trace amounts of H_2O in some electrolytes still produces Li_2O_2 on discharge, not $LiOH$ ^{27,54,141,142}. Furthermore, this is accompanied by an enhancement in capacity compared to cells discharged in dry electrolyte and must be due to H_2O promoting Li_2O_2 growth *via* a solution mechanism. This effect is most striking in glyme ethers, where a change in Li_2O_2 morphology is observed from thin films that coat electrode surfaces in dry electrolytes to large, typically toroidal, particles of Li_2O_2 when H_2O -containing electrolytes are used (Figure 1.19). This potentially beneficial effect of H_2O has been reported in electrolytes using DME,

diethylene glycol dimethyl ether, TEGDME and DMSO as solvents^{27,54,141,143}. However, it was found that LiOH does form when CH₃CN is the solvent¹⁴².

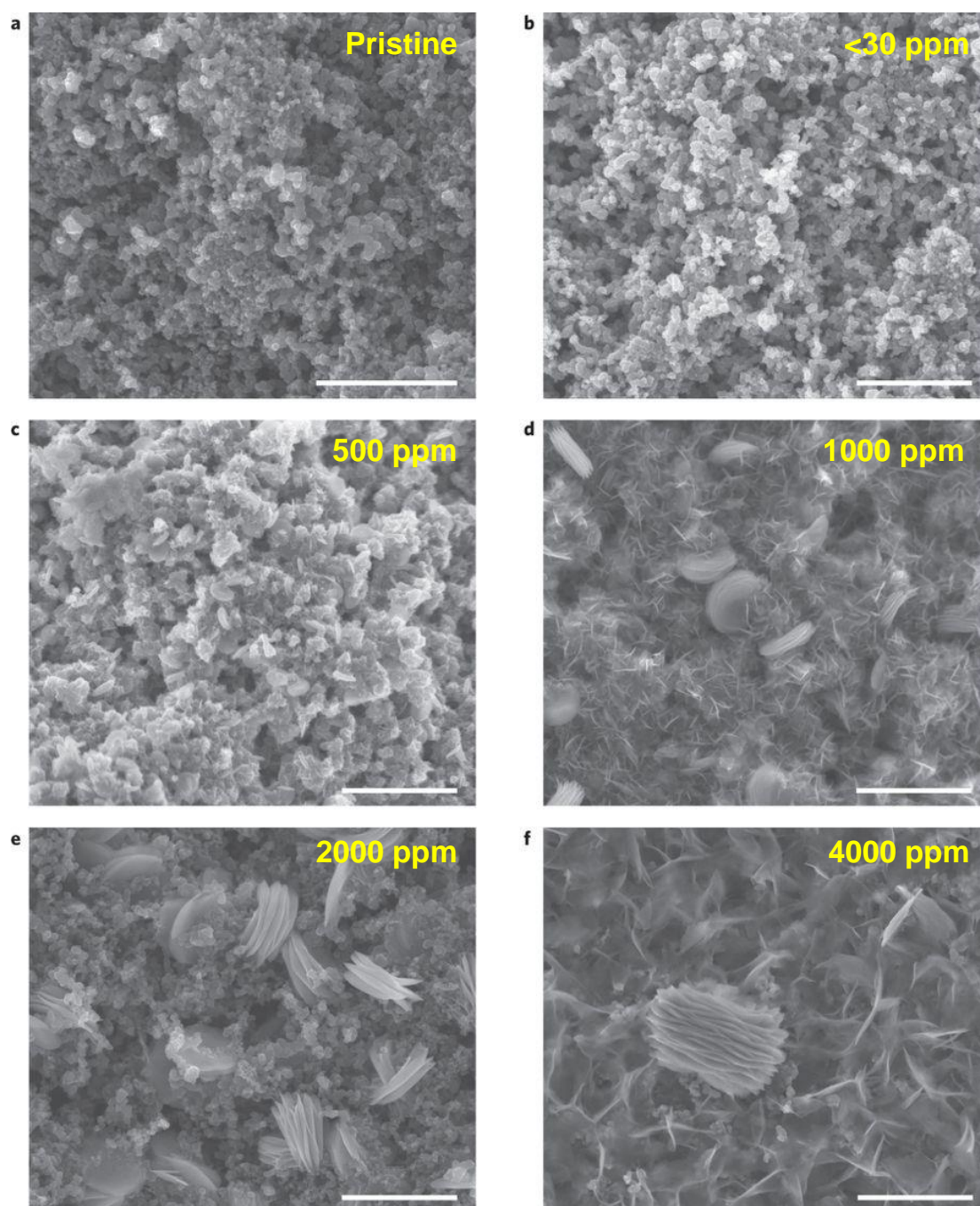
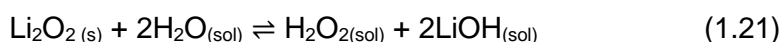


Figure 1.19: SEM images of pristine (a) and discharged positive electrodes (b-f) in an electrolyte of 1 M LiTFSI in DME and containing various H₂O concentrations, showing that H₂O promotes the formation of large Li₂O₂ particles. The H₂O concentration of each electrolyte are indicated on the SEM images. Scale bars are all 1 μm. Adapted from ref. 27.

Clearly, the solvent plays an important role in determining whether Li_2O_2 or LiOH forms. Various groups have proposed mechanisms to explain why trace amounts of H_2O are potentially not as detrimental as initially assumed. These mechanisms propose that H_2O acts in one of two ways: firstly, by stabilising the O_2^- anion due to the high Lewis acidity of H_2O ; secondly, by participating in metathesis reactions with Li_2O_2 and its intermediates. They are discussed in detail below.

Aetukuri *et al.* suggested that the Lewis acidity of H_2O could stabilise the O_2^- anion intermediate and thereby increase LiO_2 solubility²⁷. This is analogous to the DN mechanism put forward by Johnson *et al.*, where high DN solvents increase LiO_2 solubility by stabilising Li^+ in solution²². The soluble LiO_2 subsequently disproportionates to form large toroidal Li_2O_2 particles, rather than a thin film on the electrode surface. This would rationalise both the increased capacities in glyme ether solvents and the change in Li_2O_2 morphology from thin films in dry glyme ethers to large particles when H_2O is present.

The other category of mechanism involves metathesis reactions between H_2O and O_2 reduction products. Several groups have considered such reactions, the first of which was proposed by Schwenke *et al.*, who suggested that Li_2O_2 metathesises with trace amounts of H_2O in an equilibrium reaction, forming H_2O_2 , (Equation 1.21)⁵⁴. Schwenke *et al.* termed this equilibrium reaction as solubilisation of Li_2O_2 , as Li_2O_2 itself does not dissolve, but rather it is the products of the metathesis reaction that are more soluble. They can diffuse away from the electrode to grow Li_2O_2 particles from solution via the reverse reaction.



Qiao *et al.* demonstrated that the addition of H_2O to a TEGDME-based electrolyte increased the Li_2O_2 yield during discharge and rationalised this by suggesting that the intermediate species is no longer O_2^- , but HO_2^- (Figure 1.20)¹⁴¹. They reasoned that HO_2^-

is significantly less reactive than O_2^- , which is a radical, thus suppressing parasitic reactions and improving the Li_2O_2 yield. They suggested that the HO_2^- forms rapidly via O_2^- . This can then subsequently react with further H_2O to yield H_2O_2 and then reform Li_2O_2 via Equation 1.21. When cells were discharged, they showed that Li_2O_2/H_2O_2 was remarkably still the dominant product even with 30 vol% H_2O (approximately 20 M H_2O) in the electrolyte, suggesting the TEGDME can withstand astonishingly high H_2O concentrations. Similarly, these metathesis reactions can be promoted by using other molecules with an available proton, such as phenol¹⁴⁴.

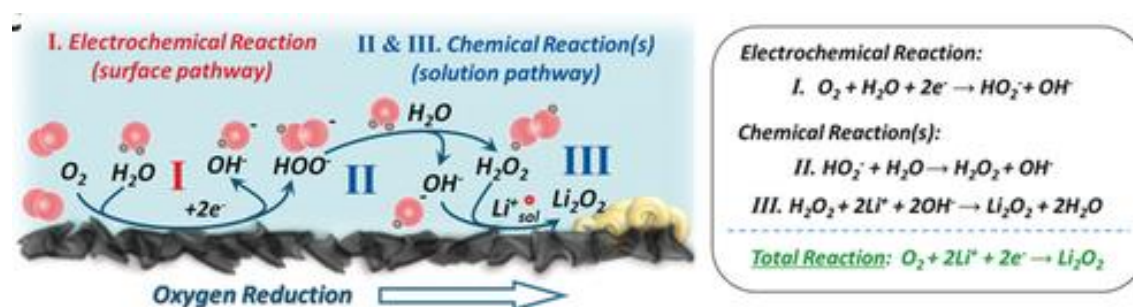


Figure 1.20: Schematic of the mechanism proposed by Qiao *et al.*, suggesting that O_2 reduction proceeds via a HO_2^- intermediate in the presence of H_2O . Reproduced from ref. 141.

Xia *et al.* proposed an analogous reaction for Na- O_2 batteries, where H_2O reacts with the electrogenerated O_2^- (ref. 145). This increases NaO_2 solubility and facilitates the growth of large cubic NaO_2 crystals. In Na- O_2 batteries, NaO_2 generally the discharge product, though it is possible for Na_2O_2 to be the product under certain discharge conditions.

The reports discussed above have demonstrated that glyme ether-based electrolytes can tolerate significant quantities of H_2O without altering the final discharge product and furthermore, enhance discharge capacities by promoting solution-based growth of Li_2O_2 particles. These reports focused on glyme ethers since they are currently the best available solvents for Li-air batteries. However, Kwabi *et al.* investigated how H_2O affects CH_3CN -based electrolytes and found evidence of $LiOH$ using *ex situ* XRD, attributing its

formation to the forward reaction in Equation 1.21¹⁴². In their discussion, they refer to LiOH as the product rather than H₂O₂, but this still implies that 2e⁻ O₂ reduction is occurring, but with the metathesis reaction (Equation 1.21) heavily favouring the forward reaction. They rationalised this by suggesting that the pK_a of H₂O in these solvents determines whether Equation 1.21 occurs. They argued that dissociation of H₂O into H⁺ and OH⁻ is required for the metathesis reaction, and therefore the pK_a of H₂O in each solvent can be used to determine whether metathesis occurs. They calculated the pK_as of H₂O in CH₃CN and DME as 35.2 and ≥47.0, respectively. The values suggest that the availability of H⁺ to react with Li₂O₂ would be far higher in CH₃CN than DME and produce LiOH and Li₂O₂ in the solvents, respectively. Kwabi *et al.* further suggested that DME solvated H₂O poorly, thus allowing it to stabilise the LiO₂ intermediate via the AN mechanism suggested by Aetukuri *et al.*²⁷

It is also possible to promote the formation of LiOH in glyme ethers by the addition of catalysts such as MnO₂ and LiI, which catalyse the rapid disproportionation of H₂O₂ to H₂O and O₂, driving Equation 1.19 and leading to a build-up of LiOH^{140,146}. However, oxidising LiOH requires a significant overpotential, so attempts have been made to use catalysts, such as Ru and LiI, to reduce this overpotential^{140,147}. However, there is significant debate as to whether LiI in particular, acts as an LiOH oxidation catalyst¹⁴⁸⁻¹⁵¹.

1.11. A universal mechanism describing the effect of H₂O on O₂ reduction

Clearly, the role of H₂O in Li-O₂ batteries is complex. The choice of solvent can promote a solution-based mechanism (switching from a surface mechanism in glyme ethers), thereby increasing discharge capacities, or change the discharge product altogether and form LiOH rather than Li₂O₂. Uncovering a mechanism that is consistent with all of these observations is non-trivial, and while significant attempts have been made to address why H₂O affects Li-O₂ cells in these ways, I believe that none of the mechanisms proposed to date adequately explains what occurs in all of these solvents.

At first glance, it appears that the mechanism proposed by Kwabi *et al.*¹⁴² is contradicted by observations reported by Aetukuri *et al.*²⁷ and vice versa. The pK_a mechanism implies that LiOH should form in DMSO, as the pK_a of H₂O in DMSO is nearly identical to that for CH₃CN, 35 and 35.2, respectively. However, Aetukuri *et al.* reported Li₂O₂ toroids forming in H₂O-containing DMSO. Similarly, the AN mechanism predicts that formation of Li₂O₂ particles would be promoted by the addition of H₂O to any low DN solvent. While glyme ethers and CH₃CN all possess low DNs (<20), Kwabi *et al.* demonstrated that large LiOH particles form in CH₃CN.

However, in both cases, there was limited characterisation of the discharge products. Aetukuri *et al.* present only SEM images of particles in DMSO, assuming they were Li₂O₂ due to their toroidal morphology. A further complication with DMSO is that it reacts with O₂⁻ and Li₂O₂, resulting in the formation of LiOH even in anhydrous DMSO. Kwabi *et al.* provide XRD patterns showing LiOH in H₂O-containing CH₃CN, but as discussed earlier, this could result from a chemical reaction (Equation 1.21) and/or electrochemical reactions (Equations 1.18-1.20), making it difficult to determine the (electro)chemistry during discharge. Because of the ambiguity of these characterisations, it is not possible to say conclusively that either mechanism is incorrect.

The metathesis mechanism, first proposed by Schwenke *et al.*⁵⁴, satisfactorily explains the effect of H₂O in glyme ethers and is backed up by spectroscopic evidence. However, this mechanism fails to address why 4e⁻ O₂ reduction does not occur, particularly when the H₂O concentration is significant, as in the study by Qiao *et al.*, nor do the AN and pK_a mechanisms. It would not be unreasonable to assume that the 4e⁻ reduction could occur, but each mechanism only considers how H₂O may facilitate 2e⁻ O₂ reduction.

This crucial gap in knowledge will be the main focus of this thesis. I will seek to establish why 4e⁻ O₂ reduction appears to be unfavourable in H₂O-containing Li-air electrolytes and identify the concentrations of H₂O required to induce the 4e⁻ reduction. I will initially focus on DMSO and CH₃CN for two reasons. Firstly, they form Li₂O₂ via solution and

surface mechanisms, respectively, allowing me to probe the effect of H₂O on the soluble LiO₂ intermediate and solid Li₂O₂ deposits separately. Secondly, there has been limited prior work concerning these solvents, and in order to develop a universal theory to rationalise the effect of water in Li-air cells, a thorough understanding of the effect in multiple different solvents is required.

I will start by exploring the effects of H₂O on O₂ reduction in the absence of Li⁺ by using tetrabutylammonium perchlorate as the salt. I aim to identify the chemical species formed during O₂ reduction via both electrochemical and spectroscopic means, and how they change with H₂O concentration. This will allow me to establish whether H₂O is involved in chemical or electrochemical reactions and if either the AN or pK_a mechanism occurs in both DMSO and CH₃CN.

I will then consider O₂ reduction in the presence of Li⁺ and H₂O in DMSO, CH₃CN and TEGDME, again identifying the O₂ reduction products using a combination of electrochemical and spectroscopic methods. TEGDME is also investigated here, as it is a solvent commonly used in Li-air research and provides an additional set of data, which any mechanism must explain satisfactorily. With a thorough understanding of the effect of H₂O in all three solvents, I hope to identify the key factors that determine the O₂ reduction product in the H₂O-containing solvents and propose a mechanism consistent with both my observations and those in previous reports.

Finally, the discharge product(s) in DMSO-, CH₃CN- and TEGDME-based electrolytes at a range of H₂O concentrations will be unambiguously identified. This will involve using pressure cells to measure O₂ consumption *in situ*, which will identify when 4e⁻ O₂ reduction becomes favourable in each solvent. Having confirmed H₂O concentrations at which only 2e⁻ reduction occurs in the electrolytes, cells will be discharged in humid O₂ atmospheres to confirm only 2e⁻ O₂ reduction occurs. Furthermore, this will identify the degree to which a GHU would be required to dry a gas stream.

1.12. References

- 1 Navas-Anguita, Z., García-Gusano, D. & Iribarren, D. A review of techno-economic data for road transportation fuels. *Renew. Sustain. Energy Rev* **112**, 11-26 (2019).
- 2 European Environment Agency. *Explaining road transport emissions*. (2016).
- 3 Blomgren, G. E. The Development and future of lithium ion batteries. *J. Electrochem. Soc.* **164**, A5019-A5025 (2017).
- 4 Armand, M. & Tarascon, J. M. Building better batteries. *Nature* **451**, 652-657 (2008).
- 5 Girishkumar, G., McCloskey, B., Luntz, A. C., Swanson, S. & Wilcke, W. Lithium-air battery: promise and challenges. *J. Phys. Chem. Lett.* **1**, 2193-2203 (2010).
- 6 Christensen, J. *et al.* A critical review of Li/air batteries. *J. Electrochem. Soc.* **159**, R1-R30 (2012).
- 7 Jung, R., Metzger, M., Maglia, F., Stinner, C. & Gasteiger, H. A. Chemical versus electrochemical electrolyte oxidation on NMC111, NMC622, NMC811, LNMO, and conductive carbon. *J. Phys. Chem. Lett.* **8**, 4820-4825 (2017).
- 8 Bruce, P. G., Freunberger, S. A., Hardwick, L. J. & Tarascon, J.-M. Li-O₂ and Li-S batteries with high energy storage. *Nat. Mater.* **11**, 19-29 (2012).
- 9 Black, R., Adams, B. & Nazar, L. F. Non-aqueous and hybrid Li-O₂ batteries. *Adv. Energy Mater.* **2**, 801-815 (2012).
- 10 Lu, J. *et al.* Aprotic and aqueous Li-O₂ batteries. *Chem. Rev.* **114**, 5611-5640 (2014).
- 11 Gierszewski, P. J., Finn, P. A. & Kirk, D. W. Aqueous lithium salt blanket (ALSB) concept properties of LiOH and LiNO₃ aqueous solutions. *Fusion Eng. Des.* **13**, 59-71 (1990).

- 12 He, P., Wang, Y. & Zhou, H. Titanium nitride catalyst cathode in a Li-air fuel cell with an acidic aqueous solution. *Chem. Commun.* **47**, 10701-10703 (2011).
- 13 Wang, Y. & Zhou, H. A lithium-air battery with a potential to continuously reduce O₂ from air for delivering energy. *J. Power Sources* **195**, 358-361 (2010).
- 14 Kumar, B. *et al.* A solid-state, rechargeable, long cycle life lithium–air battery. *J. Electrochem. Soc.* **157**, A50-A54 (2010).
- 15 Blurton, K. F. & Sammells, A. F. Metal/air batteries: Their status and potential — a review. *J. Power Sources* **4**, 263-279 (1979).
- 16 Abraham, K. M. & Jiang, Z. A polymer electrolyte-based rechargeable lithium/oxygen battery. *J. Electrochem. Soc.* **143**, 1-5 (1996).
- 17 Read, J. Characterization of the lithium/oxygen organic electrolyte battery. *J. Electrochem. Soc.* **149**, A1190-A1195 (2002).
- 18 Read, J. *et al.* Oxygen transport properties of organic electrolytes and performance of lithium/oxygen battery. *J. Electrochem. Soc.* **150**, A1351-A1356 (2003).
- 19 Ogasawara, T., Debart, A., Holzapfel, M., Novak, P. & Bruce, P. G. Rechargeable Li₂O₂ electrode for lithium batteries. *J. Am. Chem. Soc.* **128**, 1390-1393 (2006).
- 20 Lalore, C. O., Mukerjee, S., Abraham, K. M., Plichta, E. J. & Hendrickson, M. A. Elucidating the mechanism of oxygen reduction for lithium-air battery applications. *J. Phys. Chem. C* **113**, 20127-20134 (2009).
- 21 Lalore, C. O., Mukerjee, S., Abraham, K. M., Plichta, E. J. & Hendrickson, M. A. Influence of nonaqueous solvents on the electrochemistry of oxygen in the rechargeable lithium–air battery. *J. Phys. Chem. C* **114**, 9178-9186 (2010).
- 22 Johnson, L. *et al.* The role of LiO₂ solubility in O₂ reduction in aprotic solvents and its consequences for Li–O₂ batteries. *Nat. Chem.* **6**, 1091-1099 (2014).
- 23 Yu, Q. & Ye, S. In situ study of oxygen reduction in dimethyl sulfoxide (DMSO) solution: a fundamental study for development of the lithium–oxygen battery. *J. Phys. Chem. C* **119**, 12236-12250 (2015).

- 24 Pearson, R. G. Hard and soft acids and bases. *J. Am. Chem. Soc.* **85**, 3533-3539 (1963).
- 25 Pasgreta, E. *et al.* Ligand-exchange processes on solvated lithium cations: DMSO and water/DMSO mixtures. *ChemPhysChem* **8**, 1315-1320 (2007).
- 26 Gutmann, V. Solvent effects on the reactivities of organometallic compounds. *Coord. Chem. Rev.* **18**, 225-255 (1976).
- 27 Aetukuri, N. B. *et al.* Solvating additives drive solution-mediated electrochemistry and enhance toroid growth in non-aqueous Li-O₂ batteries. *Nat. Chem.* **7**, 50-56 (2015).
- 28 Black, R. *et al.* Screening for superoxide reactivity in Li-O₂ batteries: effect on Li₂O₂/LiOH crystallization. *J. Am. Chem. Soc.* **134**, 2902-2905 (2012).
- 29 Peng, Z. *et al.* Oxygen reactions in a non-aqueous Li⁺ electrolyte. *Angew. Chem. Int. Ed.* **50**, 6351-6355 (2011).
- 30 Lu, Y.-C. & Shao-Horn, Y. Probing the reaction kinetics of the charge reactions of nonaqueous Li-O₂ batteries. *J. Phys. Chem. Lett.* **4**, 93-99 (2012).
- 31 Luntz, A. C. & McCloskey, B. D. Nonaqueous Li-air batteries: a status report. *Chem. Rev.* **114**, 11721-11750 (2014).
- 32 Gallant, B. M. *et al.* Influence of Li₂O₂ morphology on oxygen reduction and evolution kinetics in Li-O₂ batteries. *Energy Environ. Sci.* **6**, 2518-2528 (2013).
- 33 Mitchell, R. R., Gallant, B. M., Shao-Horn, Y. & Thompson, C. V. Mechanisms of morphological evolution of Li₂O₂ particles during electrochemical growth. *J. Phys. Chem. Lett.* **4**, 1060-1064 (2013).
- 34 Hummelshoj, J. S., Luntz, A. C. & Norskov, J. K. Theoretical evidence for low kinetic overpotentials in Li-O₂ electrochemistry. *J. Chem. Phys.* **138**, 034703 (2013).
- 35 McCloskey, B. D., Scheffler, R., Speidel, A., Girishkumar, G. & Luntz, A. C. On the mechanism of nonaqueous Li-O₂ electrochemistry on C and its kinetic

- overpotentials: some implications for Li–air batteries. *J. Phys. Chem. C* **116**, 23897-23905 (2012).
- 36 McCloskey, B. D. *et al.* Limitations in rechargeability of Li-O₂ batteries and possible origins. *J. Phys. Chem. Lett.* **3**, 3043-3047 (2012).
- 37 Kang, S., Mo, Y., Ong, S. P. & Ceder, G. A facile mechanism for recharging Li₂O₂ in Li–O₂ batteries. *Chem. Mater.* **25**, 3328-3336 (2013).
- 38 Radin, M. D. & Siegel, D. J. Charge transport in lithium peroxide: relevance for rechargeable metal–air batteries. *Energy Environ. Sci.* **6**, 2370-2379 (2013).
- 39 Ganapathy, S. *et al.* Nature of Li₂O₂ oxidation in a Li-O₂ battery revealed by operando X-ray diffraction. *J. Am. Chem. Soc.* **136**, 16335-16344 (2014).
- 40 Viswanathan, V. *et al.* Li–O₂ kinetic overpotentials: tafel plots from experiment and first-principles theory. *J. Phys. Chem. Lett.* **4**, 556-560 (2013).
- 41 Hojberg, J. *et al.* An electrochemical impedance spectroscopy investigation of the overpotentials in Li-O₂ batteries. *ACS Appl. Mater. Interfaces* **7**, 4039-4047 (2015).
- 42 Zhong, L. *et al.* In situ transmission electron microscopy observations of electrochemical oxidation of Li₂O₂. *Nano Lett.* **13**, 2209-2214 (2013).
- 43 Wen, R., Hong, M. & Byon, H. R. In situ AFM imaging of Li-O₂ electrochemical reaction on highly oriented pyrolytic graphite with ether-based electrolyte. *J. Am. Chem. Soc.* **135**, 10870-10876 (2013).
- 44 Horstmann, B. *et al.* Rate-dependent morphology of Li₂O₂ growth in Li–O₂ batteries. *J. Phys. Chem. Lett.* **4**, 4217-4222 (2013).
- 45 Adams, B. D. *et al.* Current density dependence of peroxide formation in the Li-O₂ battery and its effect on charge. *Energy Environ. Sci.* **6**, 1772-1778 (2013).
- 46 Park, J. B. *et al.* Influence of temperature on lithium-oxygen battery behavior. *Nano Lett.* **13**, 2971-2975 (2013).

- 47 Mitchell, R. R., Gallant, B. M., Thompson, C. V. & Shao-Horn, Y. All-carbon-nanofiber electrodes for high-energy rechargeable Li-O₂ batteries. *Energy Environ. Sci.* **4**, 2952-2958 (2011).
- 48 Zhai, D. *et al.* Disproportionation in Li-O₂ batteries based on a large surface area carbon cathode. *J. Am. Chem. Soc.* **135**, 15364-15372 (2013).
- 49 Xu, J. J., Wang, Z. L., Xu, D., Zhang, L. L. & Zhang, X. B. Tailoring deposition and morphology of discharge products towards high-rate and long-life lithium-oxygen batteries. *Nat. Commun.* **4**, 2438 (2013).
- 50 Fan, W., Cui, Z. & Guo, X. Tracking formation and decomposition of abacus-ball-shaped lithium peroxides in Li-O₂ cells. *J. Phys. Chem. C* **117**, 2623-2627 (2013).
- 51 Lee, J.-H. *et al.* The role of vacancies and defects in Na_{0.44}MnO₂ nanowire catalysts for lithium-oxygen batteries. *Energy Environ. Sci.* **5**, 9558-9565 (2012).
- 52 Lu, Y.-C. *et al.* The discharge rate capability of rechargeable Li-O₂ batteries. *Energy Environ. Sci.* **4**, 2999-3007 (2011).
- 53 Wang, Z.-L., Xu, D., Xu, J.-J., Zhang, L.-L. & Zhang, X.-B. Graphene oxide gel-derived, free-standing, hierarchically porous carbon for high-capacity and high-rate rechargeable Li-O₂ batteries. *Adv. Funct. Mater.* **22**, 3699-3705 (2012).
- 54 Schwenke, K. U., Metzger, M., Restle, T., Piana, M. & Gasteiger, H. A. The influence of water and protons on Li₂O₂ crystal growth in aprotic Li-O₂ cells. *J. Electrochem. Soc.* **162**, A573-A584 (2015).
- 55 Lau, S. & Archer, L. A. Nucleation and growth of lithium peroxide in the Li-O₂ battery. *Nano Lett.* **15**, 5995-6002 (2015).
- 56 Sun, B., Huang, X., Chen, S., Zhang, J. & Wang, G. An optimized LiNO₃/DMSO electrolyte for high-performance rechargeable Li-O₂ batteries. *RSC Adv.* **4**, 11115-11120 (2014).
- 57 Geaney, H. & O'Dwyer, C. Electrochemical investigation of the role of MnO₂ nanorod catalysts in water containing and anhydrous electrolytes for Li-O₂ battery applications. *Phys. Chem. Chem. Phys.* **17**, 6748-6759 (2015).

- 58 Xu, K. Nonaqueous liquid electrolytes for lithium-based rechargeable batteries. *Chem. Rev.* **104**, 4303-4418 (2004).
- 59 Debart, A., Paterson, A. J., Bao, J. & Bruce, P. G. Alpha-MnO₂ nanowires: a catalyst for the O₂ electrode in rechargeable lithium batteries. *Angew. Chem. Int. Ed.* **47**, 4521-4524 (2008).
- 60 Thapa, A. K. & Ishihara, T. Mesoporous α -MnO₂/Pd catalyst air electrode for rechargeable lithium–air battery. *J. Power Sources* **196**, 7016-7020 (2011).
- 61 Yang, Y., Sun, Q., Li, Y.-S., Li, H. & Fu, Z.-W. Nanostructured diamond like carbon thin film electrodes for lithium air batteries. *J. Electrochem. Soc.* **158**, B1211-B1216 (2011).
- 62 Xiao, J. *et al.* Investigation of the rechargeability of Li–O₂ batteries in non-aqueous electrolyte. *J. Power Sources* **196**, 5674-5678 (2011).
- 63 McCloskey, B. D., Bethune, D. S., Shelby, R. M., Girishkumar, G. & Luntz, A. C. Solvents' critical role in nonaqueous lithium–oxygen battery electrochemistry. *J. Phys. Chem. Lett.* **2**, 1161-1166 (2011).
- 64 Mizuno, F., Nakanishi, S., Kotani, Y., Yokoishi, S. & Iba, H. Rechargeable Li-air batteries with carbonate-based liquid electrolytes. *Electrochemistry* **78**, 403-405 (2010).
- 65 Freunberger, S. A. *et al.* Reactions in the rechargeable lithium-O₂ battery with alkyl carbonate electrolytes. *J. Am. Chem. Soc.* **133**, 8040-8047 (2011).
- 66 Bryantsev, V. S. & Blanco, M. Computational study of the mechanisms of superoxide-induced decomposition of organic carbonate-based electrolytes. *J. Phys. Chem. Lett.* **2**, 379-383 (2011).
- 67 Bryantsev, V. S. *et al.* Predicting solvent stability in aprotic electrolyte Li–air batteries: nucleophilic substitution by the superoxide anion radical (O₂^{•-}). *J. Phys. Chem. A* **115**, 12399-12409 (2011).
- 68 Read, J. Ether-based electrolytes for the lithium/oxygen organic electrolyte battery. *J. Electrochem. Soc.* **153**, A96-A100 (2006).

- 69 Freunberger, S. A. *et al.* The lithium-oxygen battery with ether-based electrolytes. *Angew. Chem. Int. Ed.* **50**, 8609-8613 (2011).
- 70 McCloskey, B. D. *et al.* Combining accurate O₂ and Li₂O₂ assays to separate discharge and charge stability limitations in nonaqueous Li–O₂ batteries. *J. Phys. Chem. Lett.* **4**, 2989-2993 (2013).
- 71 Adams, B. D. *et al.* Towards a stable organic electrolyte for the lithium oxygen battery. *Adv. Energy Mater.* **5**, 1400867 (2015).
- 72 Peng, Z., Freunberger, S. A., Chen, Y. & Bruce, P. G. A reversible and higher-rate Li-O₂ battery. *Science* **337**, 563-566 (2012).
- 73 Xu, D., Wang, Z., Xu, J., Zhang, L. & Zhang, X. Novel DMSO-based electrolyte for high performance rechargeable Li-O₂ batteries. *Chem. Commun.* **48**, 6948-6950 (2012).
- 74 Sharon, D. *et al.* Oxidation of dimethyl sulfoxide solutions by electrochemical reduction of oxygen. *J. Phys. Chem. Lett.* **4**, 3115-3119 (2013).
- 75 Kwabi, D. G. *et al.* Chemical instability of dimethyl sulfoxide in lithium–air batteries. *J. Phys. Chem. Lett.* **5**, 2850-2856 (2014).
- 76 Younesi, R., Norby, P. & Vegge, T. A new look at the stability of dimethyl sulfoxide and acetonitrile in Li-O₂ batteries. *ECS Electrochem. Lett.* **3**, A15-A18 (2014).
- 77 Sawyer, D. T. & Valentine, J. S. How super is superoxide? *Acc. Chem. Res.* **14**, 393-400 (1981).
- 78 Bryantsev, V. S. *et al.* The identification of stable solvents for nonaqueous rechargeable Li-air batteries. *J. Electrochem. Soc.* **160**, A160-A171 (2013).
- 79 Teodoro, L. & Alessandro, C. Chemical reactivity of aprotic electrolytes on a solid Li₂O₂ surface: screening solvents for Li–air batteries. *New J. Phys.* **15**, 095009 (2013).
- 80 Chen, Y., Freunberger, S. A., Peng, Z., Barde, F. & Bruce, P. G. Li-O₂ battery with a dimethylformamide electrolyte. *J. Am. Chem. Soc.* **134**, 7952-7957 (2012).

- 81 Walker, W. *et al.* A rechargeable Li-O₂ battery using a lithium nitrate/N,N-dimethylacetamide electrolyte. *J. Am. Chem. Soc.* **135**, 2076-2079 (2013).
- 82 Katayama, Y., Onodera, H., Yamagata, M. & Miura, T. Electrochemical reduction of oxygen in some hydrophobic room-temperature molten salt systems. *J. Electrochem. Soc.* **151**, A59-A63 (2004).
- 83 Mizuno, F. *et al.* Design of non-aqueous liquid electrolytes for rechargeable Li-O₂ batteries. *Electrochemistry* **79**, 876-881 (2011).
- 84 Das, S. *et al.* Instability of ionic liquid-based electrolytes in Li-O₂ batteries. *J. Phys. Chem. C* **119**, 18084-18090 (2015).
- 85 Hayyan, M., Mjalli, F. S., Hashim, M. A. & AlNashef, I. M. An investigation of the reaction between 1-butyl-3-methylimidazolium trifluoromethanesulfonate and superoxide ion. *J. Mol. Liq.* **181**, 44-50 (2013).
- 86 Oswald, S. *et al.* XPS investigations of electrolyte/electrode interactions for various Li-ion battery materials. *Anal. Bioanal. Chem.* **400**, 691-696 (2011).
- 87 Veith, G. M., Dudney, N. J., Howe, J. & Nanda, J. Spectroscopic characterization of solid discharge products in Li-air cells with aprotic carbonate electrolytes. *J. Phys. Chem. C* **115**, 14325-14333 (2011).
- 88 Chalasani, D. & Lucht, B. L. Reactivity of electrolytes for lithium-oxygen batteries with Li₂O₂. *ECS Electrochem. Lett.* **1**, A38-A42 (2012).
- 89 Veith, G. M., Nanda, J., Delmau, L. H. & Dudney, N. J. Influence of lithium salts on the discharge chemistry of Li-air cells. *J. Phys. Chem. Lett.* **3**, 1242-1247 (2012).
- 90 Du, P. *et al.* Compatibility of lithium salts with solvent of the non-aqueous electrolyte in Li-O₂ batteries. *Phys. Chem. Chem. Phys.* **15**, 5572-5581 (2013).
- 91 Younesi, R., Hahlin, M. & Edstrom, K. Surface characterization of the carbon cathode and the lithium anode of Li-O₂ batteries using LiClO₄ or LiBOB salts. *ACS Appl. Mater. Interfaces* **5**, 1333-1341 (2013).

- 92 Younesi, R. *et al.* Ether based electrolyte, LiB(CN)₄ salt and binder degradation in the Li–O₂ battery studied by hard X-ray photoelectron spectroscopy (HAXPES). *J. Phys. Chem. C* **116**, 18597-18604 (2012).
- 93 Nasybulin, E. *et al.* Effects of electrolyte salts on the performance of Li–O₂ batteries. *J. Phys. Chem. C* **117**, 2635-2645 (2013).
- 94 Hyoung Oh, S., Yim, T., Ekaterina, P. & Nazar, L. F. Decomposition reaction of lithium bis(oxalato)borate in the rechargeable lithium-oxygen cell. *Electrochem. Solid-State Lett.* **14**, A185-A188 (2011).
- 95 Younesi, R., Hahlin, M., Björefors, F., Johansson, P. & Edström, K. Li–O₂ battery degradation by lithium peroxide (Li₂O₂): a model study. *Chem. Mater.* **25**, 77-84 (2012).
- 96 Uddin, J., Addison, D. D., Giordani, V., Chase, G. V. & Walker, W. Alkali metal/oxygen batteries employing molten nitrate electrolytes. Patent WO 2014153551 (2014).
- 97 Miles, M. H. Rechargeable lithium-air and other lithium-based batteries using molten nitrates. Patent US 8,795,868 B1 (2014).
- 98 McCloskey, B. D. *et al.* Twin problems of interfacial carbonate formation in nonaqueous Li–O₂ batteries. *J. Phys. Chem. Lett.* **3**, 997-1001 (2012).
- 99 Ottakam Thotiyil, M. M., Freunberger, S. A., Peng, Z. & Bruce, P. G. The carbon electrode in nonaqueous Li–O₂ cells. *J. Am. Chem. Soc.* **135**, 494-500 (2013).
- 100 Gallant, B. M. *et al.* Chemical and morphological changes of Li–O₂ battery electrodes upon cycling. *J. Phys. Chem. C* **116**, 20800-20805 (2012).
- 101 Leskes, M., Moore, A. J., Goward, G. R. & Grey, C. P. Monitoring the electrochemical processes in the lithium–air battery by solid state NMR spectroscopy. *J. Phys. Chem. C* **117**, 26909-26939 (2013).
- 102 Itkis, D. M. *et al.* Reactivity of carbon in lithium-oxygen battery positive electrodes. *Nano Lett.* **13**, 4697-4701 (2013).

- 103 Xu, W. *et al.* The stability of organic solvents and carbon electrode in nonaqueous Li-O₂ batteries. *J. Power Sources* **215**, 240-247 (2012).
- 104 Xu, W. *et al.* Investigation on the charging process of Li₂O₂-based air electrodes in Li-O₂ batteries with organic carbonate electrolytes. *J. Power Sources* **196**, 3894-3899 (2011).
- 105 Nasybulin, E. *et al.* Stability of polymer binders in Li-O₂ batteries. *J. Power Sources* **243**, 899-907 (2013).
- 106 Amanchukwu, C. V., Harding, J. R., Shao-Horn, Y. & Hammond, P. T. Understanding the chemical stability of polymers for lithium-air batteries. *Chem. Mater.* **27**, 550-561 (2015).
- 107 Beyer, H., Meini, S., Tsiouvaras, N., Piana, M. & Gasteiger, H. A. Thermal and electrochemical decomposition of lithium peroxide in non-catalyzed carbon cathodes for Li-air batteries. *Phys. Chem. Chem. Phys.* **15**, 11025-11037 (2013).
- 108 Ottakam Thotiyil, M. M. *et al.* A stable cathode for the aprotic Li-O₂ battery. *Nat. Mater.* **12**, 1050-1056 (2013).
- 109 Adams, B. *et al.* The Importance of Nanometric Passivating Films on Cathodes for LiAir Batteries. *ACS Nano* **8**, 12483-12493 (2014).
- 110 Kundu, D. *et al.* Nanostructured metal carbides for aprotic Li-O₂ batteries: New insights into interfacial reactions and cathode stability. *J. Phys. Chem. Lett.* **6**, 2252-2258 (2015).
- 111 Kundu, D., Black, R., Berg, E. J. & Nazar, L. F. A highly active nanostructured metallic oxide cathode for aprotic Li-O₂ batteries. *Energy Environ. Sci.* **8**, 1292-1298 (2015).
- 112 Zhao, G., Mo, R., Wang, B., Zhang, L. & Sun, K. Enhanced cyclability of Li-O₂ Batteries based on TiO₂ supported cathodes with no carbon or binder. *Chem. Mater.* **26**, 2551-2556 (2014).
- 113 Cui, Y., Wen, Z. & Liu, Y. A free-standing-type design for cathodes of rechargeable Li-O₂ batteries. *Energy Environ. Sci.* **4**, 4727-4734 (2011).

- 114 Lee, H. *et al.* Directly grown Co_3O_4 nanowire arrays on Ni-foam: structural effects of carbon-free and binder-free cathodes for lithium–oxygen batteries. *J. Mater. Chem. A* **2**, 11891-11898 (2014).
- 115 Riaz, A. *et al.* Carbon-free cobalt oxide cathodes with tunable nanoarchitectures for rechargeable lithium-oxygen batteries. *Chem. Commun.* **49**, 5984-5986 (2013).
- 116 Lu, J. *et al.* A nanostructured cathode architecture for low charge overpotential in lithium-oxygen batteries. *Nat. Commun.* **4**, 2383 (2013).
- 117 Xie, J. *et al.* Three dimensionally ordered mesoporous carbon as a stable, high-performance Li-O_2 battery cathode. *Angew. Chem.* **127**, 4373-4377 (2015).
- 118 Assary, R. S. *et al.* The effect of oxygen crossover on the anode of a Li-O_2 battery using an ether-based solvent: insights from experimental and computational studies. *ChemSusChem* **6**, 51-55 (2013).
- 119 Giordani, V. *et al.* Synergistic effect of oxygen and LiNO_3 on the interfacial stability of lithium metal in a Li/O_2 battery. *J. Electrochem. Soc.* **160**, A1544-A1550 (2013).
- 120 Uddin, J. *et al.* Lithium nitrate as regenerable SEI stabilizing agent for rechargeable Li/O_2 batteries. *J. Phys. Chem. Lett.* **4**, 3760-3765 (2013).
- 121 Liu, Q.-C. *et al.* Artificial protection film on lithium metal anode toward long-cycle-life lithium–oxygen batteries. *Adv. Mater.* **27**, 5241–5247 (2015).
- 122 Visco, S. J., Nimon, Y. S. & Katz, B. Li/Air non-aqueous batteries. Patent US 8,652,692 B2 (2014).
- 123 Ding, F. *et al.* Dendrite-free lithium deposition via self-healing electrostatic shield mechanism. *J. Am. Chem. Soc.* **135**, 4450-4456 (2013).
- 124 Oh, S. H., Black, R., Pomerantseva, E., Lee, J.-H. & Nazar, L. F. Synthesis of a metallic mesoporous pyrochlore as a catalyst for lithium– O_2 batteries. *Nat. Chem.* **4**, 1004-1010 (2012).

- 125 Lim, H.-D. *et al.* Rational design of redox mediators for advanced Li–O₂ batteries. *Nat. Energy* **1**, 16066 (2016).
- 126 Chen, Y., Freunberger, S. A., Peng, Z., Fontaine, O. & Bruce, P. G. Charging a Li–O₂ battery using a redox mediator. *Nat. Chem.* **5**, 489–494 (2013).
- 127 Schaltin, S., Vanhoutte, G., Wu, M., Barde, F. & Fransaer, J. A QCM study of ORR-OER and an in situ study of a redox mediator in DMSO for Li–O₂ batteries. *Phys. Chem. Chem. Phys.* **17**, 12575-12586 (2015).
- 128 Lacey, M. J., Frith, J. T. & Owen, J. R. A redox shuttle to facilitate oxygen reduction in the lithium air battery. *Electrochem. Commun.* **26**, 74-76 (2013).
- 129 Park, J.-B., Lee, S. H., Jung, H.-G., Aurbach, D. & Sun, Y.-K. Redox mediators for Li–O₂ batteries: status and perspectives. *Adv. Mater.* **30**, 1704162 (2018).
- 130 Landa-Medrano, I., Lozano, I., Ortiz-Vitoriano, N., Ruiz de Larramendi, I. & Rojo, T. Redox mediators: a shuttle to efficacy in metal–O₂ batteries. *J. Mater. Chem. A* **7**, 8746-8764 (2019).
- 131 Bergner, B. J., Schurmann, A., Peppler, K., Garsuch, A. & Janek, J. TEMPO: a mobile catalyst for rechargeable Li–O₂ batteries. *J. Am. Chem. Soc.* **136**, 15054-15064 (2014).
- 132 Bergner, B. J. *et al.* Understanding the fundamentals of redox mediators in Li–O₂ batteries: a case study on nitroxides. *Phys. Chem. Chem. Phys.* **17**, 31769-31779 (2015).
- 133 Gao, X., Chen, Y., Johnson, L. & Bruce, P. G. Promoting solution phase discharge in Li–O₂ batteries containing weakly solvating electrolyte solutions. *Nat. Mater.* **15**, 882–888 (2016).
- 134 Gao, X., Chen, Y., Johnson, L. R., Jovanov, Z. P. & Bruce, P. G. A rechargeable lithium–oxygen battery with dual mediators stabilizing the carbon cathode. *Nat. Energy* **2**, 17118 (2017).
- 135 Gallagher, K. G. *et al.* Quantifying the promise of lithium–air batteries for electric vehicles. *Energy Environ. Sci.* **7**, 1555-1563 (2014).

- 136 Takechi, K., Shiga, T. & Asaoka, T. A Li-O₂/CO₂ battery. *Chem. Commun.* **47**, 3463-3465 (2011).
- 137 Gowda, S. R., Brunet, A., Wallraff, G. M. & McCloskey, B. D. Implications of CO₂ contamination in rechargeable nonaqueous Li-O₂ batteries. *J. Phys. Chem. Lett.* **4**, 276-279 (2013).
- 138 Lim, H. K. *et al.* Toward a lithium-"air" battery: the effect of CO₂ on the chemistry of a lithium-oxygen cell. *J. Am. Chem. Soc.* **135**, 9733-9742 (2013).
- 139 Yin, W., Grimaud, A., Lepoivre, F., Yang, C. & Tarascon, J. M. Chemical vs electrochemical formation of Li₂CO₃ as a discharge product in Li-O₂/CO₂ batteries by controlling the superoxide intermediate. *J Phys. Chem. Lett.* **8**, 214-222 (2017).
- 140 Li, F. *et al.* The water catalysis at oxygen cathodes of lithium-oxygen cells. *Nat. Commun.* **6**, 7843 (2015).
- 141 Qiao, Y. *et al.* From O₂⁻ to HO₂⁻ : reducing by-products and overpotential in Li-O₂ batteries by water addition. *Angew. Chem.* **56**, 4960-4964 (2017).
- 142 Kwabi, D. G. *et al.* The effect of water on discharge product growth and chemistry in Li-O₂ batteries. *Phys. Chem. Chem. Phys.* **18**, 24944-24953 (2016).
- 143 Meini, S., Piana, M., Tsiouvaras, N., Garsuch, A. & Gasteiger, H. A. The effect of water on the discharge capacity of a non-catalyzed carbon cathode for Li-O₂ batteries. *Electrochem. Solid-State Lett.* **15**, A45-A48 (2012).
- 144 Gao, X., Jovanov, Z. P., Chen, Y., Johnson, L. R. & Bruce, P. G. Phenol-catalyzed discharge in the aprotic lithium-oxygen battery. *Angew. Chem. Int. Ed.* **56**, 6539-6543 (2017).
- 145 Xia, C., Black, R., Fernandes, R., Adams, B. & Nazar, L. F. The critical role of phase-transfer catalysis in aprotic sodium oxygen batteries. *Nat. Chem.* **7**, 496-501 (2015).
- 146 Liu, T. *et al.* Cycling Li-O₂ batteries via LiOH formation and decomposition. *Science* **350**, 530-533 (2015).

- 147 Liu, T. *et al.* Understanding LiOH chemistry in a ruthenium-catalyzed Li-O₂ battery. *Angew. Chem. Int. Ed.* **56**, 16057-16062 (2017)
- 148 Shen, Y., Zhang, W., Chou, S.-L. & Dou, S.-X. Comment on “Cycling Li-O₂ batteries via LiOH formation and decomposition”. *Science* **352**, 667a (2016).
- 149 Liu, T., Kim, G., Carretero-González, J., Castillo-Martínez, E. & Grey, C. P. Response to comment on “Cycling Li-O₂ batteries via LiOH formation and decomposition”. *Science* **352**, 667b (2016).
- 150 Viswanathan, V. *et al.* Comment on “Cycling Li-O₂ batteries via LiOH formation and decomposition”. *Science* **352**, 667c (2016).
- 151 Liu, T. *et al.* Response to comment on “cycling Li-O₂ batteries via LiOH formation and decomposition”. *Science* **352**, 667d (2016).

2. Experimental methods and techniques

2.1. Electrochemical measurements

3 mm Au stick electrodes (IJ Cambria) were used for cyclic voltammetry measurements. A Au microelectrode was made in-house by sealing a 25 μm diameter Au wire (Goodfellows) in glass and then polishing the glass with several grades of sandpaper, followed by 0.1 μm alumina powder. The electrode was polished until a circular cross-section of the wire was exposed. A platinum wire electrode was used as the counter electrode for all three-electrode measurements presented in this thesis.

The reference electrode used in Chapters 3 and 4 was partially delithiated lithium iron phosphate (Li_xFePO_4), which has a stable potential of 3.45 V vs Li^+/Li in DMSO. The delithiation is achieved by chemically pre-charging LiFePO_4 . First, a putty was made from an 8:1:1 weight ratio of LiFePO_4 (MTI), Super P carbon (Alfa Aesar) and PTFE suspension (10% in H_2O , Sigma Aldrich), mixed with isopropanol. This was then spread onto a stainless steel mesh and allowed to air-dry. The LiFePO_4 was then chemically pre-charged for 15 minutes in a solution consisting of 3.6 mL 30% H_2O_2 , 1.6 mL glacial acetic acid and 250 mL ultrapure H_2O . The electrode was then rinsed with ultrapure twice, then soaked in isopropanol, before finally being left to air-dry. The electrode was then dried in a Büchi oven at 120 $^\circ\text{C}$ under vacuum overnight. The Li_xFePO_4 electrode was then immersed in a solution of 0.1 M LiClO_4 in DMSO, which also contained 1 M TBAClO_4 to improve conductivity.

Electrolyte solutions were prepared in an N_2 glove box (<0.1 ppm O_2 , <0.1 ppm H_2O). Stock solutions consisted of 0.25 M tetrabutylammonium perchlorate (TBAClO_4) or lithium perchlorate (LiClO_4) and acetonitrile (CH_3CN), dimethyl sulfoxide (DMSO) or tetraethylene glycol dimethyl ether (TEGDME). These solutions contained either 0 M, 1 M or 5 M H_2O . Electrolyte solutions with intermediate H_2O concentrations were then

made by mixing the dry and H₂O-containing stock electrolytes using volumetric pipettes (SciQuip).

Au stick electrodes were cleaned before each CV as follows. The electrodes were mechanically polished by hand using 0.1 μm alumina powder (Struers) on a neoprene polishing pad. The electrodes were then briefly sonicated in ultrapure H₂O to remove any residual alumina on the electrode surface. They were then electrochemically polished in aqueous acid (0.1 M HClO₄), before being rinsed with ultrapure H₂O and dried under vacuum at 70 °C, again using the heated ante-chamber on the N₂ glove box.

During a CV measurement, the current (i) is recorded at each potential (U) versus the reference electrode. However, CV plots are typically presented using current density (j). U may also be converted to a more convenient scale. In this thesis, CVs and RRDE plots are reported using j , based on geometric area of the electrode, and U versus the Li⁺/Li couple in DMSO.

CVs were recorded in a sealed five-necked cell, which housed the working, reference and counter electrodes along with a glass bubbler and outlet to allow high-purity N₂ or O₂ (N6.0 grade, BOC) to be bubbled through the electrolyte. Background CVs were recorded under N₂ to establish the electrochemical stability window in each electrolyte and to determine the onset of H₂O reduction, *i.e.* H₂ evolution, to ensure this did not overlap with the O₂ electrochemistry window. These are presented in Appendix 1. As the H₂O concentration was increased, the onset of H₂O reduction shifted positively. Therefore, the negative potential limit was increased as appropriate to focus only on O₂ redox processes.

Saturation of the electrolytes with O₂ was confirmed in dry electrolytes by monitoring the reduction peak currents ($i_{p,red}$). If further bubbling of O₂ through the electrolyte did not increase $i_{p,red}$, the electrolyte was saturated. 2 minutes was sufficient to achieve

saturation in CH₃CN and TEGDME, while 3 minutes was required for DMSO. When recording background CVs, N₂ was bubbled for the same time in each electrolyte.

Following each measurement, the electrochemical five-necked cell was thoroughly washed with acetone and ultrapure H₂O, before being dried under vacuum at 70 °C. A heated ante-chamber on the N₂ glove box was used to allow the cell components to be taken directly into the glove box, preventing exposure to moisture.

Macroelectrode CVs were recorded on a Biologic SP-300. Linear sweep voltammograms were recorded using a CHI 1140C potentiostat and the Au microelectrode. Galvanostatic discharges of two-electrode cells were performed on a Biologic VMP3 potentiostat.

iR corrections were required for CVs in most electrolytes as they were resistive. The reference electrode measures the potential of the working electrode, but in doing so, it experiences a voltage drop (*iR_s*) due to the solution resistance, meaning it is not measuring the true potential at the working electrode. However, this voltage drop can be neglected if the solution resistance and/or the currents passed at the electrode are low. However, if this is not the case, then an *iR* correction must be applied in order to record accurate CVs. The organic solvent-based electrolytes used in this thesis have high resistances (>100 Ω in CH₃CN and DMSO, >1500 Ω in TEGDME), thus requiring *iR* corrections. These were applied by using *iR* correction functions in the potentiostat software. Solution resistances were determined at 3.45 V, where no Faradaic processes occur. No *iR* correction was applied for LSVs recorded using the Au microelectrode as the currents passed were in the nA range so the voltage drop would be negligible.

2.2. Rotating ring-disk electrode (RRDE) measurements

RRDE measurements were recorded using a ChangeDisk electrode (Pine Instruments). The disk and ring electrodes were polished separately to prevent cross-contamination. The Au disk electrode was polished identically to the Au stick electrodes used for CVs. The glassy carbon disk electrode and Pt ring electrode were mechanically polished using

0.1 μm alumina powder but were not electrochemically polished in acid. Once dried, the RRDE was carefully assembled on the bench and then dried under vacuum at 70 $^{\circ}\text{C}$ along with a five-necked cell. The cell was then assembled in a N_2 glove box ($\text{H}_2\text{O} < 0.1$ ppm). Approximately 10 mL of electrolyte was used for each measurement. As the working electrode was rotating, it was not possible to make the five-necked cell gas-tight. Therefore, following saturation of the electrolyte by bubbling with O_2 , the cell headspace was continually purged to maintain O_2 saturation whilst linear sweep voltammograms (LSVs) were recorded. Following this, the RRDE was removed from the glove box, washed with acetone and H_2O and then dried. An LSV of O_2 reduction in dry O_2 -saturated 0.25 M TBAClO_4 in DMSO was used to determine the collection efficiency of the RRDE, as the O_2/O_2^- couple is stable in this electrolyte.

RRDE LSVs are typically presented as shown in Figure 2.1. Comparison of the current density (j) at the ring and disk identifies if the redox-active molecule/ion is stable and soluble. An alternative way this could be presented is by multiplying the ring current by -1. In this case, the ring and disk curves would be expected to overlap.

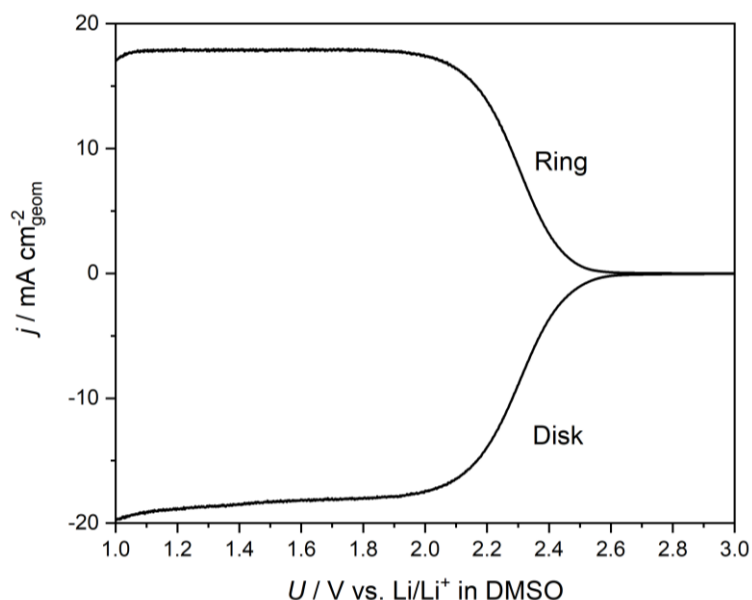


Figure 2.1: Typical LSV for an RRDE measurement with a species being reduced at the disk and re-oxidised at the ring.

In Chapters 3 and 4, a similar procedure is carried out to compare the relative amounts of $1e^-$, $2e^-$ and $4e^-$ O_2 reduction products. This involves taking two LSVs, with the ring electrode held at a different potential in each LSV, such that it selectively oxidises only $1e^-$ products in the first scan. In the second scan, the ring is held at a more positive potential, such that it oxidises the $1e^-$ products **and** some of the $2e^-$ product. To confirm that H_2O_2 could be oxidised at the Pt ring without also oxidising H_2O , CVs were recorded using a Pt working electrode with two electrolytes (0.25 M $LiClO_4$ in DMSO), one containing 1 M H_2O and the other additionally containing 0.01 M H_2O_2 . A peak due to H_2O_2 oxidation can clearly be seen before the onset of H_2O oxidation (Figure 2.2).

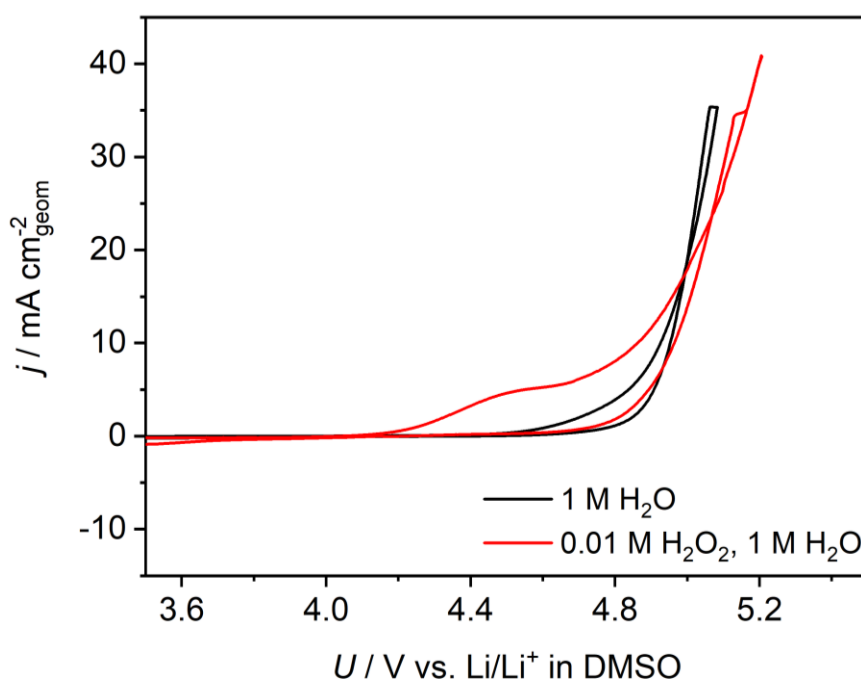


Figure 2.2: CVs recorded using a Pt working electrode to confirm that H_2O_2 is oxidised at potentials negative of H_2O oxidation. In the electrolyte containing H_2O_2 (red curve), a peak prior to H_2O oxidation is observed and is absent in the electrolyte containing only H_2O . The scan rate was 100 mV s^{-1} . Li_xFePO_4 reference and Pt counter electrodes were used.

The area underneath the ring in the first LSV (blue curves, Figure 2.3) corresponds to the $1e^-$ product and is shaded blue. The second LSV (red curves, Figure 2.3) oxidises

additional species generated at the disk so the recorded current is larger. Therefore, the area between the red and blue curves corresponds to only the $2e^-$ product and is shaded red. The green curve is the LSV of the disk electrode. Therefore, if the red curve deviates from the green curve, this indicates there are species generated at the disk that are not oxidised at the ring. This area is shaded green and typically includes some $2e^-$ and the $4e^-$ products.

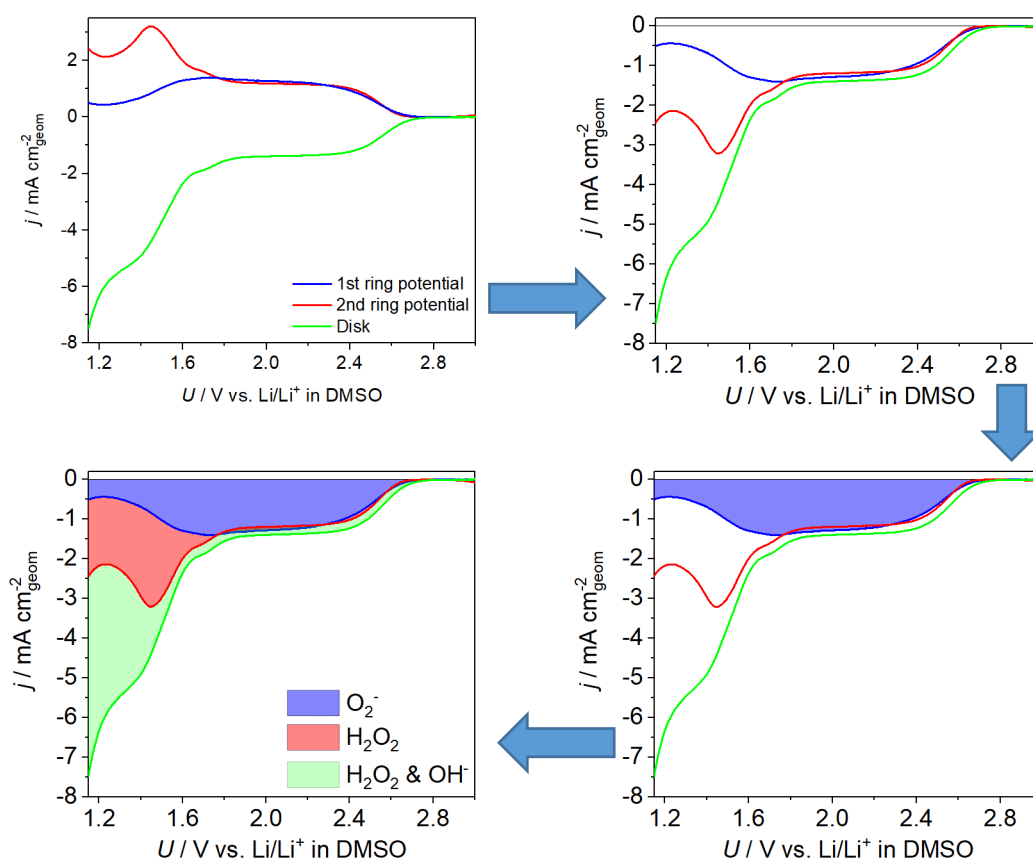


Figure 2.3: The procedure for converting standard LSVs into the plots presented in Sections 3.4 and 4.4. First, the ring currents are inverted. The area underneath the first ring curve (w.r.t. the x-axis) corresponds to $1e^-$ products formed at the disk. The area between the red and blue lines corresponds to $2e^-$ products and the area bounded by the green curve (disk current) and the red curve corresponds to any species generated at the disk that were not oxidised at the ring. In this case, it includes some of $2e^-$ products and the $4e^-$ product.

2.3. On-line mass spectrometry

Mass spectrometry is used to identify compounds by ionising a sample with an electron beam, deflecting the ionised species through an electromagnetic field and measuring the current produced at a Faraday detector due to that ion. This technique relies on the fact that not all ions are deflected equally in a given electric or magnetic field. This is because the ratio of the atomic mass of the ion to its charge (m/z) determines the degree to which it is deflected; ions with larger m/z require stronger electric/magnetic fields to achieve the same deflection as ions with lower m/z . Therefore, the electric fields used to deflect the ions can be adjusted to only allow ions with a specific m/z to reach the Faraday detector, which measures the current as a result of the ion colliding with the detector. Ions with m/z ratios that are too large or small will be deflected too little or too much, respectively, and will not collide with the Faraday detector so will not contribute to the ion current measured by the Faraday detector.

On-line mass spectrometry is a technique that uses a mass spectrometer (MS) attached to a carrier gas line to detect compounds, which are introduced upstream of the MS. The carrier gas causes the compounds to flow into the MS, where they can be identified. This technique can be quantitative if the ion current due to a compound of interest is calibrated using a gas mixture containing a known concentration of that compound. Additionally, the flow rate of the gas stream must be known so that the ideal gas law can be used to calculate the molar quantity of the compound in a sample.

An on-line MS was used in this work to measure O_2 evolution from samples of KO_2 disproportionating due to the addition of H_2O and/or Li^+ . Experiments involving CH_3CN and TEGDME used KO_2 powder due to its poor solubility in both solvents. KO_2 is slightly soluble in DMSO, so KO_2 solutions were prepared by stirring an excess of KO_2 powder in dry DMSO overnight. The solution was then centrifuged to avoid suspension of KO_2 powder, whilst two 0.5 mL aliquots of the solution were taken and placed in 2 mL glass

vials sealed with rubber bungs. One of the aliquots was used to determine the KO_2 concentration in solution by using a UV-vis titration method described in Section 2.4.

The vial containing the KO_2 powder or solution sample was attached to the online MS and Ar gas was flowed into the headspace of the vial. This process results in a small quantity of air entering the gas line. Therefore, Ar was continually flowed to purge the line until the MS reached a stable baseline O_2 concentration. Then, an H_2O -organic solvent mixture or H_2O -containing LiClO_4 -based electrolyte was injected into the vial. The injection could introduce air into the vial, artificially increase the O_2 concentration recorded by the MS, so the N_2 concentration was also monitored to detect air contamination. It confirmed that careful injection of the sample resulted in no air contamination and any O_2 measured by the MS was the result of KO_2 disproportionation. The MS reported concentrations as a percentage. This was converted to an O_2 flux by using the ideal gas law and the flow rate of the Ar carrier gas. The molar quantity of O_2 evolved over the course of the experiments could then be found by simple integration of the flux. This could be compared to the molar quantity of KO_2 in the vial at the start of each experiment, using the mass of KO_2 for CH_3CN - and TEGDME-based samples and the KO_2 solution concentration in the case of DMSO.

2.4. Ultraviolet-visible (UV-vis) spectroscopy

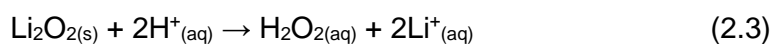
UV-vis spectroscopy is a form of absorption spectroscopy that measures the absorption of ultraviolet and visible light by molecules. Absorption of UV-vis radiation induces electronic transitions in molecules. As these energy levels are quantised, photons at specific energies, and therefore wavelengths, will be absorbed, which correspond to the difference in energies of an occupied and unoccupied orbital. The most common electronic transition is between the highest occupied molecular orbital and the lowest unoccupied molecular orbital.

Chapter 2

The Beer-Lambert law (Equation 2.1) describes the relationship between the absorption of electromagnetic radiation by an analyte and its concentration in solution, where A is the absorption of radiation at a specific wavelength, ϵ is the molar attenuation coefficient, l is the path length of the radiation travelling through the sample and c is the concentration of the molecule absorbing the radiation. This relationship means that the concentration of solutions containing unknown quantities of an analyte can be determined, provided it absorbs UV-vis radiation and that ϵ and l are known.

$$A = \epsilon \cdot l \cdot c \quad (2.1)$$

In this work, UV-vis spectroscopy was used to determine the concentration of KO_2 in DMSO solutions used for on-line mass spectrometry and to measure the Li_2O_2 yields ($Y_{\text{Li}_2\text{O}_2}$) of discharged electrodes. Both measurements involve a reaction with acid to generate H_2O_2 (Equations 2.2 and 2.3), which then complexes with titanium oxysulfate (TiOSO_4)¹. In aqueous acidic solutions, TiOSO_4 is colourless, but forms a yellow $[\text{Ti}(\text{O}_2)]^{2+}$ complex when it reacts with H_2O_2 .



A calibration curve was recorded to convert the absorbance of the $[\text{Ti}(\text{O}_2)]^{2+}$, measured at $\lambda = 405 \text{ nm}$ to a H_2O_2 concentration. First, a stock solution of $\sim 10 \text{ mM}$ H_2O_2 was made by dissolving KO_2 powder in ultrapure H_2O . The stock solution was then diluted further with various amounts of ultrapure H_2O to produce solutions with several H_2O_2 concentrations. 1 mL aliquots of these solutions were mixed with a 1 M H_2SO_4 solution containing 2% TiOSO_4 and the absorbance of the resulting yellow solutions were recorded using a UV-vis spectrometer (Thermo Evolution 200). The absorbance *versus* H_2O_2 concentration was then plotted and a line of best fit was used to generate the calibration curve (Figure 2.4).

Samples of KO_2 dissolved in DMSO were analysed by mixing a 1 mL aliquot of the solution with 1 mL of the 2% TiOSO_4 solution and then immediately measuring the UV-vis spectrum. The Li_2O_2 yields of discharged electrodes was determined by extracting the electrodes immediately after discharge and placing them in 5 mL of ultrapure H_2O and 5 mL of the 2% TiOSO_4 solution. If the absorbance measured was above 1, the solution was diluted further until within the range of the calibration curve. This is because the absorbance scale uses a \log_{10} scale, resulting in poorer sensitivity at large absorbances. The calibration curve could then be used to determine the H_2O_2 concentration and the molar quantity of KO_2 or Li_2O_2 could be calculated by multiplying by the total volume into which the sample had been dissolved (correcting for dilution factors). $Y_{\text{Li}_2\text{O}_2}$ could then be determined by comparing the moles of Li_2O_2 formed to the moles of e^- consumed during discharge.

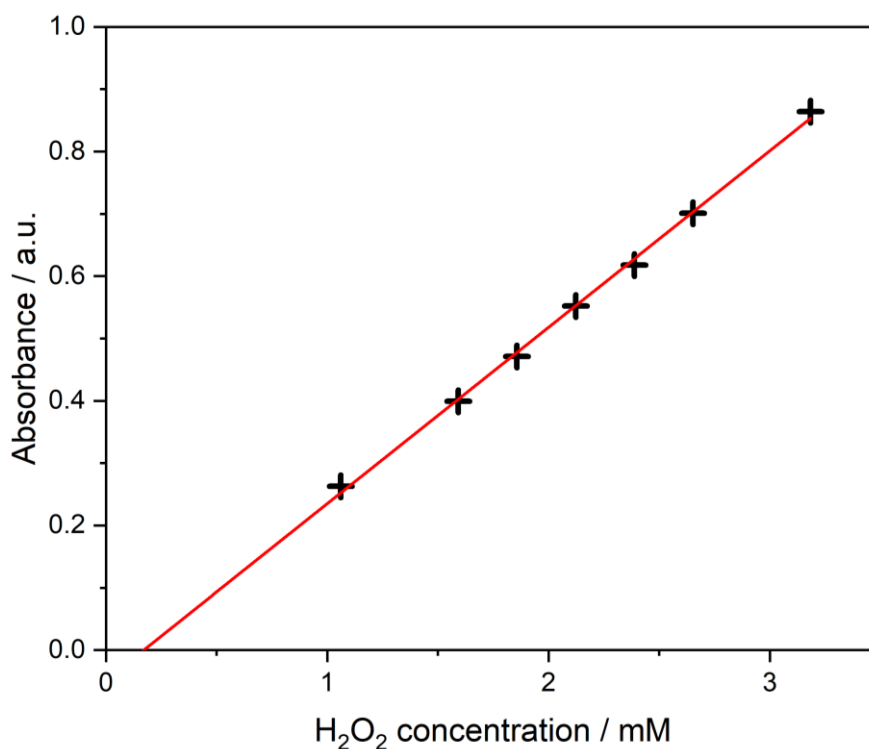


Figure 2.4: Calibration curve of the absorbance of the $[\text{Ti}(\text{O}_2)]^{2+}$ complex versus H_2O_2 concentration. The absorbance value was measured at 405 nm. The equation of the best fit line was $y = 0.2831x - 0.0484$ and the R^2 value was 0.9984.

2.5. Fourier-transform infrared (FTIR) spectroscopy

FTIR spectroscopy is another form of absorption spectroscopy. However, infrared (IR) radiation causes vibrational and rotational transitions in molecules. These transitions are used to identify molecules as different bonds absorb different characteristic frequencies of infrared radiation. Molecules are typically excited from their vibrational or rotational ground state into a higher energy state. As these energy levels are quantised, only certain frequencies of radiation that match the energy of these transitions are absorbed. Furthermore, the strength of the bond also affects the spacing of its energy levels. This means that different bonds will absorb different frequencies of IR radiation, thus allowing identification of the molecular structure of a sample. A bond will only be IR-active if the vibrational mode leads to a change in the permanent dipole of the molecule. Therefore, not all bonding modes are IR-active, e.g. O₂ and CO₂ stretches are not active, but the CO₂ bend **is** IR-active.

FTIR spectra were acquired on a ThermoFisher spectrometer using an attenuated total reflectance (ATR) accessory with a diamond crystal (SmartOrbit). Here, the IR beam is enters the ATR crystal and is internally reflected off the surface of the crystal, on which samples are placed. The sample can absorb the IR signal each time the beam reflects off this surface. A benefit of ATR over conventional transmission FTIR is that sample preparation is much simpler. In the former, the sample only needs to be clamped firmly onto the ATR crystal, while in the latter, the sample must be pressed into a pellet with an IR-transparent salt, such as KBr or CsI.

2.6. Raman spectroscopy and surface-enhanced Raman spectroscopy

Raman spectroscopy is a complementary technique to FTIR as they both probe the vibrational and rotational modes of molecular bonds. Raman spectroscopy uses a form of inelastic light scattering, known as Raman scattering. This involves using a monochromatic light source, *i.e.* a laser, to irradiate a sample. The laser interacts with the sample, momentarily exciting the bond to a virtual energy level. The bond then

relaxes back to its ground state, re-emitting light of the same wavelength. This process is known as Rayleigh scattering and is a type of elastic scattering. A very small proportion (approximately 1 in 10^7 photons) of the incident light is inelastically scattered². Here, a bond is once again excited to a virtual energy level by the laser light, but it relaxes into a different vibrational energy level to the one it occupied prior to excitation. This results in emission of a wavelength of light different to the laser light. The difference between these wavelengths is proportional to the energy of the vibrational transition and is typically converted into wavenumbers and reported as a Raman shift. In order for a bond to be Raman-active, the polarisability of the bond must change as it vibrates.

The intensity of Raman signals is typically very low, since most of the incident light on a sample undergoes Rayleigh scattering. This means that measuring Raman spectra of species at low concentrations is challenging. This can be overcome by using a surface-enhancement phenomenon, which enhances the Raman signal at some metal surfaces by many orders of magnitude³. The mechanism of this phenomenon is not fully understood, but it is believed that the enhancement is caused by the generation of surface plasmons on roughened metal surfaces when irradiated by a laser⁴. This effect only manifests on specific metals such as Au, Ag and Cu. If a roughened metal electrode is used, the surface-enhancement allows the acquisition of *in situ* spectra whilst performing electrochemical measurements. In this way, it is possible to identify the species involved in redox processes at the electrode surface.

Here, *in situ* surface-enhanced Raman spectroscopy (SERS) was carried out in an airtight 5-electrode electrochemical cell. The Au working electrode, roughened by electrochemical cycling in an aqueous 0.5 M KCl electrolyte, was used in combination with a 785 nm diode laser. Raman spectra were recorded using a confocal Raman microscope (Renishaw) with a 20x 0.45 NA objective (Nikon).

2.7. Nuclear magnetic resonance (NMR) spectroscopy

NMR spectroscopy exploits a property of nuclei called spin (I). Nuclei with non-zero I will have $2I+1$ nuclear spin states, which, under normal conditions, are degenerate. However, when placed in a strong magnetic field, the spin states line up with the external field, either in the same direction or against the external field. This splits the energies of the spin states, with those opposing the external field being highest in energy. Nuclei are distributed amongst these spin states almost equally, with only slightly more nuclei occupying the lowest spin state. A nucleus in the ground state can be excited to a more energetic spin state by a radio frequency (RF) pulse. The resonant frequency of a nucleus is the frequency of the RF pulse that causes excitation. The relaxation of the nucleus back to the ground state emits a radio wave with an energy equal to the difference in energies of the excited and ground state spins. This radio wave induces a current in the spectrometer, which is detected.

The chemical environment will affect the splitting of the spin states, because when the external magnetic field is applied, a current is induced in the electron cloud of a molecule. This induces a magnetic field within the molecule and the nuclei experience the sum of the applied and induced magnetic fields. The magnetic fields induced in a molecule will depend on its structure and can shield or deshield nuclei from the external field, that is reduce or increase the apparent magnetic field experienced by a nucleus. This means that the splitting of the energy levels of nuclei in different chemical environments will be different and therefore, they will resonate at different frequencies, allowing different nuclei in a molecule to be distinguished.

NMR spectra are reported as chemical shifts, not frequencies. This is achieved by comparing the resonant frequency of nuclei in a sample to that of a reference sample and using Equation 2.4

$$\delta = (V_{\text{sample}} - V_{\text{reference}}) / V_{\text{reference}} \times 10^6 \quad (2.4)$$

where δ is the chemical shift of a nucleus, ν_{sample} is the resonant frequency of the nucleus and $\nu_{reference}$ is the resonant frequency of the reference.

2.8. X-ray diffraction (XRD)

XRD is one of the most commonly used characterisation techniques used for identification of crystalline materials. Methods such as Rietveld refinement can also determine the crystal structure of novel or unknown samples.

Crystalline materials consist of regularly repeating arrays of atoms with a constant interplanar distance between layers in the crystallographic plane. Because of this regular spacing, the plane can act as a diffraction grating for electromagnetic radiation of wavelengths of similar magnitude (or smaller) to the interplanar spacing. X-rays typically used for XRD are of the order of 1 Å, similar to the spacing of atoms between layers, so X-rays will diffract. However, when X-rays are diffracted by a crystal plane, they usually interfere destructively. The diffracted X-rays must interfere constructively to be detected. The Bragg equation describes the conditions at which this occurs,

$$2d \sin\theta = n\lambda \quad (2.5)$$

where d represents the distance between two layers of a crystallographic plane, θ is the incident angle of the X-rays, λ is the wavelength of the X-ray and n is an integer value. This equation arises because the X-rays must be in-phase to interfere constructively. X-rays diffracted by different layers of a crystal plane will have different path lengths (Figure 2.5) and therefore the difference in path length must be an integer number, n , of the wavelength of the X-ray, λ , which corresponds to a distance of $2d \sin\theta$.

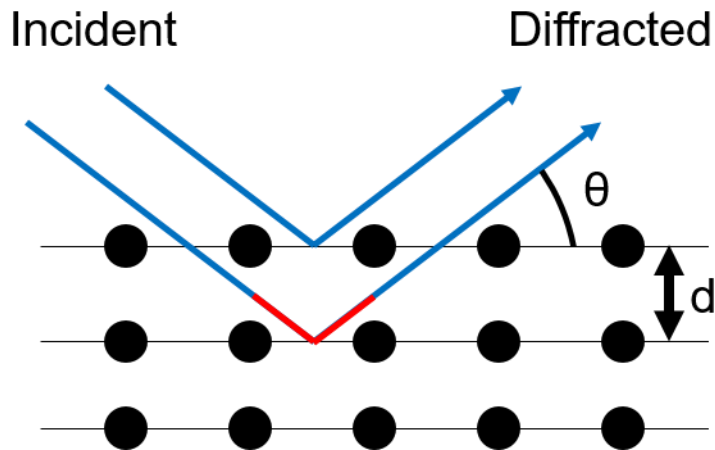


Figure 2.5: Schematic showing the condition required for constructive interference of X-rays when diffracted. The lower X-ray beam path is longer than the upper by the distance indicated in red.

2.9. Scanning electron microscopy and energy-dispersive X-ray spectroscopy

Scanning electron microscopy (SEM) uses high-energy electrons focused into a beam to image samples. When the electron beam hits the surface of a sample, it can interact in a number of ways. An electron bound to a nucleus can be ejected by collision with an electron from the beam, generating a secondary electron. This can be used to acquire an image. Alternatively, the electrons in the beam can be back-scattered by atoms.

The electron beam may also eject a core electron from an atom. A higher energy electron rapidly fills the vacancy and emits X-ray radiation corresponding to the energy of the transition. This phenomenon is used for energy-dispersive X-ray (EDX) spectroscopy.

Secondary electron images were recorded on a Zeiss Merlin microscope at 3 kV acceleration voltage. Electrode samples were fixed with copper adhesive tape in an N_2 glove box and put in an air-sensitive transfer holder to prevent exposure to air between the glove box and SEM. EDX spectroscopy was carried out at 3 kV with a built-in Oxford Instruments X-Max 150 Silicon drift detector and analysed using the Aztec software package.

2.10. References

- 1 Schwenke, K. U., Metzger, M., Restle, T., Piana, M. & Gasteiger, H. A. The influence of water and protons on Li_2O_2 crystal growth in aprotic Li-O_2 cells. *J. Electrochem. Soc.* **162**, A573-A584 (2015).
- 2 Galloway, T. A. & Hardwick, L. J. Utilizing in situ electrochemical SHINERS for oxygen reduction reaction studies in aprotic electrolytes. *J. Phys. Chem. Lett.* **7**, 2119-2124 (2016).
- 3 Gittleson, F. S. *et al.* Raman spectroscopy in lithium-oxygen battery systems. *ChemElectroChem* **2**, 1446-1457 (2015).
- 4 Moskovits, M. Surface-enhanced spectroscopy. *Rev. of Mod. Phys.* **57**, 783-826 (1985).

3. Effect of H₂O on O₂ reduction in TBA⁺-based electrolytes

3.1. Introduction

A theory that adequately describes the effects of H₂O across the range of solvents used in Li-air batteries has yet to be presented (Section 1.11). Li₂O₂ has been reported as the product of O₂ reduction in H₂O-containing dimethyl sulfoxide (DMSO)-based and glyme ether-based electrolytes, while LiOH is found in H₂O-containing acetonitrile (CH₃CN)-based electrolytes^{1,2}. Various groups have made significant attempts to understand the influence of H₂O on O₂ reduction but none have provided a mechanism to explain their observations in these solvents and, therefore, there is currently no consensus on the role of H₂O on O₂ reduction in determining the discharge product¹⁻⁴. Furthermore, these studies have largely relied on data collected using two-electrode cells and predominantly *ex situ* analysis of discharge products, potentially resulting in intermediate species remaining undetected and incorrect assumptions concerning the role of H₂O in the O₂ reduction mechanism. Therefore the effects of H₂O on O₂ reduction products was investigated in order to find a universal mechanism for the role of H₂O in any solvent used in aprotic Li-O₂ batteries.

In this chapter, I describe the examination of the O₂ electrochemistry in aprotic electrolytes in the presence of up to 5 M H₂O, covering a larger range of H₂O concentrations than most previous studies have used. This should facilitate the observation of how and when the O₂ reduction mechanism shifts from the aprotic mechanism to a protic mechanism or mechanisms. Here, tetrabutylammonium (TBA⁺) based electrolytes are used as ideal electrolytes to enable fundamental electrochemical methods and approaches. For example, TBA⁺ is used in place of Li⁺ because a passivating Li₂O₂ film forms when O₂ reduction occurs in the presence of Li⁺. This Li₂O₂ film would complicate the use of many electrochemical equations such as the Levich equation, as they have been solved for systems in which all species are soluble⁵. Using

TBA⁺ therefore reduces the complexity of the systems and can provide valuable information on how O₂ reduction is affected by H₂O. Furthermore, the mechanisms proposed thus far in the literature should be observable whether TBA⁺ or Li⁺ are used. The studies by Aetukuri *et al.* and Kwabi *et al.* propose that it is the interaction of H₂O with O₂⁻ and the solvent, respectively, which account for the discharge products they report^{1,2}. DMSO and CH₃CN are used in place of tetraethylene glycol dimethyl ether (TEGDME), as they have very different donor numbers that result in solution and surface mechanisms, respectively, when used with Li⁺-based electrolytes. Thus, this will allow the examination of the effect of H₂O on the surface and solution mechanisms in isolation in Chapter 4.

The objectives in this Chapter are to utilise these ideal electrolyte systems to explore the effect of H₂O on the aprotic O₂ reduction, identify the H₂O concentrations required for formation of protic O₂ reduction products, *e.g.* H₂O₂ and OH⁻, and identify the species formed using *in situ* characterisation methods. In doing so, I expect to be able to comment on the validity of the acceptor number (AN) mechanism proposed by Aetukuri *et al.*, as the H₂O solvation effects they suggest should manifest in the voltammetry.

3.2. Experimental

3.2.1. Materials

Tetrabutylammonium perchlorate (TBAClO₄, ≥99.0%, Sigma-Aldrich), tetrabutylammonium hydroxide 30-hydrate (TBAOH·30H₂O, ≥99.0%, Sigma-Aldrich) and potassium superoxide (KO₂, Sigma-Aldrich) were used as received. DMSO (puriss. p.a., dried, ≤0.02% H₂O, Sigma-Aldrich) was distilled under vacuum. CH₃CN (electronic grade, 99.999% trace metals basis, Sigma-Aldrich) was distilled under Ar. Following distillation, solvents were transferred to an Ar glove box and dried using freshly activated 4Å molecular sieves for a minimum of 72 hours. The H₂O content of the dried solvents was measured using a Karl Fischer titrator (Mettler Toledo). The solvents were used

when the H₂O content was <5 ppm. The above chemicals were all stored in an Ar glove box (<0.1 ppm O₂, < 0.1 ppm H₂O, MBraun). Ultrapure H₂O (18.2 MΩ cm⁻¹, Milli-Q, Merck Millipore) was used to make up electrolyte solutions with known H₂O concentrations. High purity N₂ and O₂ gases (N6.0 grade, BOC) were used for saturating electrolyte solutions. These gases were passed through a moisture trap (Agilent) upstream of the electrochemical cell to dry the gases further. The H₂O content of dry electrolytes, *i.e.* no intentionally added H₂O, was tested using the Karl Fischer and found to be <10 ppm.

3.2.2. Voltammetry

The full methodology of cyclic voltammetry and rotating ring-disk electrode (RRDE) measurements are described in Chapter 2. Background cyclic voltammograms (CVs) were recorded under N₂ to determine electrolyte stability windows and to identify the onset of H₂O reduction and oxidation. These are presented in Appendix 1. All potentials are quoted versus the Li/Li⁺ couple in DMSO.

3.2.3. Simulations of voltammograms

CVs were simulated using DigiElch software as follows. Experimental CVs with 0 M H₂O were used to determine the electrochemical parameters for the O₂/O₂⁻ redox couple. The O₂/O₂⁻ couple was the only modelled electrochemical reaction and the potential (E), charge transfer coefficient (α) and heterogeneous rate constant (k_s) were all optimised by the software. The diffusion coefficients for O₂ and O₂⁻ (D_{O_2} and $D_{O_2^-}$, respectively) were then optimised by the software and used for all simulations containing the solvent. These values are shown in Table 3.1. Literature values for the diffusion coefficients of H₂O in CH₃CN and DMSO were used ($5.78 \times 10^{-5} \text{ cm}^2 \text{ s}^{-1}$ and $8.00 \times 10^{-5} \text{ cm}^2 \text{ s}^{-1}$, respectively)^{6,7}. No published values for the diffusion coefficients of HO₂ in either CH₃CN or DMSO could be found, so the O₂⁻ diffusion coefficients in each solvent were used as an approximation. iR corrections were applied to experimental CVs, so the solution resistance in each CV was known and were included in the simulations. The temperature was set to 20 °C.

Table 3.1: Parameters optimised by the simulation software in the dry electrolyte systems. These values were used in simulations of the H₂O-containing electrolytes.

Solvent	E / V	α	$k_s / \text{cm s}^{-1}$	$D_{O_2} / \text{cm}^2 \text{s}^{-1}$	$D_{O_2^-} / \text{cm}^2 \text{s}^{-1}$
CH ₃ CN	2.54500	0.48086	1.4301×10^{-4}	4.0775×10^{-5}	1.2055×10^{-5}
DMSO	2.57288	0.48716	3.1874×10^{-4}	2.3051×10^{-5}	6.5040×10^{-6}

For simulations in H₂O-containing electrolytes, it was assumed that H₂O did not affect the electrochemical O₂ reduction step, allowing the values for E , α and k_s to be fixed to the values found in the dry electrolytes for other simulations. However, this restricted simulations to ≤ 0.25 M and ≤ 1 M H₂O in CH₃CN and DMSO, respectively. Above these concentrations, the onset potential of O₂ reduction shifted positively, indicating H₂O was directly involved in proton-coupled O₂ reduction, which was not modelled. The optimised D_{O_2} and $D_{O_2^-}$ values from the dry CVs were also used.

The equilibrium reaction between O₂⁻ and H₂O was assumed to be a kinetically fast proton transfer step. The forward reaction rate was constrained to a value of $1 \times 10^{11} \text{ s}^{-1}$ to ensure that backward reaction rate was also kinetically fast when K_{eq} was optimised.

3.3. Electrochemical response of O₂/O₂⁻ couple to H₂O

3.3.1. Cyclic voltammograms

O₂ reduction in aprotic solvents has been well studied. In electrolytes containing tetraalkylammonium-based cations, e.g. TBA⁺, O₂ is reduced to O₂⁻, and the redox couple is typically quasi-reversible, e.g. in DMSO, though can be electrochemically irreversible in some electrolytes, e.g. in CH₃CN (Figure 3.1). O₂⁻ is a stable anion, which complexes with TBA⁺, and can be oxidised back to O₂ (ref. 8). When the electrode is scanned from a more positive to a more negative potential (right to left in Figure 3.1), reduction of O₂ to O₂⁻ is observed as a cathodic current. Here, the O₂ reduction peak occurs at 2.35 V and 2.25 V in DMSO and CH₃CN, respectively. When the potential is then swept back,

oxidation of O_2^- is seen as an anodic current with a peak at 2.75 V and 2.8 V in DMSO and CH_3CN , respectively.

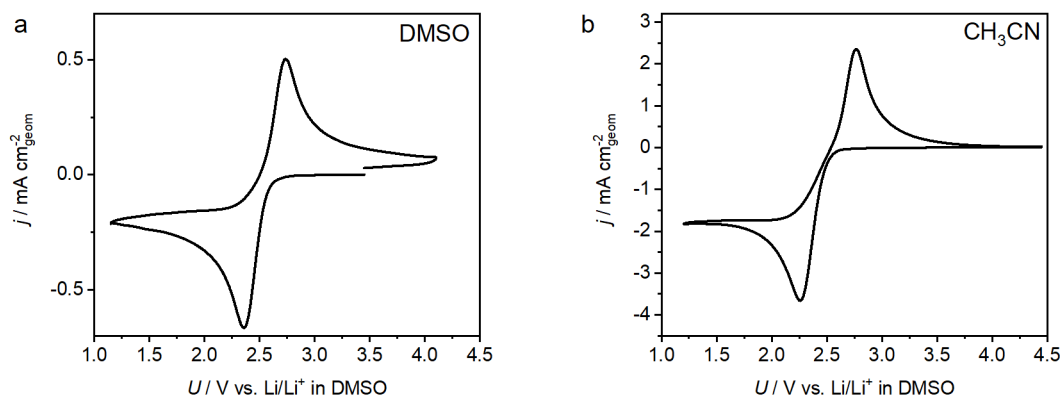


Figure 3.1: CVs showing the O_2/O_2^- redox couple in O_2 -saturated dry electrolytes (<10 ppm H_2O). The electrolytes consisted of O_2 -saturated 0.25 M TBAClO₄ in DMSO (a) and CH_3CN (b). The scan rate was 100 mV s^{-1} . Au working, Li_xFePO_4 reference and Pt counter electrodes were used.

The effect of introducing H_2O to the CH_3CN -based electrolyte is discussed first. Figure 3.2 shows the CV responses of the O_2/O_2^- redox couple to the presence of H_2O from 0 M H_2O to 5 M H_2O . It can be clearly seen that O_2 reduction is unaffected by the presence of low H_2O concentrations (<0.25 M H_2O), as the reduction peak potential, $E_{P,red}$, and onset of O_2 reduction do not shift due to the presence of H_2O (solid lines in inset, Figure 3.2). However, there is a positive shift in the oxidation peak potential, $E_{P,ox}$, and decay in peak anodic current, $i_{P,ox}$, (trend indicated by blue arrow in Figure 3.2) over this range of H_2O concentrations. Aetukuri *et al.* proposed that H_2O solvates O_2^- due to its high AN^2 , and if this were the case, increased O_2^- solvation would lower its activity and therefore, one would expect the entire redox couple to shift positively, based on the Nernst equation (Equation 3.1),

$$E = E^0 - \frac{RT}{nF} \ln \frac{a_{red}}{a_{ox}} \quad (3.1)$$

Since $E_{P,ox}$ is shifting positively independent of $E_{P,red}$, this clearly demonstrates that H_2O does not solvate O_2^- to any significant extent, directly contradicting the AN mechanism proposed by Aetukuri *et al.*²

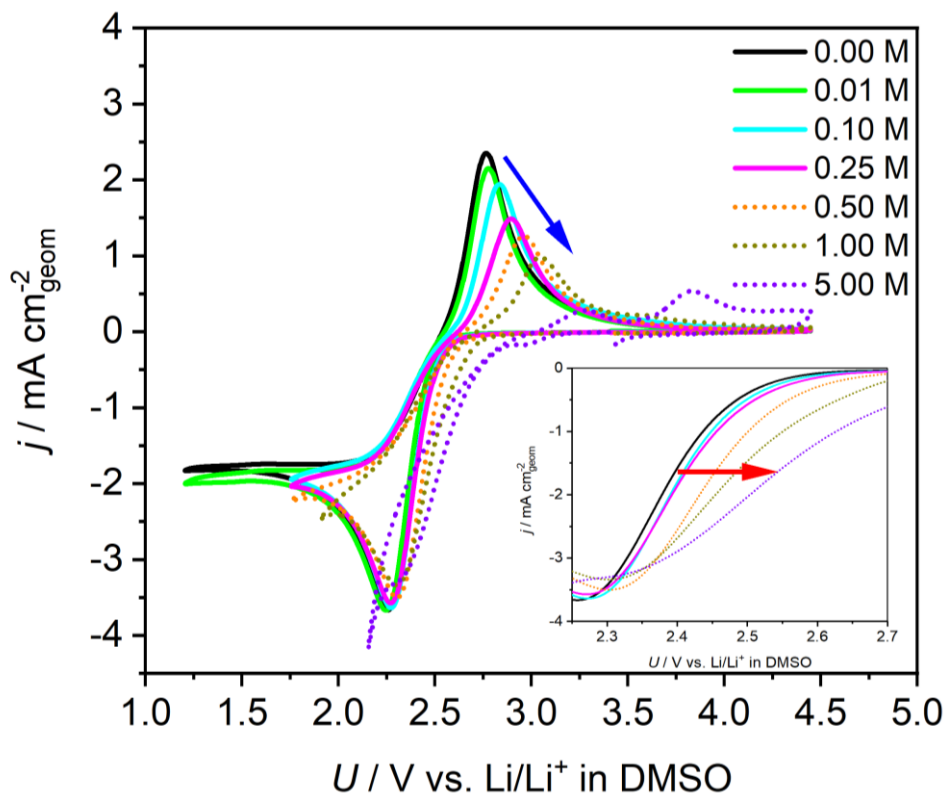
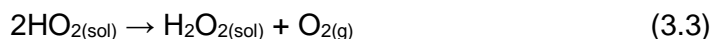


Figure 3.2: CVs recorded in CH_3CN demonstrating that O_2^- oxidation is affected at lower H_2O concentrations than O_2 reduction. The electrolytes were O_2 -saturated and contained 0.25 M $TBAClO_4$ and various H_2O concentrations as indicated in the legend. Dashed lines indicate electrolytes that undergo a proton-coupled O_2 reduction. The inset is an expanded view of the reduction wave, showing the positive shift of its onset. The scan rate was 100 mV s^{-1} . Au working, Li_xFePO_4 reference and Pt counter electrodes were used.

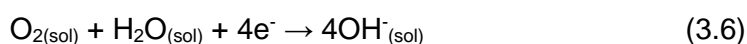
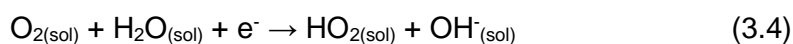
The decay in $i_{P,ox}$ and positive shift of $E_{P,ox}$ continues as the H_2O concentration is further increased, up to 5 M, with these changes becoming more pronounced (Figure 3.2). This behaviour is indicative of the electrogenerated O_2^- species undergoing a subsequent chemical reaction, i.e. an E-C mechanism involving H_2O . O_2^- is known to react with protic

species to form HO₂ (Equation 3.2), which can then disproportionate to H₂O₂ (Equation 3.3). In these organic electrolytes, H₂O is likely to provide the source of protons necessary for these reactions to occur.



The decay in $i_{\text{P,ox}}$ can be explained by considering Equations 3.2 and 3.3. As the H₂O concentration increases, the equilibrium of Equation 3.2 will shift to favour the forward reaction, leading to an increased concentration of HO₂. This can then disproportionate irreversibly via Equation 3.3, causing $i_{\text{P,ox}}$ to decrease, as O₂⁻ has been consumed before oxidation can occur. A new oxidation peak at 3.85 V can be seen in the electrolyte with 5 M H₂O that could be due to the oxidation of this H₂O₂. The cause of the positive shift of $E_{\text{P,ox}}$ is not immediately obvious, but may involve the equilibrium in Equation 3.2. However, this is conjecture and requires other means to confirm the causes of the oxidation peak trend. Therefore, CV simulations were performed and are discussed in the following section.

Given sufficiently high H₂O concentrations, >0.25 M H₂O, there is a positive shift in the onset of O₂ reduction (red arrow and dashed CVs, Figure 3.2), indicating that a new reduction process is occurring, namely a proton-coupled O₂ reduction, which is typically the first step in aqueous O₂ reduction mechanisms⁹.



However, it is unlikely that the protic O₂ reduction products, H₂O₂ and/or OH⁻, form at the potentials applied here (Equations 3.5 and 3.6). $i_{\text{P,red}}$ does not increase, as would be expected if the 2e⁻ or 4e⁻ transfer were occurring, for H₂O concentrations ≤1 M. However,

there is a slight increase in $i_{P,red}$ at a 5 M H_2O concentration and is now due to the $E_{P,red}$ for $2e^-$ and/or $4e^-$ O_2 reduction lying close to $E_{P,red}$ for the $1e^-$ O_2 reduction. It is difficult to explicitly determine the reaction products using CVs alone, so other techniques must be used to identify these products. Attempts to identify the nature of the O_2 reduction products using an electrochemical technique, RRDE measurements, and a spectroscopic technique, surface-enhanced Raman spectroscopy (SERS), are discussed in Sections 3.4 and 3.6, respectively.

In the DMSO-based electrolyte, similar changes to the O_2/O_2^- redox couple with increasing H_2O content are observed (Figure 3.3) as in CH_3CN , but significantly higher concentrations of H_2O are required to induce these effects. There are negligible changes to the onset potential of O_2 reduction at H_2O concentrations ≤ 1 M, demonstrating that proton-coupled O_2 reduction requires in excess of 1 M H_2O to occur (Figure 3.3 inset), which is at least four times that in CH_3CN . Furthermore, the decay in $i_{P,ox}$ and positive shift of $E_{P,ox}$ are also less pronounced between 0 M and 5 M H_2O in DMSO, when compared to CH_3CN (Figure 3.3 and Figure 3.2, respectively). This suggests that aprotic O_2 reduction in DMSO is more resistant to the presence of H_2O . These results are consistent with reports in the literature that found CH_3CN to be more susceptible to protic O_2 reduction than DMSO in Li^+ -based electrolytes^{1,2}. Since this occurs both with and without Li^+ , the solvent must play a significant role in determining whether aprotic O_2 electrochemistry occurs at a given H_2O concentration. It is therefore crucial to understand how H_2O affects O_2 reduction in different solvents and why the H_2O -solvent interactions can lead to different O_2 reduction products. This will be addressed in both this chapter and Chapter 4, with the aim of developing a mechanism that rationalises O_2 reduction in H_2O -containing organic solvent-based electrolytes that should enable the development of H_2O -tolerant solvents for the $Li-O_2$ battery, bringing it a step closer to the Li -air battery.

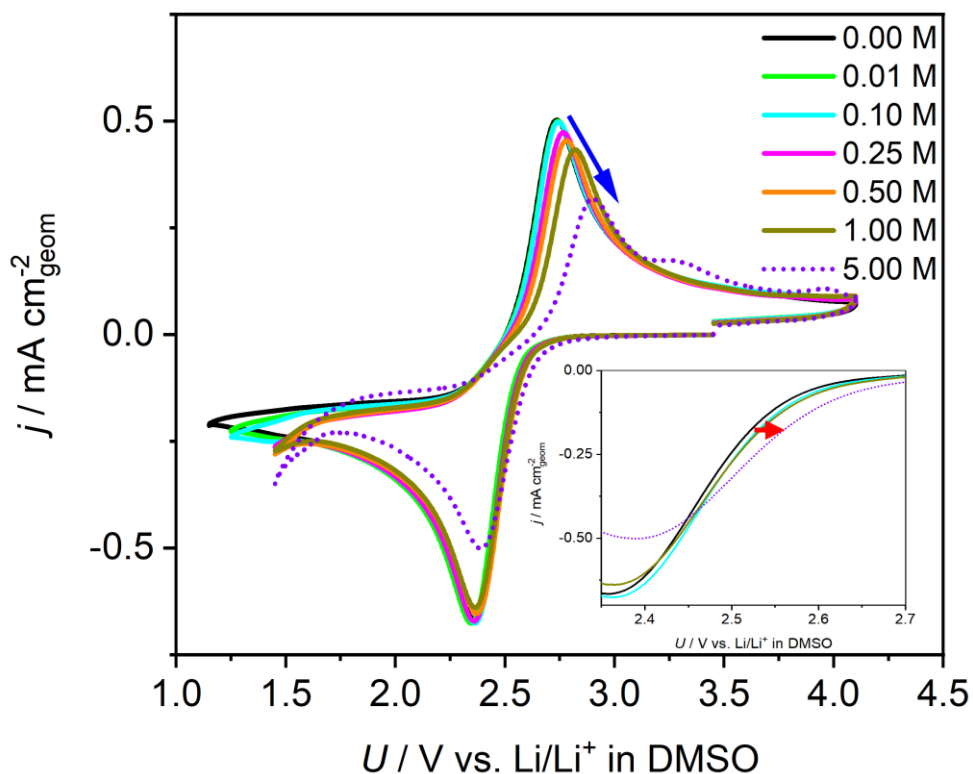


Figure 3.3: CVs recorded in DMSO demonstrating O_2^- oxidation is affected at lower H_2O concentrations than O_2 reduction. The electrolytes were O_2 -saturated 0.25 M TBAClO₄ at various H_2O concentrations as indicated in the legends. Dashed lines indicate electrolytes that undergo a proton-coupled O_2 reduction. The inset is an expanded view of the reduction wave, showing the positive shift of its onset. The scan rate was 100 mV s^{-1} . Au working, Li_xFePO_4 reference and Pt counter electrodes were used.

3.3.2. Simulations of voltammetric responses

In the previous section, I proposed an E-C mechanism to account for the trend in oxidation peaks during O_2 reduction, involving an equilibrium between O_2^- and HO_2 and subsequent disproportionation of HO_2 to H_2O_2 . To confirm that both these reactions contribute to the trend in oxidation peaks, CV responses were simulated using DigiElch. The methodology used to obtain the simulated CVs is described in Section 3.2.3.

Three different models were used and the detailed reactions for each are shown in Table 3.2. Each model begins with electrochemical O_2 reduction to O_2^- , followed by different

combinations of the chemical steps expected to occur between O_2^- and H_2O . The first mechanism, Model 3.1, assumes O_2^- reacts irreversibly with H_2O , forming HO_2 , which then disproportionates. The second mechanism, Model 3.2, involves an equilibrium between O_2^- and HO_2 , and where HO_2 does not disproportionate, while, in the final mechanism, Model 3.3, the O_2^-/HO_2 equilibrium and disproportionation of HO_2 both occur. The software then optimised the equilibrium and reaction rate constants of Equations 3.2 and 3.3. By comparing the simulated CVs to the experimental CVs, one can identify whether Equations 3.2 and 3.3 contribute to the oxidation peak response.

Table 3.2: Summary of Models 3.1, 3.2 and 3.3 showing the reactions used when simulating the E-C mechanism during voltammetry of O_2 in electrolytes containing H_2O . All models start with electrochemical generation of O_2^- . Models 3.1 and 3.2 individually consider O_2^- disproportionation and the O_2^-/HO_2 equilibrium, respectively, while Model 3.3 simulates both.

Model 3.1	Model 3.2	Model 3.3
$O_2 + e^- \rightarrow O_2^-$	$O_2 + e^- \rightarrow O_2^-$	$O_2 + e^- \rightarrow O_2^-$
$O_2^- + H_2O \rightarrow HO_2 + OH^-$	$O_2^- + H_2O \rightleftharpoons HO_2 + OH^-$	$O_2^- + H_2O \rightleftharpoons HO_2 + OH^-$
$2HO_2 \rightarrow H_2O_2 + O_2$		$2HO_2 \rightarrow H_2O_2 + O_2$

Considering first O_2 reduction in CH_3CN , Figure 3.4 shows simulated CVs using Models 3.1-3.3 at selected H_2O concentrations up to 1 M, overlaid with the experimental CVs from Figure 3.2. The simulations using Model 3.1 demonstrate that disproportionation of O_2^- leads to a decay in $i_{P,ox}$, as expected for a decrease in concentration of the electroactive species in the vicinity of the electrode (Figure 3.4, green circles). However, the oxidation potential is unchanged, meaning disproportionation of O_2^- alone cannot account for the shift of $E_{P,ox}$.

Model 3.2 also produces simulations with poor fits to the experimental CVs. Here, $E_{P,ox}$ shifts positively with increasing H_2O concentration, but $i_{P,ox}$ does not decay, suggesting

that the equilibrium alone also cannot account for the oxidation peak trend. However, Models 3.1 and 3.2 separately produce one of the components (decay in $i_{p,ox}$ and shift of $E_{P,ox}$, respectively) seen experimentally. Therefore, Model 3.3 incorporated both the O_2^-/HO_2 equilibrium and HO_2 disproportionation to see if they combine to produce simulated CVs that fit the experimental data better.

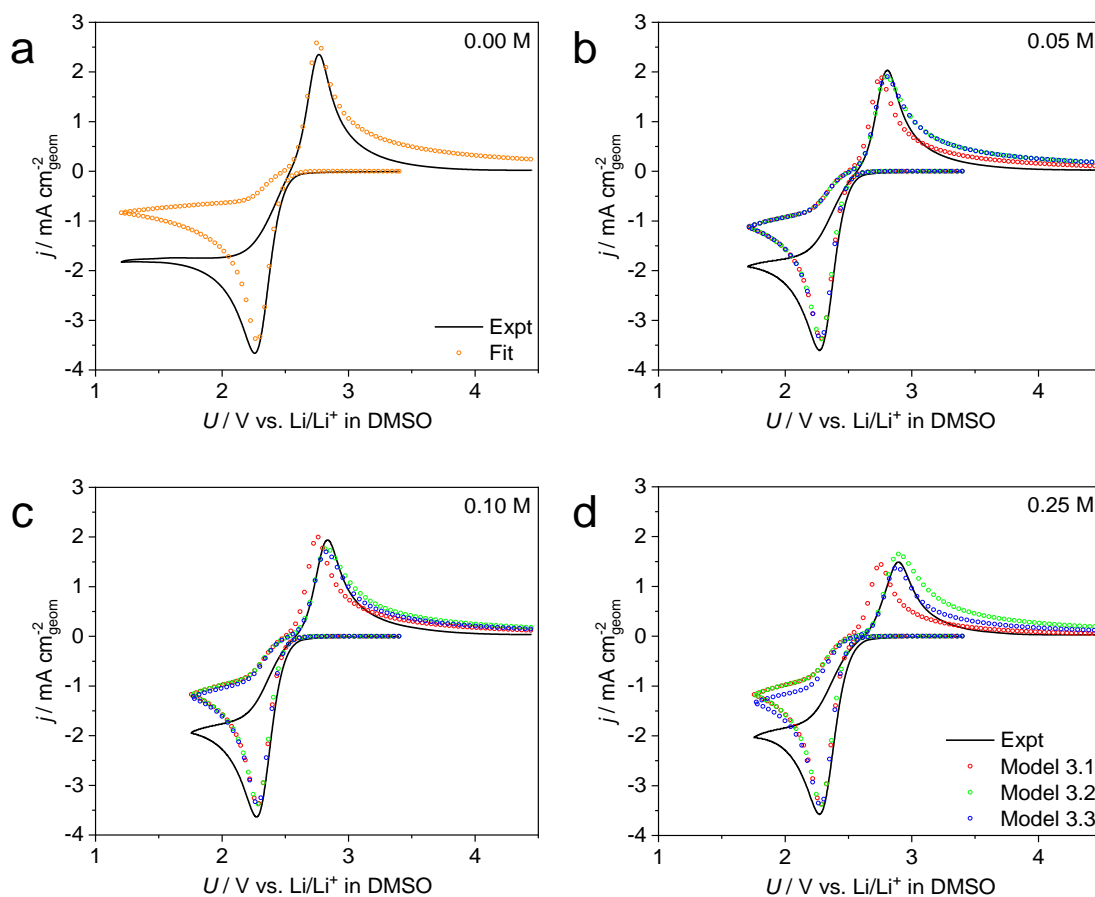


Figure 3.4: Simulations of the CV responses for the O_2/O_2^- couple in the presence of H_2O showing that both disproportionation of HO_2 and an equilibrium between O_2^- and HO_2 (Model 3.3) occur in CH_3CN -based electrolytes. Experimental CVs are reproduced from Figure 3.2. Both disproportionation (red circles, Model 3.1) and the O_2^-/HO_2 equilibrium (green circles, Model 3.2) alone fit the experimental data poorly. The circles in panel (a) shows the simulated CV in dry electrolyte used to fix the parameters of the electrochemical step for other simulations.

This is indeed the case, with both the $i_{p,ox}$ decaying and positive shift of $E_{p,ox}$ as the H_2O concentration increases (Figure 3.4, red circles), suggesting that H_2O leads to the formation of HO_2 and its subsequent disproportionation. Furthermore, the values for K_{eq} and k_f for Equations 3.2 and 3.3, respectively, both increase as the H_2O concentration increases, as one would expect when H_2O is involved in these reactions (Table 3.3).

Table 3.3: Equilibrium constant and reaction rate constant values obtained from optimised CVs using Model 3.3, showing that the formation and subsequent disproportionation of HO_2 occurs more readily in CH_3CN than DMSO.

Solvent	H_2O concentration / M	K_{eq}	$k_f / M^{-1} s^{-1}$
CH_3CN	0.05	0.15578	0.0013
	0.10	0.17799	1.3943
	0.25	0.37587	2.6798
DMSO	0.25	2.2771×10^{-3}	0.023714
	0.50	2.7501×10^{-3}	0.086013
	1.00	5.6206×10^{-3}	0.3777

In DMSO, simulations of each model generate the same trends as in CH_3CN (Figure 3.5). However, Models 3.1 and 3.2 appear to fit the experimental CVs reasonably well, particularly below 1 M H_2O , but this is because the changes to the experimental oxidation peaks are more subtle than in CH_3CN . Overall, the simulations using Model 3.3 still appear to provide the best fit to the experimental CVs. The K_{eq} and k_f values (Table 3.2) are much smaller than for CH_3CN , suggesting that CH_3CN is more sensitive than DMSO to both chemical and electrochemical reactions involving H_2O .

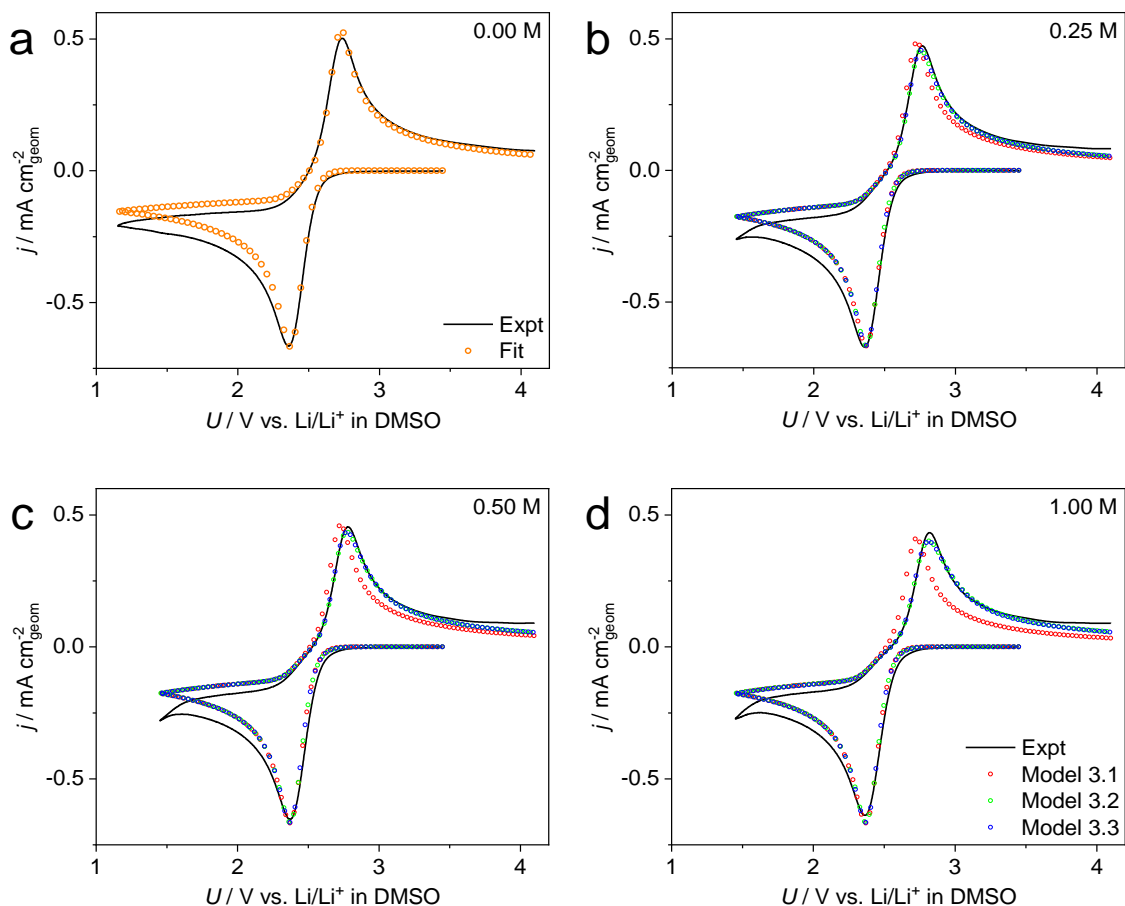


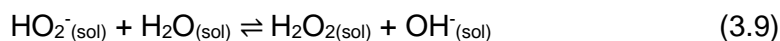
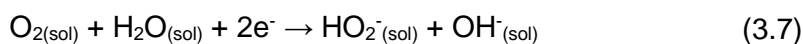
Figure 3.5: Simulations of the CV responses for the O_2/O_2^- couple in the presence of H_2O showing that both disproportionation of HO_2 and an equilibrium between O_2^- and HO_2 (Model 3.3, blue circles) occurs in DMSO-based electrolytes. Experimental CVs are reproduced from Figure 3.3. The circles show simulated CVs obtained using Models 3.1-3.3 in DigiElch. The circles in panel (a) show the simulated CV in dry electrolyte used to fix the parameters of the electrochemical step for the other simulations.

3.4. Identification of reaction pathways in solvent/ H_2O mixtures

The presence of H_2O allows new protic oxygen reduction reactions to occur, leading to products typically seen in aqueous O_2 reduction, namely HO_2 , H_2O_2 (or HO_2^-) and potentially OH^- , that cannot form via aprotic routes. Therefore, in H_2O -containing organic electrolytes, it should be possible to produce both aprotic and protic products, depending on the precise conditions, e.g. H_2O concentration, solvent system, applied potentials. In

Section 3.3.1, it was proposed that the positive shift of the O_2 reduction peak with increasing H_2O content is due to the onset of protic O_2 reduction, which could ultimately lead to the $4e^-$ product, OH^- . However, given that aqueous O_2 reduction can occur via multiple pathways, and with multiple competing products, identification of which of the $1e^-$, $2e^-$ or $4e^-$ reduction products formed, and in what quantities was attempted. In the following discussion, O_2^- and HO_2^- refer to $1e^-$ reduction products, H_2O_2 and HO_2^- refer to $2e^-$ reduction products and OH^- the $4e^-$ reduction product.

To prevent the irreversible formation of OH^- in Li-air cells, it is critical to establish the conditions at which it does form. Formation of $2e^-$ reduction products (Equations 3.7 and 3.8) can be tolerated since HO_2^- , H_2O_2 and Li_2O_2 are all in equilibrium with each other via proton transfer steps such as Equations 3.9 and 3.10. It is likely that HO_2^- and H_2O_2 oxidise at similar potentials to Li_2O_2 , but even if this were not the case, the equilibria would allow oxidation to proceed via the species with the most negative $E_{P,ox}$, provided the oxidation does not become kinetically-limited.



Therefore, oxidation of any $2e^-$ reduction products is, in theory, possible. At the operating potentials required for Li- O_2 batteries, uncatalysed oxidation of the $4e^-$ reduction product is not possible, so is effectively irreversible and hence undesirable.

RRDE measurements were used to identify the $1e^-$, $2e^-$ and $4e^-$ reduction products. The full methodology is described in Chapter 2, but to summarise, two oxidising potentials were used at a Pt ring electrode to oxidise either $1e^-$ reduction products or $1e^-$ and some $2e^-$ reduction products that formed at the disk electrode. A potential of 3.75 V was used

to oxidise all $1e^-$ reduction products *i.e.* quantitative identification of O_2^- and HO_2^- . A potential of 4.3 V oxidised all $1e^-$ reduction products and some $2e^-$ reduction products *i.e.* qualitative identification of HO_2^- and H_2O_2 . Any remaining current unaccounted for at the ring was assigned to $4e^-$ reduction products and further $2e^-$ reduction products that were not oxidised by the ring at 4.3 V. The proportion of the $1e^-$, $2e^-$ and $4e^-$ reduction products were found by comparing the ring currents and disk currents. The blue, red and green traces are the current densities due to $1e^-$ species, $1e^-$ and some $2e^-$ species and the disk current density, respectively. The relative proportion of $1e^-$ reduction products, $2e^-$ reduction products and further $2e^-$ and $4e^-$ reduction products are indicated by the blue, red and green shaded areas, respectively.

In both dry systems (Figures 3.6a and 3.7a), as the disk is scanned negatively, reduction of O_2 occurs and once a sufficient overpotential is applied, all O_2 at the disk is reduced and a steady-state limiting current (i_L) is reached, resulting in a plateau. The current is dependent on the rotation rate of the electrode, which induces mass transport to the electrode and reduces the size of the diffusion layer compared to a quiescent electrolyte. This described by the Levich equation,

$$i_L = 0.62nFAD_0^{2/3}\omega^{1/2}\nu^{-1/6}C_0^* \quad (3.11)$$

where i_L is the limiting current (A), n is the number of electrons involved in the electron transfer, F is the Faraday constant ($C\ mol^{-1}$), A is the electrode area (cm^2), D_0 is the diffusion constant of the oxidised species ($cm^2\ s^{-1}$), ω is the electrode rotation rate ($rad\ s^{-1}$), ν is the kinematic viscosity of the electrolyte ($cm^2\ s^{-1}$) and C_0^* is the bulk concentration of the oxidised species ($mol\ cm^{-3}$).

Since O_2^- is stable in the dry electrolytes, it is fully oxidised at the ring and accounts for all of the current passed at the disk. Hence, there is only a blue shaded area in the dry polarisation curves (Figures 3.6a and 3.7a).

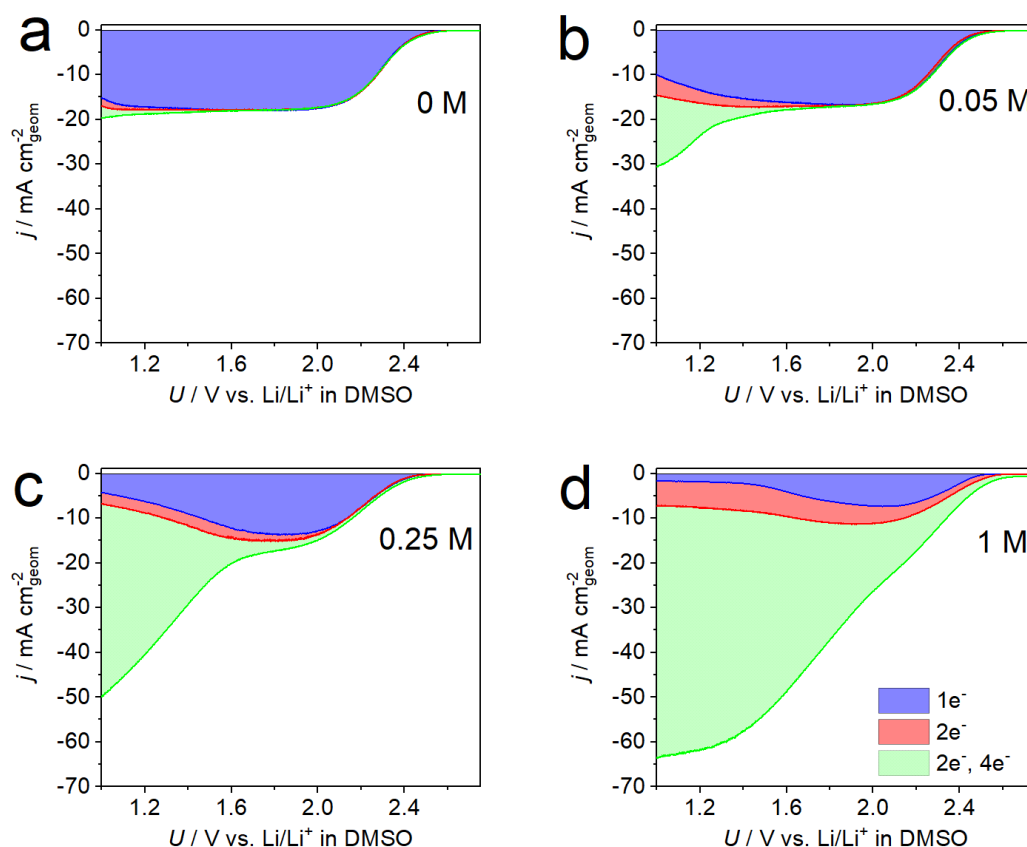


Figure 3.6: RRDE polarisation curves showing that 2e⁻ and 4e⁻ O₂ reduction initially occurs at potentials negative of the 1e⁻ reduction in CH₃CN, but at 1 M H₂O, the 1e⁻, 2e⁻ and 4e⁻ reductions occur simultaneously. The blue and red shaded areas indicate current passed due to 1e⁻ and 2e⁻ products, respectively. The green shaded area is due to further 2e⁻ products and the 4e⁻ product. Electrolytes consisted of O₂-saturated 0.25 M TBAClO₄ in CH₃CN with H₂O concentrations as indicated on plots. Ring potentials for 1e⁻ and 2e⁻ O₂ reduction products were 3.75 V and 4.3 V, respectively. 5 mm Au working, Pt ring, Li_xFePO₄ reference and Pt counter electrodes were used. The scan rate and rotation rate were 20 mV s⁻¹ and 1000 rpm, respectively.

If we now consider CH₃CN, on addition of 0.05 M H₂O, at potentials >1.8 V, there is very little change to the reduction current (Figure 3.6b). The blue shaded area indicates that only 1e⁻ O₂ reduction occurs. However, at potentials <1.8 V, the appearance of red and green shaded areas on the plot indicate that 2e⁻ and 4e⁻ products form, and below 1.4 V, a new cathodic peak is observed at the disk (green trace) along with a decay in the

amount of O_2^- that forms (a decrease in the blue shaded area). Background polarisation curves recorded under N_2 (Appendix 1) confirm this peak is not due to H_2 evolution. Therefore, the new peak at negative potentials is due to protic O_2 reduction.

When the H_2O concentration was increased to 0.25 M, this protic peak shifts positively to an onset potential of ~ 1.6 V and leads to a much larger disk current, indicating that the $4e^-$ reduction becomes more favourable (Figure 3.6c). There is limited formation of H_2O_2 at potentials < 1.6 V (red shaded area), suggesting that the major product at these potentials is now OH^- . At potentials between 1.6 V and 2 V, $1e^-$ products dominate, but small amounts of the $2e^-$ and $4e^-$ products also form, while at potentials > 2 V, only the $1e^-$ reduction product forms. At 1 M H_2O , the protic peak shifted positively to such an extent that OH^- forms at all potentials (Figure 3.6d) and at potentials below 2 V, OH^- is the dominant product.

In DMSO, the overall trend is similar, but, as in the CVs in Section 3.3.1, significantly higher H_2O concentrations are required to induce $4e^-$ reduction (Figure 3.7). Even at 0.25 M H_2O , the $1e^-$ reduction product is the sole product at potentials as low as 1.4 V (Figure 3.7b). There is a slight increase in current density at lower potentials (green trace), suggesting that protic O_2 reduction occurs at potentials just beyond the electrochemical window used here. The protic peak can be observed at 1 M H_2O , having shifted further positive, with the appearance of the green and red shaded areas (Figure 3.7c). Despite the significant quantity of H_2O (~ 1.8 vol%), only the $1e^-$ product forms at potentials > 1.6 V. Even more surprisingly, at 5 M H_2O , the $1e^-$ product still remains the exclusive product above 1.8 V (blue shaded area), while at lower potentials, a mixture of the $1e^-$, $2e^-$ and $4e^-$ products forms as indicated by the blue, red and green shaded areas (Figure 3.7d).

The Levich equation can be used to calculate n from i_L and determine whether O_2 is reduced to the $1e^-$, $2e^-$ or $4e^-$ products. To calculate n , the values of D_O , ν and C_O^* are required. Literature values for D_O and C_O^* were used ($7.05 \times 10^{-5} \text{ cm}^2 \text{ s}^{-1}$ and 8.1 mM, respectively, in CH_3CN and $2.30 \times 10^{-5} \text{ cm}^2 \text{ s}^{-1}$ and 2.1 mM, respectively, in DMSO)^{8,10,11},

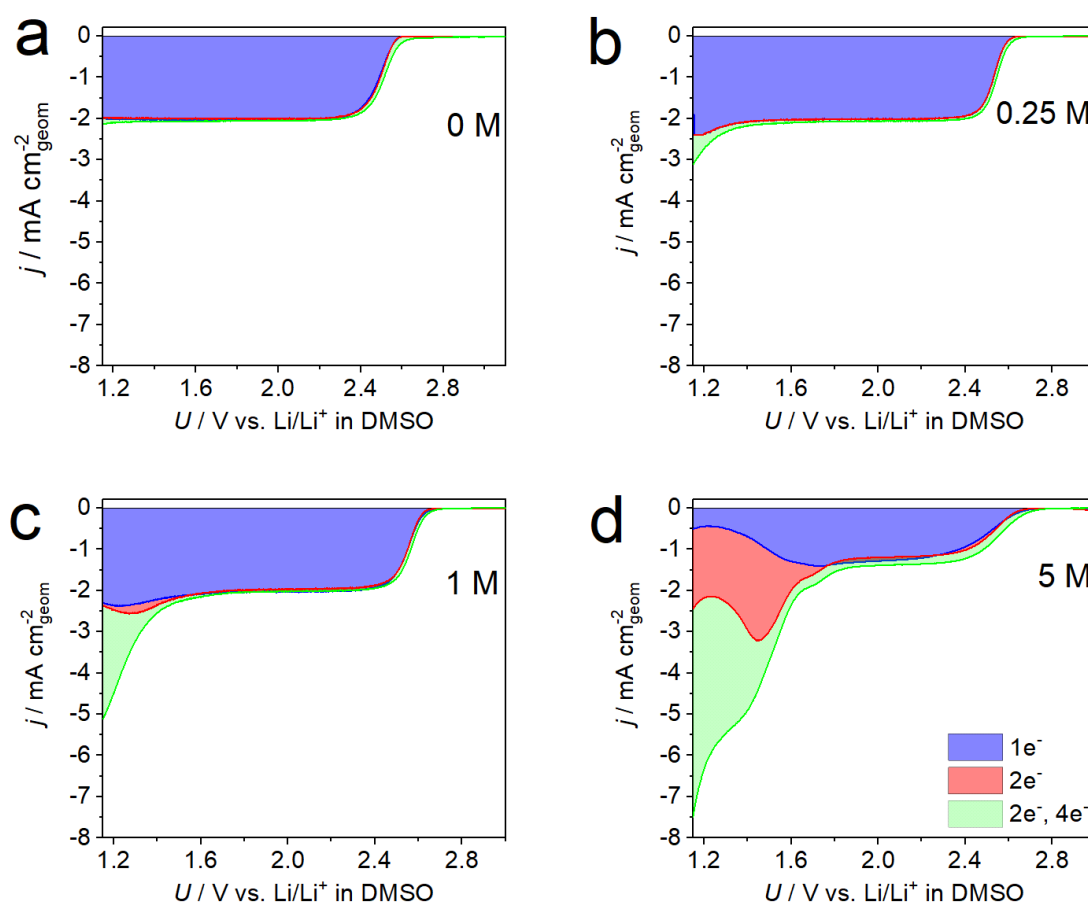


Figure 3.7: RRDE polarisation curves showing that 2e⁻ and 4e⁻ O₂ reduction occur at potentials significantly negative of the 1e⁻ reduction in DMSO. The blue and red shaded areas indicate current passed due to 1e⁻ and 2e⁻ products, respectively. The green shaded area is due to further 2e⁻ products and the 4e⁻ product. Electrolytes consisted of O₂-saturated 0.25 M TBAClO₄ in DMSO with H₂O concentrations as indicated on plots. Ring potentials for 1e⁻ and 2e⁻ O₂ reduction products were 3.75 V and 4.3 V, respectively. Au working, Pt ring, Li_xFePO₄ reference and Pt counter electrodes were used. The scan rate and rotation rate were 20 mV s⁻¹ and 1000 rpm, respectively. while ν for each electrolyte was measured experimentally using a kinematic viscometer (SVM 3000, Anton Paar). The same C_0^* was used for both the dry and H₂O-containing electrolytes. However, C_0^* is likely to decrease in the latter since O₂ is less soluble in H₂O than DMSO and CH₃CN (0.258 mM, 2.1 mM and 8.1 mM, respectively)^{8,12}. If this were corrected for, the calculated values of n would increase. Table 3.4 shows the calculated values for n in the dry electrolytes and H₂O-containing electrolytes, 5 M in DMSO and 1

M in CH₃CN, along with the current densities, j_L , and ν used to calculate them. In the H₂O-containing electrolytes, there were no distinct plateaus for the 2e⁻ and 4e⁻ reduction reactions, so values for the current density were taken at 1.3 V and 1.2 V in DMSO and CH₃CN, respectively.

Table 3.4: Number of electrons, n , involved transferred during O₂ reduction in CH₃CN and DMSO-based electrolytes. The experimentally measured parameters, j_L and ν , used to calculate n are also included.

Solvent	H ₂ O concentration / M	j_L / mA cm ⁻²	ν / cm ² s ⁻¹	n
CH ₃ CN	0	17.20	0.006455	0.912
	1	61.76	0.006688	3.226
DMSO	0	2.037	0.025343	1.057
	5	5.430	0.032364	2.944

In the dry electrolytes, n should equal 1 as O₂⁻ is the only product. The values calculated for n in DMSO and CH₃CN are 1.057 and 0.912, respectively, indicating that the 1e⁻ reduction of O₂ occurs here. In the H₂O-containing electrolytes, the calculated values increase to 2.944 and 3.226 in DMSO and CH₃CN, respectively, indicating that a mixture of the 1e⁻, 2e⁻ and 4e⁻ O₂ reductions occur and supports the assignment of at least a portion of the green shaded areas in Figures 3.6-3.7 to the 4e⁻ reduction.

The CVs and RRDE results presented so far were carried out on Au disk electrodes. The use of noble metal-based electrodes could alter the protic O₂ reduction products that form, since metals such as gold and platinum have been extensively studied in aqueous O₂ reduction for potentially beneficial catalytic effects. Furthermore, noble metals are unlikely to be used as practical electrodes in Li-O₂ batteries, due to their high cost and weight. Typical Li-O₂ batteries use carbon-based electrodes for several reasons including their low mass, which improves the specific energy of the cell, and low cost. Therefore, the RRDE measurements were repeated with a glassy carbon (GC) disk and

Pt ring electrode to confirm that the observed trends were not limited to Au electrodes and will therefore be relevant in understanding the influence of H₂O in Li-O₂ batteries (Figure 3.8). Polarisation curves were recorded using electrolytes containing 0 M and 0.25 M H₂O. The latter concentration was chosen because the 4e⁻ reduction begins to overlap with the 1e⁻ reduction in CH₃CN but not in DMSO.

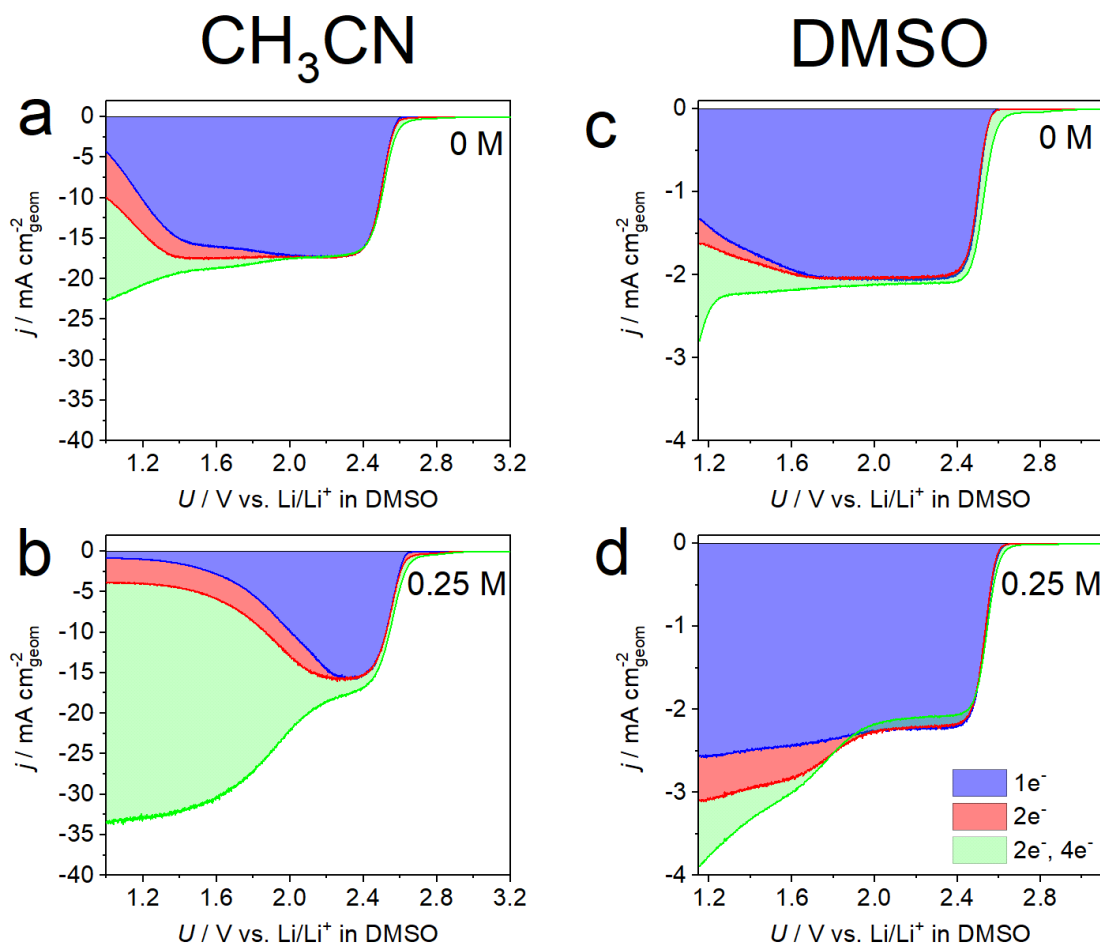


Figure 3.8: RRDE polarisation curves showing that, with a GC disk electrode, the 4e⁻ product forms much more readily in CH₃CN than DMSO. The H₂O concentrations used were 0 M (a,b) and 0.25 M (c,d). Experimental conditions were identical to those in Figure 3.6 and Figure 3.7, except for a GC disk electrode replacing the Au electrode.

In dry CH₃CN (Figure 3.8a), O₂⁻ readily formed at approximately ≤ 2.5 V. However, at potentials < 2 V, parasitic electrochemistry began to occur, as the current due to O₂⁻ (blue

shaded area) begins to decay, while the appearance of the red and green shaded areas identify new species being oxidised at the ring. As H₂O was not present, electrolyte decomposition is the likely cause, catalysed by the GC electrode, as this does not occur as readily with a Au electrode. With 0.25 M H₂O (Figure 3.8b), the O₂⁻ peak decays significantly and is replaced by the 4e⁻ product, just as with the Au electrode, though here this change occurs at around 2.4 V compared to 2.0 V with Au.

In dry DMSO (Figure 3.8c), O₂⁻ forms stably at potentials between 2.0-2.5 V, while at more negative potentials, there is evidence of electrolyte degradation, as in CH₃CN. When H₂O is present (Figure 3.8d), O₂⁻ still forms at potentials above 2.0 V, while 2e⁻ and 4e⁻ reduction products begin to form at potentials <2.0 V, in addition to the O₂⁻ that would be expected to form. Furthermore, GC appears to be a poorer substrate than Au for maintaining 1e⁻ O₂ reduction in H₂O-containing electrolytes, as it produces a greater quantity of the 2e⁻ and 4e⁻ reduction products, indicated by the increased red and green shaded areas in Figure 3.8d compared to Figure 3.7b.

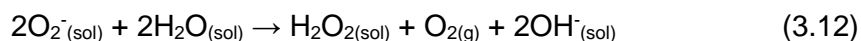
Overall, the RRDE results confirm the trends seen in the CVs, where O₂ reduction is largely unaffected at low H₂O concentrations (≤0.25 M H₂O in CH₃CN, ≤1 M H₂O in DMSO), but at higher concentrations, protic O₂ reduction, and in particular, the 4e⁻ reduction occur. The H₂O concentration required to induce 4e⁻ O₂ reduction is influenced by the organic solvent. DMSO is only capable of undergoing 4e⁻ O₂ reduction (in addition to 1e⁻ and 2e⁻ O₂ reduction) with 5 M H₂O at potentials below 2 V (though this is substrate-dependent), while in CH₃CN, 4e⁻ reduction occurs at all reducing potentials in the presence of 1 M H₂O. Use of GC electrodes also results in the formation of 2e⁻ and 4e⁻ reduction products at similar potentials to those when Au electrodes are used.

3.5. Chemical routes to protic O₂ reduction products from O₂⁻ and H₂O

H₂O₂ and OH⁻ can form chemically from O₂⁻ in the presence of H₂O. O₂⁻ is known to disproportionate in aqueous environments, forming both peroxide and oxide species¹³.

It is therefore possible that some of the H_2O_2 and/or OH^- detected by the RRDE measurements may not have been formed electrochemically, but from chemical reactions following the initial O_2^- generation. This is certainly the case in CH_3CN , where CV simulations identified that disproportionation to H_2O_2 readily occurs (Section 3.3.2). If OH^- could also form spontaneously via a chemical pathway, avoiding accumulation of LiOH in a Li-air cell would prove extremely challenging. Therefore, it was necessary to identify whether a viable chemical pathway for OH^- formation exists in H_2O -containing electrolytes.

Formation of H_2O_2 and OH^- from O_2^- leads to O_2 evolution via Equations 3.12 and 3.13, respectively.



The O_2/O_2^- molar ratio is different if O_2^- disproportionates to H_2O_2 or OH^- (0.5 and 0.75, respectively). Therefore, on-line mass spectrometry was used to quantify O_2 evolution from the mixing of O_2^- samples with H_2O -containing solvents, allowing determination of the O_2/O_2^- ratio and thus the extent of disproportionation. Full experimental details are provided in Chapter 2. Figure 3.9 shows the O_2 fluxes (normalised to the initial KO_2 quantity) obtained when H_2O -containing solvents were added to KO_2 samples connected to an on-line mass spectrometer (MS).

In DMSO (Figure 3.9a), O_2 evolution was very slow when DMSO/ H_2O mixtures containing <1 M H_2O were added to the KO_2 sample, with O_2 evolution taking approximately 1 hour to reach peak flux. Furthermore, when mixture containing only 0.1 M H_2O was used, O_2 evolution increased negligibly, suggesting that disproportionation is very slow at such H_2O concentrations and is omitted from the figure for clarity. However, significant O_2 evolution was observed by the MS when mixtures containing 1 M and 5 M H_2O concentrations were added to the KO_2 samples. Here, the peak O_2 fluxes

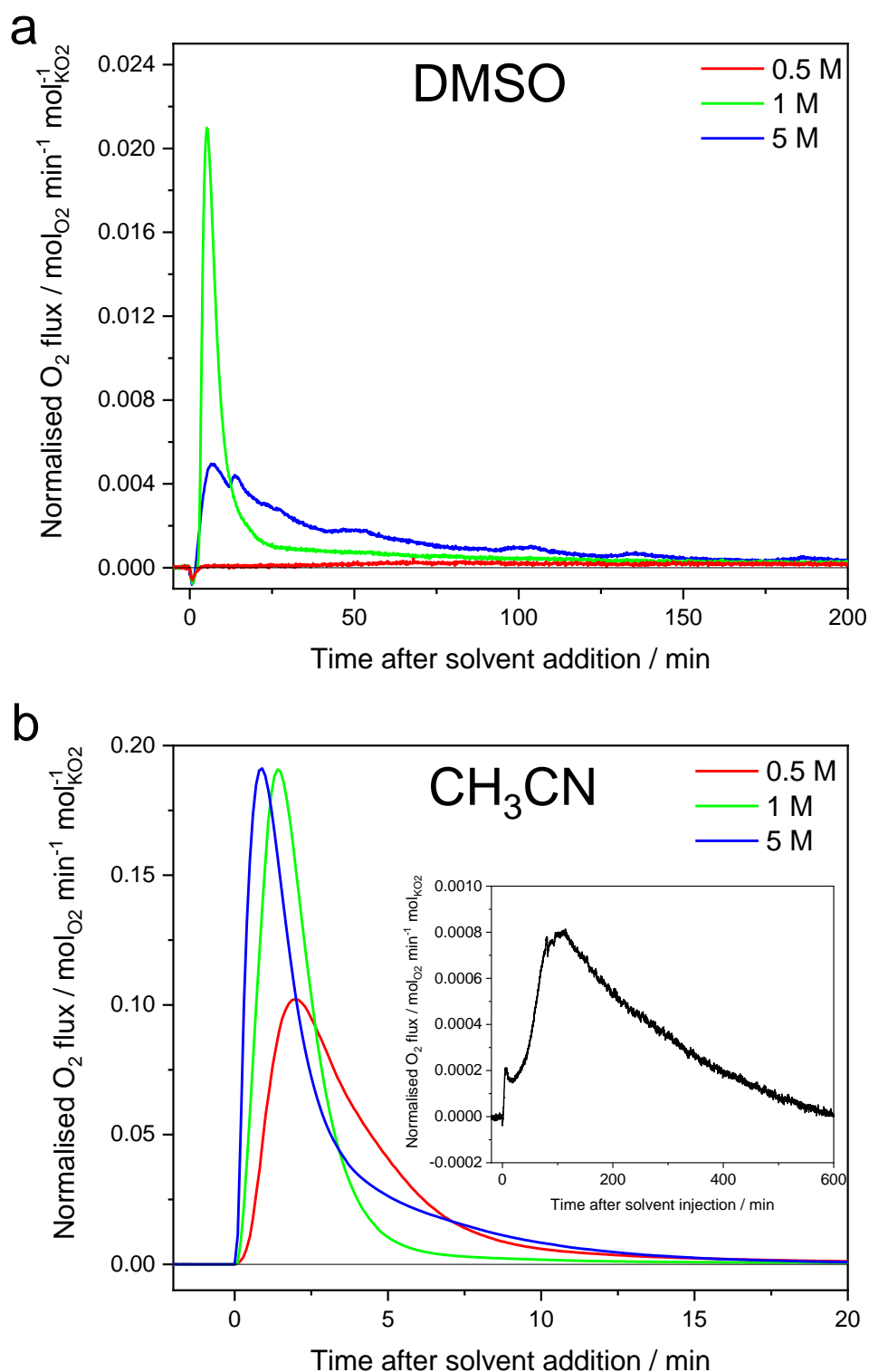


Figure 3.9: O₂ evolution profiles from samples of KO₂ mixed with H₂O-containing DMSO (a) and CH₃CN (b), showing slow O₂ evolution in DMSO and significantly faster O₂ evolution in CH₃CN. The O₂ flux is normalised to the molar quantity of KO₂ in each sample. The H₂O concentrations used are indicated in the legends. The inset in panel (b) shows the slow O₂ evolution with 0.1 M H₂O in CH₃CN.

occurred within 10 minutes of solvent addition, demonstrating that the kinetics of the disproportionation reaction(s) increase as the H₂O concentration increases. This is to be expected based on the stoichiometry of Equations 3.12 and 3.13, which are second order with respect to H₂O. However, the reaction rate with 5 M H₂O is slower than with 1 M H₂O, evidenced by a broader O₂ flux and lower peak value. This is likely to be caused by increased viscosity of the 5 M H₂O mixture compared to the 1 M H₂O mixture, which would reduce diffusion of HO₂ and therefore slow the disproportionation reaction. A similar increase in viscosity was measured for 5 M H₂O electrolyte solution compared to the dry electrolyte (Table 3.3).

In CH₃CN (Figure 3.9b), the O₂ fluxes indicate that disproportionation is significantly more rapid at each H₂O concentration compared to DMSO. The peak O₂ flux is approximately an order of magnitude higher in CH₃CN than DMSO and O₂ evolution nearly ceases within 15 minutes at H₂O concentrations of 0.5 M and above. Even at a 0.1 M H₂O concentration, O₂ evolution is discernible but occurs over the course of several hours. Furthermore, this supports the findings in Section 3.3, where reactions between O₂⁻ and H₂O appeared to be more rapid in CH₃CN.

Figure 3.10 shows the O₂/O₂⁻ ratios obtained at various H₂O concentrations in DMSO and CH₃CN and calculated by integration of the O₂ fluxes from Figure 3.9. In DMSO, the O₂/O₂⁻ ratios are significantly below 0.5 for all H₂O concentrations used, indicating that incomplete disproportionation of O₂⁻ to H₂O₂ within the timescale of the experiment. Following the initial O₂ peak when the DMSO solutions were added, the flux decayed to a steady value close to 0 mol_{O₂} min⁻¹ mol_{KO₂}⁻¹ (Figure 3.9a). In CH₃CN and at H₂O concentrations >0.1 M H₂O, the O₂/O₂⁻ ratios are around 0.5, indicating that O₂⁻ fully disproportionates to H₂O₂, but not OH⁻. If this were the case, the ratios would continue to increase towards 0.75. These results identify that the 4e⁻ product, OH⁻, does not form chemically and therefore, the presence of OH⁻ in the RRDE data must be produced

electrochemically. Furthermore, it demonstrates that the solvent influences not only the electrochemical reactions H_2O participates in, but also the chemical reactions.

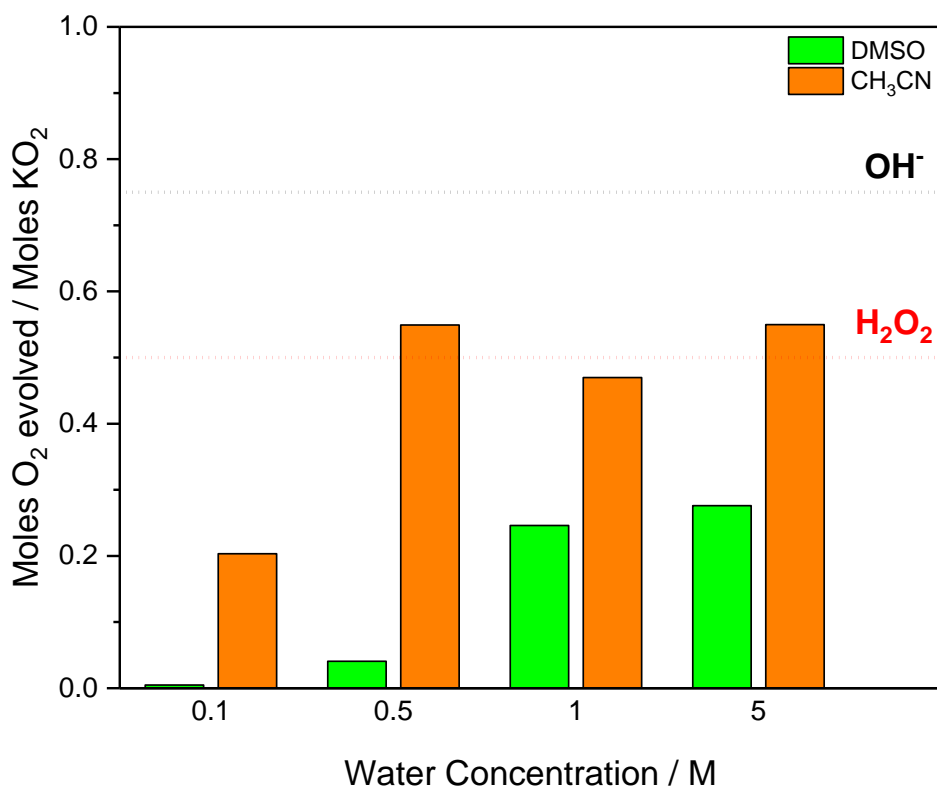


Figure 3.10: O_2/O_2^- molar ratios identifying that O_2^- disproportionates to H_2O_2 , not OH^- , in H_2O -containing CH_3CN and DMSO . The O_2/O_2^- ratio depends on which disproportionation product form; H_2O_2 leads to a value of 0.5 (red line) and OH^- leads to a value of 0.75 (black line). The O_2/O_2^- ratios were calculated by integrating the O_2 flux curves in Figure 3.9.

3.6. Spectroscopic identification of ORR intermediates/products

The electrochemical analyses so far have identified that as the H_2O concentration is increased, the electrochemistry switches from an aprotic ($1e^-$ reduction) to protic mechanism ($2e^-$ and $4e^-$ reduction). RRDE provides only indirect evidence of the electrochemically generated species so, *in situ* SERS was used to identify species formed at the electrode surface during O_2 reduction (Figure 3.11). In the dry electrolytes,

two signals due to O_2^- are seen at $\sim 480\text{ cm}^{-1}$ and $\sim 1110\text{ cm}^{-1}$ when reducing potentials are applied. These are due to Au – O_2^- , and O – O^- stretches, respectively.

As H_2O was introduced into both electrolytes, the O_2^- Raman signals were still observed during reduction (Figure 3.11). This demonstrates that O_2^- is still generated even in the presence of significant H_2O concentrations, $>0.5\text{ M}$. However, a new signal was seen at 1130 cm^{-1} in H_2O -containing electrolytes, appearing as a shoulder to the main 1110 cm^{-1} peak. This suggests that a new species is generated, which could be HO_2 , as this is expected to form in these electrolyte systems. Various literature values have been reported for HO_2 , ranging from 1097 cm^{-1} to 1140 cm^{-1} (refs. 14-17). In solution, HO_2 should have a higher wavenumber than O_2^- , since there is less e^- density in the π^* O-O orbitals, resulting in a stronger O-O bond. Thus, this shoulder is tentatively assigned to the HO_2 species, and the observation of this peak in both solvents further strengthens this assignment. An H_2O_2 peak would be expected at 880 cm^{-1} . However, two TBA^+ vibrational modes occur at this Raman shift, making it difficult to assign any changes in the spectra to H_2O_2 . While the peak does increase in intensity as the H_2O concentration increases, this could be caused by the TBA^+ ions rearranging in the inner Helmholtz layer due to the presence of H_2O , leading to a potential enhancement of the salt Raman signals.

Depending on the H_2O concentration and applied potentials, OH^- can form either electrochemically ($4e^-$ reduction) or as a chemical product ($1e^-$ and $2e^-$ reduction). In either case, the generation of OH^- indicates that protic O_2 reduction occurs, so *in situ* spectroscopic identification of OH^- was attempted. However, this was complicated by the presence of H_2O in the electrolytes. OH^- and H_2O share a vibrational mode, the O-H stretch, and furthermore, this is the only vibrational mode that OH^- possesses. Therefore, signals characteristic of O-H stretches would be observed whenever H_2O is present, preventing unambiguous observation of OH^- . To overcome this problem, the oxidation of Au by OH^- was exploited (Figure 3.12).

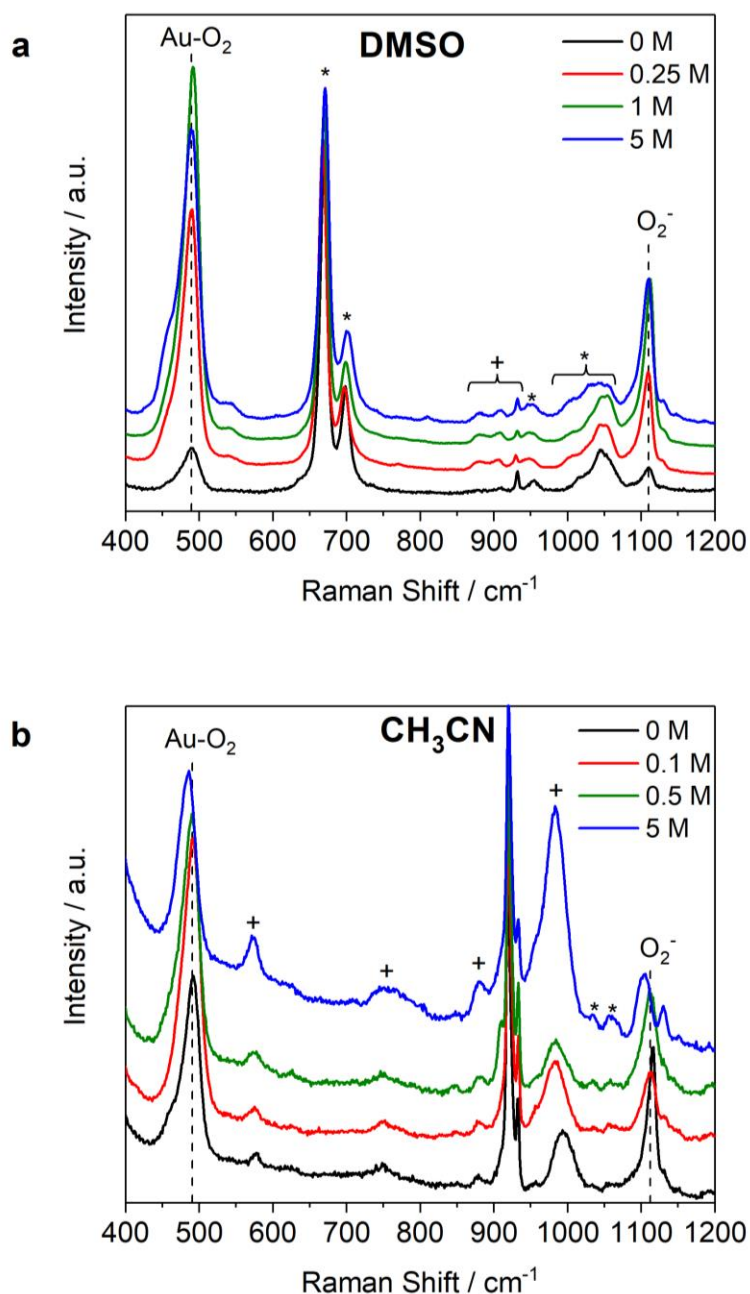


Figure 3.11: SER spectra acquired during O₂ reduction at a roughened Au electrode in DMSO- (a) and CH₃CN-based (b) electrolytes showing O₂⁻ forming at all H₂O concentrations used. The electrolytes were O₂-saturated 0.25 M TBAClO₄ in DMSO or CH₃CN and containing H₂O concentrations as indicated in the legends. Spectra were acquired whilst holding the Au electrode at 2.2 V and 2.35 V in DMSO and CH₃CN, respectively. A 785 nm laser, x20 objective and 1200 l/mm grating were used. + and * indicate solvent and salt signals, respectively (reference values in Appendix 2).

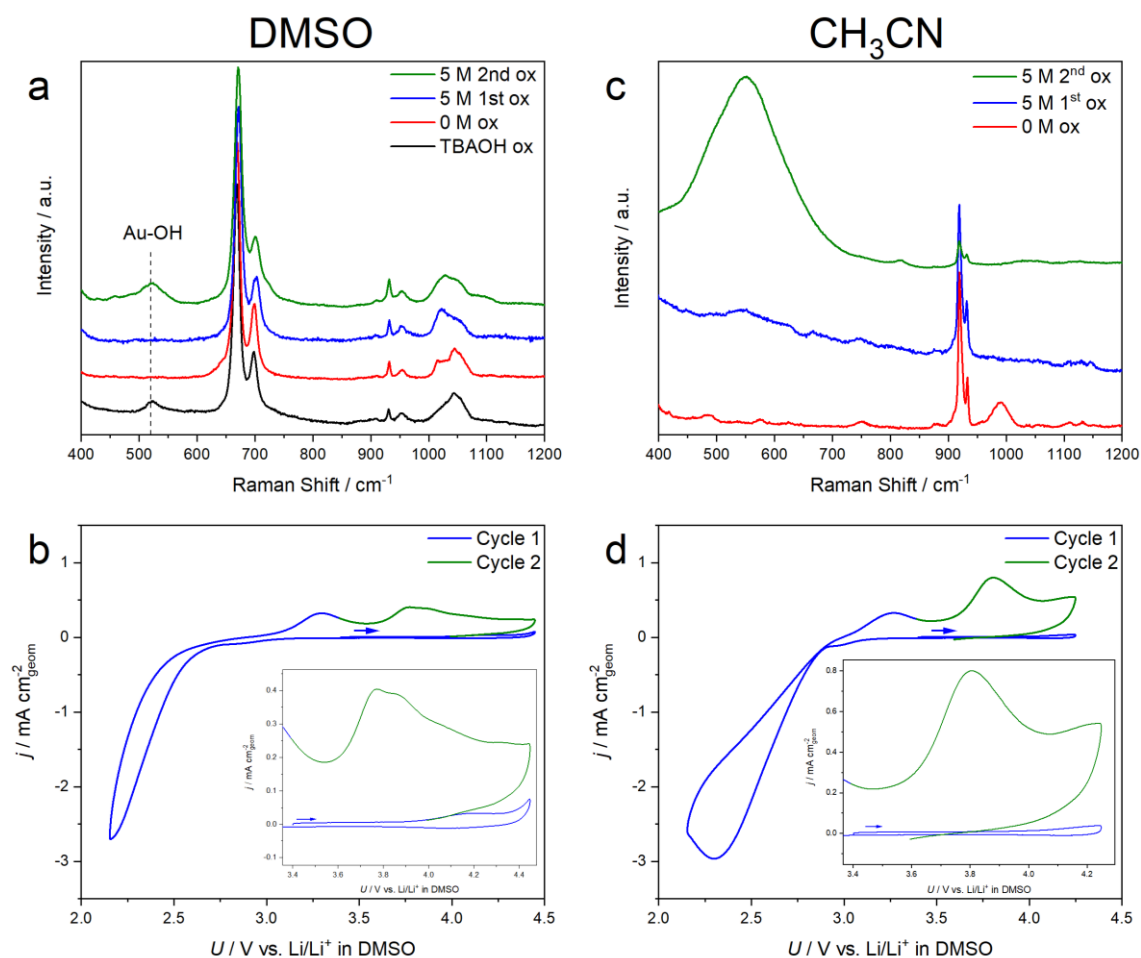


Figure 3.12: SER spectra (a,c) and CVs (b,d) demonstrating that Au(OH)₃ only forms in H₂O-containing electrolytes following a preceding O₂ reduction step. Electrolytes were 0 M or 5 M H₂O 0.25 M TBAClO₄ in DMSO (a,b) or CH₃CN (c,d). The reference spectrum (black curve, a) was recorded using the following salt concentrations: 0.01 M TBAOH; 0.24 M TBAClO₄; 5 M H₂O. Spectra were acquired whilst holding a roughened Au electrode at 4.2 V. A 785 nm laser, x20 objective and 1200 l/mm grating were used. CVs were recorded with 5 M H₂O in electrolytes, beginning with an anodic sweep from 3.4 V (indicated by blue arrows). A roughened Au working, Ag wire reference and Pt counter electrode were used. CV scan rate 100 mV s⁻¹.

When the potential of a Au electrode is cycled in alkaline aqueous solutions, Au(OH)₃ forms at less positive potentials than Au₂O₃ and possesses a Raman signal^{18,19}. Crucially, oxidation of Au with OH⁻ occurs at less positive potentials than H₂O itself, so

careful control of the applied potentials affords selectivity for OH^- . To validate the technique, an electrolyte consisting of 5 M H_2O 0.24 M TBAClO_4 in DMSO was doped with 0.01 M TBAOH to generate the $\text{Au}(\text{OH})_3$ Raman signal *in situ*. When an oxidising potential of 4.25 V was applied to the Au electrode in this electrolyte (black curve, Figure 3.12a), a new peak was observed in the SER spectrum, where $\text{Au}(\text{OH})_3$ peaks are found. When the same potential was applied in pristine dry TBAClO_4 electrolytes (red curves, Figure 3.12a,c), this peak was not seen. Similarly, when pristine electrolytes containing 5 M H_2O were held at 4.25 V (blue curve, Figure 3.12), no OH^- peak was observed, and no Faradaic processes occurred at positive potentials in the CVs (blue traces, Figure 3.12b,d). This confirms that H_2O cannot oxidise Au at this potential in DMSO and CH_3CN . When those same electrolytes then underwent O_2 reduction, OH^- should have formed. When the electrode was again held at 4.25 V (green curve, Figure 3.12a,c), the Au-OH peak was observed, showing that the OH^- was generated during reduction and the Faradaic processes associated with this oxidation can be seen in the CVs (green traces, Figure 3.12b,d). At the reducing potentials applied here, OH^- will be a product of 1e^- or 2e^- reduction of O_2 in DMSO (in addition to HO_2 or H_2O_2 , respectively), but in CH_3CN is likely to result from 4e^- O_2 reduction. Thus, this provides indirect spectroscopic evidence that H_2O is involved in electrochemical and/or chemical reactions during O_2 reduction in these electrolytes.

3.7. Conclusions

In this chapter, I have established that H_2O participates in various chemical and electrochemical reactions during O_2 reduction in aprotic solvents and introduces pathways to several new products. The clearest example of this is that it is possible to form HO_2 , H_2O_2 and OH^- in both CH_3CN -based and DMSO-based electrolytes, provided there is a sufficient concentration of H_2O and the correct reducing potential is applied. Furthermore, as the H_2O concentration is increased, these protic reduction products form at increasingly positive potentials, to the extent that in CH_3CN with 1 M H_2O and at all

reducing potentials, the dominant product is OH^- , which would be catastrophic for the cyclability of a Li- O_2 cell. However, in DMSO with 1 M H_2O , very negative potentials are required for $4e^- \text{O}_2$ reduction at the positive electrode, which lies outside its operating potential in Li- O_2 cells. Therefore, if the conditions required for $4e^- \text{O}_2$ reduction are similar in Li^+ -containing electrolytes, it should be possible to avoid electrochemical LiOH formation in DMSO at low overpotentials.

The solvent clearly plays an important role in controlling the electrochemical and chemical reactions during O_2 reduction. As already noted, much less H_2O is required to alter the electrochemical reactions in CH_3CN . However, the equilibrium and rate constants for HO_2 formation and disproportionation, respectively, were higher in CH_3CN than DMSO, demonstrating that the solvent also influences these chemical reactions. This was in line with O_2 evolution measurements, which also found disproportionation to be faster in CH_3CN . Furthermore, SERS experiments showed that while OH^- forms on O_2 reduction in both DMSO and CH_3CN , a greater quantity forms in CH_3CN , which had a far more intense $\text{Au}(\text{OH})_3$ peak than DMSO.

I found no evidence to suggest that O_2^- is preferentially solvated by H_2O due to its high AN, when present in organic solvent-based electrolytes, as suggested by Aetukuri *et al.*² Instead, at low H_2O concentrations, O_2^- and H_2O are involved in a chemical equilibrium with HO_2 and OH^- . Provided the HO_2 concentration is low enough that disproportionation is negligible, O_2^- is conserved over time. This has been exploited in Na- O_2 batteries as a method of phase-transfer catalysis, where the equilibrium is between NaO_2 and the more soluble HO_2 .

Similarly, the pK_a mechanism proposed by Kwabi *et al.* is not supported by my results¹. Their mechanism would suggest that O_2 reduction in H_2O -containing DMSO and CH_3CN should be similar, since the pK_a of H_2O in both solvents is nearly identical (35.0 and 35.2, respectively). However, CH_3CN promotes the $4e^-$ reduction far more readily than DMSO.

Furthermore, I have determined that H₂O can induce disproportionation of O₂⁻ to H₂O₂, but not OH⁻. Therefore, OH⁻ formation can be avoided by careful control of the reduction conditions, that is, the applied potentials and H₂O concentration in the electrolyte. This has important implications for chemical and electrochemical reactions involving protic species. A mixed H₂O-organic solvent system could be used to control the selectivity of a reaction to favour a product that would otherwise be an intermediate in a purely aqueous or organic electrolyte. It is possible, for example, that such an approach could be used in electrochemical synthesis of organic compounds, resulting in new synthetic routes and improved yields. In the context of Li-air batteries, if selectivity for Li₂O₂ over LiOH is maintained in Li⁺-based electrolytes, it may be possible to avoid LiOH formation in H₂O-containing cells. This will be considered in Chapter 4.

3.8. References

- 1 Kwabi, D. G. *et al.* The effect of water on discharge product growth and chemistry in Li-O₂ batteries. *Phys. Chem. Chem. Phys.* **18**, 24944-29453 (2016).
- 2 Aetukuri, N. B. *et al.* Solvating additives drive solution-mediated electrochemistry and enhance toroid growth in non-aqueous Li-O₂ batteries. *Nat. Chem.* **7**, 50-56 (2015).
- 3 Schwenke, K. U., Metzger, M., Restle, T., Piana, M. & Gasteiger, H. A. The influence of water and protons on Li₂O₂ crystal growth in aprotic Li-O₂ cells. *J. Electrochem. Soc.* **162**, A573-A584 (2015).
- 4 Qiao, Y. *et al.* From O₂⁻ to HO₂⁻ : reducing by-products and overpotential in Li-O₂ batteries by water addition. *Angew. Chem.* **56**, 4960-4964 (2017).
- 5 Bard, A. J. & Faulkner, L. R. *Electrochemical Methods. Fundamentals and Applications*. 2nd edition, (Wiley, 2001).
- 6 Easteal, A. J. Tracer diffusion of water in organic liquids. *J. Chem. Eng. Data* **41**, 741-744 (1996).

- 7 Borin, I. A. & Skaf, M. S. Molecular association between water and dimethyl sulfoxide in solution: a molecular dynamics simulation study. *J Chem. Phys.* **110**, 6412-6420 (1999).
- 8 Laoire, C. O., Mukerjee, S., Abraham, K. M., Plichta, E. J. & Hendrickson, M. A. Influence of nonaqueous solvents on the electrochemistry of oxygen in the rechargeable lithium-air battery. *J. Phys. Chem. C* **114**, 9178-9186 (2010).
- 9 Ge, X. *et al.* Oxygen reduction in alkaline media: from mechanisms to recent advances of catalysts. *ACS Catal.* **5**, 4643-4667 (2015).
- 10 Vasudevan, D. & Wendt, H. Electroreduction of oxygen in aprotic media. *J. Electroanal. Chem.* **392**, 69-74 (1995).
- 11 Gunasekara, I., Mukerjee, S., Plichta, E. J., Hendrickson, M. A. & Abraham, K. M. Microelectrode diagnostics of lithium-air batteries. *J. Electrochem. Soc.* **161**, A381-A392 (2014).
- 12 Benson, B. B. & Krause, D. The concentration and isotopic fractionation of oxygen dissolved in freshwater and seawater in equilibrium with the atmosphere. *Limnol. Oceanogr.* **29**, 620-632 (1984).
- 13 Hayyan, M., Hashim, M. A. & AlNashef, I. M. Superoxide ion: generation and chemical implications. *Chem. Rev.* **116**, 3029-3085 (2016).
- 14 Paukert, T. T. & Johnston, H. S. Spectra and kinetics of the hydroperoxyl free radical in the gas phase. *J. Chem. Phys.* **56**, 2824-2838 (1972).
- 15 Nelander, B. The peroxy radical as hydrogen bond donor and hydrogen bond acceptor. A matrix isolation study. *J. Phys. Chem. A* **101**, 9092-9096 (1997).
- 16 Crawford, M. A., Wallington, T. J., Szente, J. J., Maricq, M. M. & Francisco, J. S. Kinetics and mechanism of the acetylperoxy + HO₂ Reaction. *J. Phys. Chem. A* **103**, 365-378 (1999).
- 17 Cooper, P. D., Moore, M. H. & Hudson, R. L. Infrared detection of HO₂ and HO₃ radicals in water ice. *J. Phys. Chem. A* **110**, 7985-7988 (2006).

Chapter 3

- 18 Diaz-Morales, O., Calle-Vallejo, F., de Munck, C. & Koper, M. T. M. Electrochemical water splitting by gold: evidence for an oxide decomposition mechanism. *Chem. Sci.* **4**, 2334-2343 (2013).
- 19 Zhang, Y., Gao, X. & Weaver, M. J. Nature of surface bonding on voltammetrically oxidized noble metals in aqueous media as probed by real-time surface-enhanced Raman spectroscopy. *J. Phys. Chem.* **97**, 8656-8663 (1993).

4. Effect of H₂O on aprotic O₂ reduction in Li⁺-based electrolytes

In Chapter 3, the electrochemistry of O₂ reduction was considered in an idealised Li⁺-free system to understand how H₂O affects O₂ reduction directly. There, H₂O was identified as providing a source of protons that result in the formation of new O₂ reduction products, namely HO₂, H₂O₂ and OH⁻. However, the potentials required to form OH⁻ were markedly different in acetonitrile (CH₃CN) and dimethyl sulfoxide (DMSO) at any given H₂O concentration. For example, at 1 M H₂O in CH₃CN, the 1e⁻, 2e⁻ and 4e⁻ products are generated simultaneously at all reducing potentials, while in DMSO, 4e⁻ reduction occurs ~0.8 V negative of the 1e⁻ reduction. The understanding developed in the ideal system is now used to explore the behaviour of O₂ reduction in electrolytes containing both H₂O and Li⁺. These electrolyte systems are representative of the conditions in Li-O₂ batteries and understanding what occurs during O₂ reduction in them will be critical if the technology is to be successfully developed.

4.1. Background on O₂ reduction

Of the mechanisms proposed in the literature to explain how H₂O affects O₂ reduction, the acceptor number (AN) mechanism proposed by Aetukuri *et al.* and the pK_a mechanism suggested by Kwabi *et al.* are inconsistent with the results presented thus far^{1,2}. There was, however, evidence of metathesis reactions, which convert O₂⁻ to HO₂. This type of reaction has been proposed by several groups in Li⁺-based electrolytes³⁻⁶. This mechanism adequately explains why H₂O induces solution phase growth of Li₂O₂ at low H₂O concentrations. However, it does not explain the different products found in CH₃CN and glyme ether-based electrolytes. The mechanism proposed by Kwabi *et al.*² attempted to rationalise the formation of LiOH in CH₃CN through the changing acidity of H₂O in different solvents but their reasoning considers it a by-product of the metathesis reaction, where H₂O₂ is also formed. Furthermore, if they had attributed the LiOH found

in CH₃CN to the 4e⁻ O₂ reduction reaction, their mechanism would also expect LiOH to form in DMSO, but this is not the case. Therefore, to the best of my knowledge, no mechanism exists to adequately explain the differing discharge products in the range of H₂O-containing solvents used for Li-O₂ research.

I have three main objectives in this Chapter. The first is to identify how the presence of Li⁺ alters O₂ reduction in H₂O-containing DMSO and CH₃CN. This will be achieved by repeating the electrochemical and spectroscopic analyses and comparing the conditions required to induce 4e⁻ O₂ reduction in these electrolytes. Secondly, I will also investigate another solvent, tetraethylene glycol dimethyl ether (TEGDME), one of the family of glyme ethers commonly used in Li-O₂ batteries. Previous work involving two-electrode cells suggests that some H₂O can be tolerated. Therefore, I will seek to establish if this is the case in three-electrode cells and furthermore, identify the H₂O concentration required to result in 4e⁻ reduction. Finally, but most importantly, the insights from these results and those in Chapter 3 should enable me to develop a universal mechanism to rationalise why LiOH will form more readily in some H₂O-containing electrolytes than others.

4.2. Experimental

4.2.1. Materials

Lithium perchlorate (LiClO₄, ≥99.0%, Sigma-Aldrich), tetrabutylammonium hydroxide-30 hydrate (TBAOH.30H₂O, ≥99.0%, Sigma-Aldrich) and potassium superoxide (KO₂, Sigma-Aldrich) were used as received. The KO₂ purity was 98% and was determined using an iodometric titration. DMSO (puriss. p.a., dried, ≤0.02% H₂O, Sigma-Aldrich) was distilled under vacuum. TEGDME (99%, Sigma Aldrich) was also distilled under vacuum, but with the addition of 1 g sodium metal (Sigma Aldrich) and 8.5 g benzophenone (Sigma Aldrich) into 500 mL TEGDME to scavenge organic radicals formed during distillation. CH₃CN (electronic grade, 99.999% trace metals basis, Sigma-Aldrich) was

distilled under Ar (N4.8 grade, Pureshield, BOC). Following distillation, solvents were transferred to an Ar glove box and dried using freshly activated 4Å molecular sieves for a minimum of 72 hours. The H₂O content of the dried solvents was measured using a Karl Fischer titrator (Mettler Toledo). The solvents were used when the H₂O content was <5 ppm. The above chemicals were all stored in an Ar glove box (<0.1 ppm O₂, < 0.1 ppm H₂O, MBraun). Ultrapure H₂O (18.2 MΩ cm⁻¹, Milli-Q, Merck Millipore) was used to make up electrolyte solutions with known H₂O concentrations. High purity N₂ and O₂ gases (N6.0 grade, BOC) were used for saturating electrolyte solutions. These gases were passed through a moisture trap (Agilent) upstream of the electrochemical cell to dry the gases further. The H₂O content of dry electrolytes, *i.e.* no intentionally added H₂O, was tested using the Karl Fischer and found to be <10 ppm.

Triethylphosphine oxide (Et₃PO, >98%, ACROS Organics) was dried in a N₂ glove box (<0.1 ppm H₂O) prior to use for NMR measurements. The salt was dissolved in dichloromethane (<5 ppm H₂O), activated molecular sieves were added and the solution was left to dry for a minimum of 48 hours. Once the solution achieved a H₂O content <5 ppm (confirmed using a Karl Fischer titrator), the molecular sieves were removed and the dichloromethane was evaporated by heating at 45 °C for 5 hours. The salt was then stored in a N₂ glove box (<0.1 ppm O₂, <0.1 ppm H₂O).

4.2.2. Rotating ring-disk electrode (RRDE) preparation

The general methodology for RRDE measurements is described in Chapter 2. Data analysis for this method requires two RRDE voltammograms with reproducible disk current profiles. When recording RRDE polarisation curves using a Au disk electrode with CH₃CN- and TEGDME-based electrolytes, the disk current profiles were highly variable when using the standard electrode preparation described in Chapter 2. Mechanical polishing may alter the surface facets of Au after each preparation and it has previously been reported that O₂ reduction in H₂O-containing organic solvents is sensitive to the Au surface, possibly causing the observed variability⁷. Therefore, the Au

disk preparation was modified to minimise structural changes to the electrode surface in these electrolytes, by using flame-annealing rather than mechanical polishing. First, any residual electrolyte on the electrode was rinsed off with H₂O, then dried and flame-annealed in a propane flame for several minutes. The electrode was cooled under a flow of Ar gas for 15 minutes to prevent the formation of an oxide layer and then acid-cycled as previously described.

4.2.3. Nuclear magnetic resonance (NMR) spectroscopy

Solution NMR measurements were carried out on a Bruker Avance III HD nanobay NMR equipped with a 9.4T magnet. Samples were prepared in a N₂ glove box (<0.1 ppm O₂, <0.1 ppm H₂O) and placed into airtight 5 mm NMR tubes sealed with Young's valves. As these measurements were probing intermolecular interactions, the presence of any deuterated solvent in the sample would affect the chemical shifts (δ) of the species of interest. Therefore, sealed capillary tubes containing reference solutions were placed inside the NMR tubes to prevent mixing with the samples. 1 M LiCl in D₂O (δ = 0 ppm) and 85% D₃PO₄ in D₂O (δ = 0 ppm) were used for ⁷Li and ³¹P NMR spectra, respectively. A constant temperature of 25 °C was maintained for all measurements.

4.2.4. Determination of ANs of solvent/H₂O mixtures

ANs were determined using Et₃PO as first described by Mayer *et al.*⁸ A stock solution of approximately 200 mg of Et₃PO in 4 mL of solvent or H₂O-containing solvent was prepared in a glove box. Aliquots of this stock solution were diluted with further solvent or H₂O-containing solvent to produce five solutions containing approximately 10, 20, 30, 40 and 50 mg of Et₃PO per mL. Mayer *et al.* reported AN values using diphenylphosphinic chloride (Ph₂POCl) as a reference, so an NMR spectrum of Ph₂POCl was recorded with the D₃PO₄ capillary reference to allow conversion of δ between the two references. The chemical shifts were not corrected for the magnetic susceptibilities of the solutions, as was done originally by Mayer *et al.* ANs have been measured without correcting for the magnetic susceptibility of samples previously in ionic liquids⁹, but this

requires a calibration curve to convert the chemical shifts to the AN scale produced by Mayer *et al.* The ^{31}P δ of Et_3PO was determined in several dry solvents (ethanol, 1,2-dimethoxyethane, dimethylformamide, CH_3CN and DMSO) and H_2O , which were then plotted against the AN values reported by Mayer *et al.* to create a calibration curve (Figure 4.1). The R^2 value of the best-fit line is 0.9987, indicating a nearly ideal fitting of the experimental values, despite neglecting the correction for magnetic susceptibility.

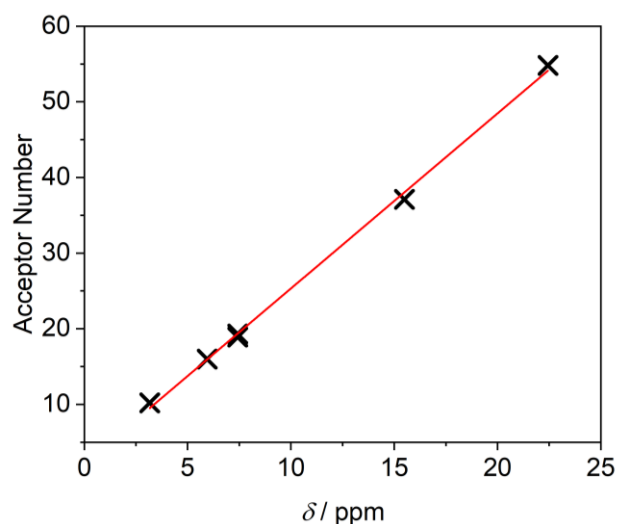


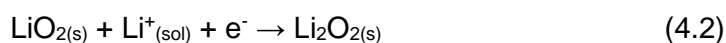
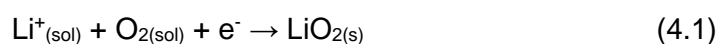
Figure 4.1: Calibration curve generated from ^{31}P δ of Et_3PO in several pure solvents versus the literature AN values of the solvents.

4.2.5. Raman spectroscopy

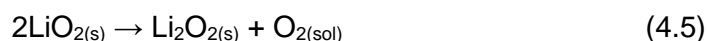
O-H stretching modes of H_2O in CH_3CN , DMSO and TEGDME were measured using a 633 nm HeNe laser using an airtight sample holder with a sapphire window and an inverted microscope on a Renishaw inVia system. Spectra consist of 500 scans, each lasting 30 seconds with a laser power of 50 mW, averaged to produce one spectrum. To prevent excessive heating by the laser, a large sample volume (10 mL) was used and between each scan, the laser was closed to the sample for 30 seconds to allow heat dissipation.

4.3. Electrochemical response of O_2/O_2^- couple to H_2O

The presence of Li^+ dramatically alters the electrochemistry at the positive electrode, as LiO_2 , the analogue of $TBAO_2$, is thermodynamically unstable and exists only as an intermediate species. It goes on to form Li_2O_2 via either a surface or solution mechanism, which is determined by the solubility of LiO_2 . Solvents that are poor Lewis bases, with low donor numbers (DNs) do not stabilise Li^+ sufficiently to allow LiO_2 to dissolve in solution. Therefore, when O_2 is reduced on the electrode surface, it combines with Li^+ to form LiO_2 adsorbed on the electrode (Equation 4.1), where it is subsequently reduced to Li_2O_2 (Equation 4.2). This is the O_2 reduction mechanism in CH_3CN .



If the solvent is a good Lewis base (high DN), such as DMSO, it provides enough stabilisation to Li^+ that LiO_2 has some solubility. O_2 reduction begins with reduction of O_2 to O_2^- , not LiO_2 , remaining dissolved in the electrolyte and diffuses away from the electrode surface (Equation 4.3). The dissolved LiO_2 is in equilibrium with surface adsorbed LiO_2 (Equation 4.4), disproportionates over time to form Li_2O_2 (Equation 4.5).



These O_2 reduction mechanisms lead to dramatic differences seen in the CVs when compared with CVs recorded in TBA^+ -based electrolytes (Figure 4.2). Li_2O_2 is insoluble in the organic solvents used in $Li-O_2$ research and accumulates as a solid on the electrode surface. Furthermore, Li_2O_2 is electrically insulating, so will passivate the electrode surface as it builds up. This can be clearly seen in both DMSO and CH_3CN , as

the O_2 reduction current decays towards zero at more negative potentials, rather than plateauing to a diffusion-limited current as with TBA^+ .

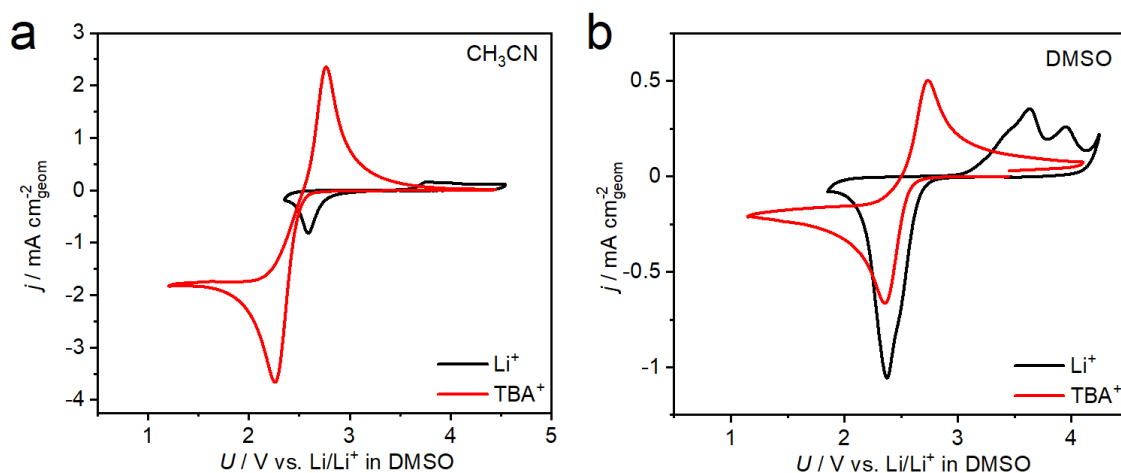


Figure 4.2: CVs contrasting the different electrochemical reactions occurring in dry TBA^+ -based and Li^+ -based electrolytes, with a soluble O_2^- product in the former but an insoluble Li_2O_2 product in the latter. The electrolytes were O_2 -saturated 0.25 M $TBAClO_4$ or $LiClO_4$ in CH_3CN (a) and DMSO (b) as indicated in the legend. The H_2O concentration was <10 ppm in all cases. The $TBAClO_4$ CVs are reproduced from Figure 3.1. The scan rate was 100 mV s^{-1} . Au working, Li_xFePO_4 reference and Pt counter electrodes were used.

Furthermore, Li_2O_2 oxidation requires significantly higher potentials than $TBAO_2$, demonstrating the electrochemical irreversibility that has been one of the major issues facing the $Li-O_2$ battery. In both CH_3CN and DMSO, Li_2O_2 oxidation results in multiple peaks, which shows that oxidation is a complex multi-step process. It has been suggested that oxidation proceeds via delithiation of the Li_2O_2 surface, followed by disproportionation of the now Li-deficient surface¹⁰. Furthermore, the precise morphologies of Li_2O_2 deposits are likely to affect the oxidation potentials, making analysis of Li_2O_2 oxidation non-trivial¹¹. Here, the focus is primarily on how O_2 reduction is affected by H_2O and a rigorous analysis of the oxidation processes is not attempted.

The effect of H₂O in CH₃CN-based electrolytes is discussed first. Figure 4.3 shows CVs for O₂ electrochemistry at various H₂O concentrations between 0 M (defined here as <10 ppm H₂O) and 1 M. It is clear that peak reduction current ($i_{P,red}$) increases monotonically as the H₂O concentration is increased. At 1 M H₂O, $i_{P,red}$ is approximately 9 times that in the dry electrolyte. This suggests that H₂O is delaying electrode passivation in some way, sustaining further O₂ reduction. The change to the oxidation peaks is modest in comparison, with the peak oxidation current ($i_{P,ox}$) only visibly increasing when the H₂O concentration exceeds 0.05 M (inset, Figure 4.3).

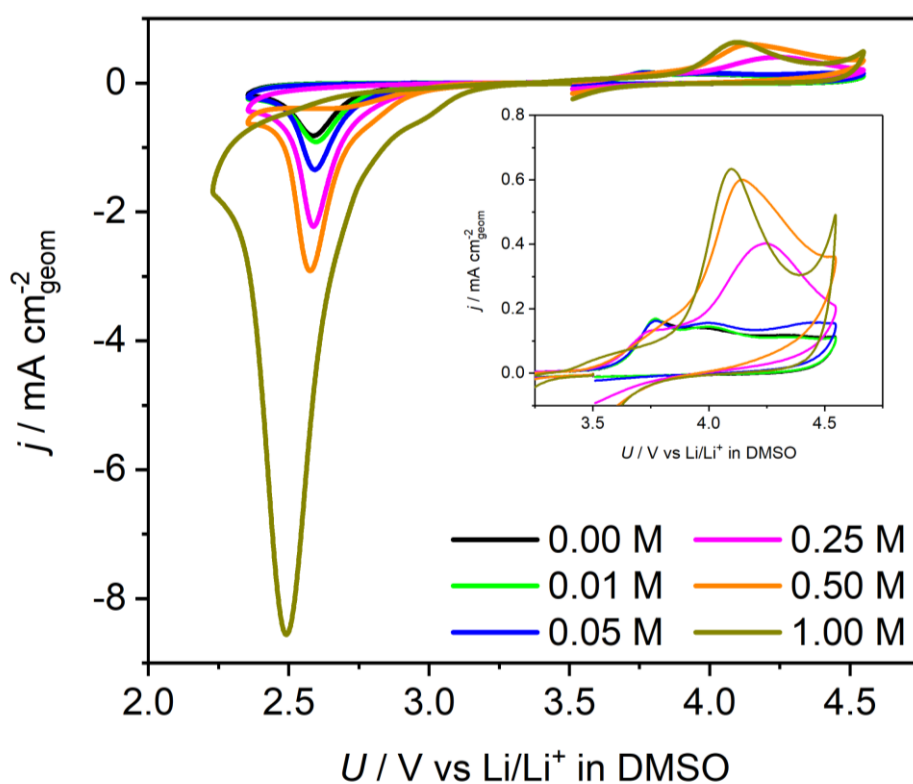


Figure 4.3: CVs recorded in CH₃CN showing the rapid increase in $i_{P,red}$ as the H₂O concentration is increased. Inset shows an expanded view of the oxidation peaks. The electrolyte was O₂-saturated 0.25 M LiClO₄ in CH₃CN with H₂O concentrations as indicated in the legend. The scan rate was 100 mV s⁻¹. Au working, Li_xFePO₄ reference and Pt counter electrodes were used.

Furthermore, the Coulombic efficiency ($Q_{\text{ox}}/Q_{\text{red}}$) of the $\text{O}_2/\text{Li}_2\text{O}_2$ redox couple decreases as the H_2O concentration increases (Table 4.1), indicating that an increasing proportion of O_2 reduction products are not oxidised. If H_2O acts as a phase-transfer catalyst, as suggested by Schwenke *et al.*³, solid Li_2O_2 would be converted to H_2O_2 . This should promote both the reduction of O_2 and the oxidation of $\text{Li}_2\text{O}_2/\text{H}_2\text{O}_2$. However, this is not the case, as O_2 reduction is enhanced much more than oxidation of the discharge product, suggesting that LiOH forms on reduction, as it cannot be oxidised at the potentials used here. While the CVs indicate that H_2O alters the discharge product from Li_2O_2 to LiOH , other experimental techniques are required to confirm this. Therefore, RRDE and surface-enhanced Raman spectroscopy (SERS) were used to identify the O_2 reduction products and are discussed in Sections 4.4 and 4.6, respectively.

Table 4.1: The Coulombic efficiency ($Q_{\text{ox}}/Q_{\text{red}}$) of the $\text{O}_2/\text{Li}_2\text{O}_2$ redox couple decreases as the H_2O concentration increases. Values for the charge passed on reduction and oxidation, Q_{red} and Q_{ox} , were obtained from the CVs in Figure 4.3.

H_2O concentration / M	Q_{red} / mC	Q_{ox} / mC	$Q_{\text{ox}}/Q_{\text{red}}$
0.00	0.1562	0.08918	0.57093
0.01	0.1824	0.09787	0.53657
0.05	0.2302	0.1053	0.45743
0.25	0.3782	0.1827	0.48308
0.50	0.6535	0.2432	0.37215
1.00	1.9760	0.2348	0.11883

O_2 reduction in DMSO is completely different to CH_3CN . Figure 4.4 shows O_2 electrochemistry in the presence of various H_2O concentrations between 0 M and 5 M. The first reduction peak ($E_{\text{p,red1}}$) forming O_2^- occurs at ~ 2.5 V and only shifts positively at H_2O concentrations >1 M. This is to be expected, based on the response in the TBA^+ -based electrolyte since, in both cases, O_2^- exists as an ion in solution. When the H_2O concentration is >1 M, the onset of $E_{\text{p,red1}}$ shifts positively, as in the TBA^+ -based

electrolyte, again indicating that the proton-coupled O_2 reduction to form HO_2 now occurs,

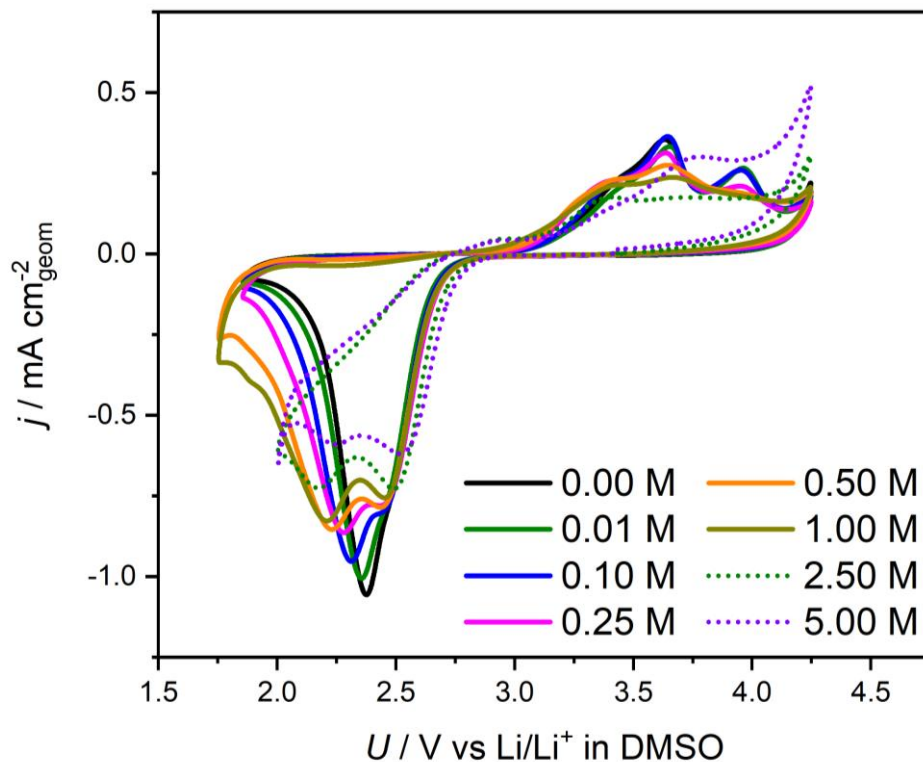
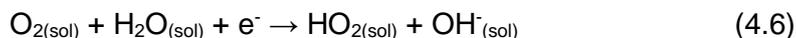
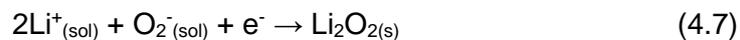


Figure 4.4: CVs recorded in DMSO demonstrating that H_2O concentrations ≤ 1 M do not affect the generation of O_2^- , but shift the second electrochemical reduction step to Li_2O_2 negatively. Dashed CVs indicate H_2O concentrations where proton-coupled O_2 reduction occurs. The electrolyte was O_2 -saturated 0.25 M $LiClO_4$ in DMSO with H_2O concentrations as indicated in the legend. The scan rate was 100 mV s^{-1} . Au working, Li_xFePO_4 reference and Pt counter electrodes were used.

The potential of the second reduction peak ($E_{P,red2}$) to form Li_2O_2 (Equation 4.7) shifts negatively as the H_2O concentration is increased (Figure 4.4). It initially occurs at ~ 2.37 V, almost overlaying $E_{P,red1}$, but the addition of H_2O gradually shifts $E_{P,red2}$ negatively, such that at 1 M H_2O , $E_{P,red2}$ now occurs at 2.21 V, making the two peaks easily resolved visually. The Nernst equation (Equation 4.8) stipulates that the negative shift in $E_{P,red2}$ is

due to changes in the activity of the chemical species involved, *i.e.* an increase in activity of Li_2O_2 , a decrease in activity of O_2^- ($a_{\text{O}_2^-}$) and/or Li^+ (a_{Li^+}), or a combination of these.



$$E = E^0 - \frac{RT}{nF} \ln \frac{a_{\text{red}}}{a_{\text{ox}}} \quad (4.8)$$

As Li_2O_2 is a pure substance, its activity is unity, so changes to $a_{\text{O}_2^-}$ and/or a_{Li^+} must account for the shift in $E_{\text{P,red2}}$. As in the TBA⁺-based electrolyte, O_2^- and HO_2 are in equilibrium, which lowers the O_2^- concentration, and therefore $a_{\text{O}_2^-}$. However, changes to a_{Li^+} may also contribute. It is reasonable to expect that Li^+ will interact with H_2O molecules, since Li^+ is a strong Lewis acid and H_2O is a strong Lewis base. Solvation of Li^+ by H_2O would mean Li^+ is more stable, *i.e.* a_{Li^+} is lowered. The solvation environment of Li^+ can be qualitatively probed using ^7Li NMR. An increasing chemical shift (δ) indicates increased solvation strength of Li^+ by H_2O . Figure 4.5 shows that as the H_2O concentration increases from 0 M to 5 M, the ^7Li δ increases monotonically, indicating that H_2O does solvate and stabilise Li^+ . Therefore, the negative shift of $E_{\text{P,red2}}$ as the H_2O concentration increases is caused by both a drop in the activity of O_2^- and Li^+ , due to formation of HO_2 and solvation by H_2O , respectively.

On oxidation, three peaks are seen in the dry electrolyte (Figure 4.4). There is relatively little change to the oxidation peaks as the H_2O concentration is increased. Of the three oxidation peaks, the two at higher potentials decrease up to 2.5 M H_2O . This may be due to changes in the morphology of Li_2O_2 particles formed, altering the proportion of different Li_2O_2 surfaces able to oxidise at different potentials. At 5 M H_2O , a substantial change to the oxidation peaks occurs, which now appear to consist of two peaks before the onset of electrolyte degradation at the positive limit of the potential window. This suggests a more significant change to the nature of the reduction products formed on the electrode.

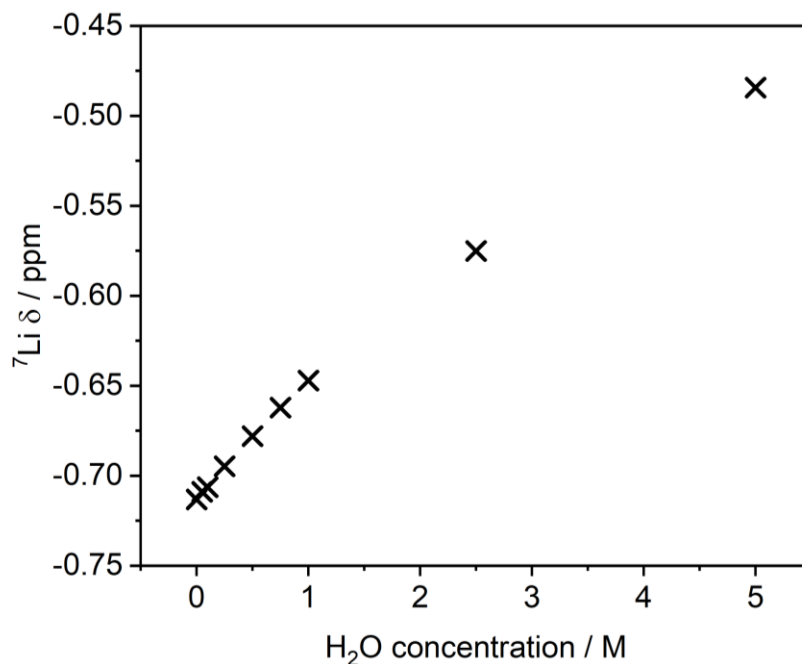


Figure 4.5: ${}^7\text{Li}$ δ of 0.25 M LiClO_4 in H_2O -containing DMSO showing that the chemical shift increases with H_2O concentration, indicating greater Li^+ solvation. Spectra are referenced with respect to 1 M LiCl in D_2O ($\delta = 0$ ppm).

However, as with CH_3CN , one can only speculate with CV data alone, and therefore, RRDE and SERS measurements were performed to identify how H_2O alters the O_2 reduction products and are discussed in Sections 4.4 and 4.6, respectively.

4.4. Identification of reaction pathways in solvent/ H_2O mixtures

As multiple O_2 reduction reactions could occur in the presence of H_2O , the RRDE measurements from Section 3.4 were repeated in the Li^+ -based electrolytes to identify which O_2 reduction products form.

The presence of Li^+ alters the RRDE polarisation curves significantly compared to those in TBA^+ -based electrolytes. This is because Li_2O_2 deposits on the disk electrode and passivates it as the cathodic sweep progresses, so reduction peaks rather than steady state plateaus are observed. Furthermore, detection of soluble O_2^- at the ring is solvent-dependent; very little, if any, ring current is expected in CH_3CN (low DN solvent), but in DMSO (high DN solvent), O_2^- should be detected at the ring electrode.

Using the same protocol as in Section 3.4, these experiments allowed quantification of the amount of soluble $1e^-$ reduction products (O_2^- and HO_2^-) and provided a qualitative indication of soluble $2e^-$ reduction products (H_2O_2 , $LiOOH$ and HO_2^-). These correspond to the blue and red shaded areas, respectively, in Figures 4.5-4.10. The green shaded areas consist of further $2e^-$ reduction products and the $4e^-$ product ($LiOH$), in addition to solid Li_2O_2 formed on the disk. This complicates analysis of any changes to the green shaded areas but can be overcome by assuming that the green shaded areas in the dry electrolytes corresponds to solid Li_2O_2 and will not change with H_2O concentration. Therefore, any increase to the green shaded area can be attributed to additional $2e^-$ and $4e^-$ reduction reactions occurring *i.e.* additional formation of H_2O_2 , $LiOOH$, HO_2^- and/or $LiOH$. As in Chapter 3, Au and glassy carbon (GC) disk electrodes were used to identify whether the electrode material plays any role in catalysing the $2e^-$ or $4e^-$ reactions in the presence of H_2O . Furthermore, in Li- O_2 cells, the positive electrode is typically made from various types of carbon, so RRDE measurements using a GC electrode will more closely replicate the reactions occurring in such cells. In the following discussion, the trends as a function of H_2O concentration using each electrode are first addressed individually before being compared.

The effect of H_2O on CH_3CN with a Au disk is considered first (Figure 4.6). In the dry electrolyte (Figure 4.6a), there is negligible solubility of O_2^- (blue shaded area) and almost all the current at the disk goes towards forming surface-bound Li_2O_2 (green shaded area). As the H_2O concentration is steadily increased (Figure 4.6b-d), the overall disk current increases significantly, consistent with the voltammograms in Section 4.3. However, RRDE allowed identification of the cause of the increased reduction current. Very little of the $1e^-$ and $2e^-$ reduction products were detected at the three H_2O concentrations used (0.05 M, 0.25 M and 1 M H_2O), so the increased current is attributed to the formation of the $4e^-$ product, $LiOH$. The fact that very little of the $2e^-$ products are detected (red shaded areas), suggests that the majority of the increase in the green

shaded area is mostly due to the formation of OH^- . This is consistent with the RRDE results in Chapter 3, where addition of 1 M H_2O led to OH^- becoming the dominant product.

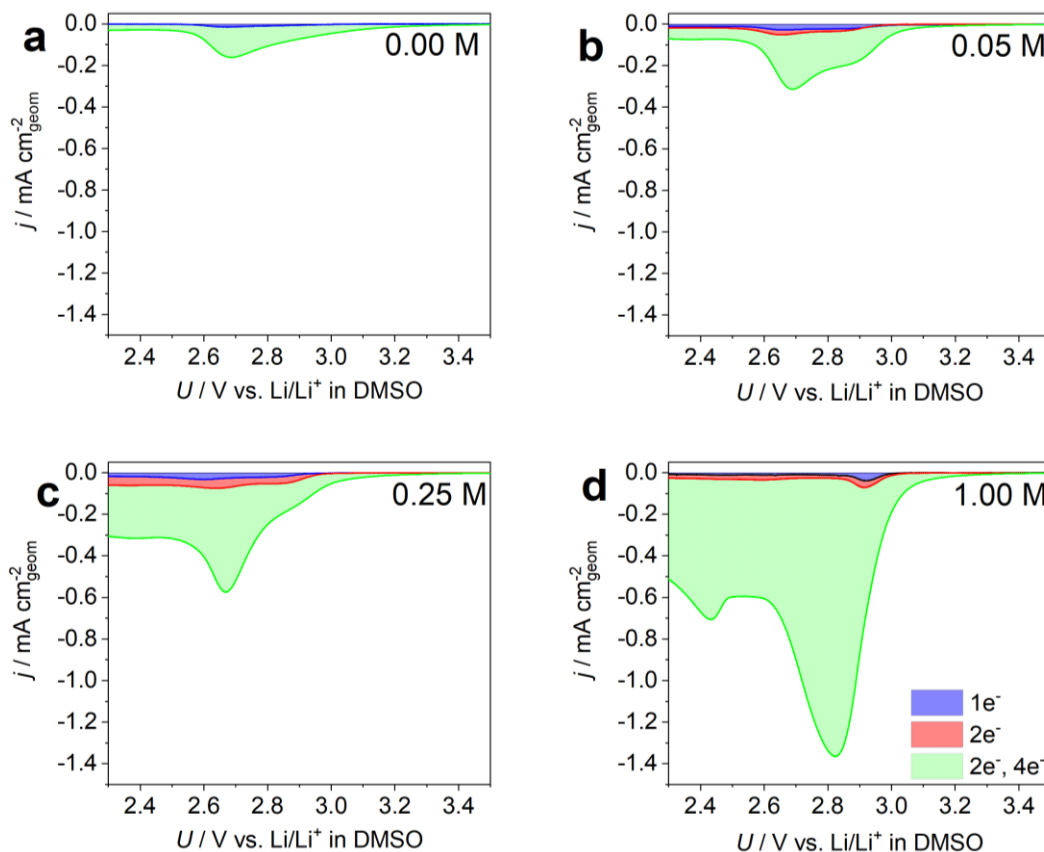


Figure 4.6: RRDE polarisation curves using a Au disk in CH_3CN showing that the significant increase in disk current is due to $4e^-$ O_2 reduction products. The blue shaded area indicates current passed due to the $1e^-$ products, the red area is due to the $2e^-$ products and the green area is due to further $2e^-$ products and the $4e^-$ product. The electrolytes were O_2 -saturated and contained 0.25 M LiClO_4 and H_2O concentrations as indicated on plots. Ring potentials for $1e^-$ (blue trace) and $2e^-$ (red trace) O_2 reduction products were 3.75 V and 4.3 V, respectively. 5 mm Au working, Pt ring, Li_xFePO_4 and Pt counter electrodes were used. The scan rate and rotation rate were 20 mV s^{-1} and 1000 rpm, respectively.

When a GC electrode was used (Figure 4.7), the same general trends are observed, with negligible LiO_2 solubility in the dry electrolyte and rapidly increasing disk currents as the H_2O concentration increases.

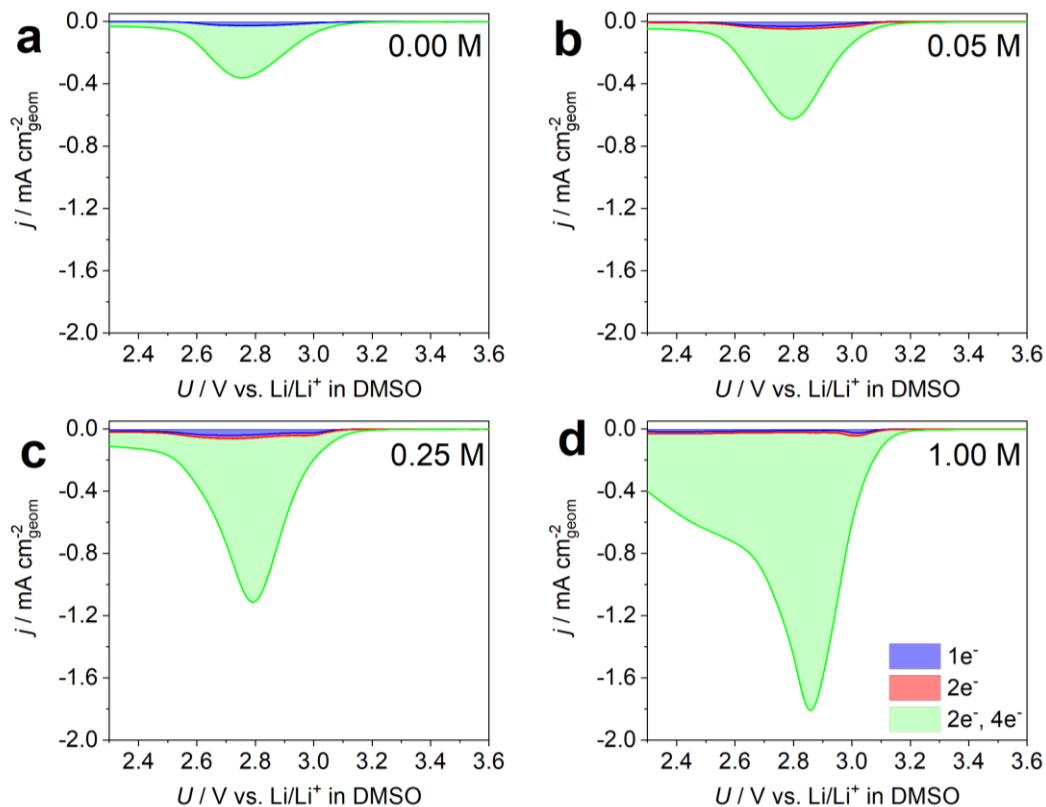


Figure 4.7: RRDE polarisation curves using a GC disk in CH_3CN showing near identical behaviour to the Au RRDE plots, demonstrating that these effects are intrinsic to the electrolyte and not the electrode substrate. The blue shaded area indicates current passed due to the $1e^-$ products, the red area is due to the $2e^-$ products and the green area is due to further $2e^-$ products and the $4e^-$ product. The electrolytes were O_2 -saturated and contained 0.25 M LiClO_4 and H_2O concentrations as indicated on plots. Ring potentials for $1e^-$ (blue trace) and $2e^-$ (red trace) O_2 reduction products were 3.75 V and 4.3 V, respectively. 5 mm GC working, Pt ring, Li_xFePO_4 and Pt counter electrodes were used. The scan rate and rotation rate were 20 mV s^{-1} and 1000 rpm, respectively.

For example, the peak disk current with 1 M H₂O in the electrolyte is over five-fold larger than in the dry electrolyte. Furthermore, almost no soluble 1e⁻ or 2e⁻ species are detected at the ring as the H₂O concentration increases, identifying that this increased current is due to the 4e⁻ product, which is in agreement with the results using the Au electrode.

There are two main differences between the Au and GC results. The first is that with a GC disk, almost no 1e⁻ and 2e⁻ reduction products form, compared to Au, where they are a minor contribution, but non-negligible, contribution to the disk current. The second difference is the prominence of a peak at ~2.4 V, which is more obvious with the Au electrode than the GC. Both of these differences are likely caused by the differences in the catalytic activity of Au and GC towards the various O₂ reduction products.

In DMSO (Figure 4.8), on a Au electrode in the dry electrolyte, there is significant O₂⁻ solubility, which can be detected at the ring electrode (blue shaded area, Figure 4.8a). This delays passivation of the disk and allows a much larger overall charge to be passed at the disk compared to CH₃CN. At all H₂O concentrations reported here no difference in the ring response was observed between the two oxidising potentials used, indicating no formation of H₂O₂. Therefore, for clarity, the red trace is omitted. At 0.25 M H₂O (Figure 4.8b), there is a significant increase in O₂⁻ (blue shaded area) and little change to the green shaded area, indicating that the Li₂O₂ passivating layer still forms, but at a potential ~100 mV more negative. The broadening of the O₂⁻ peak is due to stabilisation of the LiO₂ intermediate in solution, as discussed in Section 4.3, where E_{P₂,red} was seen to shift negatively. When the H₂O concentration is increased to 1 M (Figure 4.8c), the O₂⁻ peak further broadens, but a shoulder is now visible below 2.4 V, and the green shaded area has increased significantly. The shoulder indicates a loss of O₂⁻, implying that some OH⁻ forms at these, more negative, potentials. This is more clearly seen with 5 M H₂O in the electrolyte (Figure 4.8d), as there is an obvious reduction in the blue shaded area, while the green shaded area increases further. This loss of O₂⁻ indicates that OH⁻ forms a significant proportion of the O₂ reduction products at potentials <2.5 V.

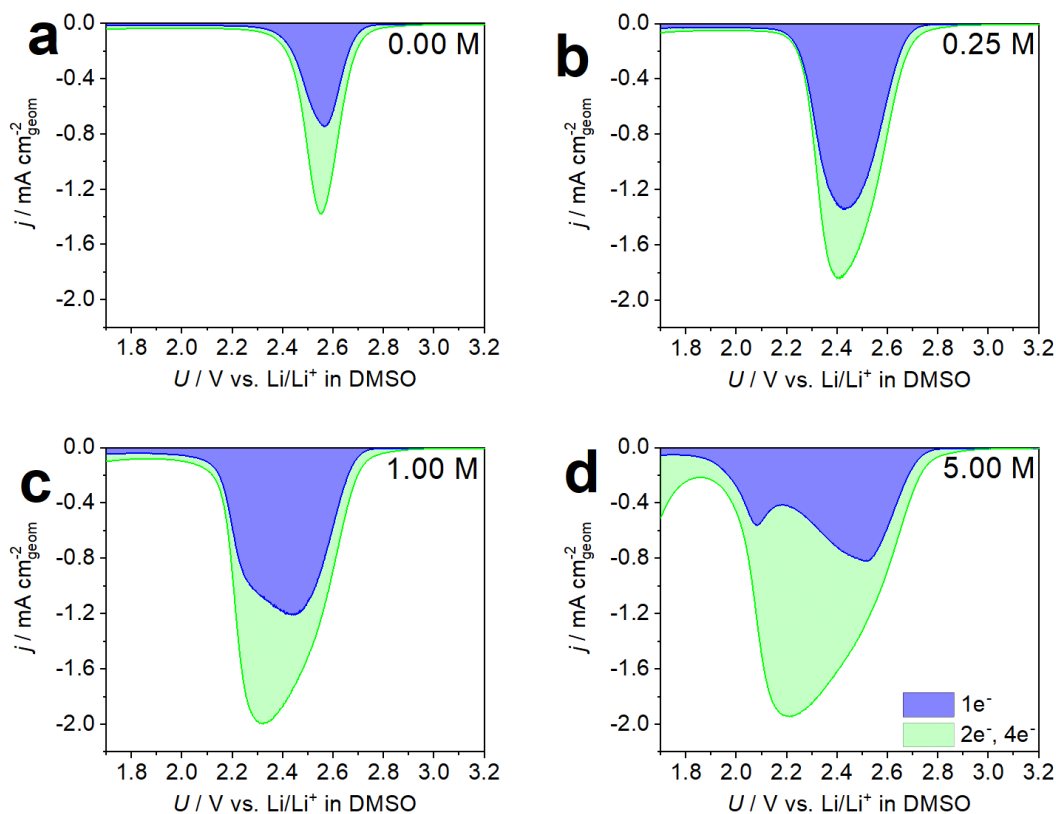


Figure 4.8: RRDE polarisation curves using a Au disk in DMSO showing that LiO_2 solubility is enhanced by H_2O up to 1 M H_2O and that above this concentration, $4e^-$ reduction products form. The blue shaded area indicates current passed due to the $1e^-$ products and the green area is due to the insoluble $2e^-$ product and the $4e^-$ product. The electrolytes were O_2 -saturated and contained 0.25 M LiClO_4 and H_2O concentrations as indicated on plots. The ring potential for $1e^-$ (blue trace) O_2 reduction products was 3.75 V. 5 mm Au working, Pt ring, Li_xFePO_4 and Pt counter electrodes were used. The scan rate and rotation rate were 20 mV s^{-1} and 1000 rpm, respectively.

The same overall trends are seen when a GC electrode is used (Figure 4.9). Again, no soluble $2e^-$ species are detected so the red trace is omitted for clarity. In the dry electrolyte there is significant O_2^- solubility (blue shaded area, Figure 4.9a), which is enhanced as the H_2O concentration is increased to 0.25 M. This peak broadens at 1 M H_2O , before decaying significantly at 5 M H_2O . This follows the same pattern as the Au electrode, where the stabilisation of the LiO_2 intermediate is enhanced up to 1 M H_2O , at

which point the $4e^-$ reduction begins to occur, and becomes more prominent when the H_2O concentration increases further.

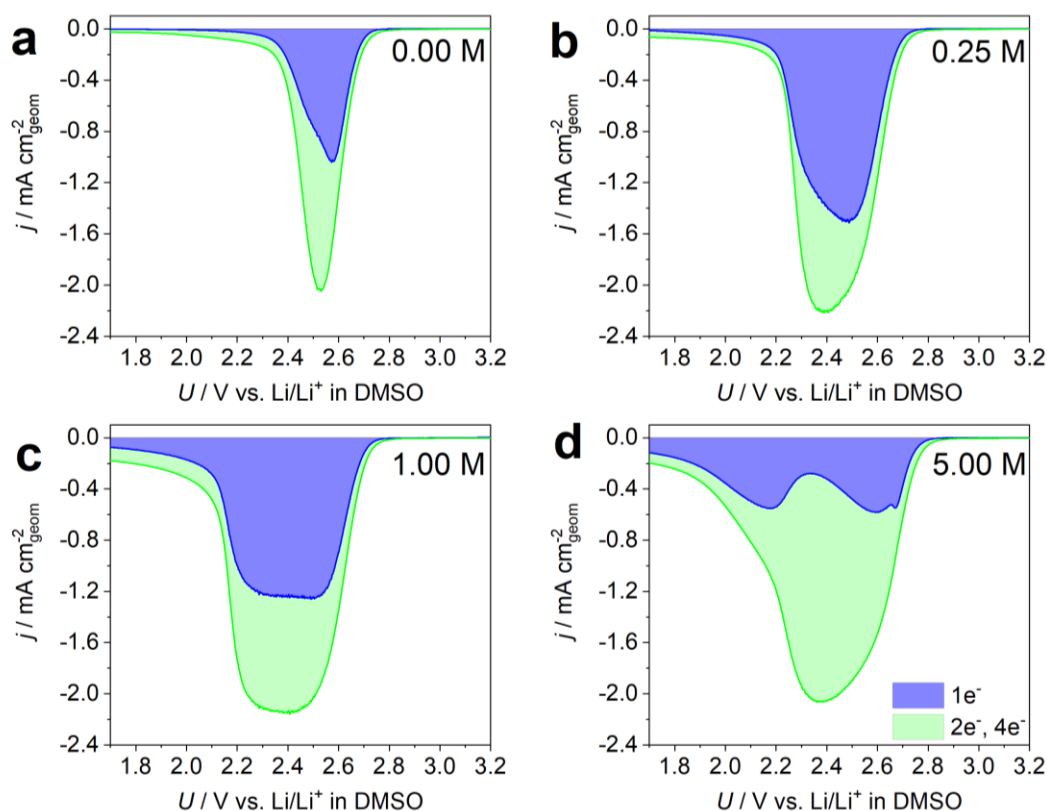


Figure 4.9: RRDE polarisation curves using a GC disk in DMSO showing near identical behaviour to the Au RRDE plots, demonstrating that these effects are intrinsic to the electrolyte and not the electrode substrate. The blue shaded area indicates current passed due to the $1e^-$ products and the green area is due to insoluble Li_2O_2 and the $4e^-$ product. The electrolytes were O_2 -saturated and contained 0.25 M $LiClO_4$ and H_2O concentrations as indicated on plots. The ring potential for $1e^-$ O_2 reduction products was 3.75 V. 5 mm GC working, Pt ring, Li_xFePO_4 and Pt counter electrodes were used. The scan rate and rotation rate were 20 mV s^{-1} and 1000 rpm, respectively.

There was no significant difference between the Au and GC data. The broadening of the $1e^-$ peak is more obvious with the GC electrode at 1 M, again, likely to be due to

differences in the catalytic activity of Au and GC electrodes towards $1e^-$ and $4e^-$ O_2 reduction.

An interesting feature in the 5 M H_2O RRDE plots is a small increase in the O_2^- peak at approximately 2.1 V (Figures 4.8d and 4.9d). This feature occurs on both Au and GC electrodes, suggesting a process that is intrinsic to O_2 reduction, which occurred precisely when the total disk current rapidly decays, *i.e.* when passivation of the disk occurs. This unexpected increase in O_2^- formation was attributed to loss of the directly exposed electrode surface. Once the Au or GC surface is covered by at least a monolayer of Li_2O_2 , its ability to catalyse the $4e^-$ reduction will be significantly diminished. However, the Li_2O_2 film will still be thin and therefore conductive enough to support O_2 reduction, so O_2^- will form a larger proportion of the products, hence the increase in O_2^- detected at the ring relative to the overall current.

To summarise the behaviour in DMSO, addition of H_2O concentrations up to and including 1 M is beneficial to $2e^-$ O_2 reduction by stabilising the LiO_2 intermediate, which causes reduction of LiO_2 to occur at lower potentials, delaying passivation of the electrode. Furthermore, LiO_2 solubility is increased, allowing LiO_2 to diffuse away from the electrode, rather than chemically disproportionating, which would also lead to passivation of the electrode. With 5 M H_2O present, the formation of significant amounts of $LiOH$ occurs.

CH_3CN and DMSO were chosen as solvents because the surface and solution O_2 reduction mechanisms could be probed individually, but these results show that the solvent plays a crucial role in determining which O_2 reduction products form. Therefore, O_2 reduction in TEGDME was also analysed. This solvent is one of a family of glyme ethers that are used extensively in $Li-O_2$ research and are currently the best commercially-available solvents for $Li-O_2$ batteries. Other groups have reported that H_2O in glyme ethers is beneficial at low H_2O concentrations, typically <5000 ppm, equivalent to approximately $0.3 M^{-3}$. One report suggested that a TEGDME-based electrolyte

containing 30 vol% H₂O (approximately 20 M) still resulted in 2e⁻ O₂ reduction, which is an astonishing and promising result, if it can be replicated⁶.

RRDE experiments with TEGDME were performed (Figure 4.10), since this technique provides information on how O₂ reduction responds to H₂O as well as the nature of the O₂ reduction products and is therefore more useful than CVs alone.

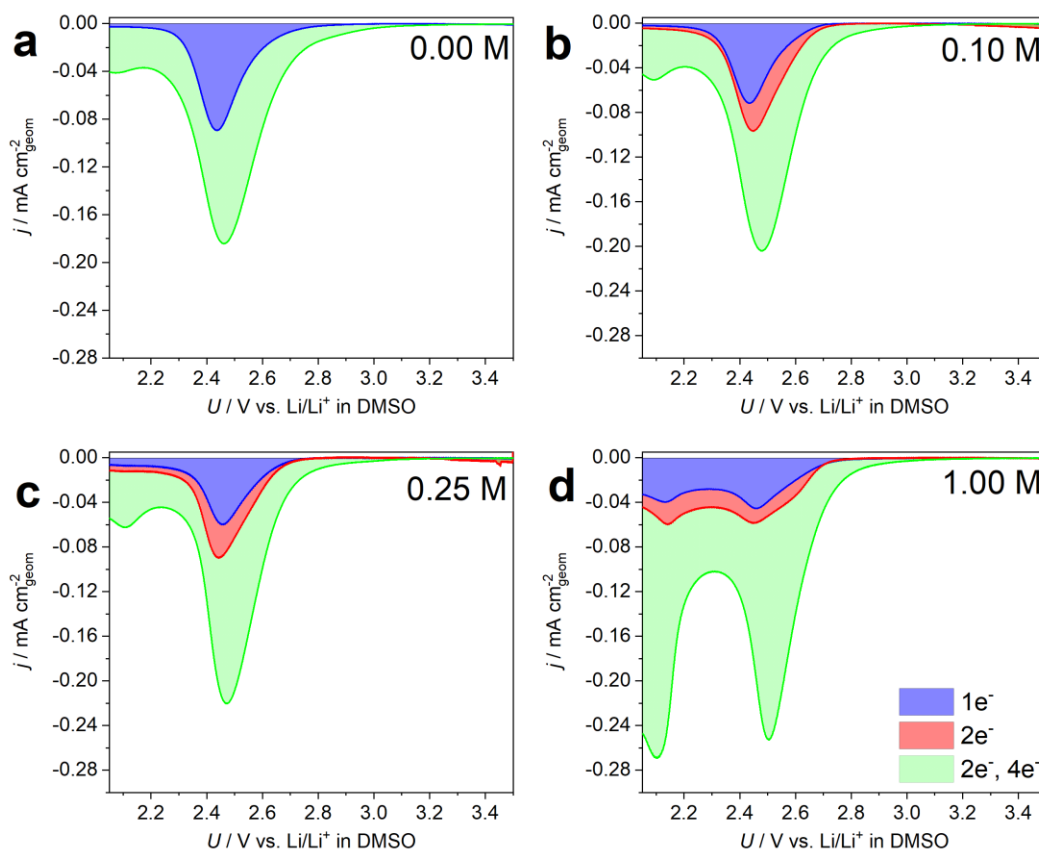


Figure 4.10: RRDE polarisation curves using a Au disk in TEGDME showing that the 4e⁻ reduction occurs at potentials negative of 2e⁻ reduction. The blue shaded area indicates current passed due to the 1e⁻ products, the red area is due to the 2e⁻ products and the green area is due to further 2e⁻ products and the 4e⁻ product. The electrolytes were O₂-saturated and contained 0.25 M LiClO₄ and H₂O concentrations as indicated on plots. Ring potentials for 1e⁻ and 2e⁻ O₂ reduction products were 3.75 V and 4.3 V, respectively. 5 mm Au working, Pt ring, Li_xFePO₄ and Pt counter electrodes were used. The scan rate and rotation rate were 20 mV s⁻¹ and 1000 rpm, respectively.

TEGDME has an intermediate DN of 17¹², so O_2^- has some solubility in the dry electrolyte and an O_2^- peak is seen. As the H_2O concentration is increased from 0 M to 1 M, two main trends can be observed. The first and most obvious is the appearance of a new peak at ~ 2.1 V, which is observed with 0.1 M H_2O (Figure 4.10b). When the H_2O concentration is increased to 0.25 M (Figure 4.10c), this peak increases slightly in magnitude, but at 1 M H_2O (Figure 4.10d), the peak is now much larger, similar in magnitude to the peak at 2.5 V. This peak is attributed to the $4e^-$ reduction product, LiOH, for two reasons. It increases in magnitude as the H_2O concentration is increased. Furthermore, it occurs at negative potentials, consistent with the appearance of the OH^- peak in both CH_3CN and DMSO.

The second trend is an increase in the disk current of the peak at ~ 2.5 V, which is not accompanied by a similar increase in the O_2^- or H_2O_2 detected at the ring. This would suggest that the increasing current results from the $4e^-$ reduction. However, I have suggested that the peak at ~ 2.1 V is due to the $4e^-$ reduction. It is likely that the disk current of the 2.5 V peak increases due to the formation of soluble $2e^-$ reduction products as the H_2O concentration is increased, but these products should, therefore, be detected at the ring. This is not the case and is likely caused by the oxidation potential of H_2O_2 shifting positively, in a similar way to the $4e^-$ reduction seen in DMSO. Since only a portion of the $2e^-$ reduction products are oxidised at the ring potential used (4.3 V), which remains constant for each H_2O concentration, a positive shift in the oxidation potential of H_2O_2 would reduce the proportion of H_2O_2 detected at the ring.

A similar trend was observed when a GC disk was used (Figure 4.11). As the H_2O concentration was increased, the $1e^-$ and $2e^-$ reduction products detected by the ring remained approximately constant, while the green shaded area corresponding to $4e^-$ reduction increased in area. Additionally, the peak observed at ~ 2.1 V using the Au RRDE is absent here. It is possible that the $4e^-$ O_2 reduction occurs at potentials beyond the negative limit used here. To confirm that the $4e^-$ reduction occurs at 2.1 V and is not

responsible for changes to the peak at 2.5 V on both Au and GC electrode requires an alternative method of quantifying the electrochemical reactions during reduction. This is addressed in Chapter 5.

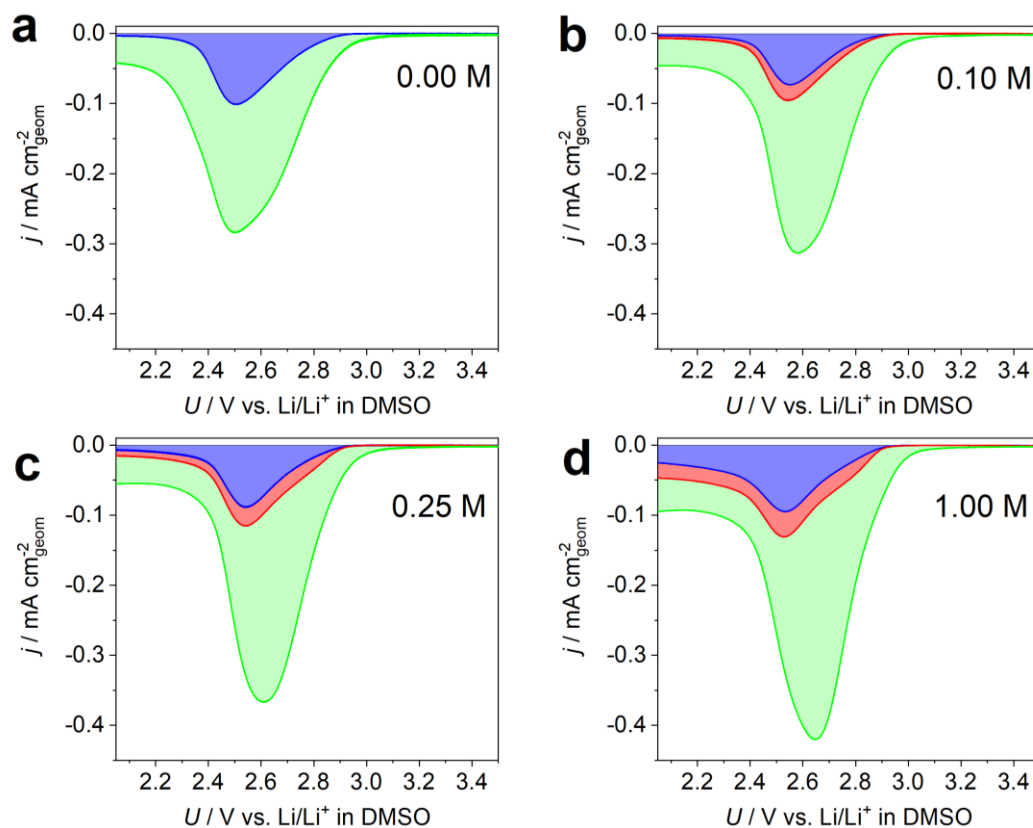
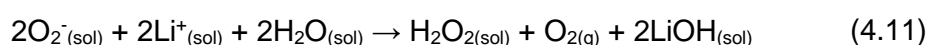
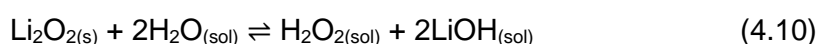
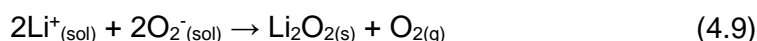


Figure 4.11: RRDE polarisation curves using a GC disk in TEGDME showing near identical behaviour to the Au RRDE plots, demonstrating that these effects are intrinsic to the electrolyte and not the electrode substrate. The blue shaded area indicates current passed due to the $1e^-$ products, the red area is due to the $2e^-$ products and the green area is due to further $2e^-$ products and the $4e^-$ product. The electrolytes were O_2 -saturated and contained 0.25 M $LiClO_4$ and H_2O concentrations as indicated on plots. Ring potentials for $1e^-$ and $2e^-$ O_2 reduction products were 3.75 V and 4.3 V, respectively. 5 mm GC working, Pt ring, Li_xFePO_4 and Pt counter electrodes were used. The scan rate and rotation rate were 20 mV s^{-1} and 1000 rpm, respectively.

4.5. Chemical routes to protic O₂ reduction products from O₂⁻ and H₂O

The results presented so far in this chapter identify the conditions under which Li₂O₂ and LiOH are formed electrochemically. However, as discussed in Chapter 3, it could be possible for the 4e⁻ product to form via a chemical route, with reactions analogous to those presented in Chapter 3. There, TBA⁺ was a spectator ion, so could be excluded from the reaction scheme. However, Li⁺ has been explicitly included here since it participates in the reactions. It is known that if O₂⁻ is mixed with a solution of a Li⁺-based salt in an organic solvent, e.g. LiClO₄ in DMSO, Li⁺ reacts with O₂⁻, forming Li₂O₂ and evolving O₂ (4.9). If H₂O is present, Li₂O₂ can then react to form H₂O₂ (4.10). Alternatively, O₂⁻ could react with H₂O to form H₂O₂ directly (4.11). Overall, it is inconsequential for the Li-O₂ battery whether Li₂O₂ or H₂O₂ forms, since they are equivalent peroxide species that interconvert via Equation 4.10. However, disproportionation of O₂⁻ to LiOH in the presence of both Li⁺ and H₂O (4.12) is undesirable, due to the difficulty in oxidising LiOH. Therefore, it is important to identify whether this can occur.



As in Chapter 3, the molar ratio of O₂ to O₂⁻ for disproportionation to peroxo-species (H₂O₂, LiOOH and/or Li₂O₂) and LiOH are 0.5 and 0.75, respectively. An online mass spectrometer was used to measure the quantity of O₂ evolved from samples of KO₂ mixed with electrolytes containing 0 M, 1 M and 5 M H₂O and Figure 4.12 shows the molar ratio of O₂ evolved to KO₂ in the sample initially. In all cases, the ratios lie between 0.4 and 0.5, demonstrating that O₂⁻ disproportionates only to peroxide species and that the formation of LiOH identified using RRDE is exclusively electrochemical. The

deviation from the ideal value of 0.5 is experimental as there will be errors in the quantity of KO_2 and the O_2 evolution measured with the mass spectrometer.

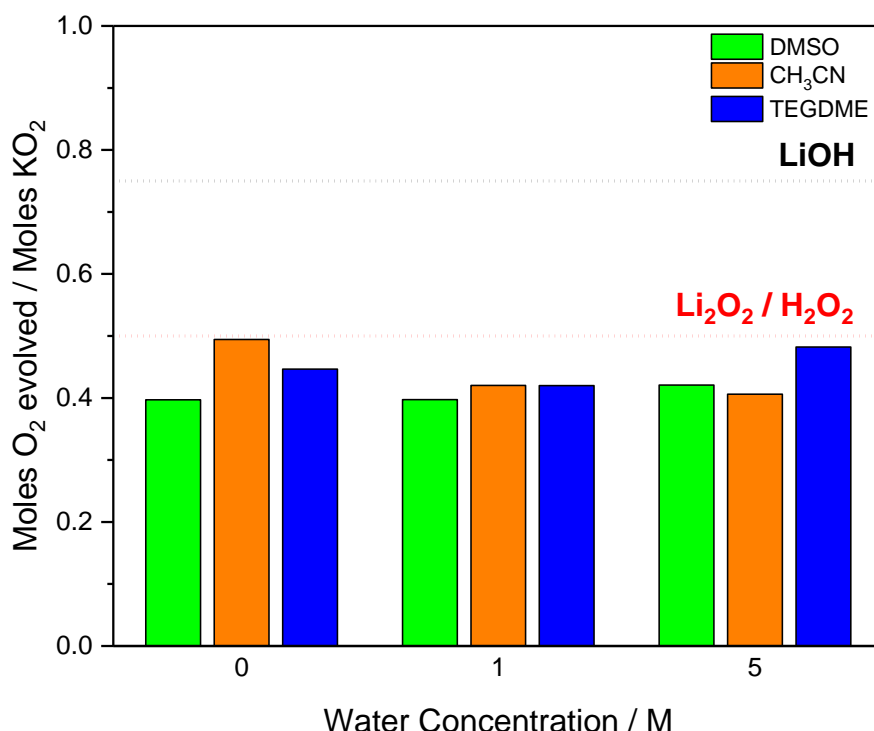


Figure 4.12: O_2/O_2^- ratios demonstrating O_2^- disproportionates to peroxide species when H_2O -containing electrolytes are added. The electrolytes were 0.25 M LiClO_4 in DMSO (green bars), CH_3CN (orange bars) and TEGDME (blue bars). The quantity of O_2 evolved was determined using an online mass spectrometer. Dashed red and black lines indicate the ratios expected for disproportionation to peroxide and hydroxide species, respectively.

4.6. Spectroscopic identification of ORR intermediates/products

The electrochemical analyses discussed thus far provide indirect evidence for the O_2 reduction species forming in H_2O -containing electrolytes. As in Chapter 3, SERS measurements were used to complement the electrochemical analyses and attempted to identify the O_2 reduction products now in Li^+ -based electrolytes. It was not, however, possible to perform SERS measurements with TEGDME, as the solvent has Raman bands that overlap with signals from O_2 reduction intermediates and products, making

interpretation of the spectra very challenging. Therefore, the following discussion concerns results obtained in CH_3CN and DMSO.

In CH_3CN , the reducing potential applied was 2.4 V, negative of the reduction peak. This potential was required to generate sufficient concentration of O_2 reduction species at the electrode to acquire signals, particularly in the dry electrolyte. Figure 4.13 shows the surface-enhanced Raman (SER) spectra in CH_3CN -based electrolyte at four H_2O concentrations, chosen in order to identify the products that form as O_2 reduction shifts from the aprotic mechanism to the protic mechanism.

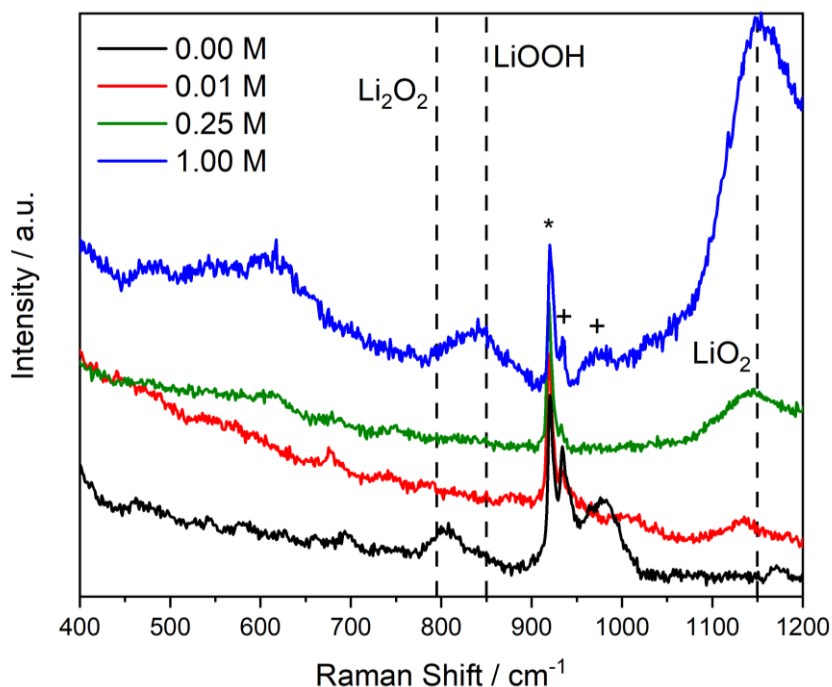


Figure 4.13: SER spectra acquired in CH_3CN showing the generation of LiO_2 in H_2O -containing electrolytes despite a large overpotential, while in the dry electrolyte only Li_2O_2 is detected. Dashed lines indicate the Raman shifts of O_2 reduction products. The electrolytes were O_2 -saturated 0.25 M LiClO_4 in CH_3CN and containing H_2O concentrations as indicated in the legend. Spectra were acquired whilst holding a constant potential of 2.2 V and 2.35 V at the Au electrode in DMSO and CH_3CN , respectively. A 785 nm laser, x20 objective and 1200 l/mm grating were used. * and + indicate solvent and salt peaks, respectively (reference values in Appendix 2).

In the dry electrolyte (black trace), a signal due to Li_2O_2 at $\sim 800\text{ cm}^{-1}$ is seen, but no LiO_2 is detected, as the low applied potential means LiO_2 cannot build-up on the electrode surface and is instead quickly reduced to Li_2O_2 . When 0.01 M H_2O is present (red trace), the signal due to Li_2O_2 disappears and a peak is now observed at $\sim 1130\text{ cm}^{-1}$, in the region where LiO_2 and HO_2 signals occur. These changes are most likely due to solubilisation of Li_2O_2 that forms on the electrode. Any Li_2O_2 that forms on the electrode would be removed as H_2O_2 or LiOOH and allows the $1e^-$ intermediate to build-up. This peak grows in intensity when the H_2O concentration is increased to 0.25 M (green trace). At a 1 M H_2O concentration (blue trace), the peak at 1130 cm^{-1} has grown significantly in intensity, suggesting that H_2O promotes the formation of a $1e^-$ intermediate species. Given that the final product at this H_2O concentration is LiOH , it is likely that some HO_2 forms in the initial O_2 reduction step, as in the TBA^+ -based electrolytes (Section 3.6, Figure 3.12). Furthermore, a new signal is seen in the peroxo region at $\sim 840\text{ cm}^{-1}$. This is likely due to the LiOOH species, as reported by Qiao *et al.* in TEGDME-based electrolytes, and is an intermediate species that can be further reduced to LiOH ⁶.

In DMSO, the SER spectra (Figure 4.14) were recorded at 2.65 V, which is a low overpotential for O_2^- formation. Therefore, in the dry electrolyte (black trace), signals due to both Li_2O_2 and O_2^- can be seen, as O_2^- is being generated electrochemically, which disproportionates to Li_2O_2 within the timescale of spectrum acquisition. As the H_2O concentration increases, the Li_2O_2 signal progressively decreases in intensity and is barely visible at 5 M H_2O . This is likely due to H_2O stabilising the LiO_2 intermediate to such an extent that disproportionation is negligible. However, the O_2^- signal is seen at all H_2O concentrations, indicating that O_2 reduction always proceeds via a superoxide intermediate.

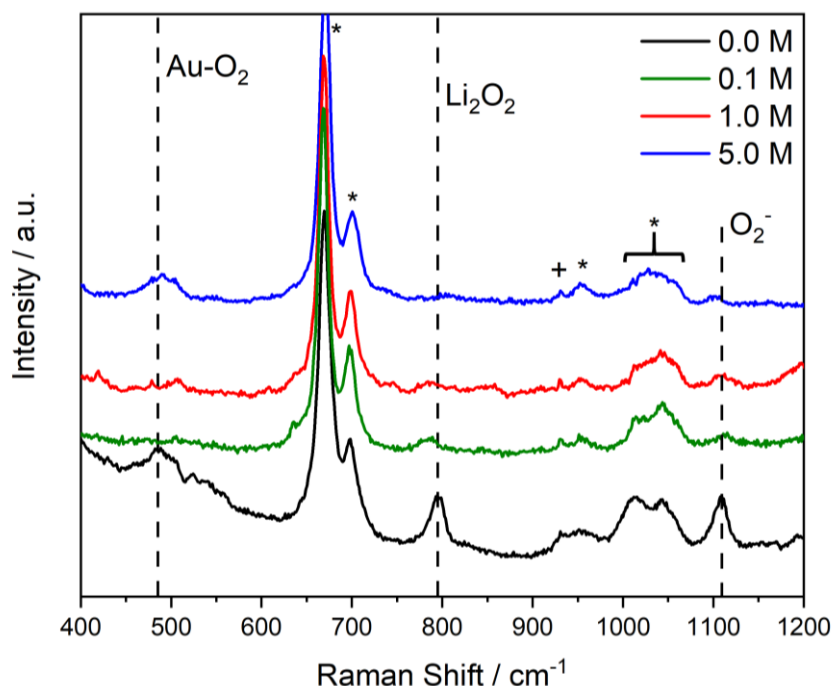


Figure 4.14: SER spectra acquired in DMSO showing that O_2^- is generated even with 5 M H_2O and the loss of the Li_2O_2 signal as the H_2O concentration increases, suggesting it is removed by a metathesis reaction with H_2O . Dashed lines indicate the Raman shifts of O_2 reduction products. The electrolytes were O_2 -saturated 0.25 M LiClO_4 in DMSO and containing H_2O concentrations as indicated in the legend. Spectra were acquired whilst holding the Au electrode at 2.2 V and 2.35 V in DMSO and CH_3CN , respectively. A 785 nm laser, x20 objective and 1200 l/mm grating were used. * and + indicate solvent and salt peaks, respectively (reference values in Appendix 2).

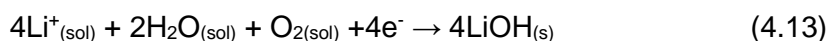
4.7. OH^- formation mechanism in mixed organic solvent/ H_2O electrolytes

The results presented thus far have thoroughly examined the fundamental chemical and electrochemical reactions occurring during O_2 reduction. The key findings have been that in electrolytes using CH_3CN , DMSO and TEGDME as solvents, the $4e^-$ product (OH^-) is only generated electrochemically. Furthermore, the H_2O concentrations and potentials required differ considerably between solvents. However, in all cases, $E_{P,\text{red}}$ for LiOH formation shifts positively as the H_2O concentration increases, but the rate at which this shifts occurs depends profoundly on the solvent. It is therefore evident that the solvents

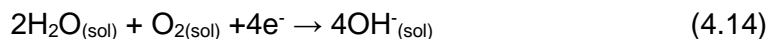
play a crucial role in $4e^-$ reduction of O_2 . I now consider the species with which the solvent interacts to rationalise my observations and propose a mechanism for determining whether OH^- is generated in water-containing organic solvent-based electrolytes.

4.7.1. Solvent effects on the $4e^-$ O_2 reduction reaction

The changes to the onset potential of the $4e^-$ reduction that occur as the H_2O concentration and solvent are varied must be attributed to differences in the relative Gibbs free energy (ΔG) of species in Equation 4.13.



Furthermore, these variations occur both in TBA⁺-based and Li⁺-based electrolytes, so while Li⁺ may contribute to the changes in ΔG , this effect occurs at a more fundamental level. Therefore, understanding changes to the ΔG of species in Equation 4.14 should allow rationalisation of the effect of water on O_2 reduction in organic solvent-based electrolytes.



The ΔG of H_2O is considered first. Determination of ΔG of solvation of H_2O by organic solvent molecules is not trivial, and typically requires computational modelling, which is beyond the scope of the work presented here. However, enthalpies of mixing (ΔH_{mix}) can be used to gauge the degree to which H_2O is stabilised in each solvent. Literature values for ΔH_{mix} of CH_3CN , TEGDME and DMSO are $+0.983 \text{ kJ mol}^{-1}$, $+0.022 \text{ kJ mol}^{-1}$ and $-1.079 \text{ kJ mol}^{-1}$, respectively¹³⁻¹⁵. DMSO readily forms hydrogen bonds (H-bonds) with H_2O , demonstrated by the exothermic enthalpy of mixing. These H-bonds result in the formation of DMSO- H_2O clusters, which has been characterised spectroscopically using soft X-rays¹⁶. It is assumed that H_2O molecules, in CH_3CN and TEGDME, and DMSO- H_2O clusters (at low H_2O concentrations) are randomly distributed, such that the entropy in all three solvents is approximately the same. Thus, changes to ΔG would arise mainly from the enthalpic contribution. For a $4e^-$ reaction, $E_{P,red}$ shifts by $\sim 2.6 \text{ mV}$ for every 1 kJ

mol^{-1} change in ΔG . Since the difference in ΔH_{mix} between CH_3CN and DMSO is approximately 2 kJ mol^{-1} , $E_{\text{P,red}}$ would be expected to shift by only 5 mV. Therefore, solvation of H_2O by the organic solvents plays a very minor part in determining $E_{\text{P,red}}$ of OH^- .

The second species to consider is O_2 , specifically its solubility in each solvent. O_2 solubility in pure CH_3CN , TEGDME, and DMSO is 8.1 mM, 4.43 mM and 2.1 respectively. It is assumed here that the values do not change significantly when H_2O is present at low concentrations ($<1 \text{ M}$). While the solubility does vary, the changes are small and cannot account for the large differences in $E_{\text{P,red}}$ observed.

Since neither H_2O solvation nor O_2 solubility can account for the propensity of OH^- formation in each solvent, solvent effects on the OH^- ion must be considered and this is explored in the following section.

4.7.2. Stabilisation of OH^-

H_2O is likely to interact with OH^- ions if both are present in the organic electrolytes, given the strong hydrogen bonding and proton exchange that occurs between these species. Aetukuri *et al.* proposed that the high AN of H_2O , which is 54.8, could act to stabilise the O_2^- ion generated during aprotic O_2 reduction¹. Whilst results presented in Chapter 3 show that the solvation of O_2^- is negligible, it does highlight the fact that H_2O could stabilise any anion. This includes OH^- , which would shift $E_{\text{P,red}}$ for both the $2e^-$ and $4e^-$ reactions positively, since OH^- is a product in both cases. Furthermore, as the H_2O concentration is increased, the degree of stabilisation of OH^- should increase due to an increasing number of favourable interactions between OH^- and H_2O , explaining the continual increase of $E_{\text{P,red}}$ with H_2O concentration.

However, this does not explain why OH^- forms readily in CH_3CN , but not in DMSO or TEGDME, and is the result of assuming that only H_2O could stabilise OH^- , which neglects the organic solvents. Johnson *et al.* have previously shown that Li^+ solvation is

determined by the Lewis basicity of the solvent, which is measured as the DN¹⁷. Therefore, it is proposed that OH⁻ is stabilised by both H₂O and the organic solvents, but that the Lewis acidities of the organic solvents vary and could account for products in each solvent system, that is, the Lewis acidity of the H₂O/organic solvent mixture determines OH⁻ stabilisation. Therefore, the AN of the three solvents containing H₂O at various concentrations was measured using the method first described by Mayer *et al.*⁸ The method uses the ³¹P δ of a probe molecule, Et₃PO, and a calibration curve is used to convert the value to a number between 0 and 100, with a higher number indicating a stronger Lewis acid. Further experimental details can be found in Chapter 2.

Figure 4.15 shows the ANs in the three solvents as a function of H₂O concentration, with markedly different trends in each solvent. The AN of dry CH₃CN is 19 and as the H₂O concentration increases, the AN steadily rises, reaching a value of 29 at 1 M H₂O, showing that the H₂O-containing CH₃CN is much better at stabilising OH⁻ than dry CH₃CN. The AN of dry DMSO is also 19 but, as the H₂O concentration increases, the AN increases much more slowly, reaching a value of 24 at 1 M H₂O. Dry TEGDME has an AN of 12 and, when H₂O is added, the AN increases rapidly, at a similar rate to CH₃CN. However, since its initial AN was much lower than CH₃CN, the AN is only 23 at 1 M H₂O, slightly lower than that of DMSO. Therefore, H₂O-containing CH₃CN is a much more effective Lewis acid than TEGDME or DMSO and OH⁻ stabilisation should follow the trend TEGDME < DMSO < CH₃CN at H₂O concentrations < 1 M. This is indeed the trend observed for the 4e⁻ reduction product in both TBA⁺-based and Li⁺-based electrolytes. This also explains the results reported by other groups using these solvents and would likely explain why Li₂O₂ forms in other glyme ether solvents. Dry DME and diethylene glycol dimethyl ether also possess low ANs, 10.2 and 9.9, respectively⁸, and the AN would be expected to increase at a similar rate to TEGDME, so their ANs at a 1 M H₂O concentration would be similar to TEGDME, and therefore also poor at stabilising OH⁻.

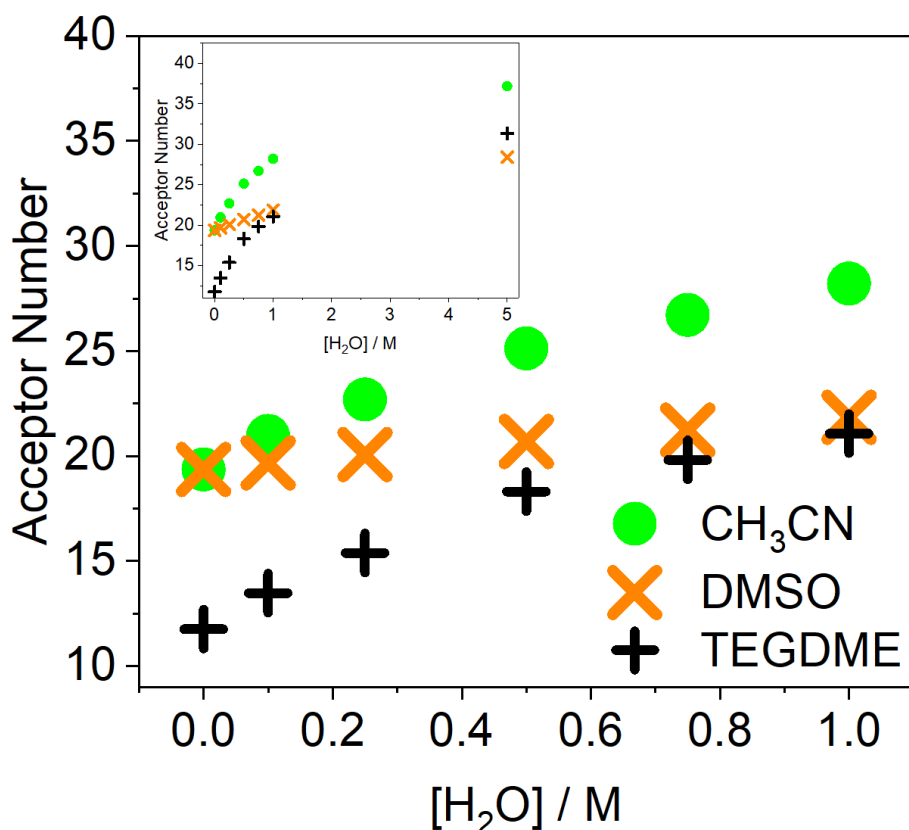


Figure 4.15: A plot showing that the ANs of H₂O/TEGDME and H₂O/DMSO mixtures are lower than H₂O/CH₃CN mixtures for any given H₂O concentration. The inset includes the AN values at 5 M H₂O. ANs were determined using ³¹P NMR of Et₃PO in the solutions and a calibration curve was used to convert the chemical shifts to AN values.

To confirm this mechanism, I sought to characterise OH⁻ stability by alternative means. As the ANs show that OH⁻ stabilisation varies with organic solvent, this should affect not only E_{P,red} for OH⁻ formation, but E_P for any reaction involving OH⁻. This includes the oxidation of Au, which initially forms Au(OH)₃ (Equation 4.15), followed by Au₂O₃ and, at more positive potentials, O₂ evolution¹⁸. The first step in Au oxidation will be controlled by the stability of OH⁻ and the Au surface, specifically the Au facets on the electrode surface. Therefore, the E_{P,ox} for Equation 4.15 should follow the AN trend, TEGDME < DMSO < CH₃CN, as the Nernst equation (Equation 4.8) states that the oxidation will occur at increasingly positive potentials as the activity of OH⁻ is reduced

i.e. as OH^- becomes more stabilised. It should also be noted that the stability of surface facets of Au can also have an effect on $E_{\text{P,ox}}$.

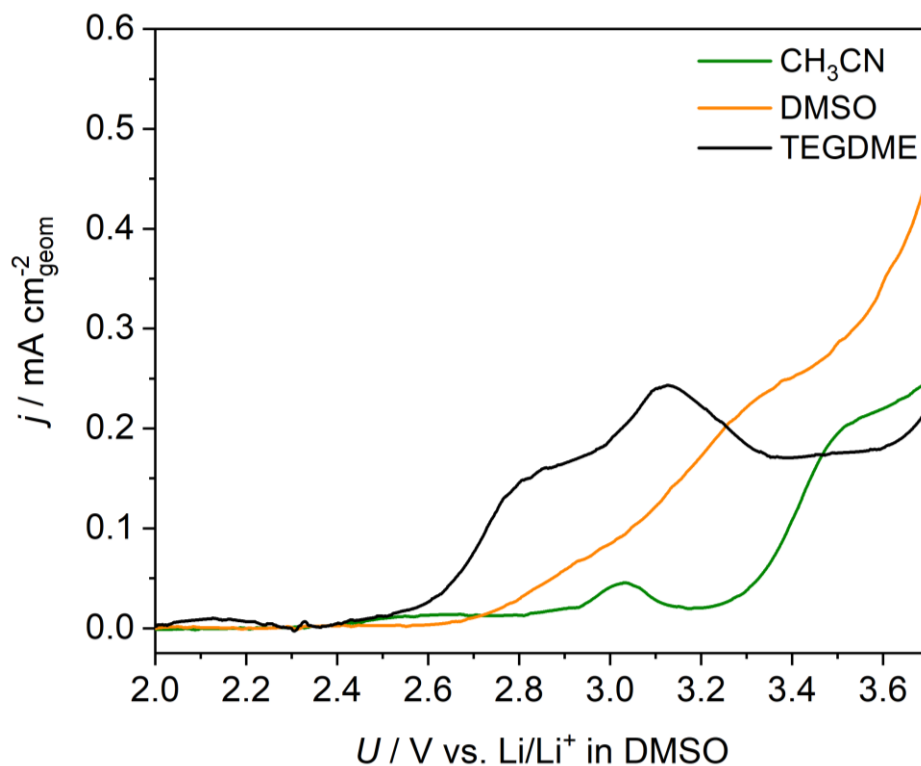
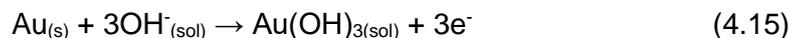


Figure 4.16: Linear sweep voltammograms with a Au microelectrode showing that $E_{\text{P,ox}}$ for Au oxidation to $\text{Au}(\text{OH})_3$ is dependent on the solvent and correlates with the AN trend of the H_2O -containing solvents. The electrolyte consisted of N_2 -saturated 10 mM TBAOH and 1 M H_2O in each solvent, as indicated in the legend. A 25 μm diameter Au microelectrode was used as the working electrode. The reference and counter electrodes were Li_xFePO_4 and Pt, respectively. Scan rate 50 mV s^{-1} .

A Au microelectrode was used to record the oxidation of Au by OH^- in the three solvents containing 10 mM TBAOH and 1 M H_2O . Microelectrodes only pass small currents, typically in the 0.1-10 nA range and, therefore, the solution resistance is negligible. It was used here so that no supporting electrolyte would be required, ensuring that other anions would not affect the $E_{\text{P,ox}}$ of Equation 4.15. Linear sweep voltammograms in

TEGDME, DMSO and CH₃CN are presented in Figure 4.16 and show the expected trend, with Au(OH)₃ forming at more negative potentials in TEGDME and more positive potentials in CH₃CN, with DMSO lying between them. This, therefore, supports the AN mechanism proposed above.

4.7.3. H₂O/solvent interactions

The AN data shows that, for each solvent, addition of H₂O leads to an increase in the AN of the resulting mixtures. However, the rate of increase in DMSO is much lower and is likely to be a result of strong hydrogen-bonding (H-bonding) in DMSO-H₂O clusters, meaning there is very little enthalpic benefit for H₂O to disrupt these clusters in order to H-bond with itself over DMSO. Therefore, DMSO suppresses the Lewis acidity of H₂O. However, this raises the question of how H₂O interacts with TEGDME and CH₃CN. It is possible that clusters of H₂O within these solvents (not solvent-H₂O clusters as was the case in DMSO) form rather than mixing and this leads to the rapid increase in AN, as the Et₃PO probe molecules encounters these clusters within the H₂O/solvent mixtures. However, consideration of the ΔH_{mix} suggests clustering is unlikely to occur. Since ΔH_{mix} for CH₃CN and TEGDME are both endothermic, the entropy of mixing must be sufficient to make the process spontaneous. However, H₂O-H₂O clustering is unlikely to result in a large gain in entropy as it necessarily requires a high degree of ordering of the H₂O molecules.

To conclusively rule out clustering as the cause of the rapid AN increase, the H₂O bonding environment was probed using Raman spectroscopy. Bulk H₂O has several O-H stretching modes, some of which arise from H-bonded O-H and others from non-H-bonded, *i.e.* non-interacting, O-H. H-bonded modes occur at Raman shifts below 3500 cm⁻¹, while non-H-bonded modes occur above 3500 cm⁻¹ (ref. 19). Therefore, if H₂O clustering occurs in CH₃CN or TEGDME, Raman signals below 3500 cm⁻¹ would be observed.

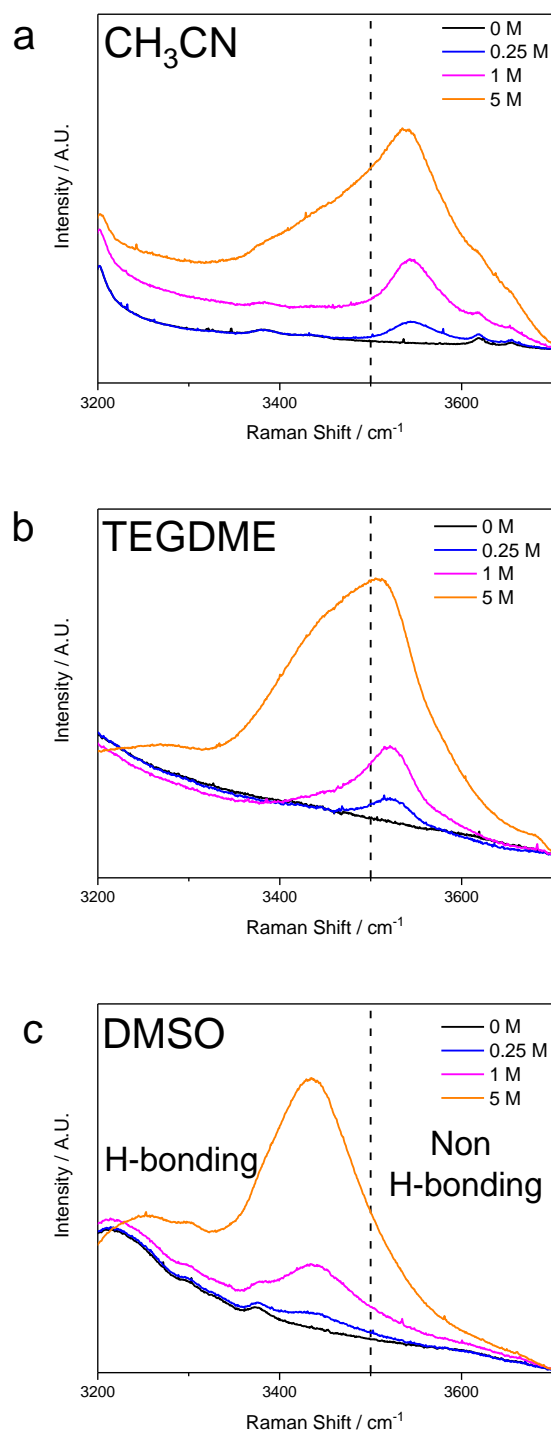


Figure 4.17: Raman spectra identifying H-bonding in DMSO at all H_2O concentrations used but only above 1 M in CH_3CN and TEGDME. The O-H stretch of H-bonding and non-H-bonding H_2O occurs above and below 3500 cm^{-1} , respectively, and is indicated on the plots with a dashed line. Spectra were acquired with a 633 nm HeNe laser using an airtight sample holder. Reference spectra of the dry solvents are included for comparison.

Figure 4.17 shows the Raman spectra H₂O-containing CH₃CN, TEGDME and DMSO in the spectral window for O-H stretches. Spectra of the dry solvents are also shown to confirm whether any solvent signals occur in the spectra. In dry CH₃CN, there is a minor solvent signal at ~3375 cm⁻¹. When the solvent contains 0.25 M H₂O, a new signal appears at ~3550 cm⁻¹, characteristic of H₂O that is not H-bonding, *i.e.* not clustering. When 1 M H₂O is present, this signal grows in intensity, but no other signals appear, again demonstrating that the H₂O is non-interacting. When the H₂O concentration is increased to 5 M, a signal or signals appear below 3500 cm⁻¹, indicating that there are enough H₂O molecules in the mixture to form H-bonds, since the mixture contains ~9 vol% H₂O. In TEGDME, the same trend is seen. With 0.25 M H₂O, a signal at ~3520 cm⁻¹ occurs, again indicating non-H-bonded H₂O. When the H₂O concentration is increased to 1 M, this signal becomes more intense, but a shoulder appears at 3450 cm⁻¹, which indicates that a small proportion of the H₂O may now be H-bonding. At 5 M H₂O, both peaks grow in intensity, again showing that H₂O will H-bond once it is present in sufficient quantities. In DMSO, however, at 0.25 M H₂O, the O-H stretch occurs at ~3425 cm⁻¹, indicating H-bonding occurs at much lower H₂O concentrations than in CH₃CN or TEGDME. This is expected since DMSO is a good H-bond donor and is known to form H₂O-DMSO clusters. As the H₂O concentration increases to 1 M and 5 M, this signal becomes more intense as H₂O continues to H-bond with DMSO and/or itself. Overall, these results show that H₂O does not cluster in CH₃CN and TEGDME and rather mixes randomly within the solvent, whereas in DMSO, H₂O clusters with the solvent as a result of strong H-bonding between them. This confirms the enthalpy of mixing data and shows mixing is enthalpically-driven in DMSO, while in CH₃CN and TEGDME, it is entropically-driven.

4.7.4. Implications of mechanism on solvent choice

Having considered all species involved in the 4e⁻ reduction reaction, it has been demonstrated that it is the ability of the H₂O/organic solvent mixture to stabilise OH⁻ (the

Lewis acidity of the mixture) that predominantly determines whether LiOH will form in a given H₂O-containing electrolyte. Armed with this knowledge, it is now possible to provide selection criteria for potential Li-O₂ battery solvents that should be tolerant to the presence of H₂O. Solvents with a low AN are required so that the H₂O-containing electrolytes remain poor Lewis acids. Of the organic solvents that are commercially available, glyme ethers are currently some of the best solvents in this regard. It is also beneficial for the solvent to be a good Lewis base (high DN), so that it complexes H₂O and limits the increase in AN that H₂O would otherwise cause. Furthermore, if a solvent possesses both a low AN and high DN, it would be expected to be more tolerant to H₂O than either TEGDME or DMSO, as both effects should combine to result in an electrolyte with an initially low AN that also increases slowly as H₂O is introduced.

4.8. Conclusions

In this Chapter, I have elucidated the reactions occurring at the positive electrode when DMSO-, CH₃CN- and TEGDME-based electrolytes contain H₂O. As expected, based on the results in Chapter 3, CH₃CN was more sensitive to H₂O than DMSO, with LiOH readily forming even when the H₂O concentration was <0.1 M. The presence of Li⁺ makes the 4e⁻ reduction of O₂ to LiOH sufficiently favourable that it occurs at the same potentials as Li₂O₂ formation regardless of H₂O concentration, with LiOH becoming the dominant product at 1 M H₂O. In DMSO, the 4e⁻ reduction only occurs at H₂O concentrations >0.5 M, and even then, it occurs negative of the 1e⁻ and 2e⁻ reduction potentials. This means that, provided the discharge potential of a cell is kept positive of the 4e⁻ reaction, cells with significant H₂O concentrations should still form Li₂O₂. Similarly, in TEGDME, the 4e⁻ reduction appears to be negative of the 2e⁻ reduction, but this requires confirmation by additional experiments and is explored in Chapter 5.

The potentials at which the 4e⁻ reduction occurred in each solvent with 1 M H₂O differed dramatically, indicating that the electrolyte plays a crucial role in determining whether LiOH forms on discharge. Therefore, the effect of the solvent on each species in the 4e⁻

reduction reaction was examined. Solvent effects on O₂ and H₂O were insufficient to explain the large changes in potential between solvents, but the stabilisation of OH⁻ changed significantly with solvent and accounted for the propensity to form LiOH in each solvent. In the case of H₂O-containing solvents, OH⁻ is stabilised when the mixture as a whole is a good Lewis acid, which can be measured through its AN. The Lewis acidity of each electrolyte increases with H₂O concentration, explaining why the 4e⁻ reduction becomes progressively more favourable. Furthermore, the Lewis acidities of 1 M H₂O solutions of DMSO and TEGDME were found to be much lower than CH₃CN. Thus, this mechanism can account for why LiOH forms readily in the latter, but not the former solvents, something no other mechanism has achieved.

4.9. References

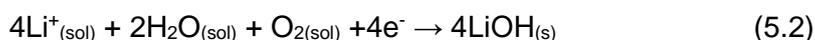
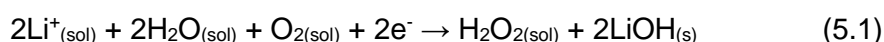
- 1 Aetukuri, N. B. *et al.* Solvating additives drive solution-mediated electrochemistry and enhance toroid growth in non-aqueous Li-O₂ batteries. *Nat. Chem.* **7**, 50-56 (2015).
- 2 Kwabi, D. G. *et al.* The effect of water on discharge product growth and chemistry in Li-O₂ batteries. *Phys. Chem. Chem. Phys.* **18**, 24944-24953 (2016).
- 3 Schwenke, K. U., Metzger, M., Restle, T., Piana, M. & Gasteiger, H. A. The influence of water and protons on Li₂O₂ crystal growth in aprotic Li-O₂ cells. *J. Electrochem. Soc.* **162**, A573-A584 (2015).
- 4 Xia, C., Black, R., Fernandes, R., Adams, B. & Nazar, L. F. The critical role of phase-transfer catalysis in aprotic sodium oxygen batteries. *Nat. Chem.* **7**, 496-501 (2015).
- 5 Xia, C. *et al.* Direct evidence of solution-mediated superoxide transport and organic radical formation in sodium-oxygen batteries. *J. Am. Chem. Soc.* **138**, 11219-11226 (2016).
- 6 Qiao, Y. *et al.* From O₂⁻ to HO₂⁻: reducing by-products and overpotential in Li-O₂ batteries by water addition. *Angew. Chem.* **56**, 4960-4964 (2017).

- 7 Staszak-Jirkovský, J. *et al.* Water as a promoter and catalyst for dioxygen electrochemistry in aqueous and organic media. *ACS Catal.* **5**, 6600-6607 (2015).
- 8 Mayer, U., Gutmann, V. & Gerger, W. The acceptor number - a quantitative empirical parameter for the electrophilic properties of solvents. *Monatsh Chem* **106**, 1235-1257 (1975).
- 9 Schmeisser, M., Illner, P., Puchta, R., Zahl, A. & van Eldik, R. Gutmann donor and acceptor numbers for ionic liquids. *Chem. Eur. J.* **18**, 10969-10982 (2012).
- 10 Lu, Y.-C. & Shao-Horn, Y. Probing the reaction kinetics of the charge reactions of nonaqueous Li–O₂ batteries. *J. Phys. Chem. Lett.* **4**, 93-99 (2012).
- 11 Gallant, B. M. *et al.* Influence of Li₂O₂ morphology on oxygen reduction and evolution kinetics in Li–O₂ batteries. *Energy Environ. Sci.* **6**, 2518-2528 (2013).
- 12 Laoire, C. O., Mukerjee, S., Abraham, K. M., Plichta, E. J. & Hendrickson, M. A. Influence of nonaqueous solvents on the electrochemistry of oxygen in the rechargeable lithium–air battery. *J. Phys. Chem. C* **114**, 9178-9186 (2010).
- 13 Morcom, K. W. & Smith, R. W. Enthalpies of mixing of water+methyl cyanide. *J. Chem. Thermodynamics* **1**, 503-505 (1969).
- 14 López, E. R., García, J., Legido, J. L., Coronas, A. & Fernández, J. Experimental and predicted excess enthalpies of the 2,2,2-trifluoroethanol–water–tetraethylene glycol dimethyl ether ternary system using binary mixing data. *J. Chem. Soc. Faraday Trans.* **91**, 2071-2079 (1995).
- 15 Cowie, J. M. G. & Toporowski, P. M. Association in the binary liquid system dimethyl sulfoxide – water. *Can. J. Chem.* **39**, 2240-2243 (1961).
- 16 Engel, N. *et al.* DMSO-water clustering in solution observed in soft X-ray spectra. *J. Phys. Chem. Lett.* **3**, 3697-3701 (2012).
- 17 Johnson, L. *et al.* The role of LiO₂ solubility in O₂ reduction in aprotic solvents and its consequences for Li–O₂ batteries. *Nat. Chem.* **6**, 1091-1099 (2014).

- 18 Diaz-Morales, O., Calle-Vallejo, F., de Munck, C. & Koper, M. T. M. Electrochemical water splitting by gold: evidence for an oxide decomposition mechanism. *Chem. Sci.* **4**, 2334-2343 (2013).
- 19 Singh, S. & Krueger, P. J. Raman spectral studies of aqueous solutions of non-electrolytes: dimethylsulfoxide, acetone and acetonitrile. *J. Raman Spectrosc.* **13**, 178-188, (1982).

5. Discharge studies of Li-O₂ cells under wet conditions

In Chapters 3 and 4, the effect of H₂O on O₂ reduction was studied in three-electrode electrochemical cells, where changes to the electrochemical responses in the voltammetry were occurring at the working electrode (positive electrode). A novel unifying mechanism based on the ability of the electrolyte to stabilise OH⁻ was proposed to explain the propensity of different electrolytes to form Li₂O₂ or LiOH during discharge. The mechanism rationalised why the 4e⁻ reduction occurred more readily in CH₃CN-based electrolytes than DMSO- and TEGDME-based electrolytes when containing the same H₂O concentrations. It also appears to be consistent with previous work, which reported Li₂O₂ in glyme ether solvents and DMSO, but LiOH in CH₃CN. However, the majority of these reports focussed on glyme ethers, and those that did investigate DMSO and CH₃CN only confirmed the discharge product by *ex situ* characterisations. Given that LiOH can form both during 2e⁻ and 4e⁻ O₂ reduction in the presence of H₂O (Equations 5.1 and 5.2, respectively), *ex situ* analysis is unlikely to provide conclusive proof of whether 2e⁻ or 4e⁻ reduction occurs in cells. Therefore, it is particularly important to establish which electrochemical reactions occur in DMSO and CH₃CN, which will require *in situ* or *operando* techniques.



As discussed in Chapter 1, the tolerance of the electrolyte to H₂O will have important design implications for the gas-handling unit (GHU) in practical Li-air batteries and consequently the practical energy density of the battery at a pack level. In a worst-case scenario, where H₂O content of the gas stream entering the battery must be <1 ppm, the GHU contributes 32% of the mass and 35% of the volume of the battery pack¹. Therefore, it is critical to identify electrolytes that can tolerate high H₂O concentrations whilst

maintaining $2e^-$ O_2 reduction, allowing less complex and lighter GHUs that would improve the pack-level specific and volumetric energy densities.

My first objective is to confirm the O_2 reduction products in two-electrode cells with CH_3CN , DMSO and TEGDME at various H_2O concentrations between 0 M and 1 M. Given the results in Chapter 4, CH_3CN is expected to form the $4e^-$ product on discharge, even at H_2O concentrations <0.25 M, whereas in DMSO and TEGDME, the $2e^-$ reduction should still occur at 1 M H_2O . Here, pressure cells, an *in situ* technique, will be used to determine the electrochemical reaction(s) occurring at the positive electrode on discharge and will be complemented by *ex situ* characterisation of the electrode. This should remove any doubt regarding the discharge products in H_2O -containing DMSO and CH_3CN and confirm that the acceptor number (AN) mechanism is valid.

My second objective is to confirm that $Li-O_2$ cells can be discharged in humid O_2 atmospheres and still result in $2e^-$ O_2 reduction. The pressure cells results will have identified suitable H_2O concentrations, but the humidities required to produce these H_2O concentrations will need to be determined. Cells will then be discharged in O_2 atmospheres at these humidities and the discharge product(s) characterised *ex situ* to confirm that Li_2O_2 forms when discharging cells in humid O_2 . It will then be possible to comment on the implications for the GHU.

5.1. Experimental

5.1.1. Two-electrode cell components

Two electrode cells (pressure cells and open cells) consisted of a Super P carbon positive electrode, glass fibre separators and a freestanding Li_xFePO_4 negative electrode. Positive electrodes were made as follows. A putty consisting of 90 wt% Super P carbon (Alfa Aesar) and 10 wt% PTFE suspension (Sigma Aldrich), mixed with isopropanol, was spread on 24 mm diameter circular disks of stainless-steel mesh to

achieve a carbon mass loading of 4 mg cm^{-2} . The electrodes were left to air-dry overnight. Li_xFePO_4 electrodes were made from a putty consisting of 80 wt% LiFePO_4 (MTI), 10 wt% Super P carbon and 10 wt% PTFE suspension, mixed with isopropanol. The putty was rolled out to form a sheet of thickness $350 \mu\text{m}$ and left to air-dry overnight. 24 mm diameter LiFePO_4 electrodes were then punched from the sheet. 26 mm diameter glass fibre separators (Whatman) were also punched in the same way. A Büchi oven was used to thoroughly dry all cell components, at elevated temperature under vacuum, to prevent inadvertent addition of H_2O due to contact with the electrolyte in the assembled cell. The electrodes and glass fibre separators were dried at $120 \text{ }^\circ\text{C}$ and $300 \text{ }^\circ\text{C}$ respectively under vacuum, all for a minimum of 24 hours. Once dried, the Büchi tube was taken directly into a glove box to prevent exposure of the dried cell components to moisture.

5.1.2. Pressure cells

Pressure cells were designed in-house and used to determine O_2 consumption during discharge (Figure 5.1). A 1" diameter Swagelok fitting housed the Li-O_2 cell, which consisted of a Li_xFePO_4 electrode, 2 glass fibre separators and a Super P carbon electrode (supported on steel mesh). 1.5 mL of electrolyte was added to the cell. Spacers were placed on top of the carbon electrode to create headspace for O_2 . The cell was assembled and sealed in a N_2 glove box ($<0.1 \text{ ppm H}_2\text{O}$). O_2 gas was then purged slowly through the system by opening the valves at the top of the cell. Cells using DMSO- and TEGDME-based electrolytes were purged for two minutes, while for CH_3CN -based electrolytes, O_2 was only purged through the cell for one minute to minimise evaporation of the solvent. Once purged, the valves were sealed and the cell was placed in a bench-top incubator at $20 \text{ }^\circ\text{C}$. The cell was connected to a potentiostat, which also monitored the pressure transducer reading. The cell was allowed to reach thermal equilibrium at open circuit for several hours before the discharge was started. Cells were discharged at $50 \mu\text{A cm}^{-2}$.

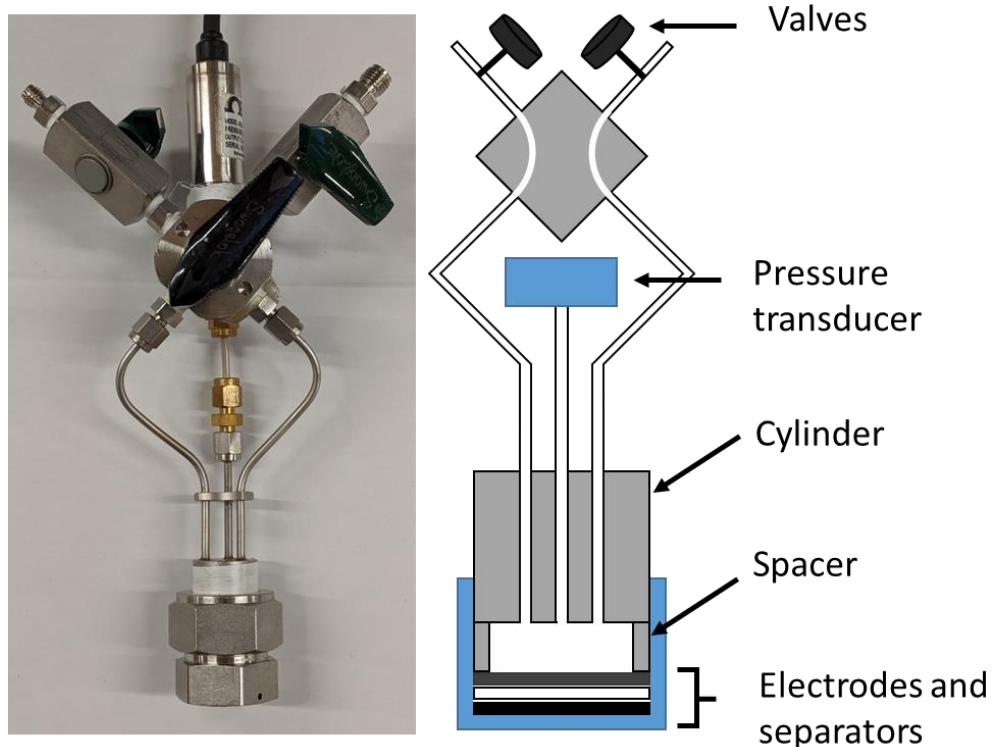


Figure 5.1: Image (left) and schematic (right) of the pressure cell design.

Following discharge, the pressure inside the cell was allowed to reach equilibrium and the difference in pressure prior to and following discharge was used to calculate the O_2 consumption. This required the cell headspace volume to be known. This was determined using a calibration tube, of known volume, which was attached to one of the valves and sealed under reduced pressure. The cell was placed under atmospheric pressure and sealed, before the calibration tube was opened to the cell. The changes in pressure allow the headspace volume to be calculated.

5.1.3. Relative humidities

The relationship between the relative humidity (RH) of a gas and the H_2O concentration in solvents and electrolytes was determined as follows. Solvents and electrolytes containing various concentrations of H_2O (subsequently referred to as humidifying solutions) were used to humidify dry N_2 atmospheres. A glass bottle containing 100 mL of the humidifying solution and a stirrer bar were placed in an airtight container along with a humidity data logger (Omega Engineering). This was assembled in a N_2 glove box

(H_2O <0.1 ppm) and subsequently placed into a bench-top incubator at 20 °C or 25 °C. The container was placed on a stirrer plate to ensure the humidifying solution was continuously mixed and was left for a minimum of 24 hours to allow dissolved H_2O to evaporate and humidify the N_2 gas. After reaching equilibrium, the container was opened on the bench and the H_2O concentration of the humidifying solution was immediately determined using a Karl Fischer titrator. The density of the solution was also determined by weighing a 1 mL volume of the solution. This allowed conversion of the H_2O concentration from ppm to M.

5.1.4. Open cell discharges

An airtight plastic container was modified in-house to allow two-electrode cells to be discharged whilst open to a humidified O_2 atmosphere. Stainless steel tubing and valves were added to the sides of the container using bulkhead fittings (Swagelok) with O-rings to maintain an airtight seal. The metal tubing allowed the container to be purged with O_2 when sealed and served as the electrical contacts through the container walls. The container was sealed with a greased rubber gasket housed in the lid. Cells were assembled inside a N_2 glove box (<0.1 ppm H_2O) as described for pressure cells, with the exception of the current collector on the positive electrode side of the cell, which consisted of a hollow tube to expose the electrode to the atmosphere in the container. Dry 0.25 M LiClO_4 in TEGDME was added to the cells. An open bottle of H_2O -containing 0.25 M LiClO_4 in TEGDME acted as the humidifying solution. A stirrer bar was added to the bottle to allow the solution to be stirred in the incubator to rapidly humidify the atmosphere. The initial H_2O concentration of the humidifying solution was ~1.1 M to ensure that when the relative humidity of the atmosphere reached equilibrium, the H_2O concentration in solution was 1 M. The cell, humidifying solution and humidity sensor were sealed in the container and O_2 was then purged through the container for 10 minutes, before being placed in a bench-top incubator at 20 °C. The humidifying solution was continuously stirred with a stirrer plate. To rule out the possibility of CO_2 and

additional moisture leaking into the container, the RH within the incubator was checked periodically and always maintained a RH of >30%. If a leak were present, the RH within the container would tend towards the external RH, rather than plateauing at 13%, or maintaining 0% when discharged in a dry O₂ atmosphere.

5.1.5. Post-discharge characterisation

Following discharge, the positive electrodes were either used for *ex situ* characterisations or titrated using a UV-vis technique to determine the Li₂O₂ yield. For positive electrodes used in *ex situ* characterisations, the container was taken into an Ar glove box (<0.1 ppm O₂, <0.1 ppm H₂O) immediately after discharge to prevent exposure of the positive electrode to air when the container was opened, as Li₂O₂ reacts with CO₂, forming Li₂CO₃. The electrode was then extracted from the cell and washed three times with dry CH₃CN (<5 ppm H₂O) and dried under vacuum for 30 minutes. The electrode was then kept under an inert atmosphere (N₂ or Ar) or under vacuum at all times during characterisation.

Fourier-transform infrared (FTIR) spectra were recorded on a Nicolet 6700 spectrometer (ThermoFisher) using an attenuated total reflectance accessory (SmartOrbit) housed in a N₂ glove box (<0.1 ppm H₂O).

X-ray diffraction (XRD) patterns were recorded using a Rigaku Miniflex XRD instrument housed in a N₂ glove box (<0.1 ppm H₂O). The X-ray source was Cu K_α (1.5406 Å) and electrode samples were placed on a zero-background Si sample holder.

Secondary electron images were recorded on a Zeiss Merlin scanning electron microscope (SEM) at 3 kV acceleration voltage. Electrode samples were fixed with copper adhesive tape in an N₂ glove box and put in an air-sensitive transfer holder to prevent exposure to air between the glove box and SEM. Energy-dispersive X-ray (EDX) spectroscopy was carried out at 3 kV with a built-in Oxford Instruments X-Max 150 Silicon drift detector and analysed using the Aztec software package.

5.2. Identification of reactions occurring in full cells

5.2.1. Discharge studies using pressure cells

The discharge product in metal-O₂ batteries are typically monitored using one of two *operando* techniques. One is by using a mass spectrometer to measure O₂ consumption from a mixture of O₂ and a carrier gas, typically Ar, whilst the cell is discharging. This technique is called differential electrochemical mass spectrometry (DEMS). However, DEMS is incompatible with volatile solvents such as CH₃CN, which will evaporate under the constant flow of the carrier gas, prematurely terminating the discharge.

The second *operando* technique is the use of pressure cells. These consist of a sealed cell with known headspace and a pressure transducer. During discharge, O₂ gas from the headspace is consumed, resulting in a decrease in pressure. Using the ideal gas law, this can be converted into the number of moles of O₂ consumed and compared to the charge passed, allowing the number of e⁻ per O₂ molecule (e⁻/O₂) to be calculated and therefore identifying the discharge product(s), based on their O₂ reduction reactions (Table 5.1).

Table 5.1: O₂ reduction reactions that generate e⁻/O₂ values of 2 and 4.

2e⁻/O₂	4e⁻/O₂
$2\text{Li}^+ + \text{O}_2 + 2\text{e}^- \rightarrow \text{Li}_2\text{O}_2$	
$2\text{Li}^+ + \text{O}_2 + \text{H}_2\text{O} + 2\text{e}^- \rightarrow \text{LiOOH} + \text{LiOH}$	$4\text{Li}^+ + \text{O}_2 + 2\text{H}_2\text{O} + 4\text{e}^- \rightarrow 4\text{LiOH}$
$2\text{Li}^+ + \text{O}_2 + 2\text{H}_2\text{O} + 2\text{e}^- \rightarrow \text{H}_2\text{O}_2 + 2\text{LiOH}$	

As the cell is sealed during discharge, the solvent will not evaporate to dryness, provided the headspace volume is small enough, such that this method is compatible with CH₃CN. 2e⁻ and 4e⁻ O₂ reduction products result in e⁻/O₂ values of 2 and 4, respectively. Pressure cells cannot distinguish between the different 2e⁻ products, that is whether Li₂O₂, LiOOH and/or H₂O₂ form, but, in any case, these species are in equilibrium. An e⁻/O₂ value

between 2 and 4 indicates a mixture of the $2e^-$ and $4e^-$ products, with values above and below 3 identifying that LiOH and Li_2O_2 are the dominant product, respectively. It should be noted that side reactions could also cause the e^-/O_2 ratio to increase above 2.

Figure 5.2 shows the trends in the e^-/O_2 ratio with H_2O concentration in the three solvents obtained from pressure cells discharged 0 M and 1 M H_2O . In DMSO (orange crosses), e^-/O_2 value of 1.87 and 1.94 were obtained in dry and 1 M H_2O cells, respectively. This is clearly shown by the near-identical gradient of the pressure decay (Figure 5.3a). Had any LiOH formed, the gradient in the 1 M H_2O cell would be much shallower. At intermediate H_2O concentrations, the e^-/O_2 values ranged between 1.90-1.95. This clearly shows that only Li_2O_2 is forming electrochemically as would be expected at the discharge potential in these cells, ~ 2.6 V, as RRDE results indicate that at this potential, LiOH does not form (See Figures 4.7 and 4.8). This confirms that the toroids observed by Aetukuri *et al.* in H_2O -containing DMSO were indeed Li_2O_2 (ref. 2).

The pressure cells discharged using TEGDME (black crosses, Figure 5.2) follow the same trend as DMSO. Between 0 M and 1 M H_2O , the e^-/O_2 ratio lies in the range 1.87-2.02, confirming that LiOH is not formed within this range of H_2O concentrations. The e^-/O_2 values are 2.02 and 1.96 in the dry and 1 M H_2O cells, respectively. The decrease in the e^-/O_2 ratio from 0 M to 0.1 M occurred consistently over multiple cells. As in DMSO, comparison of the pressure drops in cells discharged with 0 M H_2O and 1 M H_2O show nearly identical gradients (Figure 5.4a).

In dry CH_3CN , the e^-/O_2 ratio is 1.80, suggesting O_2 is not fully reduced to Li_2O_2 in the cell (green circles, Figure 5.2). However, it is well known that once LiO_2 forms in CH_3CN , it quickly reacts to form Li_2O_2 , so a ratio of 2 should be obtained. The cause of this unusually low e^-/O_2 ratio could not be accounted for, but the pressure cells are being used here to determine whether $4e^-$ O_2 reduction occurs in 2-electrode cells. If one assumes that the e^-/O_2 value in the dry electrolyte is the baseline, any increase in e^-/O_2 will indicate that the $4e^-$ reduction is occurring. As expected, as the H_2O concentration

increases, the e^-/O_2 ratio steadily rises to a value of 3.03 at 1 M H_2O , indicating that LiOH is now the dominant product. This is expected based on the electrochemistry conducted in three-electrode cells and confirms that the rapid increase in reduction currents in those measurements was due to the $4e^-$ reduction of O_2 . An obvious change in the gradient of the pressure decay is seen when cells containing 0 M H_2O and 1 M H_2O were discharged (Figure 5.5a). Furthermore, this shows that the LiOH reported by Kwabi *et al.* was mistakenly attributed to $2e^- O_2$ reduction³. This highlights the need for *in situ* measurements when a product (LiOH in this case) can form via multiple electrochemical and chemical reactions (e.g. Equations 5.1 and 5.2).

To confirm that it is possible to induce $4e^- O_2$ reduction in DMSO and TEGDME, cells were discharged containing 10 M H_2O in both electrolytes. e^-/O_2 values of 2.70 and 3.49 were obtained, respectively. It was unclear why significant $4e^- O_2$ reduction was occurring in TEGDME when Qiao *et al.* reported $2e^- O_2$ reduction with a 20 M H_2O concentration⁴.

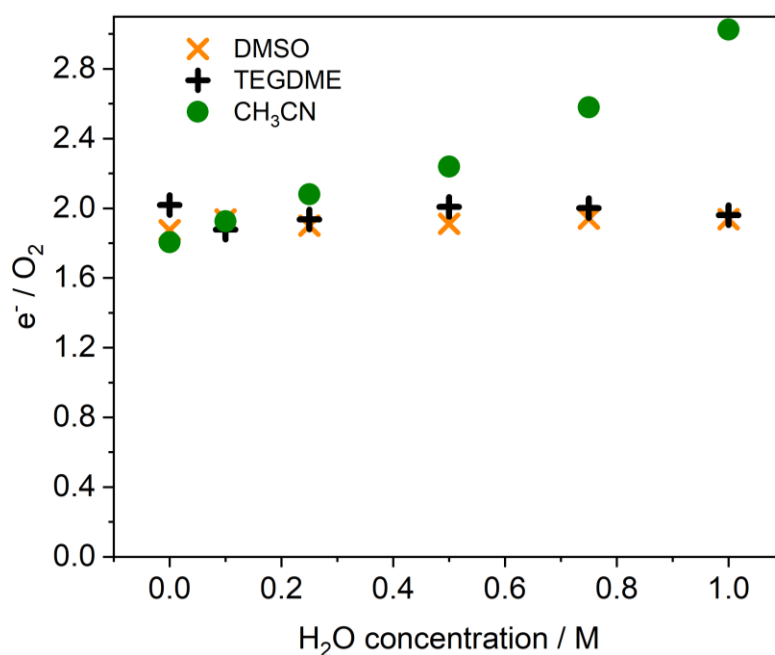


Figure 5.2: e^-/O_2 values obtained from pressure cells using DMSO, TEGDME and CH_3CN at various H_2O concentrations demonstrating the formation of Li_2O_2 up to 1 M H_2O in DMSO and TEGDME, but an increasing proportion of LiOH in CH_3CN over the same H_2O concentrations.

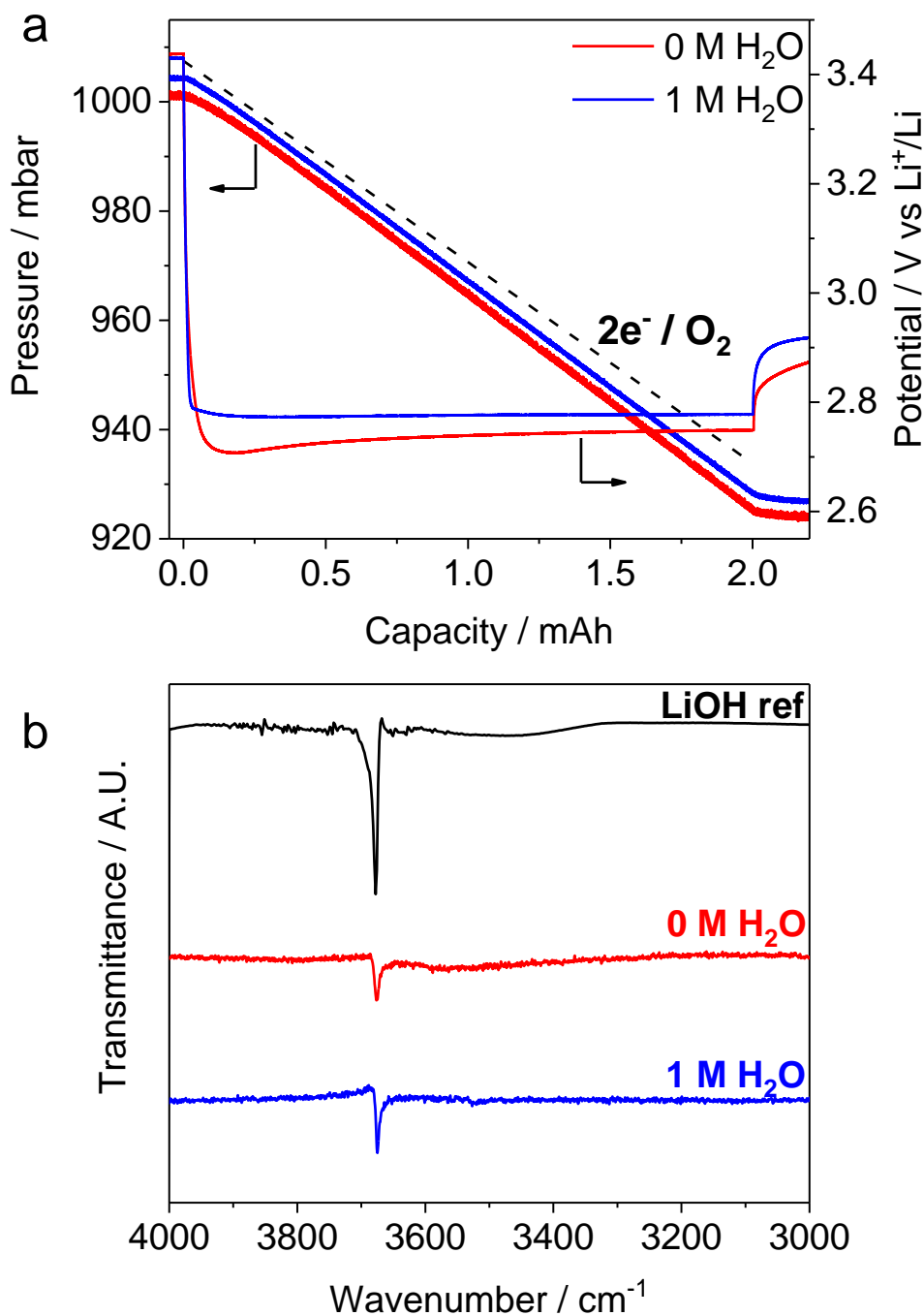


Figure 5.3: Pressure cell measurements in DMSO containing either 0 M H₂O (blue traces) or 1 M H₂O (red traces), demonstrating that the electrochemical reaction is close to the ideal value of 2 e⁻/O₂, but that electrolyte degradation leads to LiOH formation whether H₂O is present or not. Discharge and pressure decay plots are shown in panel (a), with a dashed line showing the ideal pressure decay expected for a 2e⁻/O₂ reaction. FTIR spectra of discharged positive electrodes are shown in panel (b) along with a reference spectrum for LiOH.

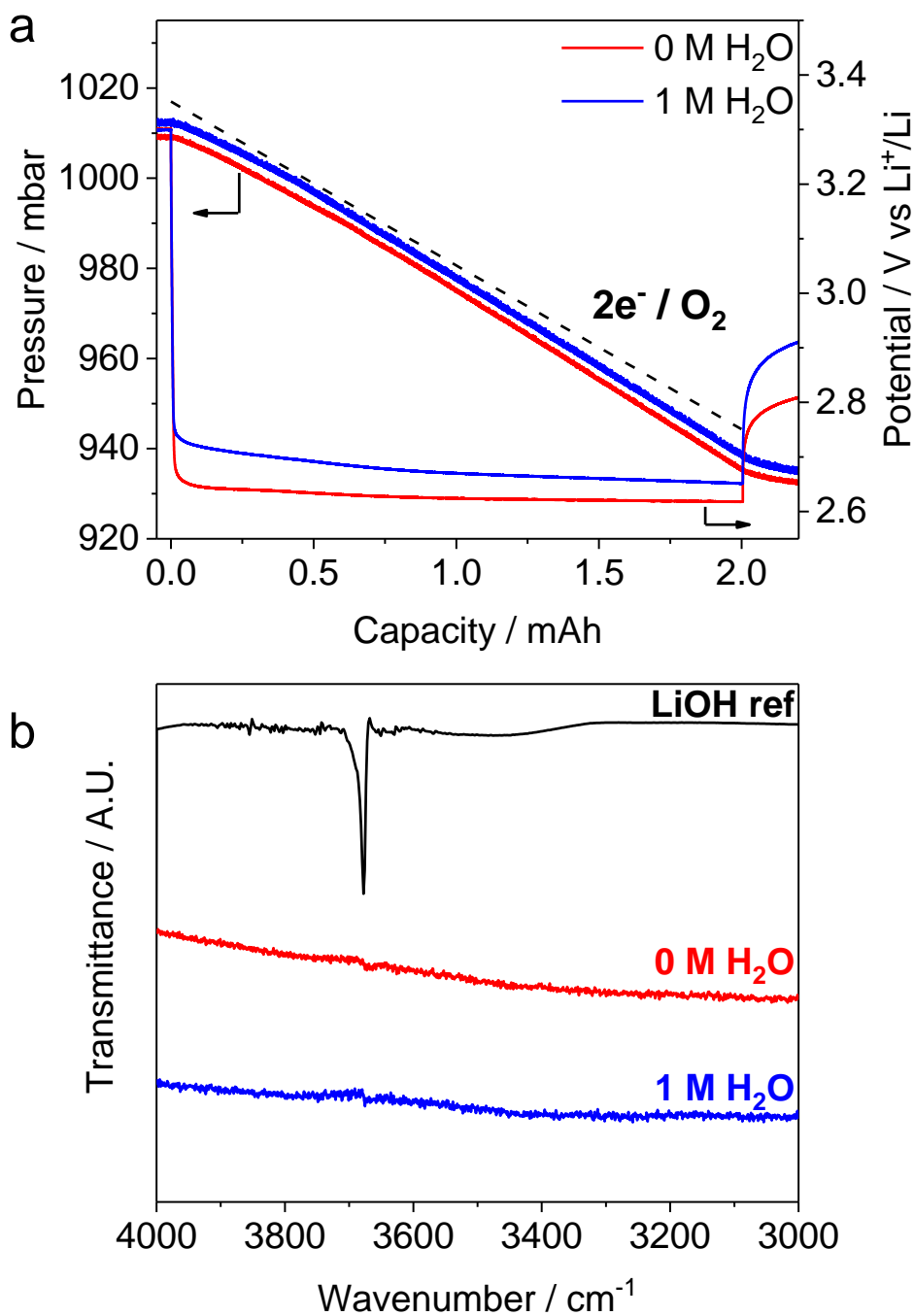


Figure 5.4: Pressure cell measurements in TEGDME containing either 0 M H₂O (blue traces) or 1 M H₂O (red traces), demonstrating that the electrochemical reaction is close to the ideal value of 2 e⁻/O₂, but that little, if any, LiOH forms whether H₂O is present or not. Discharge and pressure decay plots are shown in panel (a), with a dashed line showing the ideal pressure decay expected for a 2e⁻/O₂ reaction. FTIR spectra of discharged positive electrodes are shown in panel (b) along with a reference spectrum for LiOH.

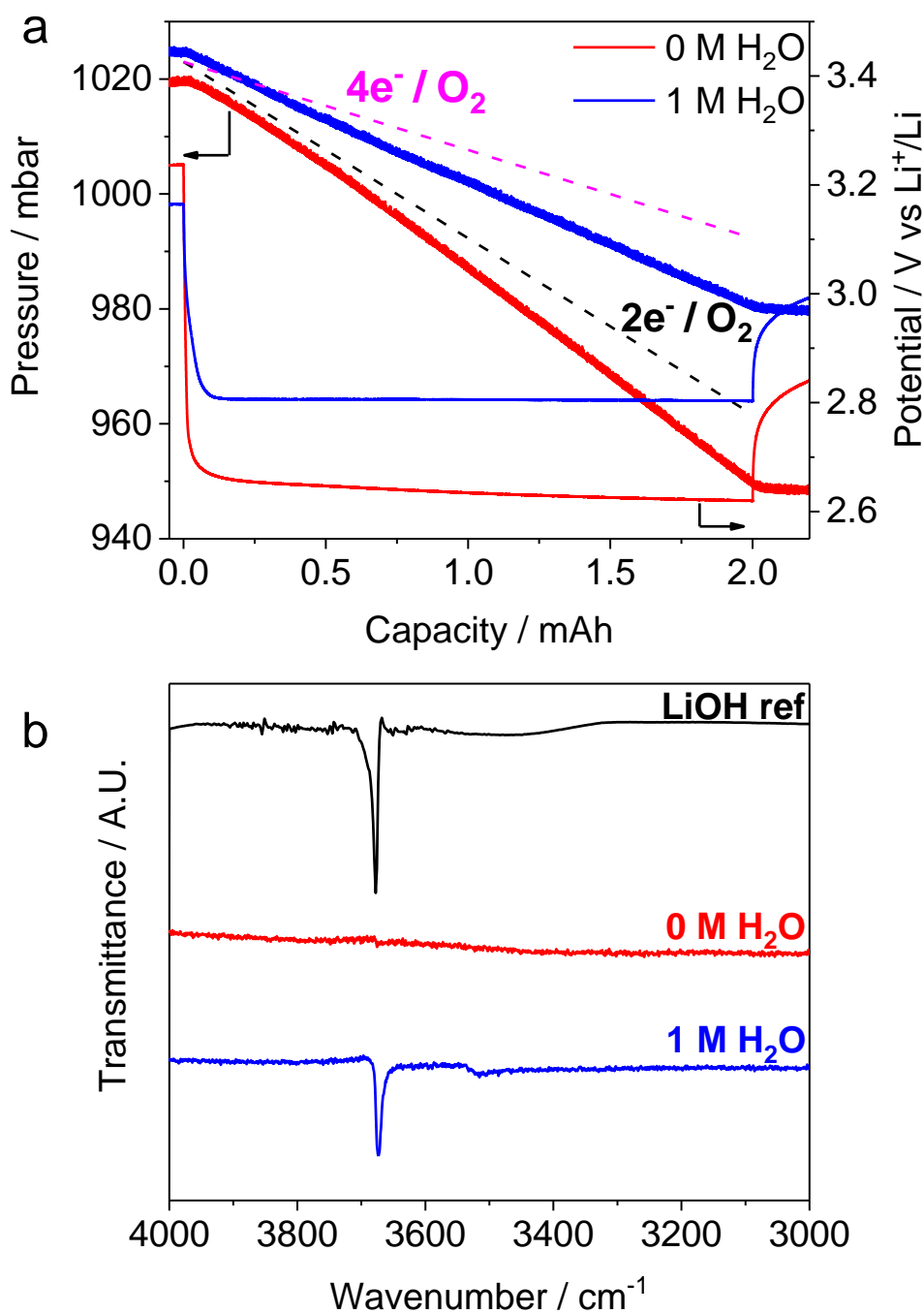


Figure 5.5: Pressure cell measurements in CH₃CN containing either 0 M H₂O (blue traces) or 1 M H₂O (red traces), demonstrating that the electrochemical reaction shifts from the 2e⁻ towards the 4e⁻ reaction when H₂O is present, with the LiOH product clearly detected in the FTIR spectrum. Discharge and pressure decay plots are shown in panel (a), with dashed lines showing the ideal pressure decay expected for 2e⁻/O₂ (black line) and 4e⁻/O₂ (pink line) reactions. FTIR spectra of discharged positive electrodes are shown in panel (b) along with a reference spectrum for LiOH.

5.2.2. *Ex situ* characterisations

Discharged electrodes were analysed *ex situ* to complement the results obtained using the pressure decay measurements. Here, electrodes were discharged in electrolytes containing either 0 M or 1 M H₂O. The electrodes were discharged to a capacity of 8 mAh to deposit sufficient discharge products on the electrodes for easy identification using FTIR and XRD. The pressure decay was monitored to confirm that the electrochemical reaction was constant throughout discharge. This was particularly important for CH₃CN as H₂O will be consumed, resulting in the H₂O concentration decreasing from 1 M to ~0.9 M.

In DMSO (Figure 5.3b), LiOH formed in the cell with dry electrolyte, but the pressure decay measurements indicate that the source of this LiOH cannot be electrochemical. DMSO is known to react with both O₂⁻ and Li₂O₂, leading to the parasitic products LiOH and dimethyl sulfone^{5,6}. The reaction mechanism involving O₂⁻ reacting with DMSO still results in 2e⁻ being consumed per O₂, which means that parasitic reactions involving O₂⁻ and Li₂O₂ will not alter the pressure decay response. Therefore, the FTIR spectrum confirms that parasitic chemical reactions produce LiOH. This means that detection of LiOH using *ex situ* characterisations are of limited value, since it will always be present. While this peak is also observed in the cell discharged with 1 M H₂O, this is again due to these parasitic chemical reactions.

In TEGDME (Figure 5.4b), in both the dry and wet electrolyte, there is a very small peak consistent with LiOH, but its low intensity makes it difficult to conclusively say whether LiOH has formed. In the dry electrolyte, this could be due to degradation of the electrolyte caused by proton-abstraction from the solvent molecules by O₂⁻^{7,8}. In the 1 M H₂O electrolyte, this could also occur, but it is likely that some Li₂O₂ has undergone metathesis, now existing as H₂O₂, along with LiOH. Therefore, when the electrode is extracted and washed with dry CH₃CN prior to the FTIR measurement, this LiOH will

precipitate onto the electrode surface and the removal of H_2O_2 prevents this LiOH converting back into H_2O .

In dry CH_3CN (Figure 5.5b), again there is a very small absorption that could be LiOH forming from solvent degradation. However, this signal is much more intense in the electrode discharged in the presence of 1 M H_2O , suggesting that significantly more LiOH forms at this increased H_2O concentration, consistent with the pressure decay measurements.

Since the FTIR spectra in the TEGDME electrodes did not rule out the presence of LiOH, these electrodes were also characterised using XRD (Figure 5.6). The electrode discharged in dry electrolyte does not have any discernible peaks due to either Li_2O_2 or LiOH. This is to be expected as Li_2O_2 forms as a thin film in this electrolyte. The film likely forms as an amorphous layer, lacking the required crystallinity to diffract X-rays. The electrode discharged in the electrolyte containing 1 M H_2O , however, has intense XRD peaks corresponding to both Li_2O_2 and LiOH. These peaks indicate that crystalline deposits of Li_2O_2 now form, which must be via a solution mechanism. This will be one or more of the metathesis reactions involving Li_2O_2 and H_2O . Furthermore, this can explain the presence of crystalline LiOH in the electrode, as the by-product in the metathesis reactions is LiOH. It must be soluble to some extent as the addition of H_2O has been shown to delay passivation of the electrode, but if the concentration reaches the solubility limit, solid LiOH will form. When the electrode is extracted after discharge and washed prior to characterisation, these deposits will remain. Furthermore, it could be possible that in washing the electrode, some of the dissolved LiOH could precipitate onto the electrode surface as the H_2O that is solvating the LiOH is removed. It should be highlighted that the LiOH seen in the XRD pattern here must come from the metathesis reaction involving Li_2O_2 , as the pressure decay for the cell was consistent with a $2\text{e}^-/\text{O}_2$ reaction.

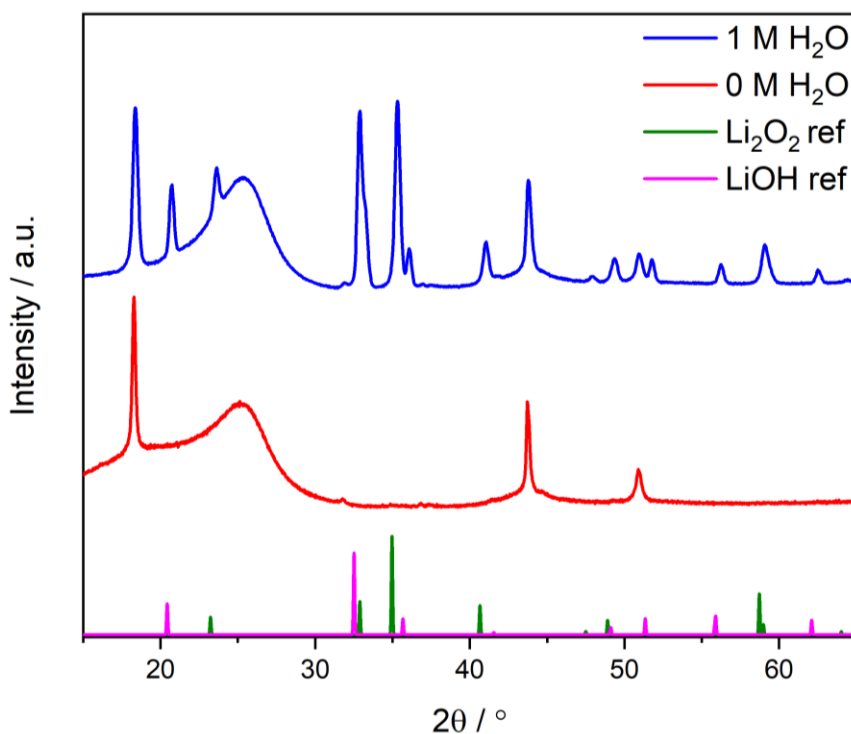


Figure 5.6: XRD patterns showing crystalline Li_2O_2 and LiOH deposits on a positive electrode discharged in TEGDME containing 1 M H_2O , but not crystalline products on an electrode discharged in dry TEGDME electrolyte. Li_2O_2 and LiOH reference patterns (green and magenta peaks, respectively) are included for comparison with the experimental peaks. A Cu K_α source was used to collect the patterns.

5.3. Discharging cells in a humid O_2 atmosphere

5.3.1. Equilibria between H_2O in the vapour and solution phases

Over the last two chapters, I have identified how H_2O affects O_2 reduction, developed a mechanism that explains why LiOH forms more easily in some solvents than others and confirmed this occurs in two-electrode cells. Thus far, H_2O was intentionally added to the electrolyte, but in a practical Li-air battery, that is, one supplied by ambient air, H_2O will enter the battery via a GHU. Therefore, the H_2O content of the gas stream after it has passed through the GHU will determine the H_2O concentration in the electrolyte. Specifically, an equilibrium will be reached between the vapour and solution phases, which will be controlled by the partial pressure of H_2O vapour ($p_{\text{H}_2\text{O}}$). Given that at 1 M

H₂O in TEGDME-based and DMSO-based electrolytes, the 4e⁻ O₂ reduction can be easily avoided, establishing the p_{H₂O} required to achieve 1 M H₂O in both electrolytes would provide a target for the GHU. In the following discussion, RH expressed as a percentage will be used as it is a dimensionless variable linked to p_{H₂O} by the following relationship

$$\%RH = 100 \times p_{H_2O}/p_{sat,H_2O} \quad (5.3)$$

where p_{sat,H₂O} is the saturated vapour pressure of H₂O at a specified temperature. Furthermore, meteorological forecasts report the H₂O content in the atmosphere using RH, making it a convenient real-world unit when considering the engineering constraints required for GHUs in Li-O₂ batteries.

As a first approximation, the relationship between RH and dissolved H₂O concentration was determined in the solvents TEGDME (Figure 5.7) and DMSO (Figure 5.8) in the absence of LiClO₄. This was done experimentally for TEGDME and was calculated using data from reference 9 for DMSO. Both data sets provide RH at 25 °C to aid comparison, but it should be highlighted that the RH to achieve a given H₂O concentration in these mixtures will vary with temperature. In order to convert H₂O concentrations from ppm to M, it was assumed that the mixtures were ideal and therefore the volume of the mixtures could be calculated from the mass of H₂O and TEGDME/DMSO in each solution.

In TEGDME (Figure 5.7), as the H₂O concentration in solution increases, the RH also increases and follows a quadratic dependence. The curve fitted to the data identifies that a RH of 30% would result in 1 M H₂O in TEGDME. Assuming a worst-case scenario with 100% RH at 25 °C, a GHU would only be required to reduce the humidity of the gas stream by approximately two-thirds, which would be readily achievable.

Furthermore, this may explain why Qiao *et al.* were able to observe 2e⁻ O₂ reduction in electrolytes with 30 vol% H₂O. They placed cells containing 40 μL of electrolyte in 650 mL of dry O₂ gas, likely causing most of the H₂O to escape into the vapour phase.

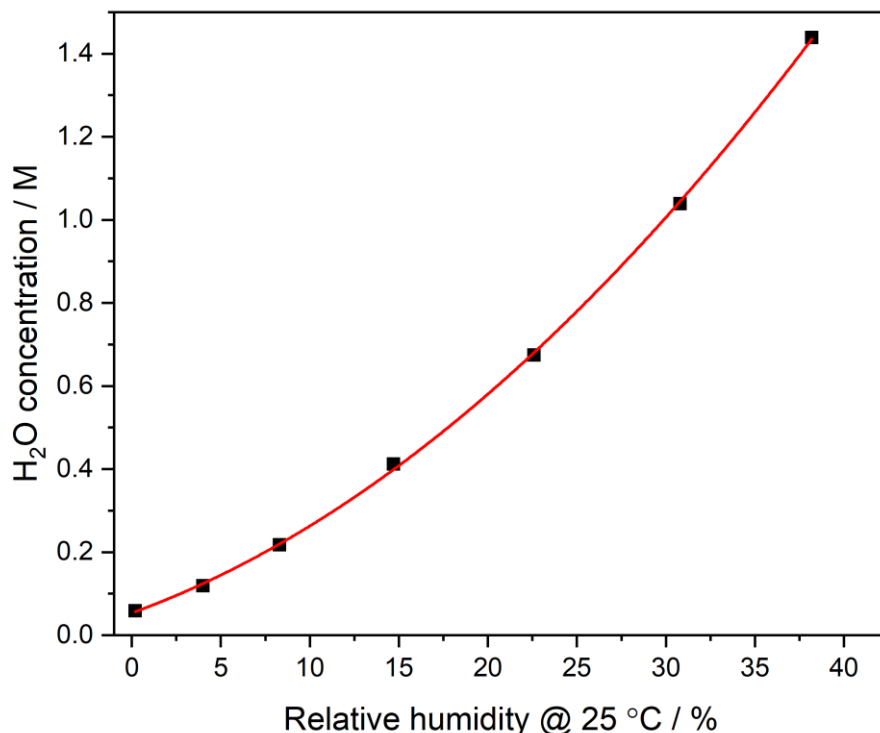


Figure 5.7: Plot showing the equilibrium between RH at 25 °C and dissolved H₂O concentration in TEGDME, where a RH of ~30% results in a 1 M H₂O concentration in the solvent. The relationship follows a quadratic dependence, which was used for the best-fit line (red line). The RH was measured with a humidity data logger and the H₂O concentration in the mixture was calculated from the H₂O content (measured using a Karl Fischer titrator) and the density of the TEGDME/H₂O mixture.

DMSO, however, absorbs significantly more H₂O from a humidified atmosphere (Figure 5.8), as a RH of only 1.24% results in 1 M H₂O in the solvent, requiring far more efficient H₂O removal from the gas stream of a Li-air battery. Furthermore, DMSO would be expected to absorb H₂O vapour as it is hygroscopic, readily H-bonding with H₂O. This highlights that DMSO and other solvents which H-bond to H₂O well, (typically, solvents with high DNS), would ultimately require significantly drier gas streams than TEGDME to avoid 4e⁻ O₂ reduction. Consequently, the GHU would be more complex than if TEGDME were utilised and it is imperative that this is considered when designing a Li-air battery pack.

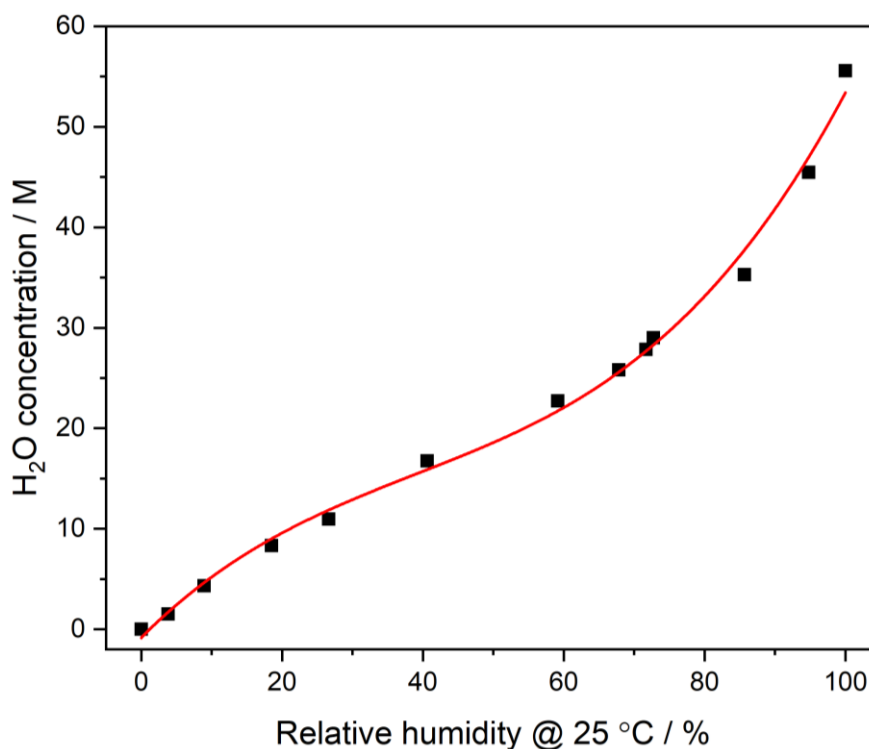


Figure 5.8: Plot showing the equilibrium between RH at 25 °C and dissolved H₂O concentration in DMSO, where H₂O concentrations of >1 M are generated by RHs below 10% RH. The relationship follows a cubic dependence, which was used for the best-fit line (red line). Points are calculated from data in reference 9.

While DMSO can avoid $4e^-$ O₂ reduction when the H₂O concentration is ≤ 1 M, it introduces a new problem, as the required humidity level would need to be much lower than for TEGDME and could make the battery impractical at the pack-level. Therefore, the initial criteria I proposed for suitable electrolytes to operate under humid conditions must be refined; these electrolytes should have **both** low ANs and DNs. The former prevents LiOH formation in the presence of H₂O, while the latter would minimise the uptake of H₂O vapour into the electrolyte, reducing the complexity of the GHU.

The DMSO humidity data demonstrates that it is possible to produce solutions containing 1 M H₂O in atmospheres with low RHs if the solvent is hygroscopic. While TEGDME itself is not hygroscopic, the salt used in this work, LiClO₄, is, and I suspected that it acts in a similar fashion, reducing the RH required to result in 1 M H₂O in the electrolyte.

Therefore, the RH measurements from Figure 5.7 were repeated with 0.25 M LiClO₄ in TEGDME and are presented in Figure 5.9. Here, the electrolyte was kept at 20 °C, identical to the pressure cells, and the electrolyte densities were measured to allow accurate conversion of H₂O concentration from ppm, as reported by the Karl Fischer titrator, to M. It is immediately obvious that the electrolyte is more hygroscopic than TEGDME alone; here, the RH required to achieve 1 M H₂O is ~13%, compared to 30% in TEGDME alone. However, 13% RH should still be easily achievable without requiring a heavy, complex GHU. Furthermore, other Li⁺-based salts that are **less hygroscopic** could be used to increase the RH at which 1 M H₂O occurs.

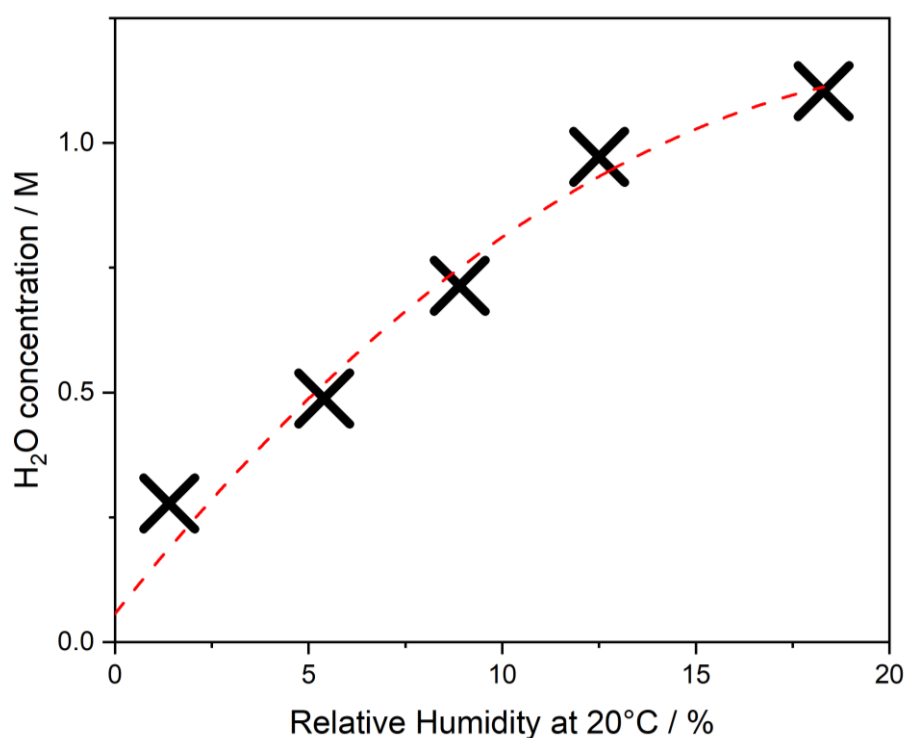


Figure 5.9: Plot showing the equilibrium between RH at 20 °C and H₂O concentration in 0.25 M LiClO₄-TEGDME electrolytes. The RH was measured with a humidity data logger and the H₂O concentration in solution was calculated from the H₂O content measured using a Karl Fischer titrator and the solution density. The best-fit line with an R² value of 0.97 is shown as the dashed red line.

5.3.2. Characterisation of discharged cells

It has now been established that a cell in an O₂ atmosphere containing a RH of 13% should result in a TEGDME-based electrolyte with 1 M H₂O, and when discharged, Li₂O₂ should form. Therefore, TEGDME-based cells were discharged in an O₂ atmosphere containing 13% RH to simulate the humid conditions in which a Li-air battery could be expected to operate. Here, a humid O₂ atmosphere was used rather than air for two reasons; firstly, to maintain the same O₂ concentration in the electrolyte as in the pressure cells, and secondly, to avoid CO₂ triggering parasitic reactions that form, for example, Li₂CO₃, which would interfere with analysis of the electrodes.

Ex situ characterisations of the positive electrodes were performed to confirm Li₂O₂, and not LiOH, forms, as in the pressure cells. Again, to aid detection of discharge products, the cells were discharged to 8 mAh.

Cells were discharged in O₂ atmospheres containing 13% RH and 0% RH with the positive electrodes analysed in one of two ways. The first was *ex situ* characterisations of the discharge product using FTIR, XRD, SEM and EDX. The same electrode was used for all of these techniques. The second analysis method was determination of the Li₂O₂ yield ($Y_{\text{Li}_2\text{O}_2}$), by means of a UV-vis titration with TiOSO₄. This method is destructive as it converts Li₂O₂ into H₂O₂ using acid, requiring a separate set of electrodes for the titration.

The discharge curves shown in Figure 5.10. Both cells quickly reach stable discharge potentials (E_{dis}), with E_{dis} at a lower potential for the 0% RH cell, consistent with the pressure cell discharge curves at 0 M and 1 M H₂O. The discharges were capacity-limited to prevent polarisation of the electrodes associated with passivation, which triggers parasitic side reactions, consuming Li₂O₂ and artificially lowering $Y_{\text{Li}_2\text{O}_2}$. Capacities of 8 mAh were used as this avoided polarisation of the electrode whilst depositing a sufficient amount of products to enable successful characterisation. $Y_{\text{Li}_2\text{O}_2}$ values of 39% and 46% were obtained for cells discharged in 0% RH and 13% RH atmospheres, respectively,

showing that a humid atmosphere was not detrimental to the formation of Li_2O_2 , as expected based on the pressure cell data. However, the overall yields for both cells were low, <50%. $Y_{\text{Li}_2\text{O}_2}$ is known to be sensitive to the type of carbon in the positive electrode; here, Super P carbon was used. To confirm that higher $Y_{\text{Li}_2\text{O}_2}$ values can be obtained with other carbon-based electrodes, cells with gas diffusion layer positive electrodes, but otherwise identical to those in Figure 5.9, were also discharged and titrated. $Y_{\text{Li}_2\text{O}_2}$ values of 68% and 61% were obtained for the cells discharged in dry and humid atmospheres, respectively, demonstrating that higher $Y_{\text{Li}_2\text{O}_2}$ values are attainable.

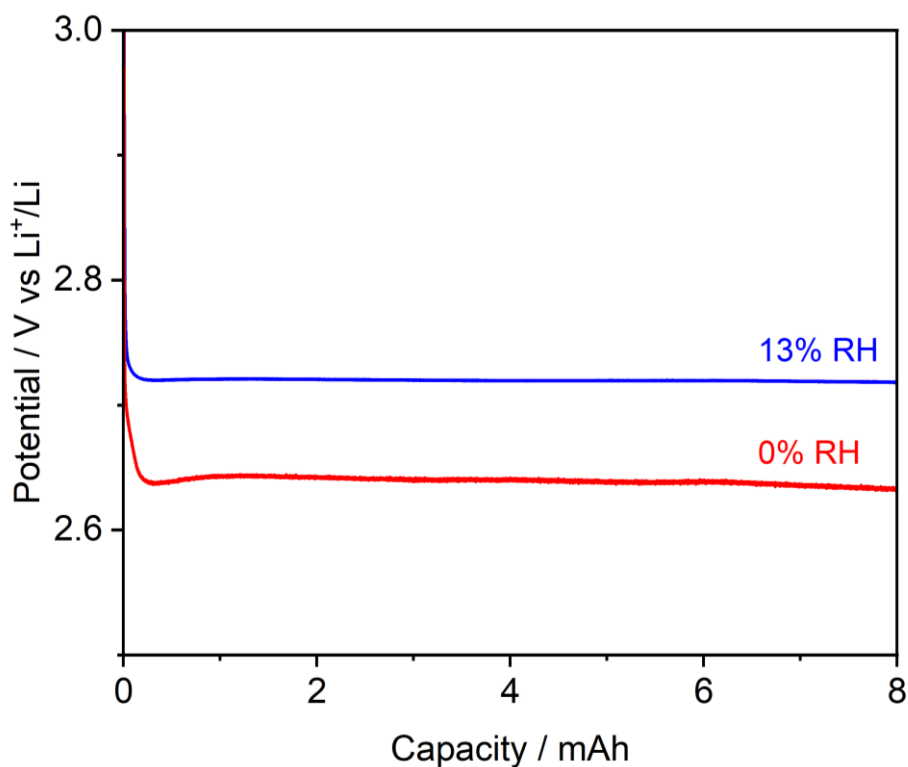


Figure 5.10: Discharge curves of Swagelok cells with positive electrodes open to O_2 atmospheres containing 0% RH (red curve) and 13% RH (blue curve). Cells consisted of Super P carbon positive electrode, glass fibre separators and Li_xFePO_4 negative electrodes. The electrolyte was dry 0.25 M LiClO_4 in TEGDME in both cases. Discharge rate, $50 \mu\text{A cm}^{-2}$.

Figure 5.11 shows the XRD patterns obtained from the positive electrode of cells discharged at 0% and 13% RH. The cell discharged in the dry atmosphere has a peak

matching the strongest reflection of the Li_2O_2 reference pattern and this peak is also very broad. Together these indicate that Li_2O_2 does not form large crystalline deposits, but rather an amorphous film. This is to be expected since O_2 reduction in dry TEGDME follows a surface mechanism, typically forming as a thin film on the electrode surface². Furthermore, there are no reflections consistent with LiOH . The XRD pattern of the cell discharged in 13% RH is markedly different. There are now multiple Li_2O_2 reflections visible and the strongest reflection is narrower than in the dry cell. This indicates that Li_2O_2 is forming larger and more crystalline Li_2O_2 deposits, which means weaker reflections can now be detected. Furthermore, LiOH reflections are also observed, which, as discussed previously, are a result of the $\text{Li}_2\text{O}_2/\text{H}_2\text{O}_2$ equilibrium.

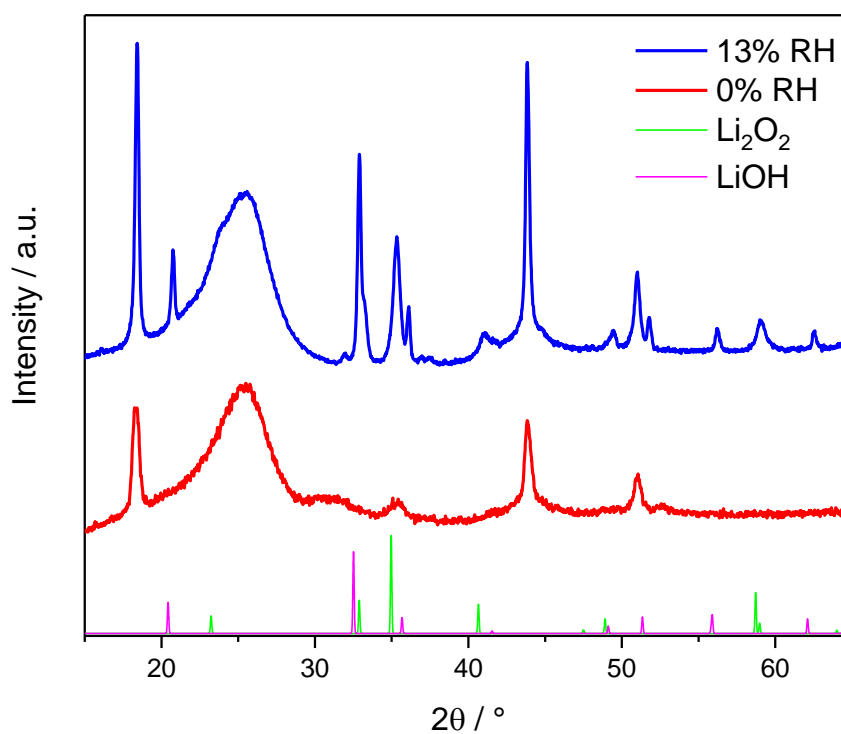


Figure 5.11: XRD patterns of discharged positive electrodes from Figure 5.9 showing Li_2O_2 forms in both cases, but the additional presence of LiOH in the 13% RH electrode. Patterns were recorded on a zero-background Si sample holder using Cu K_α radiation in a N_2 glove box. Reference spectra for Li_2O_2 and LiOH (green and magenta curves, respectively) were reproduced using data from ICSD.

However, the FTIR spectra of the electrodes contradicts the XRD patterns as the LiOH peak is absent in both electrodes (Figure 5.12). This is likely to be due to different detection limits of XRD and FTIR, with the former being more sensitive to LiOH. Indeed, similar results were obtained in the pressure cells (Figure 5.4 and Figure 5.6), where LiOH was clearly seen in XRD but a very weak peak in the FTIR may have been LiOH.

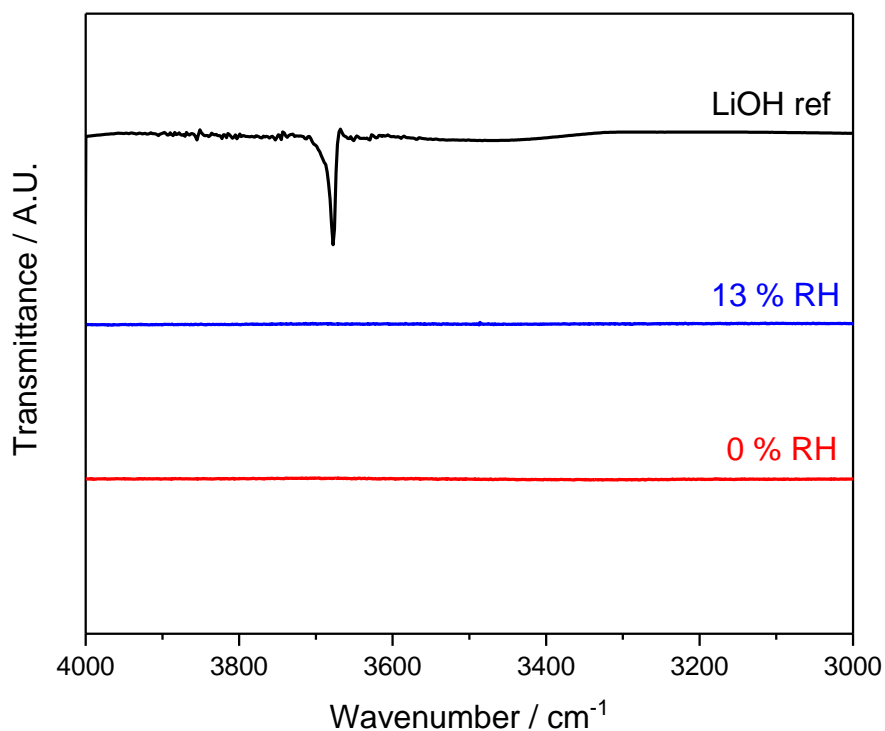


Figure 5.12: FTIR spectra of discharged positive electrodes from Figure 5.9 suggesting LiOH does not form, contradicting the XRD data in Figure 5.10. Spectra were recorded using an ATR accessory in a N_2 glove box.

The XRD patterns indicate significant morphological changes in Li_2O_2 between the dry and humid cells. The positive electrodes were therefore examined using SEM to identify the morphology of Li_2O_2 deposits in both cases. Figure 5.13 shows SEM images and oxygen EDX mapping of electrodes discharged in dry and 13% RH O_2 atmospheres. There are no visible particles on the carbon surface of the electrode discharged in the dry O_2 atmosphere (Figure 5.13a), which is to be expected since a thin film of Li_2O_2 should form. A 7 nm thick layer of Li_2O_2 would be enough to passivate the electrode

surface, which is smaller than the feature size routinely resolvable with SEM and would require analysis with transmission electron microscopy that can resolve down to an atomic level. In contrast, the surface of the electrode discharged in 13% RH (Figure 5.13c,e) has visible solid deposits. Two different morphologies were found, one of which was toroidal particles. Li_2O_2 forms this characteristic morphology when O_2 reduction occurs via the solution mechanism and has been reported numerous times in the literature. Most significantly, my results match those reported by Aetukuri *et al.*² and Schwenke *et al.*¹⁰, who were the first groups to report that, in dry glyme ether-based electrolytes, thin films of Li_2O_2 form, but when the electrolytes contain small concentrations of H_2O , toroids form instead. The second morphology found in the humid cell was a fern-like structure. This new morphology could occur for numerous reasons. The way in which Li_2O_2 grows from solution may change at high H_2O concentrations, resulting in different particle morphologies. Another possibility is that the presence of 1 M H_2O means that Li_2O_2 is solubilised, so the electrolyte contains dissolved H_2O_2 and LiOH . Following discharge, the electrode is extracted and washed with dry CH_3CN , but this would likely cause LiOH to immediately precipitate and coat the electrode surface in a thin layer of LiOH , obscuring toroidal Li_2O_2 particles beneath it. Alternatively, washing the electrode could cause Li_2O_2 to precipitate, but this reaction would be very fast compared to during the discharge and could result in this different fern-like morphology. Regardless of whether the fern-like deposits are Li_2O_2 or LiOH , the presence of visible discharge products indicates that the O_2 reduction intermediates and/or products are soluble and lead to large particles formed from solution.

EDX mapping of the electrodes was also performed to confirm that the SEM images contain O_2 reduction products. The electrode discharged in 0% RH (Figure 5.13b) was found to have O atoms across the entirety of the SEM image. This confirms, along with the XRD pattern of the electrode, that a thin film of Li_2O_2 forms on the electrode surface. In the case of the electrode discharged in 13% RH, both the toroidal (Figure 5.13d) and

fern-like deposits (Figure 5.13f) contain O atoms, indicating that they are formed from O_2 reduction. Furthermore, the EDX did not detect any Cl on the sample, ruling out the possibility that the fern-like deposits are $LiClO_4$ from the electrolyte. EDX cannot be used to detect H atoms, and as O is present in both Li_2O_2 and $LiOH$, it was not possible to definitively identify the nature of this product using this technique. However, based on $Y_{Li_2O_2}$, FTIR and XRD analyses, it is possible to say with some certainty that Li_2O_2 , not $LiOH$, is the O_2 reduction product.

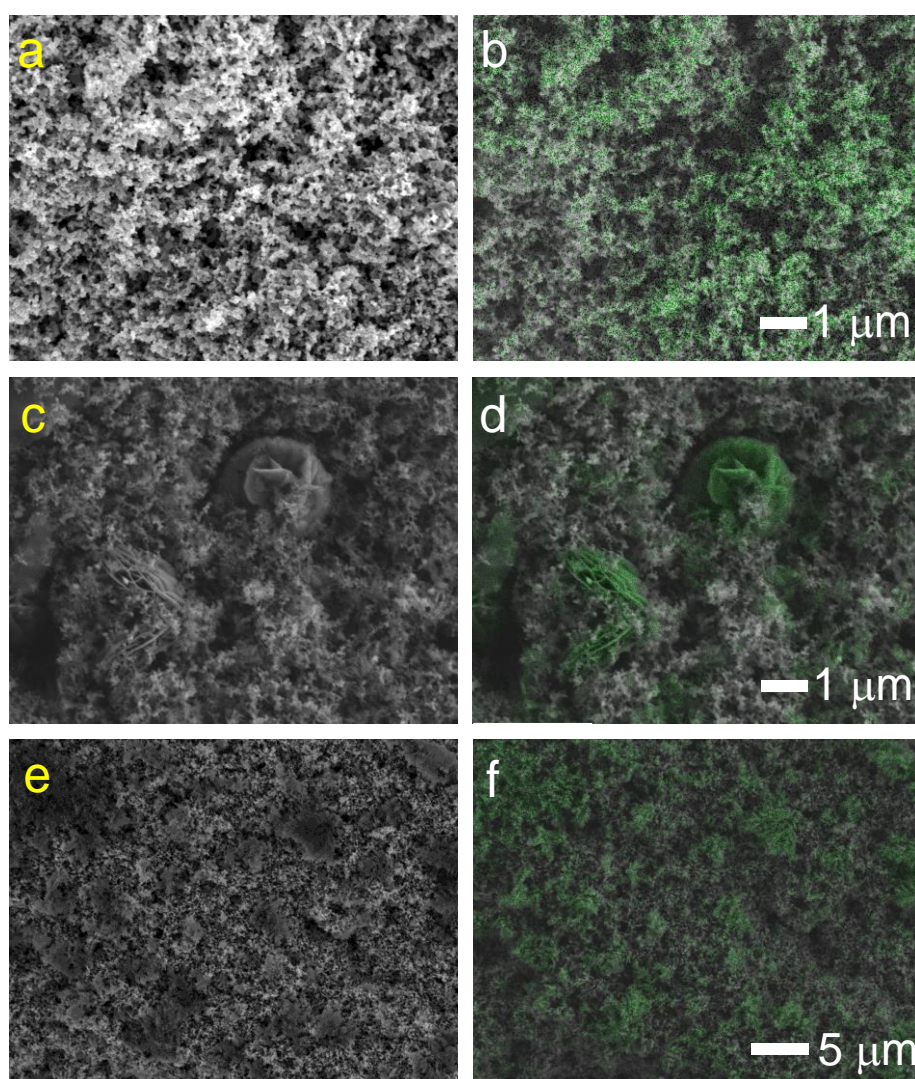


Figure 5.13: SEM images (a,c,e) and oxygen EDX (b,d,f) mapping of the positive electrodes in Figure 5.9 discharged in dry O_2 atmosphere (a,b) and 13% RH (c-f), identifying the various discharge morphologies obtained. The EDX maps are overlaid on the SEM images.

5.4. Conclusions

Pressure cells have confirmed the discharge products in CH₃CN-, TEGDME- and DMSO-based electrolytes at H₂O concentrations between 0 M and 1 M H₂O. In CH₃CN, the introduction of any H₂O leads to 4e⁻ O₂ reduction occurring simultaneously with 2e⁻ reduction. Whether the 2e⁻ or 4e⁻ reduction is the dominant reaction depends on the H₂O concentration. Below 1 M H₂O, the 2e⁻ reduction is dominant, while if the H₂O concentration is ≥1 M, the 4e⁻ reduction is dominant. In TEGDME and DMSO, only 2e⁻ O₂ reduction occurs at H₂O concentrations ≤1 M. *Ex situ* characterisation of the discharged electrodes largely supported the *in situ* results. These results confirm that the AN mechanism can rationalise the discharge product in both two-electrode and three-electrode cells.

Furthermore, I established that 1 M H₂O in the TEGDME-based electrolyte corresponds to 13% RH, which is a substantial level of humidity for the Li-O₂ battery. Cells discharged in this 13% RH O₂ atmosphere resulted in Li₂O₂ as the discharge product, demonstrating that such a humid gas stream would be acceptable in a practical Li-air battery. This humidity would be a modest target for a GHU, such that it would be likely to contribute significantly less than 32% of the battery pack mass predicted to be required for a dry gas stream. This result demonstrates reasons to be optimistic that a high energy density Li-air battery will be attainable.

5.5. References

- 1 Gallagher, K. G. *et al.* Quantifying the promise of lithium–air batteries for electric vehicles. *Energy Environ. Sci.* **7**, 1555-1563 (2014).
- 2 Aetukuri, N. B. *et al.* Solvating additives drive solution-mediated electrochemistry and enhance toroid growth in non-aqueous Li-O₂ batteries. *Nat. Chem.* **7**, 50-56 (2015).
- 3 Kwabi, D. G. *et al.* The effect of water on discharge product growth and chemistry in Li-O₂ batteries. *Phys. Chem. Chem. Phys.* **18**, 24944-24953 (2016).

- 4 Qiao, Y. *et al.* From O_2^- to HO_2^- : reducing by-products and overpotential in Li- O_2 batteries by water addition. *Angew. Chem.* **56**, 4960-4964 (2017).
- 5 Kwabi, D. G. *et al.* Chemical instability of dimethyl sulfoxide in lithium–air batteries. *J. Phys. Chem. Lett.* **5**, 2850-2856 (2014).
- 6 Sharon, D. *et al.* Oxidation of dimethyl sulfoxide solutions by electrochemical reduction of oxygen. *J. Phys. Chem. Lett.* **4**, 3115-3119 (2013).
- 7 Meini, S., Piana, M., Beyer, H., Schwämmlein, J. & Gasteiger, H. A. Effect of carbon surface area on first discharge capacity of Li- O_2 cathodes and cycle-life behavior in ether-based electrolytes. *J. Electrochem. Soc.* **159**, A2135-A2142 (2012).
- 8 Freunberger, S. A. *et al.* The lithium-oxygen battery with ether-based electrolytes. *Angew. Chem. Int. Ed.* **50**, 8609-8613 (2011).
- 9 Qian, X., Han, B., Liu, Y., Yan, H. & Liu, R. Vapor pressure of dimethyl sulfoxide and water binary system. *J. Solution Chem.* **24**, 1183-1189 (1995).
- 10 Schwenke, K. U., Metzger, M., Restle, T., Piana, M. & Gasteiger, H. A. The influence of water and protons on Li_2O_2 crystal growth in aprotic Li- O_2 cells. *J. Electrochem. Soc.* **162**, A573-A584 (2015).

6. Perspectives and future work

One of the key goals in Li-air research is to develop a battery that can operate using atmospheric O_2 . However, this risks exposing the cell to CO_2 and H_2O , which can interfere with the battery (electro)chemistry. It is well documented that CO_2 induces unwanted side-reactions that yield Li_2CO_3 , not Li_2O_2 on discharge. However, recent work has demonstrated that the effect of H_2O is more ambiguous. Depending on the electrolyte, Li_2O_2 or $LiOH$ may be the discharge product. It is imperative to understand if an electrolyte tolerates H_2O or not, since this will have consequences on the design of the battery pack. If the battery were sensitive to very low concentrations of H_2O , a sophisticated gas-handling unit (GHU) would be required to reduce the H_2O concentration to a level at which the battery comfortably operates and whose weight penalty would significantly reduce the specific energy of the battery-pack.

It is imperative to understand why an electrolyte may promote the unwanted $4e^-$ reduction of O_2 to facilitate the rational design electrolytes that will not promote it, even at molar-level H_2O concentrations. Attempts have been made to find a unifying mechanism to explain the discharge products in multiple solvents, but none can account for the discharge products in all electrolytes reported to date.

The purpose of this work was to carefully and thoroughly characterise the electrochemical reactions occurring in multiple H_2O -containing electrolytes. Ideal electrolytes, using $TBAClO_4$ as the salt, showed that the potentials and concentrations of H_2O required to induce $4e^-$ O_2 reduction differed substantially between solvents. In acetonitrile (CH_3CN), $4e^-$ reduction occurred at all O_2 reducing potentials in the presence of 1 M H_2O , while in dimethyl sulfoxide (DMSO), the $4e^-$ reduction occurred ~ 500 mV negative of the $1e^-$ reduction at H_2O concentrations of 5 M. The same overall trends were seen in Li^+ -based electrolytes. $LiOH$ formed in CH_3CN in the presence of any H_2O , while in DMSO, H_2O concentrations in excess of 1 M were required for the $4e^-$ reduction to occur. Here, tetraethylene glycol dimethyl ether (TEGDME) was also investigated and

behaved similarly to DMSO. These results showed that combination of solvent and H₂O dictated the onset potential for 4e⁻ O₂ reduction and that stabilisation of OH⁻ is the critical factor in determining this. OH⁻ is stabilised by strong Lewis acids, which have high acceptor numbers (ANs). When the ANs of H₂O/solvent mixtures were recorded, the AN value for CH₃CN was much greater than DMSO or TEGDME at all H₂O concentrations, as expected. This was confirmed using pressure cells, which detected a change from the 2e⁻ to 4e⁻ reduction in CH₃CN as the H₂O concentration increased, while it remained constant up to 1 M H₂O in DMSO and TEGDME. Together, this demonstrated that the Lewis acidity of the mixture determines whether 2e⁻ or 4e⁻ O₂ reduction occurs.

The fact that TEGDME sustains 2e⁻ O₂ reduction in the presence of 1 M H₂O is promising. The implications of this result on the performance requirements of a GHU were considered. A relative humidity of 13% at 20 °C was found to be equivalent to 1 M H₂O in solution, suggesting that a small, light-weight GHU could be used for a Li-air battery.

The unifying mechanism proposed here explains the discharge products in DMSO, CH₃CN and TEGDME, but it should also predict other solvents that would not promote the 4e⁻ reduction. Therefore, this should be tested in future work. One would expect N,N-dimethylacetamide and hexamethylphosphoramide to undergo 2e⁻ O₂ reduction in the presence of significant H₂O concentrations, based on their acceptor number values (13.6 and 10.6, respectively). However, both molecules H-bond with H₂O, like, DMSO, so would likely be unsuitable for Li-air batteries open to a humid atmosphere. Nevertheless, if these solvents are found to undergo 2e⁻ reduction at H₂O concentrations of 1 M or higher, this result would validate the mechanism. It would also be of interest to combine TEGDME with a more hydrophobic salt than was used here to check whether a battery could withstand even higher relative humidities.

Finally, a similar study involving CO₂ should also be performed to establish whether any concentration of CO₂ could be tolerated by the battery so that the GHU requirements for both H₂O and CO₂ are known.

Appendix 1: N₂ electrochemistry

Since H₂O is present in the organic electrolytes used in this work, there is the possibility that H₂ evolution or O₂ evolution could occur on the cathodic and anodic sweeps, respectively, and be confused for the O₂/O₂⁻ or O₂/Li₂O₂ redox processes. Therefore, cyclic voltammograms (CVs) were recorded under N₂ to confirm that the electrochemistry in Chapters 3 and 4 were due to O₂ reduction and not H₂ evolution nor O₂ evolution (Figures A1.1-A1.5). Separate cathodic (blue dashed lines) and anodic (red dashed lines) CVs were recorded. Fresh electrodes were used for each CV. The O₂ voltammetry from Chapter 3 and 4 are included for ease of comparison. Experimental conditions for these CVs were identical to the O₂ CVs except for the electrolytes being N₂-saturated here.

RRDE backgrounds were also recorded (Figures A1.6-A1.14). Here, only the disk currents are shown under N₂ and O₂ (reproduced from Chapters 3 and 4). The same experimental conditions were used as in Chapters 3 and 4, other than saturating with N₂.

Appendix 1

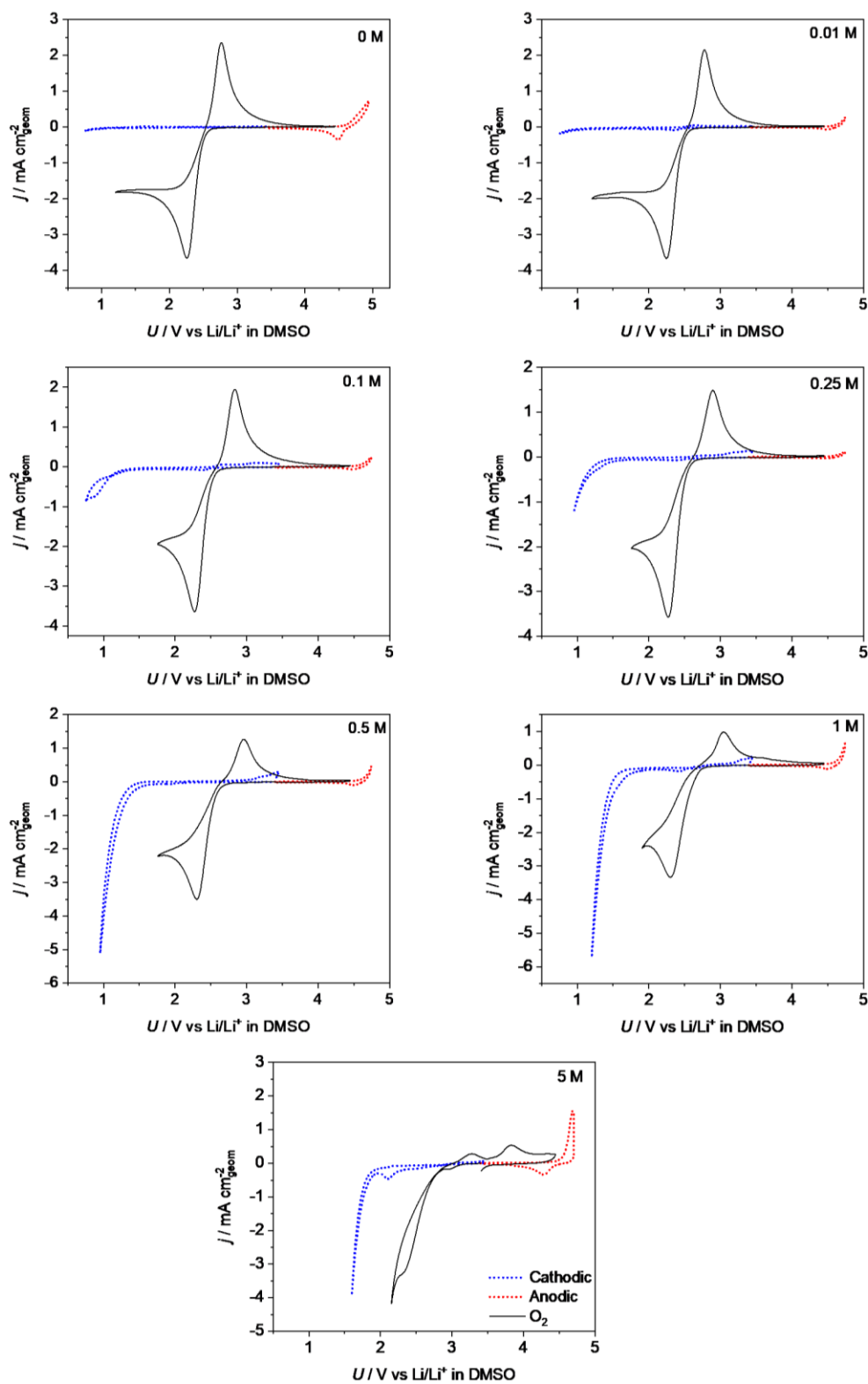


Figure A1.1: CVs recorded with N_2 -saturated 0.25 M TBAClO_4 in CH_3CN containing the indicated H_2O concentrations. O_2 CVs are reproduced from Figure 3.2.

Appendix 1

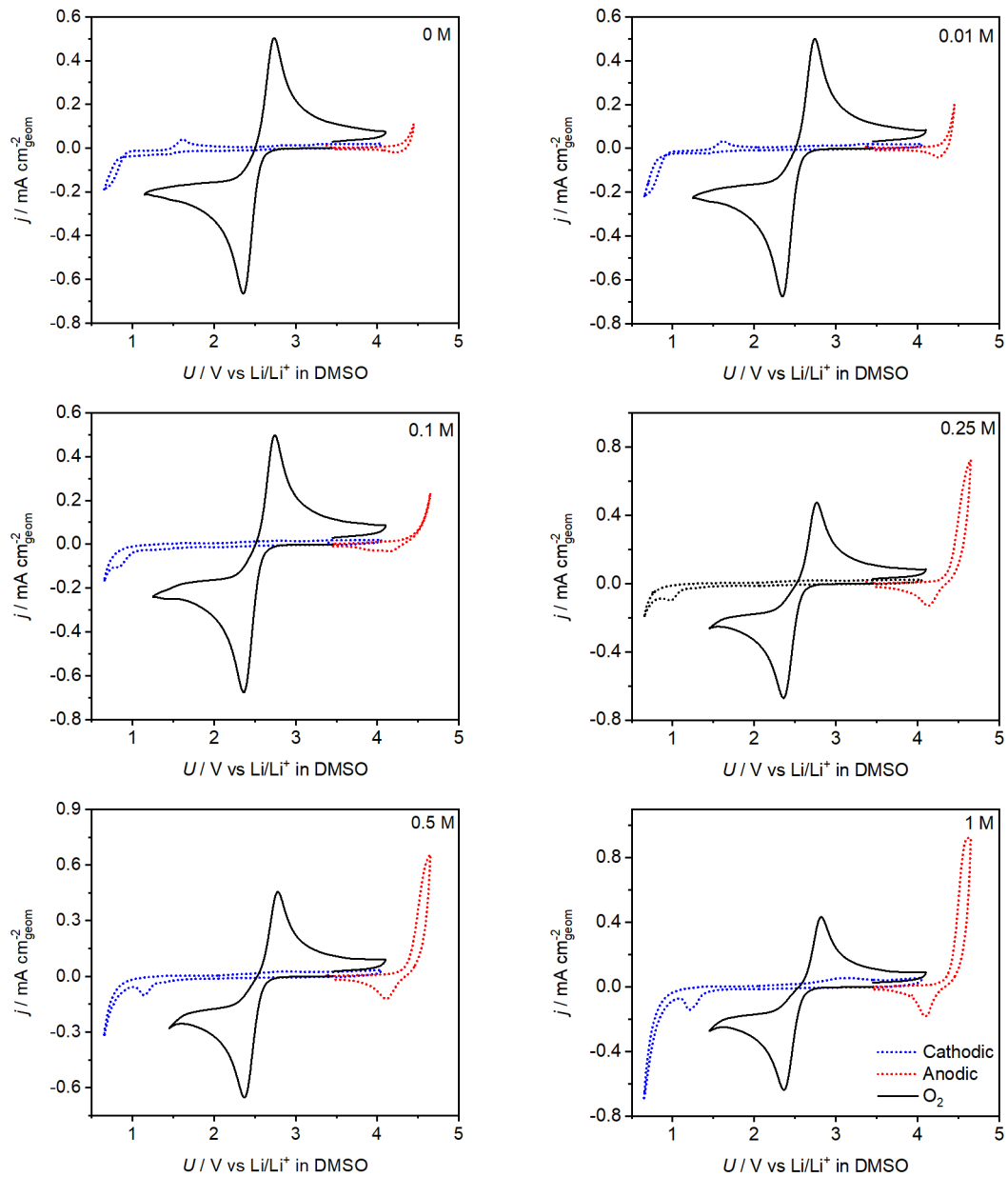


Figure A1.2: CVs recorded with N_2 -saturated 0.25 M TBAClO_4 in DMSO containing the indicated H_2O concentrations. O_2 CVs are reproduced from Figure 3.3.

Appendix 1

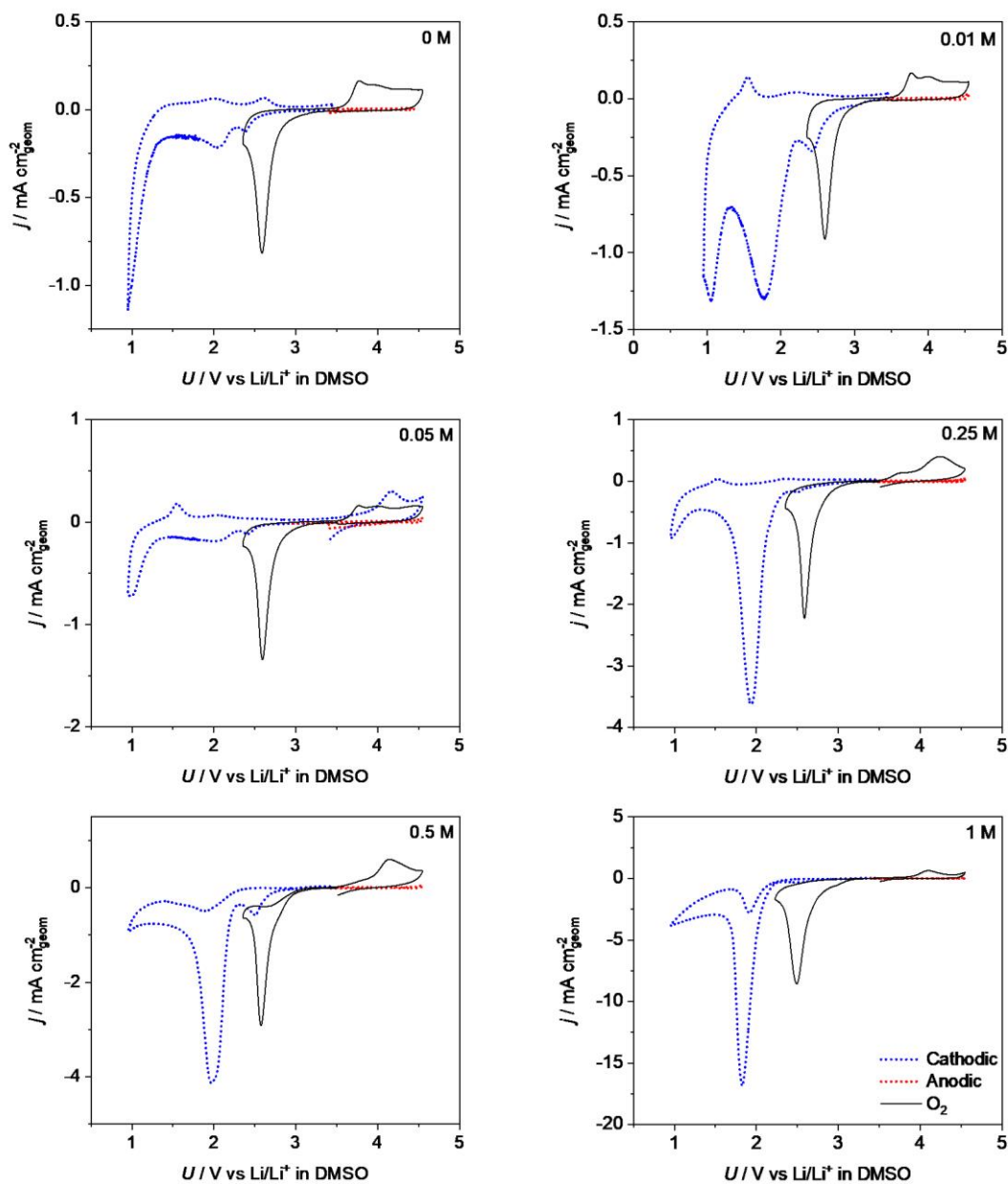


Figure A1.3: CVs recorded with N_2 -saturated 0.25 M LiClO_4 in CH_3CN containing the indicated H_2O concentrations. O_2 CVs are reproduced from Figure 4.3.

Appendix 1

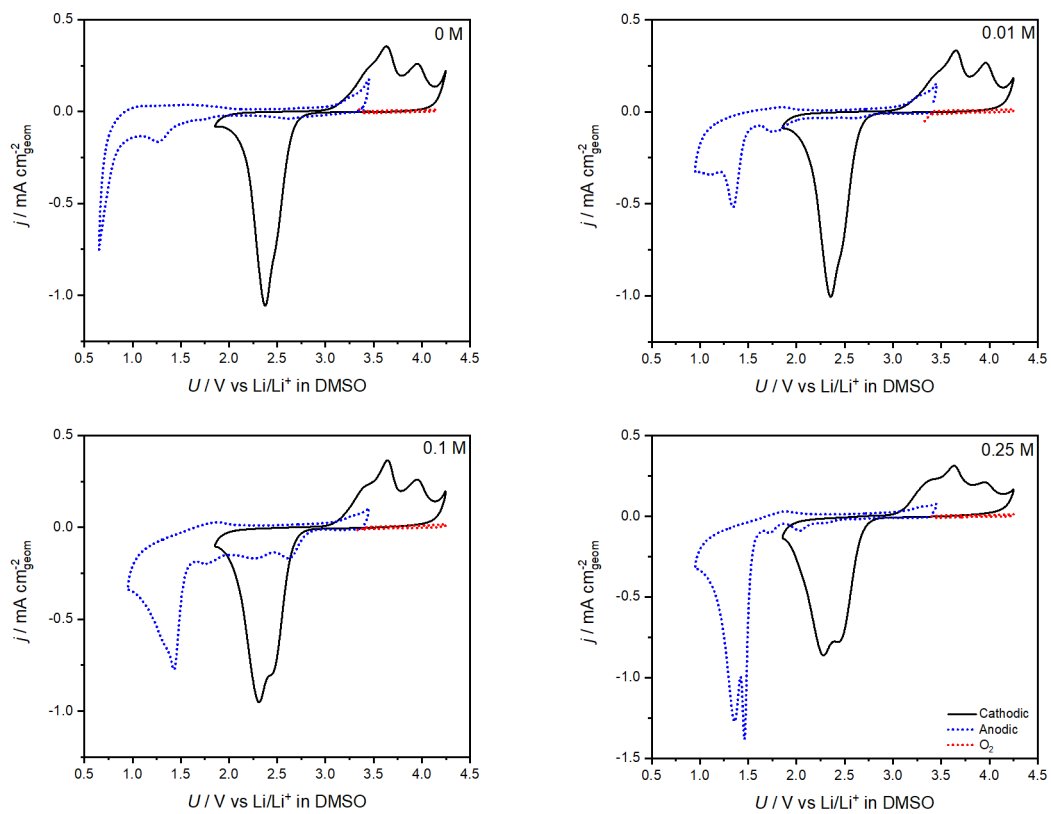


Figure A1.4: CVs recorded with N_2 -saturated 0.25 M LiClO_4 in DMSO containing the indicated H_2O concentrations. O_2 CVs are reproduced from Figure 4.4

Appendix 1

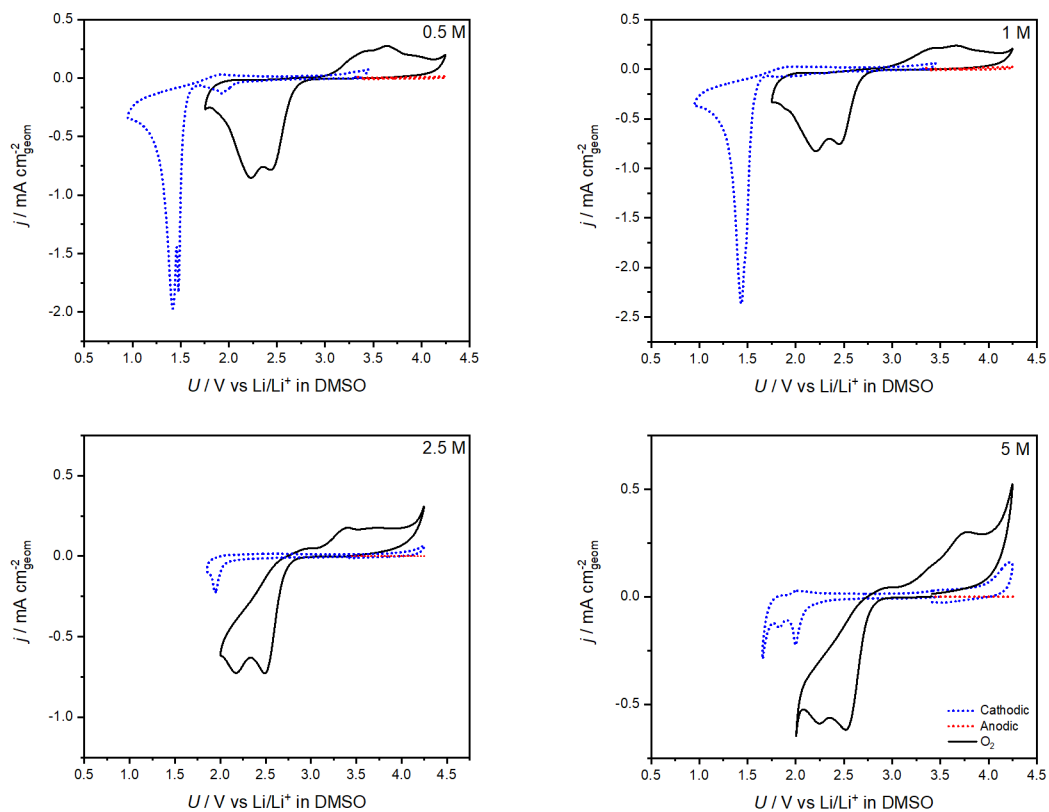


Figure A1.5: CVs recorded with N₂-saturated 0.25 M LiClO₄ in DMSO containing the indicated H₂O concentrations. O₂ CVs are reproduced from Figure 4.4.

Appendix 1

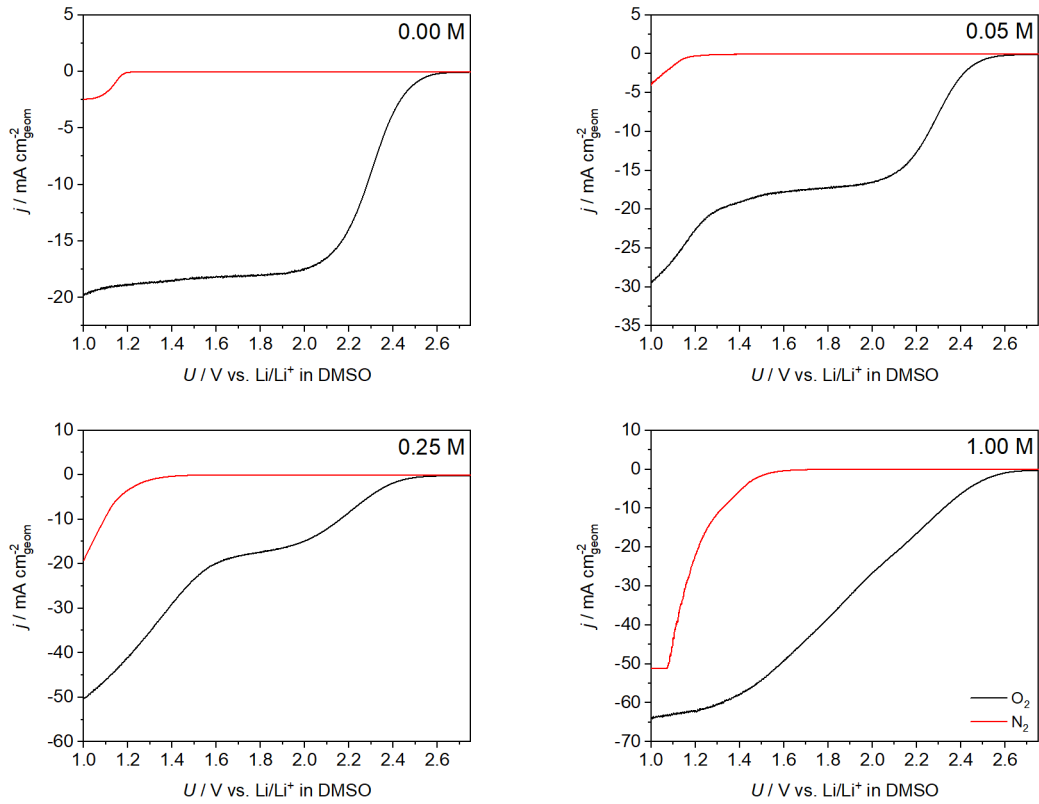


Figure A1.6: RRDE polarisation curves under N_2 (red traces) and O_2 (black traces) using a Au disk in 0.25 M TBAClO_4 in CH_3CN with the indicated H_2O concentrations.

The O_2 polarisation curves are reproduced from Figure 3.6.

Appendix 1

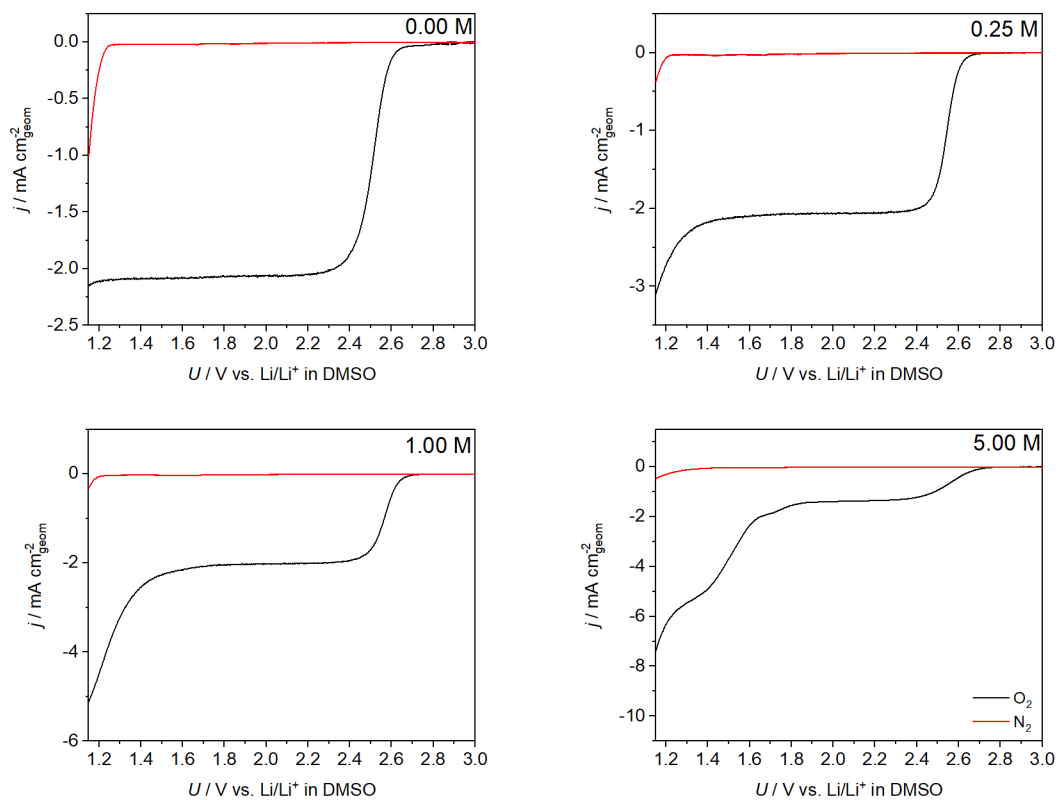


Figure A1.7: RRDE polarisation curves under N_2 (red traces) and O_2 (black traces) using a Au disk in 0.25 M TBAClO_4 in DMSO with the indicated H_2O concentrations.

The O_2 polarisation curves are reproduced from Figure 3.7.

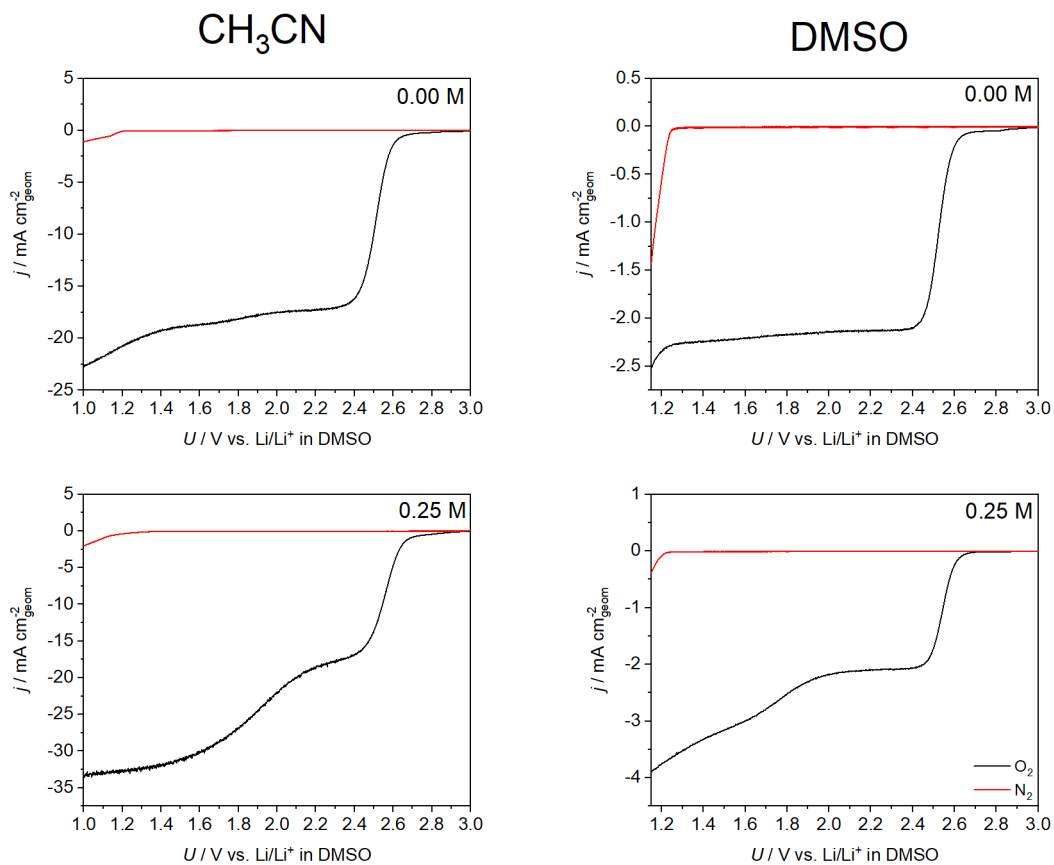


Figure A1.8: RRDE polarisation curves under N₂ (red traces) and O₂ (black traces) using a GC disk in 0.25 M TBAClO₄ in CH₃CN and DMSO with the indicated H₂O concentrations. The O₂ polarisation curves are reproduced from Figure 3.8.

Appendix 1

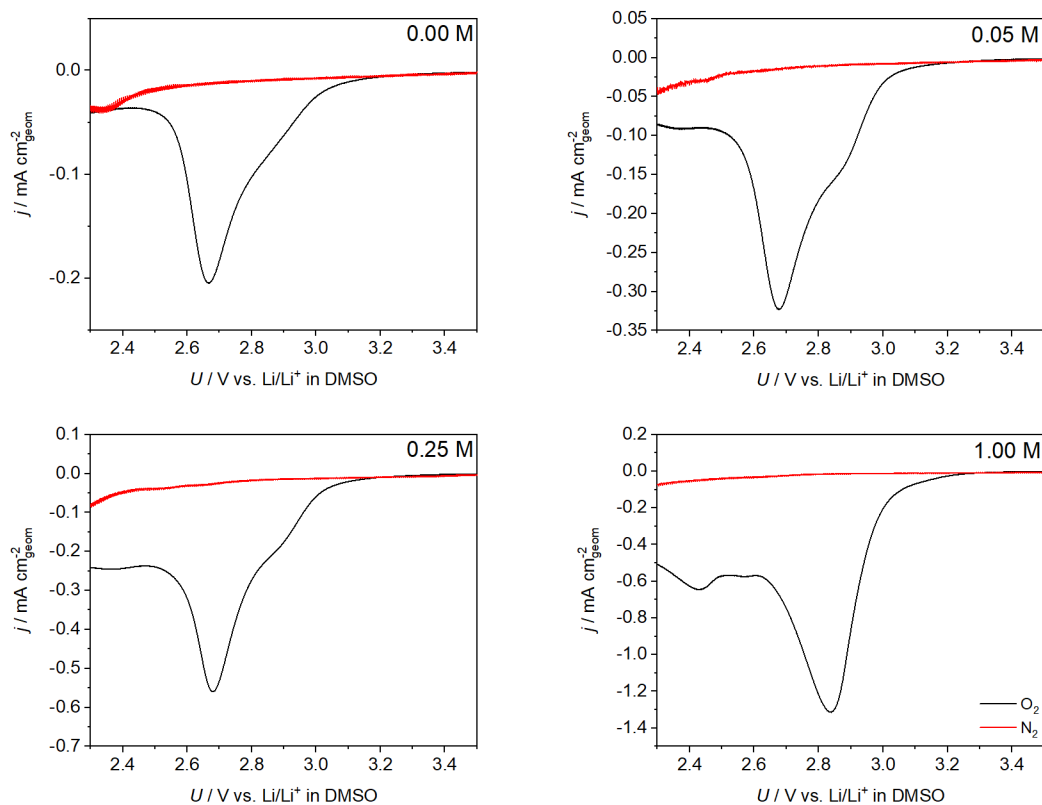


Figure A1.9: RRDE polarisation curves under N_2 (red traces) and O_2 (black traces) using a Au disk in 0.25 M LiClO_4 in CH_3CN with the indicated H_2O concentrations.

The O_2 polarisation curves are reproduced from Figure 4.6.

Appendix 1

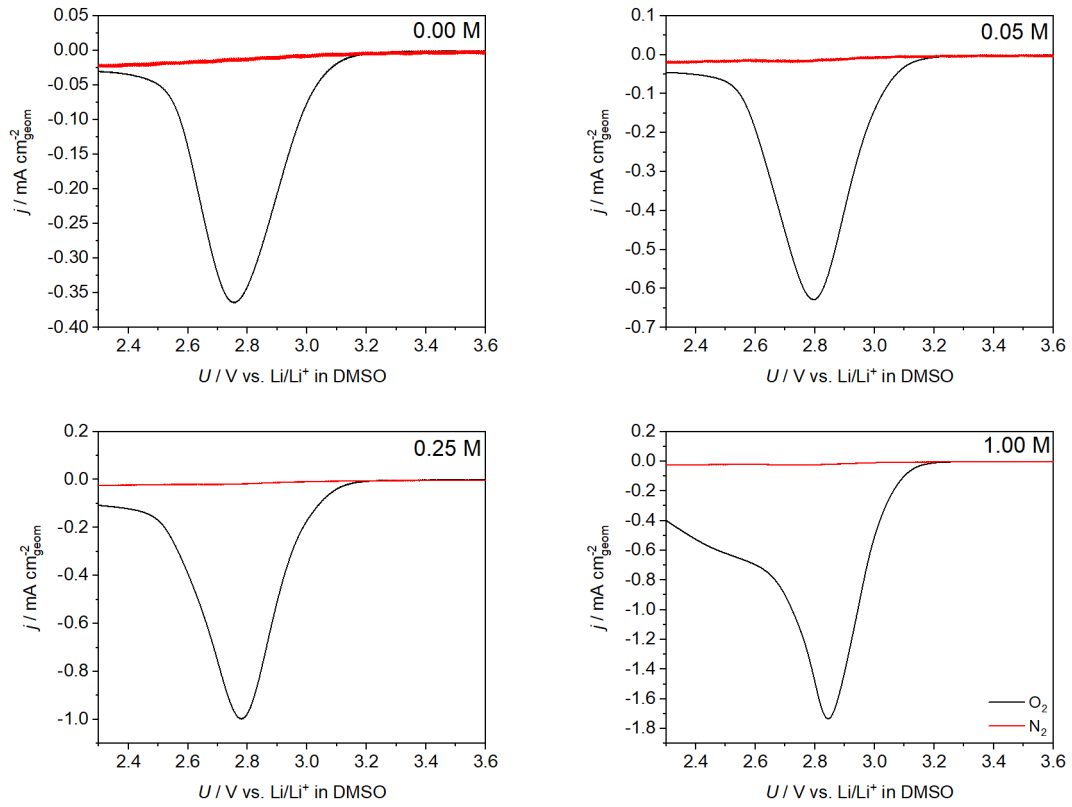


Figure A1.10: RRDE polarisation curves under N_2 (red traces) and O_2 (black traces) using a GC disk in 0.25 M LiClO_4 in CH_3CN with the indicated H_2O concentrations. The O_2 polarisation curves are reproduced from Figure 4.7.

Appendix 1

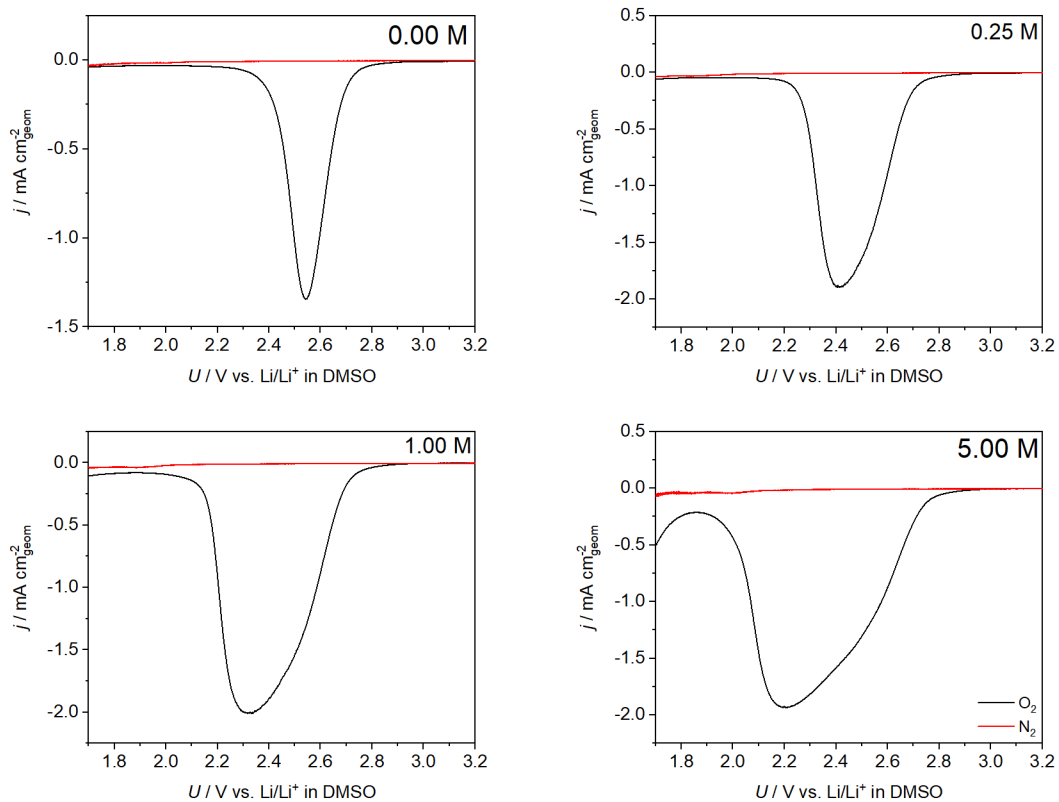


Figure A1.11: RRDE polarisation curves under N_2 (red traces) and O_2 (black traces) using a Au disk in 0.25 M LiClO_4 in DMSO with the indicated H_2O concentrations.

The O_2 polarisation curves are reproduced from Figure 4.8.

Appendix 1

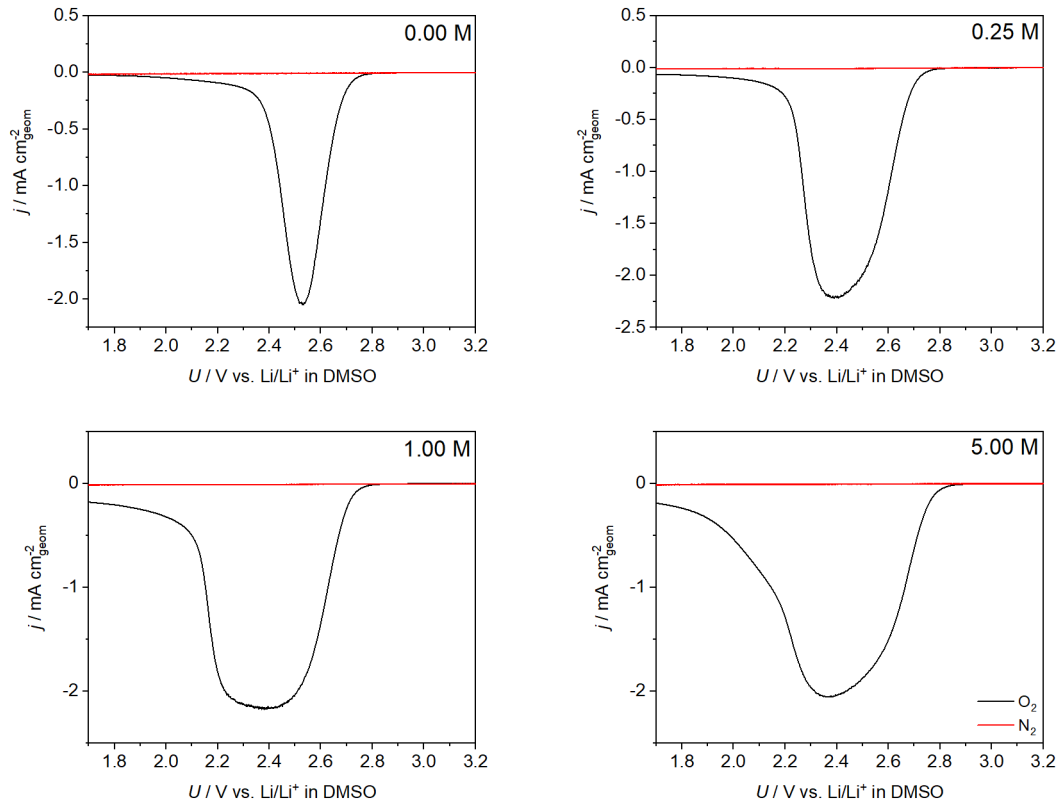


Figure A1.12: RRDE polarisation curves under N_2 (red traces) and O_2 (black traces) using a GC disk in 0.25 M LiClO_4 in DMSO with the indicated H_2O concentrations.

The O_2 polarisation curves are reproduced from Figure 4.9.

Appendix 1

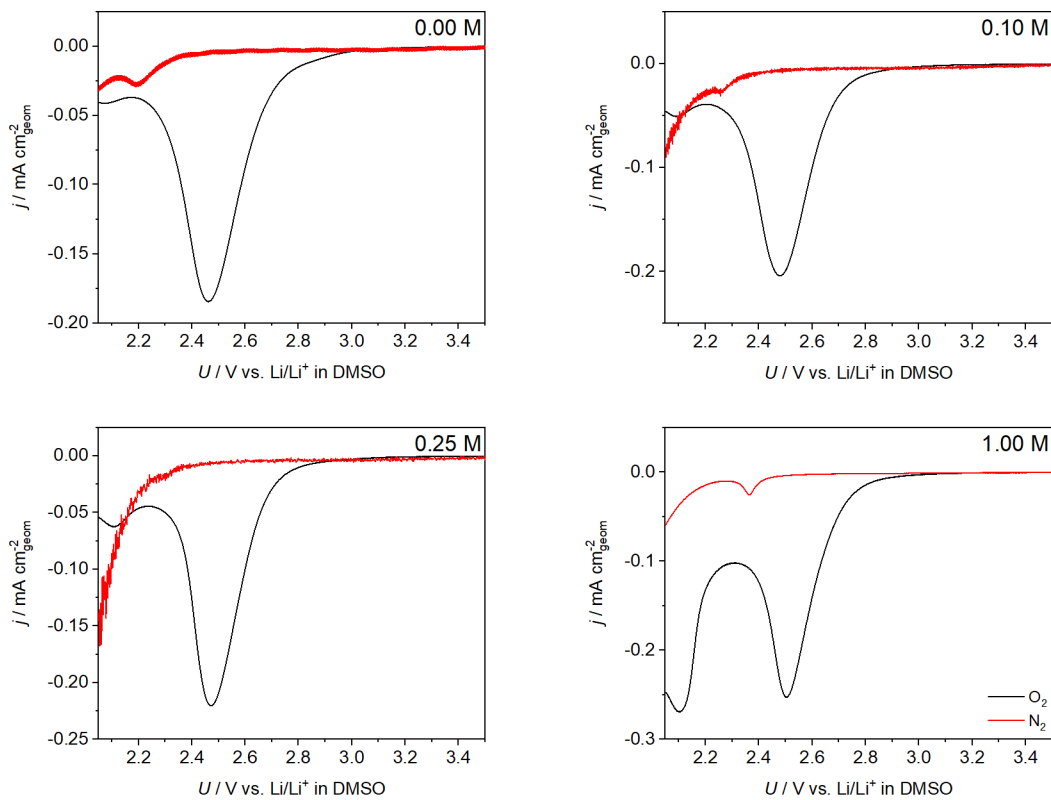


Figure A1.13: RRDE polarisation curves under N_2 (red traces) and O_2 (black traces) using a Au disk in 0.25 M LiClO_4 in TEGDME with the indicated H_2O concentrations.

The O_2 polarisation curves are reproduced from Figure 4.10.

Appendix 1

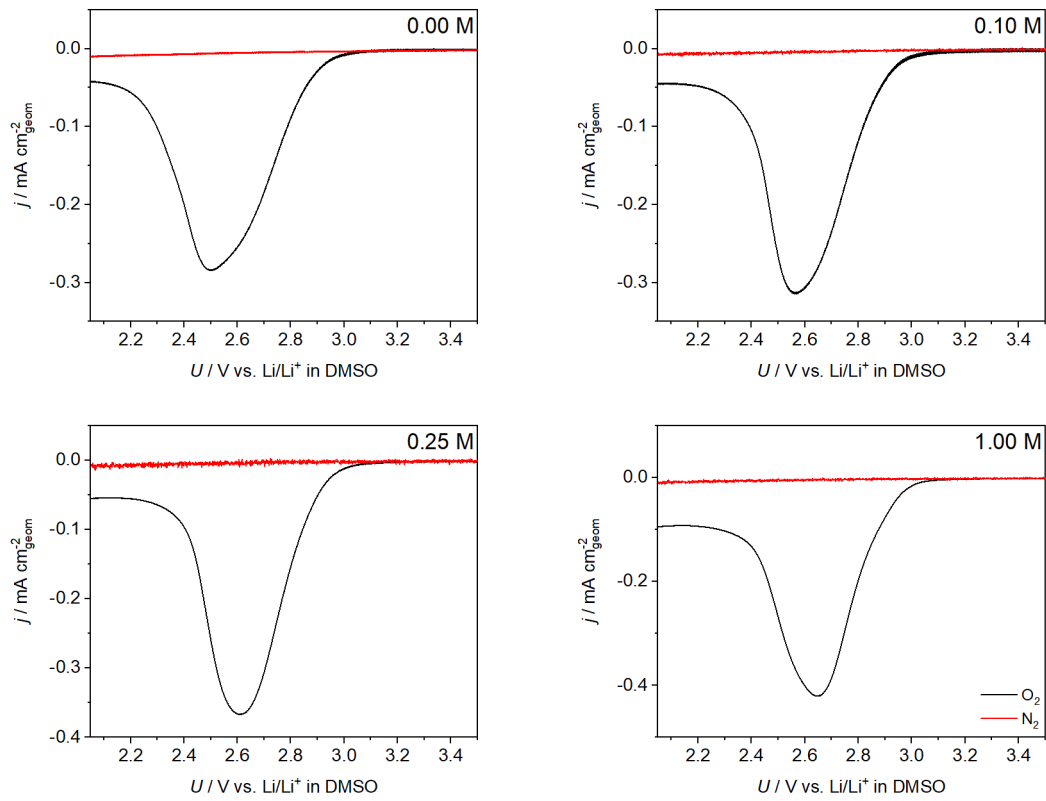


Figure A1.14: RRDE polarisation curves under N_2 (red traces) and O_2 (black traces) using a Au disk in 0.25 M LiClO_4 in TEGDME with the indicated H_2O concentrations.

The O_2 polarisation curves are reproduced from Figure 4.11.

Appendix 2

Table A2.1: Reference values for Raman signals of solvents used in SERS

Species	Mode	Raman shift / cm^{-1}	Reference
CH_3CN	CCN bending	380	1
	CCN bending overtone	754	
	C-C stretching	920	
	CH_3 rocking	1044	
DMSO	CSC out-of-plane bend	309	2
	CSO out-of-plane bend	333	
	CSO in-plane rock	382	
	CS symmetric stretch	667	
	CS antisymmetric stretch	698	
	HCH rocking	953	
	SO symmetric stretch of dimer	1026	
	SO antisymmetric stretch of dimer	1042	
SO symmetric stretch of monomer	1058		
	HCH deformation	1307	

Table A2.2: Reference values for Raman signals of ionic species present in SERS

Species	Mode	Raman shift / cm^{-1}	Reference
$\text{O}_2\text{-Au}$	Au-O stretching	490	3
O_2^-	O-O stretching	1108	3
ClO_4^-	Symmetric stretch	931	4
	CH2 twisting	1322	
	CH2 twisting	1274	
	CH3 rocking	1170	
	CH3 rocking, CC stretching	1150	
	CH3 rocking, CC stretching	1132	
	CH3 rocking, CC stretching	1108	
	CC stretching	1065	
TBA^+	CC stretching, CN stretching	1054	5
	CC stretching	1005	
	CH3 rocking, CH2 rocking, CN stretching	907	
	CH3 rocking, CC stretching	877	
	CH3 rocking, CH2 rocking, CN stretching	800	
	CH3 rocking, CH2 rocking, CN stretching	763	
	CH2 rocking	740	
	CCC deformation	253	

References

- 1 Neelakantan, P. Raman spectrum of acetonitrile. *P. India Acad. Sci A* **60**, 422-424 (1964).

Appendix 2

2 Martens, W. N., Frost, R. L., Kristof, J. and Theo Kloprogge, J., Raman spectroscopy of dimethyl sulphoxide and deuterated dimethyl sulphoxide at 298 and 77 K. *J. Raman Spectrosc.* **33**, 84-91 (2002).

3 Galloway, T. A.; Hardwick, L. Utilizing in situ electrochemical SHINERS for oxygen reduction reaction studies in aprotic electrolytes. *J. Phys. Chem. Lett.* **7**, 2119-2124 (2016).

4 Ratcliffe, C. I., Irish, D.E. Vibrational spectral studies of solutions at elevated temperatures and pressures. VI. Raman studies of perchloric acid. *Can. J. Chem.* **62**, 1134-1144 (1984).

6 del Puerto, E., Cuesta, A., Sanchez-Cortez, S., Garcia-Ramos, J. V., Domingo, C. Electrochemical SERS study on a copper electrode of the insoluble organic pigment quinacridone quinone using ionic liquids (BMIMCl and TBAN) as dispersing agents. *Analyst*, **138**, 4670-4676 (2013).